

**DEPHOSPHORIZATION KINETICS FOR REACTION OF
BLOATED METAL DROPLETS WITH OXIDIZING SLAG**

**DEPHOSPHORIZATION KINETICS FOR REACTION OF
BLOATED METAL DROPLETS WITH OXIDIZING SLAG**

By

KEZHUAN GU, B.ENG., M.ENG

A Thesis

Submitted to the School of Graduate Studies

In Partial Fulfilment of the Requirements

For the Degree

Doctor of Philosophy

McMaster University

© Copyright by Kezhuan Gu, July, 2017

DOCTOR OF PHILOSOPHY (2017) McMaster University

(Materials Science and Engineering) Hamilton, Ontario

TITLE: Dephosphorization Kinetics for Reaction of
Bloated Metal Droplets with Oxidizing Slag

AUTHOR: Kezhuan Gu, B.Eng., M.Eng., (Central South
University, China)

SUPERVISOR: Dr. Kenneth S. Coley and Dr. Neslihan Dogan

NUMBER OF PAGES: xvi, 188

ABSTRACT

Dephosphorization is one of the most important refining reactions in Steelmaking in the Basic Oxygen Furnace (BOF). Dephosphorization can only occur by reaction between the metal and the slag and is linked in a rather complex way to the decarburization of droplets in the gas-slag-metal emulsion zone. Decarburization affects dephosphorization of metal droplets by influencing the following: residence time, driving force and mass transfer of phosphorus. Residence time is the contact time of metal droplets with slag, which is determined based on the bloating behavior of metal droplets. This particular aspect of dephosphorization has been studied recently by researchers in the author's laboratory and others. Therefore, the influence of decarburization on driving force for dephosphorization and mass transfer of phosphorus in the metal phase was the main focus of this study.

The effect of decarburization on driving force for dephosphorization was studied in detail by varying decarburization rates which are a function of metal sulfur content, and determining the dynamic interfacial oxygen potential. The dephosphorization driving force was found to have a strong inverse relationship with increasing decarburization rate because the associated oxygen consumption decreases the interfacial oxygen potential. The decreased driving force further affected dephosphorization kinetics by shifting the rate controlling step, to include a greater influence of mass transport in the slag. This observation showed a good agreement with other work on dephosphorization kinetics in the published literature.

The dynamic interfacial oxygen potential, controls dephosphorization driving force, between an iron carbon alloy and oxidizing slag was calculated based on a mathematical model, which combines measured decarburization rates with mass transfer of FeO in the slag. With this model, the mass transfer coefficient of "FeO" in slag, k_{FeO} , was firstly determined as a function of the fraction of liquid slag and total iron oxide in the slag. The influence of dynamic interfacial oxygen potential on dephosphorization kinetics was sequentially analyzed by determining the time dependent interfacial phosphorus partition

ratio. The agreement with literature observations confirmed the reliability of the interfacial oxygen potential model developed in this study.

Comparing the experimentally observed dephosphorization behaviour of carbon containing droplets with that of carbon free droplets, mass transfer coefficient for phosphorus in the metal for carbon containing droplets was found to be two orders of magnitude higher than that for carbon free droplets because of the stirring effect provided by CO gas generation inside the metal droplet. By combining a theoretical analysis of CO bubble nucleation kinetics with surface renewal theory, the predicted mass transfer coefficient of phosphorus in the metal phase was in good agreement with experimentally measured results. Extension of this analysis to results from a number of published studies on dephosphorization, showed an excellent qualitative agreement with experimental observations, *i.e.*, the effect of silicon in the metal and the effect of iron oxide in the slag. The combined effect of silicon and temperature also showed agreement but the effect of temperature for silicon free metal was not fully explained.

ACKNOWLEDGEMENTS

I am greatly indebted to my supervisors, Dr. Ken Coley and Dr. Neslihan Dogan for their guidance, support and encouragement throughout my PhD studies. They were great mentors both in academic and non-academic issues. I would like to express my special gratitude to Dr. Ken Coley for all I have learnt from him, and the boundless freedom he gave me to explore new ideas in my project. I truly enjoyed all the intense discussions that we have had. Dr. Jeffrey Hoyt and Dr. Hatem Zurob are greatly appreciated for their helpful suggestions as members of my supervisory committee.

I wish to thank many faculties, researchers, staff and graduate students in the department of Materials Science and Engineering for providing a cooperative academic environment. I am particularly grateful to Brain Jamison, Xiaogang Li, Doug Culley and Ed McCaffery for their assistance in the course of this work. I also would like to thank John Thompson for his efforts to make sure the project was running smoothly. Many thanks to all people in high temperature process group and in particular, Wangzhong Mu, for his friendship and support for the past two years.

I would like to thank McMaster Steel Research Center and its member companies, Natural Science Engineering Research Council and McMaster University for financial support.

I am cordially grateful to my best friend Xiaoyue Wang who I met in McMaster University for her encouragement and support, and sharing together the good and rough time we had throughout the years.

Lastly, I wish to express my deepest gratitude to my parents, sisters and brothers for their understanding and constant support throughout my life. I dedicate this thesis to my beloved parents: Zhanqun Gu and Linong Wen.

Table of Contents

Chapter 1	1
Introduction	1
1.1 Research Background	1
1.2 The Objectives of This Study	3
1.3 Thesis Outline	4
Chapter 2	6
Literature Review	6
2.1 Thermodynamics of Dephosphorization	6
2.1.1 Reaction of Phosphorus Removal	6
2.1.2 Phosphorus in Slag	7
2.1.3 Phosphorus Partition L_P between Metal and Slag	9
2.1.4 Silicate Structure and Slag Basicity	13
2.1.5 Phosphate Capacity	17
2.2 Kinetics of Dephosphorization	19
2.2.1 Rate-Determining Step	19
2.2.2 Rate-Equations for Dephosphorization	22
2.2.3 Transient Reaction Surface Area	24
2.2.4 Shift of Rate Determining Step	27
2.2.5 Dynamic Interfacial Oxygen Potential	27
2.2.6 Mass Transfer of “FeO” in the Slag	30
2.3 Bloated Metal Droplet in BOF	31
2.3.1 Metal Droplet Generation Rate and Size Distribution	31
2.3.2 Residence Time	31
2.3.3 Decarburization and Swelling of Metal droplets	33
2.3.4 CO Nucleation inside Metal Droplet	35
2.3.5 Modeling of Dephosphorization Using Bloated Droplet Theory	37
2.3.6 Dephosphorization of Bloated Droplets	38
Chapter 3	40

The Influence of Sulfur on Dephosphorization Kinetics between Bloated Metal Droplets and Slag Containing FeO	40
3.1 Introduction.....	41
3.2 Experimental Procedure.....	43
3.3 Experimental Results	45
3.3.1 Measurement of CO Evolution Rate.....	45
3.3.2 X-ray Fluoroscopy Observations of Droplets.....	46
3.3.3 Dephosphorization of Bloated Droplets.....	48
3.4 Discussion	52
3.4.1 Effect of Sulfur on Droplet Swelling	52
3.4.2 Effect of Sulfur on CO Evolution	53
3.4.3 Dephosphorization Kinetics	58
3.4.4 Role of Partition Ratio on Reaction Kinetics	62
3.5 Conclusion	62
3.6 References.....	63
Chapter 4.....	65
The Dynamic Interfacial Oxygen Potential between Iron-Carbon Droplets and Oxidizing Slag	65
4.1 Introduction.....	66
4.2 Experimental Procedure.....	67
4.3 Results.....	68
4.3.1 Decarburization and Dephosphorization of Bloated Droplets	68
4.3.2 Mass Transfer Coefficient of FeO and Dynamic Interfacial Oxygen Potential	71
4.4 Discussion	73
4.4.1 Mass Transfer of FeO in the Slag	73
4.4.2 Dynamic Interfacial Oxygen Potential.....	79
4.4.3 The Effect of Dynamic Interfacial Oxygen Potential on Dephosphorization Kinetics	81
4.5 Conclusion	85

4.6	Appendix.....	86
4.7	References.....	93
Chapter 5.....		95
Dephosphorization Kinetics for Bloated Metal Droplets Reacting with Slag Containing FeO: The Influence of CO Bubbles on the Mass Transfer of Phosphorus in the Metal....		95
5.1	Introduction.....	96
5.2	Experimental Procedure.....	97
5.3	Experimental Results.....	100
5.3.1	Decarburization as a Function of Temperature	100
5.3.2	Droplet Swelling Behavior at Different Temperature	102
5.3.3	Dephosphorization of Droplets with and without Carbon	104
5.4	Discussion	106
5.4.1	Dephosphorization Kinetics of Carbon Free Droplets.....	106
5.4.2	Dephosphorization Kinetics of Carbon Containing Droplets.....	109
5.4.3	Estimation of k_m at Different Stages of Reaction	116
5.4.4	The Effect of Temperature on k_m	124
5.4.5	Industrial Relevance.....	128
5.5	Conclusion	129
5.6	Appendix.....	130
5.7	References.....	131
Chapter 6.....		133
An Assessment of the General Applicability of the Relationship between Nucleation of CO Bubbles and Mass Transfer of Phosphorus in Liquid Iron Alloys.....		133
6.1	Literature Review	134
6.2	Theoretical Framework.....	137
6.3	Experimental Procedure.....	142
6.3.1	Decarburization as a Function of Droplet Mass	143
6.3.2	Swelling Behavior of Droplets with Different Mass	144
6.3.3	Dephosphorization of Droplets with Different Mass.....	145
6.4	Results and Discussion	147

6.4.1	Effect of Droplet Mass	147
6.4.2	Effect of Silicon	150
6.4.3	Effect of Temperature	156
6.4.4	Effect of Iron Oxide in the Slag.....	159
6.5	Conclusion	162
6.6	Appendix.....	163
6.7	References.....	165
Chapter 7	167
Application of High Basicity Slag	167
7.1	Introduction.....	167
7.2	Experimental Procedure.....	167
7.3	Experimental Results	168
7.4	Discussion	169
7.5	Summary	172
Chapter 8	173
Concluding Remarks	173
8.1	Key Findings and Contributions	173
8.1.1	General Overview	173
8.1.2	Specific Findings	174
8.2	Future Work.....	176
Appendix	178
Error Analysis	178
Reference	181

LIST OF FIGURES

Chapter 2

Figure 2.1 Phosphide and phosphate concentrations in the CaO-Al ₂ O ₃ slag as a function of oxygen partial pressure ^[16]	7
Figure 2.2 Schematic representation of depolymerization of silicate network by the addition of basic oxides ^[49]	13
Figure 2.3 The relationship between $\log C_{PO_4^{3-}}$ and theoretical optical basicity ^[60]	18
Figure 2.4 Relationship between k_s and viscosity of slag with respect to different slag components ^[18]	21
Figure 2.5 Comparison of oxidization rates of elements in metal by FeO-slag with MnO-slag ^[77]	22
Figure 2.6 Kinetic data plots using integrated rate equation with constant surface area ^[83]	25
Figure 2.7 Kinetic data plots using integrated rate equation with time averaged surface area ^[83]	26
Figure 2.8 The interfacial oxygen potential $P_{O_2}^i$ as a function of α_m/α_s	28
Figure 2.9 The $P_{O_2}^i$ as a function of slag basicity ^[87]	29
Figure 2.10 The residence time for fully dense droplet without swelling ^[8]	33
Figure 2.11 The residence time for swelling metal droplets ^[8]	33
Figure 2.12 Schematic diagram of behavior of Fe-C droplet observed by X-ray fluoroscopy ^[14]	34
Figure 2.13 Comparison of CO generation rate between theoretical predictions and experiment measurements ^[15]	37

Chapter 3

Figure 3.1 Schematic diagram of the Furnace: 1. support rod, 2. slag, 3. X-ray generator, 4. image intensifier, 5. working tube and 6. iron pellet ^[37]	43
Figure 3.2 (a) CO gas generation with time and (b) peak decarburization rate as a function of metal sulfur content.....	46
Figure 3.3 Typical behavior of a metal droplet with 0.014 wt% S observed by X-ray fluoroscopy at 1853 K.	47
Figure 3.4 Variation of the volume of bloated droplets with respect to sulfur content and time.	47
Figure 3.5 Dephosphorization as a function of time and droplet sulfur content: (a) 0.007wt% S, (b) 0.011 wt% S, (c) 0.014 wt% S, (d) 0.017 wt% S and (e) 0.021 wt% S. 50	50

Figure 3.6 Schematic diagram of droplet behavior in terms of CO generation and dephosphorization as a function of time.	51
Figure 3.7 The effect of sulfur on incubation time for droplet swelling.	52
Figure 3.8 The effect of CO evolution rate on phosphorus partition coefficient.	55
Figure 3.9 The effect of decarburization rate on interfacial oxygen potential and phosphorus partition coefficient for this study and under steelmaking condition.	58
Figure 3.10 Dephosphorization data from Figure 3.5 are replotted as a function of time based on Eq. (3.14).	60

Chapter 4

Figure 4.1 CO gas generation with time for droplets containing different sulfur content.	69
Figure 4.2 Change of phosphorus with time for droplets containing different sulfur content.	69
Figure 4.3 Behavior of droplets before fully entering the foamy slag: (a) 0.007 wt% S, (b) 0.014 wt% S and (c) 0.021 wt% S.	70
Figure 4.4 k_{FeO} as a function of the liquid fraction of slag.	74
Figure 4.5 k_{FeO} as a function of total iron content in the slag: (a) low liquid fraction and (b) high liquid fraction.	78
Figure 4.6 Fraction of droplet surface area in the foam as a function of time.	80
Figure 4.7 The dynamic interfacial oxygen potential between bloated droplets and slag.	81
Figure 4.8 (a) phosphorus partition ratio (L_P) and (b) overall mass transfer coefficient (k_o) as a function of time for the study of bloated droplets.	82
Figure 4.9 (a) L_P and (b) k_o as a function of time for the case of Shibata <i>et al.</i> ^[4]	83
Figure 4.10 The effect of decarburization rate on overall mass transfer coefficient.	84

Chapter 5

Figure 5.1 Schematic diagram of the furnace	99
Figure 5.2 Decarburization behavior of droplets: (a) CO gas generation with time for 0.007 wt% S droplets and (b) 0.014 wt% S droplets.	101
Figure 5.3 Swelling behavior of droplets: (a) 0.007 wt% S droplets at different temperature, (b) 0.014 wt% S droplets at different temperature and (c) C-free droplets (0.007 wt% S) at 1853 K.	103
Figure 5.4 Plot of dephosphorization as a function of time: (a) 0.007 wt% S at 1913 K, (b) 0.007 wt% S at 1853 K, (c) 0.007 wt% S at 1813 K, (d) 0.007 wt% S C-free droplet at 1853 K, (e) 0.014 wt% S at 1913 K and (f) 0.014 wt% S at 1853 K.	105

Figure 5.5 Dephosphorization data from Figure 5.4(d) is replotted as a function of time based on Eq. (5.1).....	107
Figure 5.6 Cross-section view of quenched droplets: (a) 0.007 wt% S-1913 K, (b) 0.007 wt% S-1853 K, (c) 0.007 wt% S-1813K and (d) 0.007wt% S without C-1853K. 108	
Figure 5.7 Dephosphorization data from Figure 5.4 are replotted as a function of time for different temperature based on Eq. (5.2): (a) 0.007 wt% S and (b) 0.014 wt% S.....	110
Figure 5.8 The effect of temperature on phosphorus partition coefficient (L_P) at the reversion point: (a) this study and (b) calculated results for the case of Mori <i>et al.</i> ^[30] ..	114
Figure 5.9 Decarburization rate as a function of temperature: (a) this study and (b) calculated results based on the work of Mori <i>et al.</i> ^[30]	114
Figure 5.10 Dephosphorization as a function of time and temperature plotted according to Eq. (5.2) using the data in the work of Mori <i>et al.</i> ^[30] : (a) slag with NaCl and (b) slag without NaCl.	117
Figure 5.11 Re-dephosphorization data from Figures 5.4(a) and (b) are replotted as a function of time via Eq. (5.2).....	121
Figure 5.12 Mass transfer coefficients for the whole life of bloated droplet.....	123
Figure 5.13 The plot of k_m as a function of temperature: (a) this study, (b) calculated results based on the work of Mori <i>et al.</i> ^[30]	126

Chapter 6

Figure 6.1 (a) CO gas generation with time for different droplet mass and (b) the relationship between peak decarburization rate and metal droplet mass.....	144
Figure 6.2 Swelling behavior of 0.007 wt% S metal droplets with different mass.....	145
Figure 6.3 Plot of dephosphorization as a function of time at 1913 K: (a)1.5 g, (b)1.0 g, (c)0.5 g and (d)1.0 g at 1813 K.	146
Figure 6.4 (a) k_m as a function of CO gas velocity and (b) plot of k_m based on Eq.(6.11).	149
Figure 6.5 Dephosphorization data from different researchers are replotted as a function of time and silicon content based on Eq. (6.1): (a) Inoue <i>et al.</i> ^[14] , (b) Suito <i>et al.</i> ^[15] , (c) and (d) Moriya <i>et al.</i> ^[16] and (e) Diao <i>et al.</i> ^[23]	151
Figure 6.6 The relationship between h_{Si} on $\ln k_m h_{Si}^{1/2}$ based on Eq. (6.21).....	155
Figure 6.7 The effect of temperature on k_m : (a) using the data from Kitamura <i>et al.</i> ^[22] , (b) from the authors' previous work ^[33]	157
Figure 6.8 Dephosphorization data from different researchers are replotted as a function of time and FeO content based on Eq. (6.1): (a) Mori <i>et al.</i> ^[19] , (b) Wei <i>et al.</i> ^[20] and (c) Shibata <i>et al.</i> ^[21]	159
Figure 6.9 The relationship between $\ln \frac{k_m}{a_{FeO}}$ and $\frac{1}{a_{FeO}^2}$ based on Eq. (6.30).	162

Chapter 7

Figure 7.1 CO gas generation with time.	168
Figure 7.2 The change of droplet volume as a function of time.	169
Figure 7.3 Plot of dephosphorization as a function of time at 1923 K.	169
Figure 7.4 Dephosphorization data from Figure 7.3 is replotted as a function of time based on Eq. (7.1).	170

LIST OF TABLES

Chapter 3

Table 3.1 Metal droplet compositions (wt%).....	45
Table 3.2 Calculated phosphorus partition ratio and overall mass transfer coefficient	61

Chapter 4

Table 4. 1 Calculated results for different metal droplets.....	73
Table 4. 2 Calculated k_{FeO} for different researchers' work.....	75
Table 4.A1 Reactions and their equilibrium constants used in this study	88
Table 4.A2 Slag compositions (wt%).....	88
Table 4.A3 Experimental conditions and initial metal compositions (wt%).....	89
Table 4.A4 Converted k_{FeO} from rate constants determined by different researchers	92

Chapter 5

Table 5.1 Calculated k_{FeO} at different temperature	110
Table 5.2 Slag compositions (wt%) and extracted results from Mori <i>et al.</i> ^[30]	112
Table 5.3 Determined temperature coefficients for terms in Eq. (5.11).....	116
Table 5.4 Mass transfer coefficients calculated from experimental data	117
Table 5.5 Mass transfer coefficients for the case of Mori <i>et al.</i> ^[30]	118
Table 5.6 Parameters for calculating k_m of 0.007 wt% S bloated droplets in the foam .	120
Table 5.7 Calculated k_m at different stages.....	122

Chapter 6

Table 6.1 Mass transfer coefficients calculated based on data shown in Figure 6.3.....	148
Table 6.2 Mass transfer coefficients calculated from experimental data	152
Table 6.3 Mass transfer coefficients and decarburization rate from Kitamura <i>et al.</i> ^[22] .	156

Table 6.4 Determined temperature coefficients for terms in Eq. (6.23).....	158
Table 6.5 Mass transfer coefficients calculated from experimental data ^[19-21, 23]	160
Table 6.A1 Metal composition used in other researchers' work (wt%) ^[14-16, 23]	164
Table 6.A2 Metal compositions (wt%) in the work of Kitamura <i>et al.</i> ^[22]	164
Table 6.A3 Slag Compositions used in this study from other researchers (wt%) ^[19-21] ..	164

Appendix

Table A.1 Calculated errors for some experiment results	179
Table A.2 Uncertainty sources and estimation	180

List of Abbreviations and Symbols

BOF	Basic oxygen steelmaking furnace
EAF	Electric arc furnace
A	Interfacial surface area
a	Raoultian activity
C	Mole concentration
$C_{PO_4^{3-}}$	Phosphate capacity of slag
D_i	Diffusivity of species
f_i	Henrian activity coefficient of species in metal
ΔH	Heat formation of a molecular
h_i	Henrian activity of species in metal
J_s	CO nucleation rate (/cm ³ s)
J_i	Diffusion flux of transported species (mole/cm ² s)
K	Reaction equilibrium constant
k_i	Mass transfer coefficient
k	Boltzmann constant
L_P	Phosphorus partition coefficient (ratio)
M	Mass of molecule
N_{CO}	CO generation rate (mole/s)
N_A	Avogadro's number
N_o	Number of CO embryos
n_e	Number of molecules in an embryo
n_i	Number of moles of species
$P_{O_2}^i$	Interfacial oxygen potential
[wt% i]	Concentration, in mass percent, of species in metal
(wt% i)	Concentration, in mass percent, of species in slag
V_i	Volume of metal or slag
W_i	Weight of metal or slag
X_i	Equivalent cation fraction of oxides in slag
ρ_i	Density of metal or slag
η	Viscosity
r^*	Critical nucleus radius of CO bubble
μ	Gas velocity across slag-metal interface

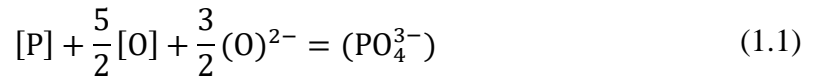
σ	Surface tension
φ	Modification number of surface tension
γ_i	Raoultian activity coefficient of species in slag
Λ	Optical basicity
χ	Pauling electronegativity

Chapter 1

Introduction

1.1 Research Background

In Ironmaking and steelmaking processes, the main sources of phosphorus in hot metal are iron ore, recycled BOF slag and coke ^[1]. Phosphorus is regarded as a detrimental impurity and requires control at relatively low contents due to its' effect on the properties of most of steel grades ^[2], such as deformability, ductility and fracture toughness. It may also segregate at the grain boundaries during the solidification of steel in continuous casting, leading to brittle phases that may cause failure during downstream processing ^[3]. Phosphorus in hot metal is removed by oxidation through the following reaction if we consider the ionic nature of slag.



In the BOF, refining reactions mainly occur at three different sites, namely the slag-metal bath contact, the impact zone and the gas-slag-metal emulsion zone. The impact zone is the area directly under the oxygen lance and has no slag present. Compared with the slag-metal bath, the gas-slag-metal emulsion zone has several thousand times the contact area which greatly increases the rates of refining reactions ^[4-6]. The emulsion zone is formed when the oxygen impinges on the metal bath at supersonic velocities, generating a tremendous amount of liquid metal droplets which mix with the slag ^[7]. The jet also reacts directly with the impact zone oxidizing iron as well as reactive elements in the metal. The metal oxides produced contribute to the formation of the slag.

Metal droplets in the emulsion play a critical role in BOF refining. Metal droplets are resident in the emulsion zone for various times before falling back into the metal bath. The residence time is the available time for droplets to react with slag. Longer residence times

will provide better overall refining rates, particularly for elements which can only react in contact with the slag such as phosphorus. Several studies have found that the residence time of metal droplets can vary from 0.2 second for dense droplets to 120 seconds for droplets which contain gas bubbles (so called bloated droplets) ^[7-10]. The swelling of a metal droplet is strongly related to the decarburization in the gas-slag-metal emulsion according to the overall reaction:



The swelling of a metal droplet depends on the balance between the diffusion rate of oxygen into the droplet and the mass transfer rate of carbon from the bulk to the surface. If the oxygen supply rate is higher than the transfer rate of carbon, CO gas would form inside the metal droplet which causes droplet swelling. The resulting bloated droplets are less dense, which will prolong their residence time, thereby enhance the rate of refining reactions such as dephosphorization.

A previous study ^[11] at McMaster University has shown that the swelling rate of metal droplets is strongly dependent on CO gas generation rate inside the metal droplets. High CO gas generation rate leads to greater swelling, which prolongs the residence time in the emulsion and is good for dephosphorization. Likewise CO formation inside the droplet may be expected to stir the metal offering high rates of phosphorus transfer ^[12]. However, a high CO generation rate will rapidly consume oxygen supplied by FeO in the slag and significantly reduce the interfacial oxygen potential, which controls the driving force for dephosphorization. Whilst this competition has been discussed in detail in the context of dephosphorization at the slag metal interface of a flat bath, the balance between the negative and the positive effects of CO gas formation inside metal droplets has not been reported. The motivation of this study is to quantify the balance between positive and negative effects on dephosphorization of bloated droplets.

1.2 The Objectives of This Study

Previous work at McMaster University and elsewhere ^[11, 13-15] has shown that the decarburization reaction between metal droplets and slag causes metal droplets to swell. In the BOF, droplet swelling enhances the refining reactions by increasing the residence time of droplets in the slag. However, during steelmaking in the BOF, both carbon and phosphorus in the metal are removed from the metal through oxidation. Rapid decarburization would lower the interfacial oxygen potential which is the driving force for dephosphorization. Therefore, understanding the interplay between decarburization and dephosphorization is crucial for developing an overall process model of the BOF. The detailed objectives of this work include:

1. To obtain quantitative data for dephosphorization of bloated droplets over a range of experimental conditions, defined by metal droplet composition, slag composition and temperature.
2. To investigate the influence of decarburization on the driving force of dephosphorization in detail by associating phosphorus removal kinetics with the decarburization rate and swelling of the metal droplets.
3. To develop an approach that can determine the mass transfer coefficient of FeO in slag under different conditions, which can be further employed to calculate the dynamic interfacial oxygen potential between metal droplets and slag.
4. To understand the stirring effect of CO bubbles on dephosphorization and obtain the relationship between CO bubble formation inside metal droplet and mass transfer coefficient of phosphorus in metal phase.
5. To test the application of findings from this study to real steelmaking conditions.

1.3 Thesis Outline

Chapter 1: Introduction. This chapter provides a general introduction to the research; describing the motivation for this study, defining detailed research objectives and presenting an outline of this thesis.

Chapter 2: Literature Review. This chapter reviews relevant literature including: fundamental principles of dephosphorization, thermodynamics of dephosphorization and slag properties, reaction kinetics and rate equations for phosphorus transfer between slag and metal, and metal droplet behavior in the emulsion zone of BOF.

Chapter 3: “The Influence of Sulfur on Dephosphorization Kinetics between Bloated Metal Droplets and Slag Containing FeO”. This chapter presents the results of a laboratory investigation on the effect of sulfur dissolved in metal droplets on their dephosphorization. The research aims to determine the dephosphorization rate as a function of CO evolution rate, the latter having previously been shown to be strongly affected by sulfur. It is demonstrated that the CO evolution rate has a significant effect on the phosphorus partition coefficient by influencing the interfacial oxygen potential. The rate controlling step for dephosphorization in this study is analyzed by employing mixed control by mass transport in both metal and slag. This work has been published: K. Gu, N. Dogan and K. S. Coley, *Metallurgical and Materials Transactions B*. 2017, DOI: 10.1007/s11663-017-1002-0. This paper was considered to be of sufficient merit to select as Editors’ Choice for Free Access.

Chapter 4: “The Dynamic Interfacial Oxygen Potential between Iron-Carbon Droplets and Oxidizing Slag”. In this chapter, a mathematical model is developed for the dynamic interfacial oxygen potential and its effect on rate controlling steps for dephosphorization. This work also investigates the mass transfer of oxygen in the slag as a function of bubble volume fraction and FeO content. This manuscript has been published: K. Gu, N. Dogan and K. S. Coley, *Metallurgical and Materials Transactions B*. 2017, DOI: 10.1007/s11663-

017-1000-2. This paper was considered to be of sufficient merit to select as Editors' Choice for Free Access.

Chapter 5: “Dephosphorization Kinetics for Bloated Metal Droplets Reacting with Slag Containing FeO: The Influence of CO Bubbles on the Mass Transfer of Phosphorus in the Metal”. To understand the role in dephosphorization kinetics, of CO bubbles nucleated inside the droplet, experimental results are compared for droplets containing carbon and those with no carbon. The effect of CO bubble formation on the mass transfer of phosphorus in the metal is also investigated at different temperatures. A version of the surface renewal model, modified to include the kinetics of CO bubble nucleation is used with some success to represent the mass transfer coefficient. This manuscript has been accepted for publication in *Metallurgical and Materials Transactions B*.

Chapter 6: “An Assessment of the General Applicability of the Relationship between Nucleation of CO Bubbles and Mass Transfer of Phosphorus in Liquid Iron Alloys”. This chapter demonstrates the generality of the version of the surface renewal model, modified in this study to include the kinetics of CO nucleation inside the metal. In order to test this model, results are presented for dephosphorization experiments conducted over a range of droplet mass. Additionally, the effects of other alloying elements in the metal, iron oxide in slag and temperature are investigated using published dephosphorization data. This manuscript has been submitted to *Metallurgical and Materials Transactions B*.

Chapter 7: Application of High Basicity Slag. In this chapter, dephosphorization kinetics of metal droplet by using real steelmaking slag with high basicity were investigated based on conclusions from previous chapters.

Chapter 8: Concluding Remarks. This chapter draws together the important findings from each of the previous chapters illustrating how each contributes to the overall picture. Finally some general conclusions are offered and future work proposed.

Chapter 2

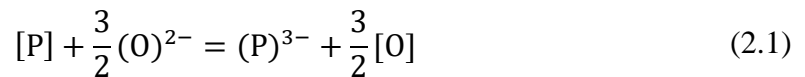
Literature Review

2.1 Thermodynamics of Dephosphorization

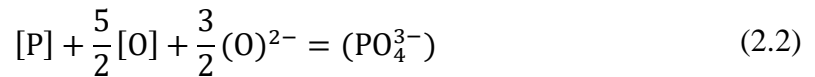
2.1.1 Reaction of Phosphorus Removal

Phosphorus in iron alloys can be either removed under oxidizing conditions or under strongly reducing conditions. When alloys contain less noble elements than iron, reducing conditions may be preferred for phosphorus removal to avoid the significant loss of those noble elements ^[16].

Under highly reducing conditions, phosphorus dissolves in the slag as a phosphide ion which can be expressed as Eq. (2.1).



While phosphorus exists as phosphate ion in the slag under oxidizing conditions as follows.



By studying the effect of oxygen partial pressure on phosphorus in the CaO-Al₂O₃ system, Momokawa *et al.* ^[16] found that when P_{O_2} is higher than about 10^{-18} atm, phosphate is predominant in the slag, but phosphide is predominant when P_{O_2} is lower than that value as shown in Figure 2.1.

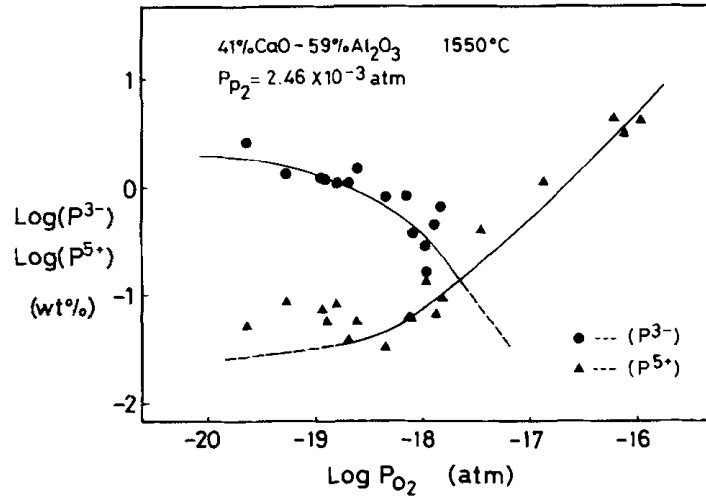


Figure 2.1 Phosphide and phosphate concentrations in the CaO-Al₂O₃ slag as a function of oxygen partial pressure ^[16]. (Reprinted with permission)

Under conventional refining conditions such as hot metal pre-treatment and BOF practice, the oxygen potential is much higher than 10^{-18} atm, and dephosphorization follows the reaction expressed as Eq. (2.2). The most reducing conditions prevalent in equilibrium with iron carbon alloys have considerably higher oxygen potentials than 10^{-18} atm. Therefore dephosphorization studies in the laboratory between iron alloys and oxidizing slags typically take place under oxidizing conditions ($P_{O_2} > 10^{-14}$ atm) ^[17-18]. The current work will continue this trend and only dephosphorization under oxidizing conditions will be discussed in this study.

2.1.2 Phosphorus in Slag

Dephosphorization is one of the most fundamental steelmaking refining processes. The recognized reaction for phosphorus removal from metal is as follows where phosphorus is assumed to form liquid P₂O₅.



where square brackets represent elements in metal, parentheses brackets are elements or compounds in slag.

The well-accepted Gibbs free energy of formation (ΔG_f°) of liquid P_2O_5 can be expressed as Eq. (2.4) ^[19],

$$\Delta G^\circ = -832384 + 632.65T \text{ (J/mole)} \quad (2.4)$$

which gives the following reaction equilibrium constant,

$$\log K_p = \frac{43480}{T} - 33.0 \quad (2.5)$$

It should be noted that at typical activities for phosphorus dissolved in liquid iron the equilibrium P_{O_2} calculated for reaction (2.3) using Eq. (2.4) and (2.5) is higher than that required to oxidize iron to FeO. Thus in practice, dephosphorization must be carried out in the presence of a slag to maintain a low activity of P_2O_5 .

By studying the binary system of SiO_2 - P_2O_5 , researchers ^[20,21] found that phosphorus exists predominantly as PO_4^{3-} and $P_2O_7^{4-}$ groups at low P_2O_5 (<0.05 mole fraction); at higher P_2O_5 contents, the PO_4^{3-} and $P_2O_7^{4-}$ groups polymerize in metaphosphate units of different chain lengths.

Colclough *et al.* ^[22, 23] concluded that P_2O_5 in slag existed in the form of tetra-calcium phosphate ($4CaO \cdot P_2O_5$) after carrying out a series of experiments on the oxidation of phosphorus, carbon and manganese from the hot metal in a basic open-hearth furnace. Herty *et al.* ^[24] assumed that phosphorus in the slag formed tri-calcium phosphate ($3CaO \cdot P_2O_5$) to carry out theoretical treatment of dephosphorization. More recent studies ^[25-26] have even proposed that P_2O_5 forms a solid solution with $2CaO \cdot SiO_2$ and precipitates around undissolved CaO particles. Iwase and co-workers ^[27] calculated the activity of P_2O_5 in equilibrium with the two solid phases di-calcium and tri-calcium phosphates based on experimental results using electrochemical technique. They also conducted several studies ^[28, 29] to investigate the formation free energies of solid solution between tri-calcium phosphate and di-calcium silicate.

Considering the ionic nature of slag and the small amount of P_2O_5 (<5 wt%) in typical BOF slag^[30], the use of Eq. (2.2) to describe the effect of slag properties on dephosphorization is well accepted. One can obtain the reaction (2.6) by combining reactions (2.2) and (2.3).



Therefore, the well-established requirements for dephosphorization would be:

- (1) Low temperature, which offers higher reaction equilibrium constant for phosphorus removal.
- (2) High activity of oxygen (oxygen potential), *i.e.*, high iron oxide content in the slag.
- (3) High slag basicity (activity of O^{2-} ion) creating a low activity coefficient for phosphorus-pentoxide in the slag as shown in Eq. (2.6).

2.1.3 Phosphorus Partition L_P between Metal and Slag

The equilibrium constant for phosphorus oxidation Eq. (2.3) can be expressed as Eq. (2.7),

$$K_{P_2O_5} = \left(\frac{a_{P_2O_5}}{h_P^2 h_O^5} \right) = \left(\frac{x_{P_2O_5} \times \gamma_{P_2O_5}}{([\text{wt}\% \text{ P}]f_P)^2 \times ([\text{wt}\% \text{ O}]f_O)^5} \right) \quad (2.7)$$

where $a_{P_2O_5}$ represents activity of P_2O_5 in slag (considering pure liquid P_2O_5 as the standard state). $x_{P_2O_5}$ is molar fraction of P_2O_5 in slag, $\gamma_{P_2O_5}$ is the activity coefficient of P_2O_5 in slag. h_P and h_O are Henrian activities of phosphorus and oxygen in steel, respectively (considering 1 mass percent solution in liquid iron as the standard state). For dilute solutions, $h_P = [\text{wt}\% \text{ P}]f_P$ and $h_O = [\text{wt}\% \text{ O}]f_O$ where f_P and f_O are the respective Henrian activity coefficients of phosphorus and oxygen in steel; $[\text{wt}\% \text{ P}]$ and $[\text{wt}\% \text{ O}]$ are concentrations of phosphorus and oxygen in the steel in weight percent.

For the convenience of theoretical treatment, Eq. (2.3) can be modified as Eq. (2.8) by dividing by 2. But $PO_{2.5}$ is the same chemical compound as P_2O_5 in the following discussion.



Then the equilibrium constant for reaction (2.8) can be written as Eq. (2.9).

$$K_{PO_{2.5}} = \left(\frac{a_{PO_{2.5}}}{h_P h_O^{2.5}} \right) = \left(\frac{x_{PO_{2.5}} \times \gamma_{PO_{2.5}}}{([\text{wt}\% P] f_P) \times ([\text{wt}\% O] f_O)^{2.5}} \right) \quad (2.9)$$

Converting $x_{PO_{2.5}}$ to (wt% $PO_{2.5}$), one can rearrange Eq. (2.9) and obtain the following equation:

$$L_P = \frac{(\text{wt}\% P)}{[\text{wt}\% P]} = \frac{K_{PO_{2.5}} \times ([\text{wt}\% O] f_O)^{2.5} \times f_P \times M_P C_s}{\rho_s \times \gamma_{PO_{2.5}}} \quad (2.10)$$

where M_P and $M_{PO_{2.5}}$ are molecular weights of phosphorus and $PO_{2.5}$, respectively; C_s and ρ_s represent molar density and mass density of the slag.

The left-hand side (LHS) of Eq. (2.10), L_P , is defined as phosphorus partition ratio between metal and slag, which is the driving force for dephosphorization. Although other definitions for L_P were used in literature, they can be converted to the same form used in Eq. (2.10), which is the widely used. Extensive studies have been carried out to measure phosphorus partition ratio L_P for different slag systems or operating conditions, including slags used in hot metal pre-treatment, BOF practice and EAF practice. Comprehensive reviews of the activity coefficient of P_2O_5 in slag and of phosphorus distribution ratio between liquid steel and slag can be found elsewhere^[31-33]. Only the most prominent are reviewed in this study.

Balajiva and coworkers^[34, 35] conducted a comprehensive study on the thermodynamics of dephosphorization during the 1940s and proposed the following equation to calculate equilibrium phosphorus partition ratio.

$$\log \frac{(\%P)}{[\%P]} = 5.9 \log(\%CaO) + 2.5 \log(\%FeO) + 0.5 \log(\%P_2O_5) - 0.5C - 0.36 \quad (2.11)$$

where C is constant for a particular temperature. The values of C at 1823 K, 1858 K and 1908 K were reported as 21.13, 21.51 and 21.92, respectively^[32]. However, equilibrium values obtained by Balajiva and coworkers have been questioned in recent times because

of later researchers showed that their measurement of equilibrium reaction temperature was incorrect ^[36]. Despite these limitations, Balajiva *et al.* did observe that the phosphorus partition ratio was enhanced by the presence of CaO and FeO in the slag and decreased with increasing temperature ^[32, 33].

In 1970s, Healy ^[37] presented a simple but widely used equation for the phosphorus distribution between liquid metal and slag from the view point of ionic theory of slag as follows:

$$\log \frac{(\%P)}{[\%P]} = \frac{22350}{T} + 0.08(\%CaO) + 2.5 \log(\%Fe_{total}) - 16 \pm 0.4 \quad (2.12)$$

Due to the simplicity and ease of calculation, Eq. (2.12) has become widely used in real steelmaking practices. However, it has been found that the phosphorus partition levels calculated using Eq. (2.12) are higher than the typical measured values in industrial basic oxygen steelmaking of similar slag composition by a factor of 2-4 ^[32].

During the 1980s Suito *et al.* ^[38-41] conducted an extensive investigation on the effect of different slag components such as CaF₂, BaO, Na₂O and MnO on phosphorus partitioning, and proposed the following correlation for phosphorus distribution in MgO-saturated slags of CaO-Fe_tO-SiO₂-P₂O₅-MnO.

$$\log \frac{(\%P)}{[\%P](\%Fe_t)^{2.5}} = 0.072\{(\%CaO) + 0.3(\%MgO) + 0.6(\%P_2O_5) + 0.6(\%MnO)\} + \frac{1150}{T} - 10.52 \quad (2.13)$$

Compared to other proposed correlations ^[19, 37], Eq. (2.13) shows a significantly lower temperature dependence of phosphorus distribution ratio.

Later combining all earlier works and more recent experiment results, Suito *et al.* ^[42] developed the following modification to Eq. (2.13) for slags containing MnO (8-16wt%)-CaO-SiO₂-Fe_tO .

$$\begin{aligned} \log \frac{(\%P)}{[\%P](\%Fe_t)^{2.5}} \\ = 0.072\{(\%CaO) + 0.3(\%MgO) + 0.6(\%P_2O_5) + 0.2(\%MnO) \\ + 1.2(\%CaF_2) - 0.5(\%Al_2O_3)\} + \frac{1150}{T} - 10.52 \end{aligned} \quad (2.14)$$

However, Eq. (2.14) was developed primarily for high MnO slags, which has limited relevance to dephosphorization in the BOF. Slags in the BOF are also free of CaF₂ which was introduced in Eq. (2.14). Zhang *et al.* [43] developed a different phosphorus partition correlation including an additional temperature term and the effect of SiO₂, which is given in Eq. (2.15).

$$\begin{aligned} \log \frac{(\%P_2O_5)}{[\%P]} = 2.5 \log(\%FeO) \\ + \frac{1}{T} [162(\%CaO) + 127.5(\%MgO) + 28.5(\%MnO)] - 6.28 \\ \times 10^{-4}(\%SiO_2)^2 + \frac{11000}{T} - 10.402 \end{aligned} \quad (2.15)$$

In 2007, Basu *et al.* [44, 45] determined the equilibrium phosphorus partition ratios between liquid steel and CaO-SiO₂-FeOx-P₂O₅-MgO slag at 1873 K and 1923 K. They investigated the influence of basicity and FeO content up to 25 wt% on phosphorus partition ratio. It was shown that phosphorus partition ratio increased significantly as basicity increases up to 2.0, then slowly increased and became practically constant at basicity greater than 2.5. They also found that L_P initially increased with increasing FeO content but then decreased after FeO content reached a certain level. These findings are consistent with other researchers' observation on the influence of FeO and CaO on phosphorus partition between slag and metal [34, 35, 38, 46-47].

More recently, after reviewing the methodology and experimental setup employed in relevant studies on phosphorus equilibrium between iron and slag, Assis *et al.* [33] presented new equilibrium phosphorus partition data between liquid iron and BOF-type slags at 1873 K, and proposed the following correlation.

$$\log \frac{(\%P)}{[\%P](\%Fe_t)^{2.5}} = (\%CaO) + 0.148(\%MgO) + 0.96(\%P_2O_5) + 0.144(\%SiO_2) \quad (2.16)$$

Since fully liquid MgO-saturated slag was employed in the work of Assis *et al.* [33], this correlation could be more representative of equilibrium for slag relevant to the BOF. However, Eq. (2.16) does not consider the effect of Al_2O_3 on phosphorus partition. Thereby, Eq. (2.16) might not be the best one to calculate phosphorus partition ratio for slag containing Al_2O_3 .

2.1.4 Silicate Structure and Slag Basicity

Eq. (2.6) for dephosphorization shows that slag basicity $a_{(O)^{2-}}$ has a significant effect. Basicity is one of most important physicochemical properties of slag systems. Since most steelmaking slags are silicate based, the slag basicity to some extent represents the complexity of the silicate structure. Silicate slags consist of 3-dimensional interconnected networks of SiO_4^{4-} tetrahedra in which silicon atoms are covalently bonded to four oxygen atoms [48]. These SiO_4^{4-} tetrahedra are joined together in the form of chains or rings via bridging oxygens. By adding basic oxides, donors of free oxygen ions, O^{2-} , the silicate network structure can be broken down into smaller units as shown in Figure 2.2.

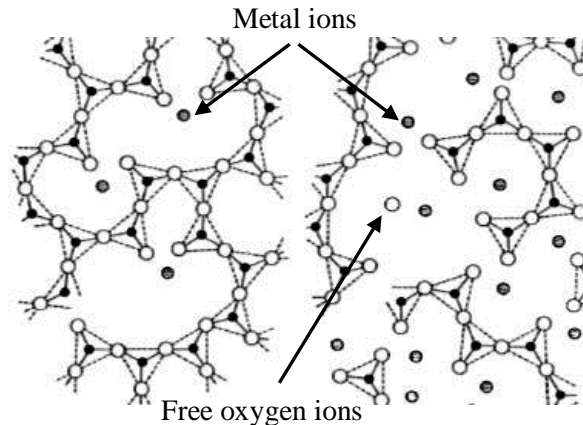


Figure 2.2 Schematic representation of depolymerization of silicate network by the addition of basic oxides [49].

The proposed equation to describe this process are as follows ^[49]:



where O° is a bridging oxygen, O^{-} represents non-bridging oxygen and O^{2-} is a free oxygen ion.

While bridging oxygens are present, any addition of basic oxides will result in breaking of the bridging connection. After all bridging oxygens have been eliminated the silicate structure will be in the form of single tetrahedral units and any additional basic oxides will dissociate into cations and O^{2-} anions. Based on the tendency to donate free oxygen ions, metal oxides can be classified into three types, *i.e.*, basic oxides, acidic oxides and neutral oxides. Basic oxides are clearly ionic with free oxygen ions and able to donate sufficient oxygen ions. The oxides, such as CaO, MgO, MnO and FeO, which can break down the network structure in molten slag are known as network breaker and are cataloged to be basic oxides ^[50]. Whereas acidic oxides are acceptors of oxygen ions and have a weaker tendency to form free oxygen ions. These oxides, for instance, SiO_2 and P_2O_5 act as network formers by forming larger complex anions in molten slags.

Neutral oxides, such as Al_2O_3 and Cr_2O_3 are defined as amphoteric oxides, which can be either basic or acidic depending on their concentration and the other oxides present. In the case of Al_2O_3 , Sano *et al.* ^[51] showed that Al^{3+} is stable in acidic slags whereas AlO_4^{5-} is stable in basic slag. Park *et al.* ^[52] found that in CaO- SiO_2 - Al_2O_3 slag, Al_2O_3 behaves as network former up to about 10wt%, while it acts as a network modifier in concentrations greater than 10 wt%.

Over decades, many empirical expressions and a number of models to represent the slag basicity have been proposed, which can be divided into two main approaches ^[53].

The first approach, also the most convenient for the plant metallurgist, is to determine the ratio of basic oxides to acidic oxides in the slag. Especially, for slags where lime and silica are the major constituent oxides, the basicity is usually defined by the concentration ratio, wt% CaO/wt% SiO_2 , which is called the “V” ratio ^[54]. If one expresses the V ratio in terms

of mole% a simple evaluation in light of the foregoing discussion reveals that for $V < 2$ there would be some bridging oxygen present and the slag would behave as an acid, consuming basic oxides in eliminating the bonds between tetrahedral. If $V > 2$ there would be no bridging oxygens and the slag would be basic in character. On the same basis, slags with $V = 2$ could be considered neutral. In practice the division between acidic and basic slags $V = 2$ is used despite the fact that it is based on a mass ratio rather than a molar ratio. Although not strictly correct, this simplified analysis works fairly well.

However, the simple wt% CaO/wt% SiO₂ ratio ignores the effects of other oxides, such as MgO and Al₂O₃ which also strongly affect slag properties. For example, the ratio (CaO+MgO)/(Al₂O₃+SiO₂) assumes that CaO and MgO behave as equivalent basic oxides, and that Al₂O₃ and SiO₂ have the same degree of acidity, neither of which is precisely true even though the ratio may offer a reasonable approximation to basicity^[55]. While some expressions consider the different degree of basicity and acidity using different coefficients for each oxide, this approach in practice can lead to some conflicting conclusions.

The other approach is the introduction of the activity of the free oxygen ion, $a_{O^{2-}}$ from the view of the ionic theory of metallurgical slags^[56]. However, single ion activities such as $a_{O^{2-}}$ can not be defined thermodynamically, nor can they be measured experimentally, due to the interdependent nature of ionic species in slags^[51]. Thus, several methods for the estimation of $a_{O^{2-}}$ have been developed.

One of such estimations was proposed by Duffy and Ingram^[57] who employed the Lewis Acid/Base concept to estimate $a_{O^{2-}}$ by evaluating the electron donor power of a slag. They observed that when probe ions such as Pb²⁺ were added to silicate glasses, shifts in frequency of the absorption band of the 6s → 6p transition observed in ultraviolet region of the spectrum can be related to the basicity of a glass or a crystal. Using CaO as the standard medium where the optical basicity $\Lambda = 1$, optical basicity of other oxides can be measured. In this approach, the optical basicity of slag is considered to represent $a_{O^{2-}}$ or more correctly the chemical potential of the O²⁻ ion, $RT \ln a_{O^{2-}}$.

Whilst it is possible to measure directly the optical basicity of many oxides this is not possible with transition metal oxides. However, Duffy and Ingram ^[58] further found the optical basicity of an oxide AO, Λ_{Ao} , is related to the Pauling electronegativity, χ , of the cation via the following equation:

$$\Lambda_{Ao} = \frac{0.74}{\chi - 0.26} \quad (2.18)$$

Therefore, it is possible to evaluate the optical basicity of transition metal oxides and determine an overall optical basicity, Λ , for metallurgical slags:

$$\Lambda = X_{AO}\Lambda_{Ao} + X_{BO}\Lambda_{Bo} + \dots \dots \quad (2.19)$$

where Λ is the optical basicity of the slag and Λ_{Ao} is the theoretical optical basicity value for a single oxide. X is the equivalent cation fraction of oxides that can be obtained through:

$$= \frac{X \text{ (mole fraction of componet A)(no. of oxygen ions in the molecule)}}{\sum \text{(mole fraction of componets)(no. of oxygen ions in the molecule)}} \quad (2.20)$$

The value of electronegativity and theoretical optical basicity calculated based on this approach for different oxides can be found elsewhere ^[59, 60].

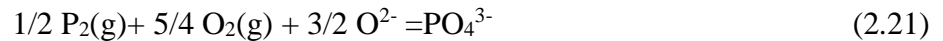
Some other methods ^[59-64] have been developed to obtain the values of optical basicity for transition metal oxides. Nakamura *et al.* ^[61] employed photoacoustic spectroscopy to determine values of optical basicity for transition metal oxides. It was also found that oxide ion refractivity is related to optical basicity in the range of 0.5-0.6 ^[59]. Thus experimental values of the refractive index was used to derive optical basicity for transition metal oxides, and showed a good agreement with values obtained from spectroscopic methods. Values of optical basicity for individual oxides were even obtained from “best fit” relationships between Λ and experimental properties ^[62-64], *i.e.*, sulphide capacities, phosphate capacities and thermodynamic properties.

It is also worth pointing out that value of Λ for transition metal oxides may vary with reactions being studied. For example, studies demonstrated that phosphorus capacities correlated better with the value of 0.51 for $\Lambda(\text{FeO})$ ^[60, 63] whereas the use of $\Lambda(\text{FeO})=1$ would be better to correlate sulphide capacities ^[64]. Therefore, there are recommended values ^[65] of Λ for different oxides, which were used to calculate slag optical basicity.

2.1.5 Phosphate Capacity

Phosphate capacity, $C_{PO_4^{3-}}$, is used to describe the dephosphorization efficiency of slag and also can be employed to correlate equilibrium data of different reactions involving O^{2-} ions as reactants. From above discussion, phosphorus partition ratio L_P between slag and metal depends on the oxygen potential, which limits the comparison of dephosphorization efficiency to systems with same oxygen potential. The phosphate capacity normalizes for oxygen potential providing a value to represent the slag property independent of oxygen potential. It should be noted that oxygen potential is defined relative to oxygen gas or dissolved atomic oxygen in the steel and is distinct from the activity of O^{2-} which is buffered by structural components of the slag.

Considering Eq. (2.21), Wanger ^[66] defined the phosphate capacity as Eq. (2.22).



$$C_{PO_4^{3-}} = \frac{(\%PO_4^{3-})}{P_{O_2}^{5/4} P_{P_2}^{1/2}} = \frac{K(a_{O^{2-}})^{3/2}}{\gamma_{PO_4^{3-}}^0} \quad (2.22)$$

where $\%PO_4^{3-}$ is the weight percent of PO_4^{3-} dissolved in slag, P_{O_2} is the oxygen potential at the slag-metal interface, and P_{P_2} is the phosphorus partial pressure in equilibrium with phosphorus in liquid iron. K is equilibrium constant for reaction (2.21). $a_{O^{2-}}$ is the activity of oxygen ions at the slag-metal interface. $\gamma_{PO_4^{3-}}^0$ is the activity coefficient of PO_4^{3-} in the slag.

Several researchers have successfully correlated phosphate capacity with the optical basicity of slag ^[60, 67-72].

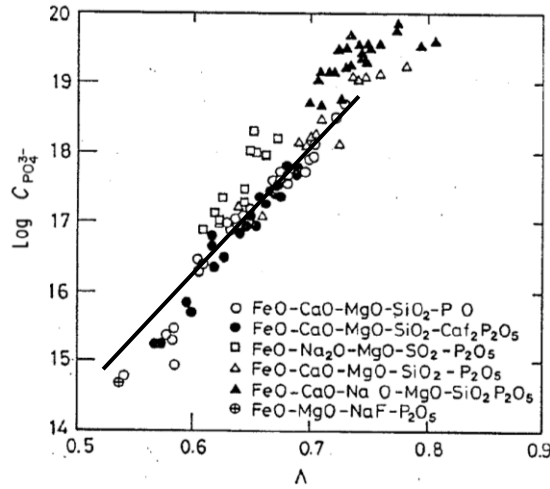


Figure 2.3 The relationship between $\log C_{PO_4^{3-}}$ and theoretical optical basicity^[60].

Reviewing different slag systems, Mori^[60] derived the following relationship between phosphate capacity and optical basicity as expressed in Eq. (2.23) based on correlations developed by Suito *et al.*^[40, 71]. As shown in Figure 2.3, Eq. (2.23) fits the experiment results very well at 1873 K.

$$\log C_{PO_4^{3-}} = 17.55 \Lambda + \frac{51670}{T} - 21.867 \quad (2.23)$$

According to the Figure 2.3, one can really recognize that the line is well fitted to these points in the range of Λ more than 0.6. Therefore, the optical basicity model is sufficiently accurate to predict the phosphate capacity of multicomponent slags. Bergman^[72] also found that the theoretical optical basicity, phosphate capacity, and temperature can be related for a wide range of slags, and these relationships do not seem to be restricted to certain components or composition limits^[73].

If one considers the following reaction^[74]:



$$\log K_P = \frac{8240}{T} - 0.28 \quad (2.25)$$

Phosphorus distribution ratio and the phosphate capacity can be related to each other as shown below:

$$L_P = \frac{(\text{wt}\% \text{ P})}{[\text{wt}\% \text{ P}]} = \frac{C_{PO_4^{3-}} P_{O_2}^{5/4} f_P M_P}{K_P M_{PO_4^{3-}}} \quad (2.26)$$

where K_P is the equilibrium constant for reaction (2.24), f_P is the henrian activity coefficient. M_P and $M_{PO_4^{3-}}$ are the molar mass of phosphorus and phosphate respectively.

From Eq. (2.26), the equilibrium phosphorus partition ratio may be determined from the oxygen potential or the oxygen potential may be determined based on knowledge of the partition ratio. It is worth noting that to determine the local equilibrium partition ratio at the interface, which is of greater importance in kinetics, the local interfacial oxygen potential must be known.

2.2 Kinetics of Dephosphorization

2.2.1 Rate-Determining Step

Since most slag-metal chemical reactions are rapid at typical steelmaking temperatures, the most likely rate determining steps for dephosphorization expressed as reaction (2.2) includes:

1. Mass transfer of phosphorus in the metal phase to the slag-metal interface;
2. Supply of oxygen in the slag to the interface, often considered phenomenologically as transport of the major reducible oxide for example FeO;
3. Mass transfer of O^{2-} from slag to the interface;
4. Mass transfer of PO_4^{3-} away from the interface to the slag.

Given the high FeO in the slag, the oxygen supply rate is relatively fast and unlikely the rate controlling step. Therefore, researchers have generally believed that the kinetics of dephosphorization was controlled by phosphorus mass transfer in liquid phase, but they

are divided between mass transfer control in the metal, slag or mixed control in both metal and slag phase ^[17, 18, 75-78].

Knowledge of dephosphorization kinetics is essential to understand the mechanism of removal of phosphorus from hot metal. Assuming reaction kinetics is controlled by mass transfer in both metal and slag, Ohguchi *et al.* ^[75] investigated the effect of silicon content on the kinetics of simultaneous dephosphorization and desulfurization of molten pig iron. They found that dephosphorization occurs after the cessation of desiliconization for iron containing high or medium silicon content (0.34 wt% and 0.13 wt%, respectively), while it takes place immediately in the case of low silicon content (0.02 wt%).

Mori *et al.* ^[76] and Wei *et al.* ^[17] studied in detail the dephosphorization associated with decarburization of carbon saturated iron with slag containing FeO. They assumed CO evolution was chemical reaction controlled at the slag-metal interface while other reactions were controlled by mass transfer in both slag and metal. These workers included the effect of temperature, different components in the slag, oxygen partial pressure in the furnace atmosphere and mechanical stirring. Mori *et al.* ^[76] found that the rate of dephosphorization increased with FeO content in the slag and the addition of NaCl or CaCl₂, while it decreased with increasing temperature from 1573 K to 1723 K.

In the study of Wei *et al.* ^[17], they showed that with increasing FeO content and the oxygen partial pressure of furnace atmosphere, the dephosphorization rate increased and the minimum phosphorus concentration in the metal decreased. They also demonstrated that the effect of mechanical stirring on the dephosphorization rate was negligible due to the combination of the positive effect on k_m (increase the mass transfer coefficient) and the negative effect on L_p (decrease the partition ratio by lowering the interfacial oxygen potential).

After investigating the effect of Fe₂O₃, CaCl₂ and CaF₂ on dephosphorization of carbon-saturated iron, Monaghan *et al.* ^[18] proposed that the rate determining step was mass transfer in the slag. They observed that increasing those slag components (Fe₂O₃, CaCl₂ and CaF₂) up to a certain level was found to increase the rate and extent of

dephosphorization, whereas further increases were found to decrease the rate and extent of the reaction because of the dilution of basic components in the slag. They further found that mass transfer coefficient in slag was a linear function of square root of slag fluidity, $1/\eta$, which is strongly affected by slag components (CaF_2 , Fe_2O_3 and CaCl_2).

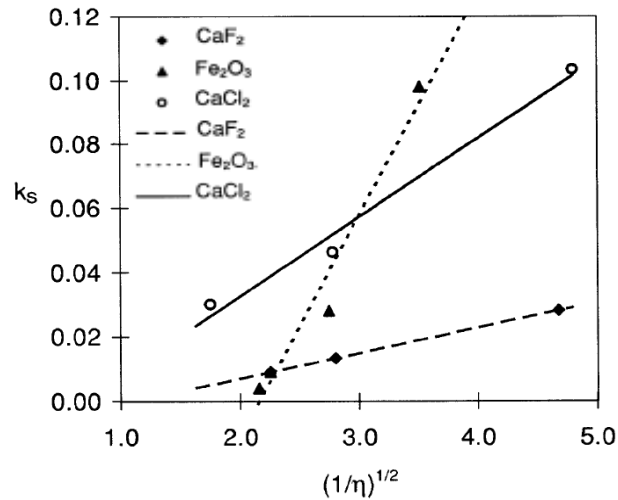


Figure 2.4 Relationship between k_s and viscosity of slag with respect to different slag components ^[18].

Shibata *et al.* ^[77] investigated the reaction kinetics of dephosphorization, in parallel with decarburization and desiliconization by varying the FeO and MnO content in the slag. They found that when oxygen was supplied by FeO in the slag, the reaction rates of all elements including phosphorus were higher than when MnO was the primary oxidant. In Figure 2.5, A-1 is the slag containing 29.7 wt% FeO whereas the slag of B-12 contains 22.4 wt% MnO. This observation suggests that FeO supplies oxygen more efficiently than MnO.

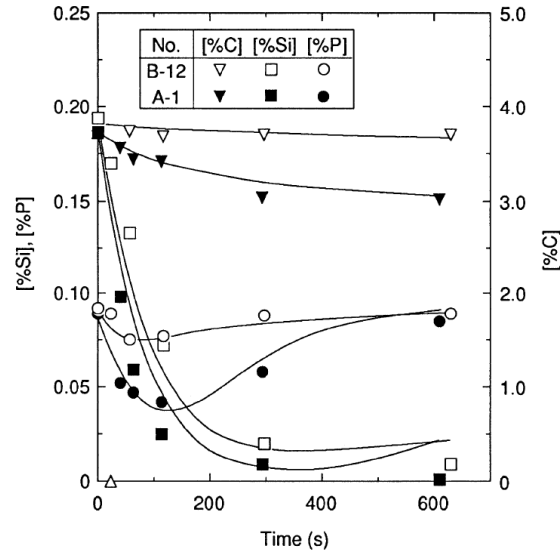


Figure 2.5 Comparison of oxidation rates of elements in metal by FeO-slag with MnO-slag^[77].

2.2.2 Rate-Equations for Dephosphorization

Since dephosphorization is well established to be controlled by phosphorus mass transfer in one or both of the liquid phases, then the respective flux equations for phosphorus mass transfer in the metal and slag can be written as follows:

$$-\frac{d[\text{wt}\% \text{ P}]}{dt} = \frac{A}{W_m} k_m \rho_m ([\text{wt}\% \text{ P}]_b - [\text{wt}\% \text{ P}]_i) \quad (2.27)$$

$$\frac{d(\text{wt}\% \text{ P})}{dt} = \frac{A}{W_s} k_s \rho_s ((\text{wt}\% \text{ P})_i - (\text{wt}\% \text{ P})_b) \quad (2.28)$$

where W_s and W_m are the mass of slag and metal respectively, k_s and k_m are the mass transfer coefficients for phosphorus in the slag and metal respectively, ρ_m and ρ_s are the densities of metal and slag, $[\text{wt}\% \text{ P}]_i$ and $(\text{wt}\% \text{ P})_i$ are phosphorus content in the metal and slag at the interface. By assuming equilibrium at the interface we can relate the interfacial concentrations of phosphorus to the equilibrium partition coefficient expressed by Eq. (2.29).

$$L_P = \frac{(\text{wt}\% \text{ P})_i}{[\text{wt}\% \text{ P}]_i} \quad (2.29)$$

The rate of change of phosphorus in the metal is related to that in the slag by a simple mass balance:

$$\frac{d(\text{wt}\% \text{ P})}{dt} W_s = -\frac{d[\text{wt}\% \text{ P}]}{dt} W_m \quad (2.30)$$

Combining Eqs. (2.27) to (2.30), the rate equation for mass transfer controlled in both slag and metal phase can be expressed as:

$$-\frac{d[\text{wt}\% \text{ P}]}{dt} = \frac{A\rho_m}{W_m} \frac{1}{\frac{\rho_m}{k_s\rho_s L_P} + \frac{1}{k_m}} ([\text{wt}\% \text{ P}]_b - \frac{(\text{wt}\% \text{ P})_b}{L_P}) \quad (2.31)$$

From Eq. (2.31), the overall mass transfer coefficient with the units of cm/s, k_o , can be written as:

$$k_o = \frac{1}{\frac{\rho_m}{k_s\rho_s L_P} + \frac{1}{k_m}} \quad (2.32)$$

In order to determine the overall mass transfer coefficient of phosphorus, it is common to normalize the driving force by integrating the rate equation. Thus Eqs. (2.27) and (2.28) yield the following integrated rate equations for mass transport in the metal and slag, respectively.

$$\text{Ln} \left[\frac{[\text{wt}\% \text{ P}]_b - [\text{pct P}]_e}{[\text{wt}\% \text{ P}]_o - [\text{pct P}]_e} \right] \left(\frac{[\text{wt}\% \text{ P}]_o - [\text{wt}\% \text{ P}]_e}{[\text{wt}\% \text{ P}]_o} \right) \left(\frac{W_m}{\rho_m A} \right) = -k_m t \quad (2.33)$$

$$\text{Ln} \left[\frac{[\text{wt}\% \text{ P}]_b - [\text{wt}\% \text{ P}]_e}{[\text{wt}\% \text{ P}]_o - [\text{wt}\% \text{ P}]_e} \right] \left(\frac{[\text{wt}\% \text{ P}]_e}{[\text{wt}\% \text{ P}]_o} \right) \left(\frac{W_s}{\rho_s A} \right) = -k_s t \quad (2.34)$$

Inspection of Eqs. (2.33) and (2.34) shows that they can both be expressed as:

$$B \ln C = -kt \quad (2.35)$$

where C is $\left[\frac{[\text{wt}\% \text{ P}]_b - [\text{wt}\% \text{ P}]_e}{[\text{wt}\% \text{ P}]_o - [\text{wt}\% \text{ P}]_e} \right]$ in both cases and B depends on the particular rate-determining step. If mass transfer in the slag is rate-determining step, $B = \left(\frac{[\text{wt}\% \text{ P}]_e}{[\text{wt}\% \text{ P}]_o} \right) \left(\frac{W_s}{\rho_s A} \right)$; if mass transfer in the metal is rate-determining step, $B = \left(\frac{[\text{wt}\% \text{ P}]_o - [\text{wt}\% \text{ P}]_e}{[\text{wt}\% \text{ P}]_o} \right) \left(\frac{W_m}{\rho_m A} \right)$. Therefore, it should be possible to determine which form of term B applies, by varying slag

or metal weights. This should allow us to identify the rate determining step and the relevant mass transfer coefficient, k .

The integrated form of the rate equation for mixed control can be expressed as Eq. (2.36) where k_o represents the overall mass transfer coefficient defined by Eq. (2.32).

$$\left(\frac{W_m}{\rho_m A} \frac{1}{1 + \frac{W_m}{L_P W_S}} \right) \text{Ln} \left[\left(1 + \frac{W_m}{L_P W_S} \right) \frac{[\text{wt}\% \text{ P}]_b}{[\text{wt}\% \text{ P}]_o} - \frac{W_m}{L_P W_S} \right] = -k_o t \quad (2.36)$$

It is worth noting that the reaction surface area A is assumed to be constant in the derivation of the foregoing rate equations, which does not hold true for most of cases. If we can express the surface area as an analytical function of time, we can include the integration of area within the rate equation. However, in most cases the best that we have is numerical data. In such a case we may substitute the time averaged surface area into Eq. (2.36) as described in Section 2.2.3.

2.2.3 Transient Reaction Surface Area

In studies of reaction between liquid iron and oxidizing slag, several workers have found that reaction interfacial area changed during the reaction for a variety of reasons ^[11-13, 78-80].

Gaye and Riboud ^[12] observed that when reacted with oxidizing slag, the surface area of Fe-C-P droplets changed due to the metal emulsification, which resulted from CO bubble evolution. They showed that the metal droplet was divided into little fragments after short reaction time, which then coalesced into a single droplet at the end of the reaction.

By investigating the dephosphorization kinetics between an Fe-P alloy and CaO-SiO₂-FeO-MgO slag, Manning and Fruehan ^[73] showed that the effective overall mass transfer coefficient ($k_o A$) decreased by a factor of up to 16 (from 0.1 drop to 0.006) as the reaction proceeded due to a decrease in slag metal emulsification towards the end of the reaction, and proposed the higher value of ($k_o A$) at the beginning of reaction is probably due to the increase of reacting surface area.

Assis *et al.* [79] and Spooner *et al.* [80] investigated the emulsification between an Fe-P alloy droplet and slag with high basicity and high FeO_t content, using micro X-ray computer tomography (XCT). They found that the surface area of the Fe-P alloy droplet increased by a factor of up to 10 due to oxygen transfer across the slag-metal interface.

Using data from the IMPHOS pilot plant trials [81], Hewage *et al.* [82] investigated the dephosphorization kinetics in the BOF. They also mentioned the dynamic interfacial area was an issue for modeling dephosphorization kinetics.

Recently, studies on decarburization of Fe-C droplets using slag containing FeO [11, 13-15] showed that Fe-C droplets would swell due to the CO generation inside metal droplet, which causes a change in surface area. This is termed as “bloated droplets” as described in Section 2.3.

The above studies show that the reaction surface area quite likely changes during the reaction, and needs to be taken into account in estimating the mass transfer coefficient using integrated rate equations, *i.e.*, an integrated interfacial area rather than instantaneous area should be used.

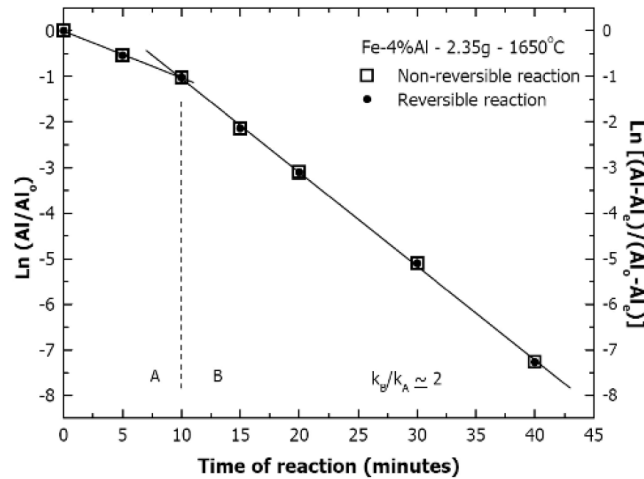


Figure 2.6 Kinetic data plots using integrated rate equation with constant surface area [83].

By studying the reaction kinetics between a Fe-Al alloy and CaO-SiO₂-Al₂O₃ slag, Rhamdhani *et al.* [83] observed that the surface area of metal droplet increased up to 4 times its original value. They further estimated the mass transfer coefficient using integrated

kinetic equations with constant surface area, and found that the plotted data splits into two different slopes as shown in Figure 2.6.

To fix this problem, Rhamdhani *et al.* proposed to use a time-averaged surface area.

$$\ln \frac{[\text{wt}\% \text{ Al}]}{[\text{wt}\% \text{ Al}]_0} = -\frac{kt}{V_m} S^*(t) \quad (2.37)$$

where $S^*(t)$ is defined as time-average surface area:

$$S^*(t) = \frac{1}{t} \int_0^t S(t) dt \quad (2.38)$$

where $S(t)$ and $S^*(t)$ are the instantaneous and integrated interfacial areas. The integrated interfacial areas can be easily calculated if the details of the $S(t)$ function are known.

Using the time-average surface area, the data in Figure 2.6 were replotted against time and the results shown in Figure 2.7. It shows that by employing the time averaged surface area the data fits a single first order rate plot.

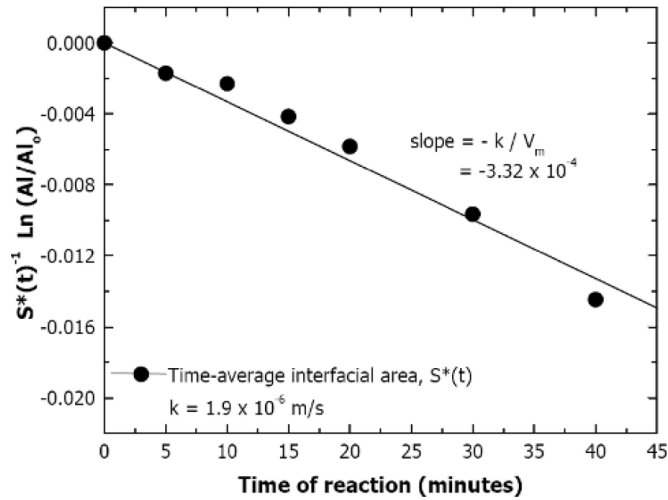


Figure 2.7 Kinetic data plots using integrated rate equation with time averaged surface area ^[83].

2.2.4 Shift of Rate Determining Step

For Eq. (2.32) representing the overall mass transfer coefficient for dephosphorization, k_o will shift between k_s and k_m depending on the magnitude of the phosphorus partition ratio L_P . The balance between control by mass transfer in the slag and by mass transfer in the metal is heavily influenced by L_P . For example, the hot metal pre-treatment process would normally offer a high L_P up to 10^4 [84-86], k_o will be essentially equal to k_m under this condition. Therefore the rate determining step for dephosphorization is more likely to be mass transfer in metal phase. In laboratory scale studies employing low basicity slag, L_P is normally of the order of 10^2 or smaller. Given this modest L_P and the fact that k_m is usually 10 times higher than k_s , one might find that k_o has the value between k_m and k_s with different fractional contribution from slag and metal phase.

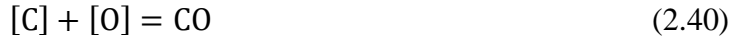
Eq. (2.26) shows that the phosphorus partition ratio L_P is strongly dependent on interfacial oxygen potential, which may change as the reaction progresses because of the oxidation of alloying elements such as carbon and silicon. The changing interfacial oxygen potential will also alter the rate determining step by affecting L_P .

For reactions between Fe-C alloys and slag containing different oxidizers, Shibata *et al.* [77] investigated the change of relative resistance to the total resistance for the transport in the metal phase R_m and in the slag phase R_s for each element (P, Si, Mn and S). They found that for FeO bearing slag, the fraction of the overall resistance to dephosphorization attributed to the metal phase, decreased from approximately unity to around 0.3 as reaction proceeded. This observation was attributed to the decreasing interfacial oxygen potential resulting in a low value of L_P .

2.2.5 Dynamic Interfacial Oxygen Potential

In oxygen steelmaking for a given simplified metal-slag system, *i.e.*, iron-carbon and slag containing FeO, the following reactions are considered to occur and reach a steady state at the interface:





Then the interfacial oxygen potential at any given time is decided by balancing the oxygen supply rate from FeO in the slag and the oxygen consumption by the formation of CO. This is illustrated in the Figure 2.8, where the interfacial oxygen potential is plotted against $\frac{\alpha_m}{\alpha_s}$, where $\alpha_m = \frac{k_m \rho_m}{100 M_C}$, $\alpha_s = \frac{k_s \rho_s}{100 M_{FeO}}$. k_m and k_s , ρ_m and ρ_s are mass transfer coefficients and density of metal and slag, respectively. M_C and M_{FeO} are molar weight of carbon and FeO, respectively.

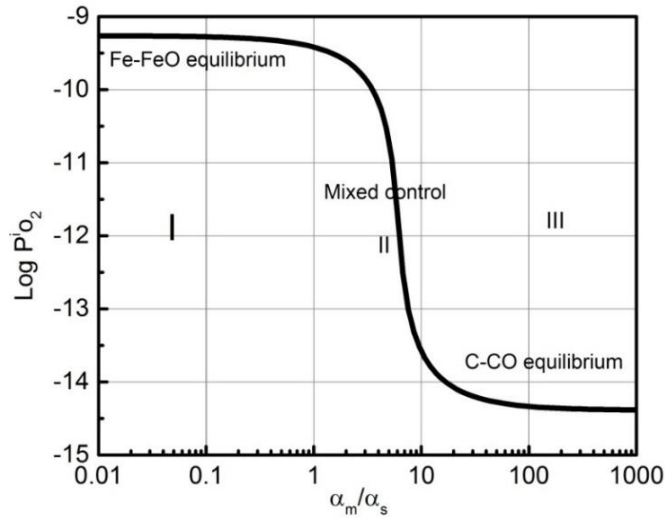


Figure 2.8 The interfacial oxygen potential $P_{O_2}^i$ as a function of α_m/α_s

Figure 2.8 can be separated into three zones, which represent different control mechanisms. At relatively lower value of $\frac{\alpha_m}{\alpha_s}$, *i.e.*, region I corresponding to a much higher mass transfer coefficient in the slag, the interfacial oxygen potential is determined by Fe-FeO equilibrium. While for higher values, *i.e.*, region III responsible for relatively higher mass transport in metal phase, it indicates oxygen transfer in slag phase is much slower compared to carbon transfer in metal phase, the interfacial oxygen potential is then dependent on the C-CO equilibrium. In between I and III is region II representing mixed control between mass transfer in the metal and slag phase, shows setting an interfacial oxygen potential between that in equilibrium with Fe-FeO and that in equilibrium with C-CO.

By studying hot metal dephosphorization, Miyamoto *et al.* [87] calculated the interfacial oxygen potential based on phosphorus partition ratio and slag composition at the reversion point. They found that $P_{O_2}^i$ varied between the value set by Fe-FeO equilibrium and that decided by C-CO equilibrium. They also showed the effect of slag basicity on the balance as presented in Figure 2.9.

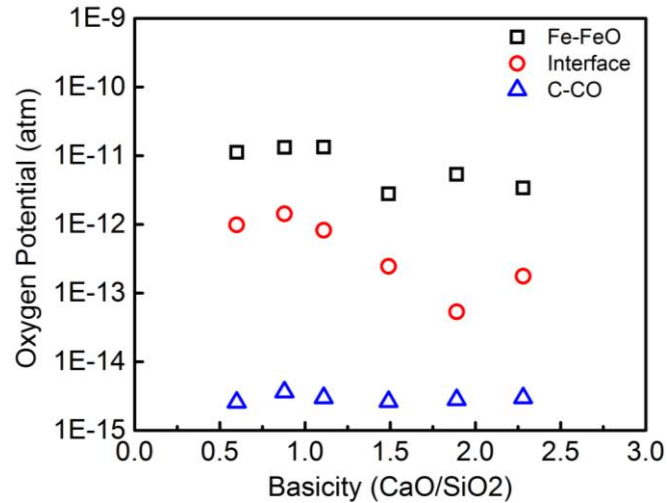


Figure 2.9 The $P_{O_2}^i$ as a function of slag basicity [87].

Based on a kinetic study of dephosphorization, Wei *et al.* [88] observed that interfacial oxygen potential increases with increasing the ratio of $Fe^{3+}/(Fe^{2+}+Fe^{3+})$ in the slag and decreases with increasing intensity of mechanical stirring. They also demonstrated that the interfacial oxygen potential ranges from 10^{-15} - 10^{-14} atm, which is 2-3 orders of magnitude smaller than the oxygen potential in the bulk slag. While Monaghan *et al.* [18] showed that the interfacial oxygen potential was close to the oxygen potential in equilibrium with the iron oxide activity in the slag, and was independent of the Fe^{3+}/Fe^{2+} ratio.

By balancing all the oxidization and reduction reactions at the interface, Shibata *et al.* [77] calculated the oxygen activity at the interface as a function of reaction time, which was found to decrease rapidly from the initial high value for FeO slag.

2.2.6 Mass Transfer of “FeO” in the Slag

Since the oxygen potential at the interface strongly depends on the oxygen supply from FeO in the slag, it is important to understand the mechanism of FeO transfer, *i.e.*, oxygen transfer in liquid slag containing iron oxide. It is well accepted that oxygen is transferred as Fe^{2+} and O^{2-} ions or as electrons, depending on the relative values of ionic and electronic conductivity. Bockris *et al.* [89] discussed that ionic conduction via oxygen ions in the slag is negligible, which is consistent with experimental measurement of transport numbers for FeO-CaO-SiO₂ slags which revealed that cations (Fe^{2+} and Ca^{2+}) are the exclusive ionic charge carriers. Similar findings have also been reported by other researchers [90-93]. While Speelman *et al.* [94] and Sasabe *et al.* [95] found that the electrons play an important role in oxygen transfer through slag.

“Iron oxide” in most slags is present as both ferric and ferrous ions and the ratio ($\text{Fe}^{2+}/\text{Fe}^{3+}$) depends on the oxidation state of the slag. Electron transfer typically occurs by “small polaron hopping” or “Mott’s transition” proposed by Mott [96]. In this mechanism, electronic conduction can take place by transfer of an electron from a low valence (Fe^{2+}) cation to a neighboring high valence cation (Fe^{3+}). Since electronic conduction via charge hopping requires neighboring divalent and trivalent iron ions to interact, the electronic conductivity is strongly affected by the number or concentration of adjacent Fe^{2+} - Fe^{3+} couples.

Employing the charge hopping theory, Barati and Coley [97,98] studied the oxygen potential dependency of total, electronic and ionic conductivities for FeO-CaO-SiO₂ slags. They found that the electronic conductivity was proportional to square of the FeO content in the slag.

2.3 Bloated Metal Droplet in BOF

2.3.1 Metal Droplet Generation Rate and Size Distribution

In basic oxygen steelmaking, metal droplets are created by the impingement of the supersonic oxygen jet which blows onto the surface of the liquid metal. The generation of metal droplet is affected by two factors. One is the momentum intensity of the gas jet, which is affected by lance height and the oxygen flow rate. The other factor is related to the properties of liquid metal, *i.e.*, density, viscosity and surface tension [99, 100]. Mathematical models have been developed to model the droplet generation rate by several researchers [99-102]. Subagyo *et al.* [102] investigated the droplet generation using an iron-slag-nitrogen gas system at high temperature. They derived the following empirical correlation of droplet generation rate with the dimensionless parameter N_B . N_B , termed as the blowing number is based on the Kelvin-Helmholtz instability criterion. The correlation describes experimental results very well for both hot and cold systems.

$$\frac{R_B}{R_G} = \frac{(N_B)^{3.2}}{[2.6 \times 10^6 + 2.0 \times 10^{-4}(N_B)^{12}]^{0.2}} \quad (2.41)$$

where R_G is the volumetric flow of blown gas in normal cubic meters per second and R_B is the droplet generation rate in kilograms per second.

Knowledge of metal droplet size distribution is also critical in estimating the significance of the gas-slag-metal emulsion zone. Number of studies [9-10, 103-105] have been carried out to investigate the size distribution of metal droplets either from plant trials or laboratory experiments. Typical droplet sizes range from 0.04 to 70mm [103].

2.3.2 Residence Time

Metal droplets are ejected into the slag layer creating a gas-slag-metal emulsion, offering a large interfacial reaction area that greatly enhances the refining rate. After spending a certain residence time in the emulsion zone, metal droplets sink back to the metal bath. Therefore, the residence time of metal droplets in the slag significantly influences the

overall refining rate, especially for dephosphorization which can only take place during metal-slag contact.

There are some discrepancies regarding the residence time of metal droplets in the emulsion zone, which is estimated from either experimental measurement^[9-10, 100, 106] or mathematical modelling^[7-8]. Price^[9] measured the residence time of metal droplets in a 90 ton converter using radioactive gold isotope tracer, obtaining an average value of 120±30 seconds. Based on the measurement of phosphorus removal rate from a 200 ton converter, Schoop *et al.*^[106] estimated the residence time to range from less than 1 to 60 seconds. Similar to Schoop *et al.*^[106], Kozakevitch^[5] suggested the residence time is probably around 1 to 2 minutes based on chemical reaction data. According to experimental results at room temperature, Urquhart and Davenport^[10] proposed a value of 0.25 seconds as the average value for the residence time of metal droplets in the emulsion. With a cold model simulation, He and Standish^[100] suggested a value of 1 minute as a reasonable value for the mean residence time in an industrial furnace. For kinetics analysis of chemical reactions in the emulsion, Oeters^[107, 108] also suggested a residence time of 1 minute as a reasonable value.

Subagyo *et al.*^[7] originally applied the concept of ballistic motion to calculate the trajectory and residence time of metal droplets ejected into slag assuming that there is no chemical reaction occurring. They demonstrated that the droplet residence time can be determined by knowing initial velocity of a droplet, the slag velocity and the physical properties of the emulsion. These workers calculated residence times of up to 0.25 second which they acknowledged could not support the observed refining rates.

Brooks *et al.*^[8] continued their work of Subagyo *et al.*^[7] and developed a model for ballistic motion of metal droplets to investigate the influences of initial ejection velocity, ejection angle and droplet diameter on droplet residence time. Using this model, they found that the residence time is less than 1 second without considering decarburization. The residence time can be prolonged to more than 60 seconds by considering swelling induced by CO generation inside the metal droplet.

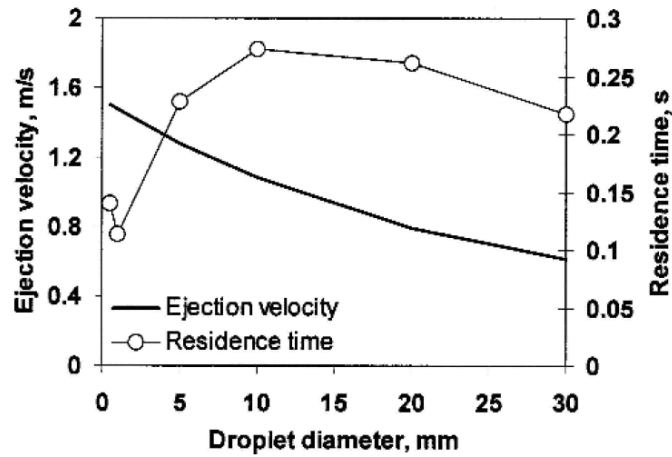


Figure 2.10 The residence time for fully dense droplet without swelling ^[8].

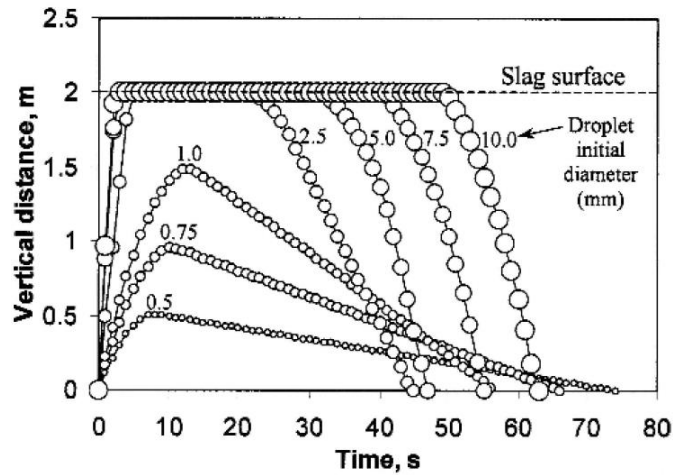


Figure 2.11 The residence time for swelling metal droplets ^[8].

2.3.3 Decarburization and Swelling of Metal droplets

CO bubbles build up within the metal droplet when CO generation rate is faster than the rate at which gas bubbles escape. This phenomenon is termed “droplet swelling or bloating”. The swollen metal droplets have less density thus increasing their residence time in the slag, which is expected to improve overall refining rates. Bloating occurs under specific conditions, *i.e.*, the oxygen supply rate from the slag into the bulk metal is higher than carbon diffusion rate from the bulk metal to the surface.

Baker *et al.* ^[109-111] observed that droplets exploded while falling through oxygen gas, which implies that rapid nucleation of CO can indeed occur inside metal droplets at high oxygen potential. When studied reactions between iron carbon droplets and oxygen gas, Gao *et al.* ^[112, 113] also observed similar phenomenon. Based on experimental data available for decarburization, Sun *et al.* ^[113] proposed a kinetic model to explain carbon boil when liquid iron droplets reacted with oxidizing gas.

During the reaction between Fe-C-S droplets and slag containing FeO, Molloseau and Fruehan ^[14] observed droplet swelling using the X-ray Fluoroscopy, which is depicted in the following series of pictures. Based on this work ^[14], Sun ^[114] developed a kinetic model to investigate the influences of FeO in slag, carbon in the droplet and the droplet size, silicon in metal and ambient pressure on swelling phenomenon of Fe-C droplets.

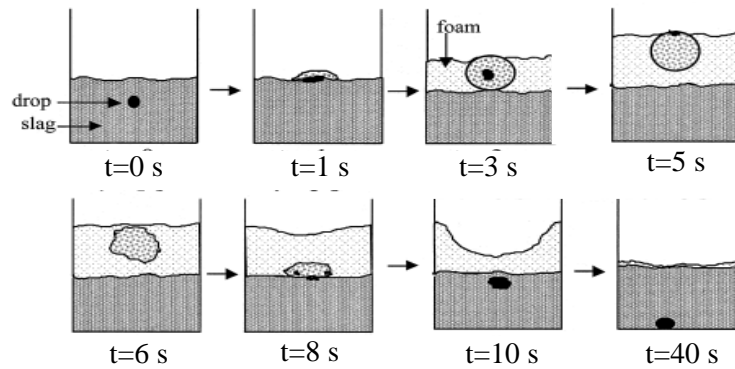


Figure 2.12 Schematic diagram of behavior of Fe-C droplet observed by X-ray fluoroscopy ^[14].

Murthy *et al.* ^[115] also found that Fe-C droplets became bloated after reacting with slag containing FeO. Recently, in an attempt to fully understand the droplet swelling phenomenon, Chen and Coley ^[11] carried out an extensive study on kinetics of droplet swelling during the reaction between Fe-C-S droplets and slag containing FeO. They investigated the influences of metal composition, FeO content and temperature on droplet swelling, and further developed a mathematical model to describe CO nucleation inside metal droplet.

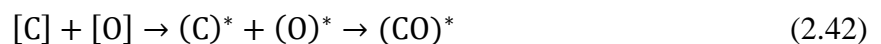
2.3.4 CO Nucleation inside Metal Droplet

Experimental observations ^[14, 15] have confirmed that CO nucleation inside metal droplet leads to droplet swelling. However, according to the theoretical calculation, a supersaturation of 5×10^4 atm ^[116, 117] is required for reasonably observable CO nucleation rates in liquid metal. This is two orders of magnitude higher than experimentally observed. The calculated supersaturation pressure, suggests that it is impossible for CO bubbles to nucleate inside a metal droplet under typical experimental conditions. A variety of possible explanations have been proposed for this disagreement. A common criticism for this disagreement is that the application of macroscopic surface tension to small clusters representing subcritical and critical nuclei is an invalid assumption ^[116].

Levine ^[118-120] suggested that the presence of doubly charged surface adsorbed oxygen ions would decrease the surface tension and the work required for the formation of an embryo inside the metal. On the other hand Kwak and Oh ^[121] mentioned that the calculated supersaturation is still at a very high value (25000 atm) even if the surface tension value is reduced to 1.0 Nm^{-1} when surface active elements are present.

Gare *et al.* ^[122] proposed that the nucleation of CO inside the droplet is heterogeneous due to the entrainment of gas in the metal droplet while Robertson and Jenkins ^[123] suggested that the CO nucleation might be invoked by “vortex nucleation” instead of homogeneous or heterogeneous nucleation. They also agreed that oxygen has a large effect on interfacial turbulence thus benefiting CO nucleation. Based on the study of the homogenous nucleation of dissolved gases in molten metal, El-Kaddah and Robertson ^[124] found that the adsorbed surface active oxygen plays an important role in nucleation.

Considering the clustering process of CO molecules, which is formed via the following reaction, Kwak and Oh ^[121] developed a homogeneous bubble nucleation model to describe CO bubble nucleation in Fe-C-O melts as described by reaction (2.42).



where $(\text{C})^*$ and $(\text{O})^*$ are activated complexes, $(\text{CO})^*$ represents a metastable CO cluster.

Since this clustering process of CO molecules is quite similar to liquid-vapor phase change phenomena ^[125-127], the nucleation rate can be written as:

$$J_s = N_o \exp\left(\frac{-\Delta H}{kT}\right) \left[\frac{2\sigma}{\pi m}\right]^{1/2} \exp\left(\frac{-16\pi(\sigma)^3}{3kT(P_{ve} - P_l)^2}\right) \quad (2.43)$$

where N_o is the number of CO embryos in the liquid, σ is the surface tension at the liquid gas interface, ΔH is the heat of formation of one CO molecule; m is the mass of one molecule; T is the temperature in Kelvin, k is the Boltzmann constant; P_{ve} is the pressure in the vapour bubble at equilibrium, and P_l is liquid pressure where $P_{ve} - P_l \approx P_{ve}$.

Chen and Coley ^[15] predicted the nucleation rate was essentially zero by using Eq. (2.43), which is inconsistent with the experimental observations of significant swelling of metal droplet. Therefore, they introduced a surface tension modifying factor φ into the nucleation equation considering the effect of dissolved oxygen on energy barrier for nucleation proposed by Levine ^[118-120]. The surface tension modifying factor φ has been estimated to have a value between 0 and 1 ^[116, 118, 127]. $\varphi = 0.023$ was obtained based on their experimental results ^[15], and used to predict the CO generation rate at different temperatures, which gave a very good agreement with the experimental results as shown in Figure 2.13. They also determined values of φ for slags with different FeO content.

$$J_s = N_o \exp\left(\frac{-\Delta H}{kT}\right) \left[\frac{2(\varphi\sigma)}{\pi m}\right]^{1/2} \exp\left(\frac{-16\pi(\varphi\sigma)^3}{3kT(P_{ve} - P_l)^2}\right) \quad (2.44)$$

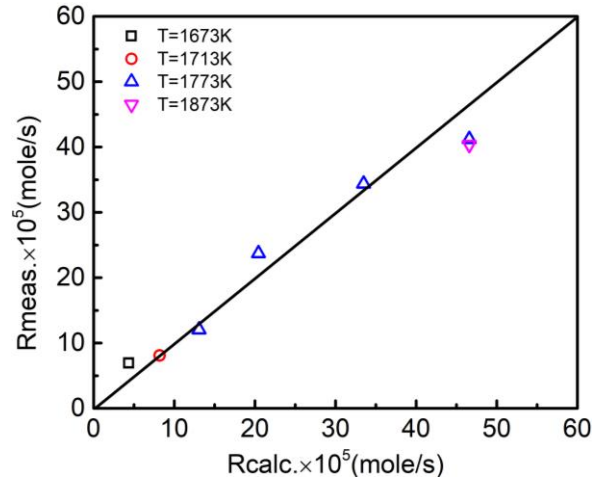


Figure 2.13 Comparison of CO generation rate between theoretical predictions and experiment measurements ^[15].

2.3.5 Modeling of Dephosphorization Using Bloated Droplet Theory

Based on the bloated droplet theory, Ankit ^[128] developed a model for dephosphorization in emulsion zone by combining the bloated droplet model and slag model. He used the correlation developed by Subagyo *et al.* ^[102] to calculate the rate of droplet generation, and the ballistic motion of droplets proposed by Brooks *et al.* ^[8] to estimate the residence time of metal droplet. The rate equation for mixed transport control was used to calculate the rate of dephosphorization.

Recently, Dogan *et al.* ^[129-131] developed a comprehensive decarburization model for the BOF, which combined micro and macro kinetics approaches to the emulsion and the bath zones with bloated droplet theory. Employing the same approach, Rout *et al.* ^[132] proposed a model for dephosphorization in the emulsion and bath zone. In this model, the dephosphorization kinetics between a single droplet and slag during its residence time is represented by Eq. (2.45) where dynamic rate parameters are taken into account due to the swelling of droplets.

$$\frac{\partial [\text{wt}\% \text{ P}]_b}{\partial t} = -\frac{k(t)A(t)}{V(t)}([\text{wt}\% \text{ P}]_b - [\text{wt}\% \text{ P}]_e) \quad (2.45)$$

where $k(t)$, $A(t)$ and $V(t)$ are dynamic parameters, changing with time. It should be noted that whilst it is appropriate to consider the time dependent surface area of bloated droplets, the volume term relates specifically to the volume of metal in the droplet which is not time dependent. More recent work by Rout *et al.* [133] has adopted a revised version of Eq. (2.45) which employs a constant droplet volume.

The Higbie's surface renewal theory was used to calculate the mass transfer coefficient of phosphorus at slag-metal droplet interface as expressed in Eq. (2.46). The contact time was estimated from the velocity of droplet u_d and diameter of droplet D_d .

$$k_P = 2 \left(\frac{D_P u_d}{\pi D_d} \right)^{1/2} \quad (2.46)$$

where D_P is the diffusivity of phosphorus in slag.

The results for dephosphorization agreed well with the industrial data as reported in their more recent work [133].

2.3.6 Dephosphorization of Bloated Droplets

As discussed above, dephosphorization of bloated metal droplets links in a complicated way with decarburization in the emulsion zone. On one hand, a higher carbon oxidation rate creates greater swelling and longer residence time. Therefore a higher rate of carbon oxidation may improve overall phosphorus oxidation. On the other hand, higher CO gas generation rates consume oxygen more rapidly at the slag-droplet interface, which greatly reduces the driving force for dephosphorization by lowering the interfacial oxygen potential. These conflicting effects are further complicated by the fact that, CO bubbles generated inside metal droplets can increase the mass transfer of phosphorus in metal phase via stirring, which offers a higher surface renewal rate. Therefore, a detailed study of this interplay is essential to understand the kinetics of dephosphorization of bloated metal droplets by reaction with slag in the BOF. It is worth noting that when investigating the reaction kinetics between drops of Fe-C, Fe-C-P and Fe-C-S alloys and oxidizing slag, Gaye *et al.* [12] observed that the dephosphorization rate of Fe-C-P drops was much faster

than for Fe-P drops due to the intensive agitation resulting from CO bubble evolution. These workers observed in the case of Fe-C-P drops, phosphorus was decreased from 1.5 to 0.006 wt% in 10 seconds. This observation indicates that stirring caused by CO bubble evolution plays a critical role in dephosphorization kinetics. But a detailed study is required to quantify the influence of CO bubble evolution on the dephosphorization driving force and mass transfer of phosphorus in the metal phase.

Based on the foregoing literature review, there is a need for a clear understanding of dephosphorization kinetics for bloated metal droplets. The objective of the current work is to quantify the competing factors affecting phosphorus partition and transfer rates in bloated metal droplets. To this end, the research will investigate the dephosphorization of iron carbon droplets as a function of decarburization rate and temperature. The effect of decarburization on the maximum phosphorus partition will be determined and used to calculate the mass transfer coefficient of FeO in the slag which will be correlated with slag properties.

The measured decarburization rates will be combined in a model with FeO mass transfer to calculate the interfacial oxygen potential as a function of time under various experimental conditions. The calculated interfacial oxygen potential will be employed in determining the time dependent interfacial phosphorus partition ratio. This will be used in turn, to determine the mass transfer coefficient for phosphorus in the metal from the overall mass transfer coefficient.

The mass transfer coefficients determined for phosphorus in the metal will be correlated with CO nucleation rates and evaluated using surface renewal theory.

Finally, the theories developed in this work will be evaluated against kinetic data from the published literature, determined for a wide range of conditions and will be tested against the dephosphorization behavior of basic slags.

Chapter 3

The Influence of Sulfur on Dephosphorization Kinetics between Bloated Metal Droplets and Slag Containing FeO

In Chapter 3, all of the experiments and data analysis were carried out by me. Nils Anderson and Brian Jamison provided assistance with furnace setup. Jim Garret aided with metal droplets preparation. Xiaogang Li and Doug Culley provided training on ICP-OES and LECO chemical analysis. Dr. Kenneth S. Coley provided much useful discussion on data analysis.

The manuscript was initially drafted by me and edited to the final version by Dr. Neslihan Dogan and Dr. Kenneth S. Coley. This chapter has been published in *Metallurgical and Materials Transactions B*. 2017, DOI: 10.1007/s11663-017-1002-0. The following Chapter is the pre-publication version of the article.

Abstract

The bloating behavior of metal droplets and the dephosphorization behavior of bloated droplets at 1853 K, were investigated using X-ray fluoroscopy coupled with constant volume pressure change measurements and chemical analysis of quenched samples. The effect of sulfur content on dephosphorization kinetics was studied during the decarburization period. The slag foamed during the reaction forming a foamy layer over a dense layer. After a short incubation period, the droplets became bloated due to internal decarburization. The bloated droplets floated from the dense slag into the foamy slag. The behavioral changes are directly related to the effect of sulfur on the incubation time for swelling. The dephosphorization reaction was very fast; droplets with low sulfur contents experienced phosphorus reversion shortly after entering the foamy slag, while those with higher sulfur content took a longer time to swell and went through reversion before they

entered the foam. The dephosphorization rate and maximum phosphorus partition were higher at lower CO evolution rates because the dynamic interfacial oxygen potential increased with the decreasing oxygen consumption rate. The rate controlling step for dephosphorization was initially a combination of mass transport in both the metal and the slag. As the iron oxide in the slag was depleted, the rate control shifted to mass transport in slag.

3.1 Introduction

During oxygen steelmaking, metal droplets created by the impact of the oxygen jet are ejected into the slag, where they are decarburized and dephosphorized by reaction with reducible oxides. Several researchers have studied aspects of droplet behavior relevant to steelmaking including, decarburization^[1-6], droplet generation^[7-16], size distribution^[17, 18] and residence time^[19]. Other workers have developed models^[20-23] and conducted plant trials^[24-28], which considered the role of droplets in overall process kinetics. Previous work in the authors' laboratory^[6] showed that droplet swelling, caused by CO formation inside the droplet, increased the droplet residence time in the slag thereby favoring decarburization. This work formed the basis of the Bloated Droplet Model, which has since been employed in an overall BOF model by workers at Swinburne University in Australia^[20, 21]. Notwithstanding very recent work, which suggests bubbles formed on the outer surface of droplets can offer similar increases in residence time, convincing experimental evidence for bloated droplets has been reported by several researchers^[5, 6, 29]. Given the importance of droplet swelling in controlling residence time and the fact that dephosphorization is only favored when slag and metal are in contact, data on dephosphorization of bloated droplets are required for the proper inclusion of dephosphorization in BOF process models.

Dephosphorization of hot metal has been studied extensively but for brevity only a subset of this work will be reviewed here. Research on phosphorus partitioning in the BOF has been reviewed by Basu *et al.*^[30] More recently, phosphorus equilibrium between liquid iron and BOF type slag has been investigated by Assis *et al.*^[31], who further developed a

corrected phosphorus partition correlation by combining other researchers' work. Several studies have been conducted on the dephosphorization kinetics of iron-carbon melts using oxidizing slag [32-35]. Mori *et al.* [32] and Wei *et al.* [33] suggested that the rate of dephosphorization was under mixed control by mass transport in both slag and metal phase. Monaghan *et al.* [34] proposed that the rate determining step was mass transfer in the slag. Assuming mass transfer in both slag and metal was rate controlling step, Manning and Fruehan [35] showed that the mass transfer parameter (kA) decreased as the reaction proceeded and appeared to be a function of interfacial tension, which changed with respect to time. Employing IMPHOS pilot plant data, Hewage *et al.* [36] investigated the dephosphorization kinetics in the BOF and found that dephosphorization cannot be explained by a simple first order equation with either static equilibrium or dynamic equilibrium values. These workers also stressed the importance of transient parameters, such as surface area, volume, residence time and mass transfer coefficient.

The present work seeks to develop a detailed quantitative understanding of the interplay between dephosphorization and decarburization of bloated droplets, and to investigate the effect of decarburization rate on a range of important factors in dephosphorization. Chen and Coley [6] showed that the rate of CO evolution during droplet swelling was primarily controlled by the nucleation of CO bubbles within the droplet. They also demonstrated that the rate of CO evolution, as a function of sulfur in the metal, went through a maximum at approximately 0.011 wt% S. This suggests that although CO evolution was controlled primarily by nucleation, bubble growth also played a role; nucleation increased with decreasing surface tension caused by sulfur, whereas bubble growth decreased due to the surface poisoning effect of sulfur. The optimum combination of increasing nucleation rate and decreasing growth rate occurred at approximately 0.011 wt% S. Given this observation, it should be possible by using droplets with different sulfur contents to determine the dephosphorization rate as a function of CO evolution rate.

3.2 Experimental Procedure

A resistance-heated vertical tube furnace (See Figure 3.1), with an 80 mm diameter alumina working tube was used for all experiments. The tube ends were sealed with O-rings and water-cooled stainless steel caps. The furnace was equipped with X-ray imaging to observe the swelling of droplets in-situ and a pressure transducer to measure gas evolution using the constant volume pressure increase technique (CVPI).

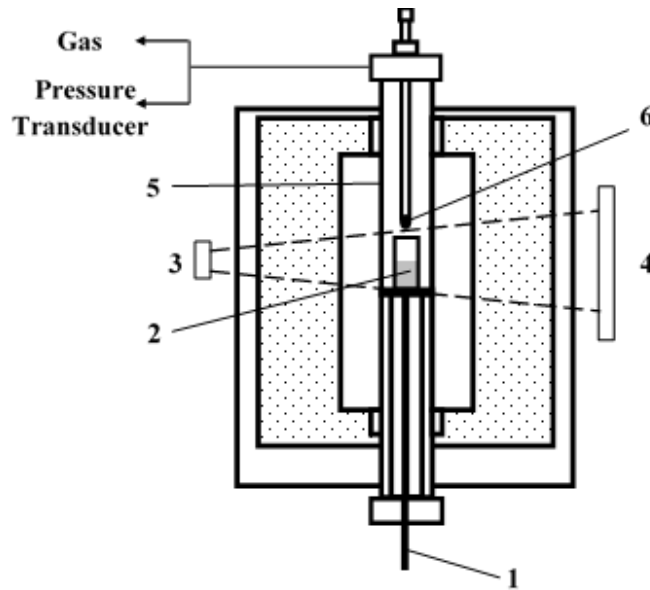


Figure 3.1 Schematic diagram of the Furnace: 1. support rod, 2. slag, 3. X-ray generator, 4. image intensifier, 5. working tube and 6. iron pellet ^[37]. (Reprinted with permission)

Fe-C-P-S droplets were prepared as follows: an appropriate amount of electrolytic iron, FeP and FeS were melted together to prepare master Fe-P-S alloys using an arc melter under an argon atmosphere. The master alloys were homogenized at 1173 K for 24 hours in a sealed tube furnace under flowing purified argon. After heat treatment, four samples were taken from different positions in the master alloy analyzed using Inductively Coupled Plasma Optical Emission Spectroscopy (ICP-OES). The master alloys were then rolled into sheet for convenient use. Finally, individual droplets were prepared by melting an appropriate quantity of master alloy along with an appropriate quantity of graphite in a vacuum arc melter. The oxygen content in metal droplets fabricated in this manner was

50 ± 20 ppm^[38]. Three sample droplets were taken from each batch of droplets to confirm the concentration of phosphorus using ICP-OES, and carbon and sulfur using LECO combustion analysis. Slags were prepared by mixing reagent grade Al_2O_3 , CaO and SiO_2 , and the mixture was held at 1073 K for 6 hours to remove moisture; FeO was added to the dry mixture to prepare slags of a desired composition. This mixture of slag was used directly for all experiments without premelting. Approximately 25 g of slag, mixed as described above, was placed in a 45 mm diameter alumina crucible and then placed in a furnace which was sealed and flushed with deoxidized argon (copper turnings 873 K). The crucible was raised into the hot-zone of the furnace and, after reaching the desired temperature, was held for one hour to allow homogenization. The metal droplet was dropped into the molten slag via a dispensing tube as shown in Figure 3.1. A hole at the bottom of the dispensing tube was sized to ensure that the droplet must melt before passing through. When the droplet melted and entered the slag, the time was set to zero. Videos were recorded by X-ray Fluoroscopy (GE OEC Medical Systems, Inc.), and a differential pressure transducer, maximum measurable range of 2 psi, was used to measure the pressure change caused by the gas evolution during the reaction. An oxygen sensor was installed at the exhaust gas outlet to monitor the oxygen partial pressure in the furnace. The support rod shown in Figure 3.1 was held in place by an O-ring and a collar. By unscrewing the collar, the crucible could be dropped into the quench chamber (water cooled stainless steel) within 1 second. Samples were quenched at different reaction times and taken for chemical analysis of phosphorus. Metal samples were dissolved in acid using a microwave digester and analyzed by ICP-OES. The slag composition for all experiments was 35 wt% SiO_2 - 32 wt% CaO -17 wt% Al_2O_3 -16 wt% FeO . Table 3.1 summarizes the composition of metal droplets used in experiments. All the experiments were conducted at the temperature of 1853 K.

Table 3.1 Metal droplet compositions (wt%).

Droplets	C	S	P
1	2.62±0.053	0.007±0.0003	0.088±0.0066
2	2.62±0.053	0.011±0.0005	0.088±0.0066
3	2.62±0.053	0.014±0.0005	0.088±0.0066
4	2.62±0.053	0.017±0.0008	0.088±0.0066
5	2.62±0.053	0.021±0.001	0.088±0.0066

3.3 Experimental Results

3.3.1 Measurement of CO Evolution Rate

Figure 3.2(a) shows the total amount of CO gas generated during reactions between slag and droplets as a function of time and droplet sulfur content. It was found that the total amount of CO generated increased with an increase in sulfur content of the droplet. For example, the total CO gas produced for droplets with 0.007 wt%, 0.014 wt% and 0.021 wt% S were 9.23×10^{-4} moles, 1.12×10^{-3} moles and 1.44×10^{-3} moles, respectively. It is also noteworthy that the initial stage of reaction, where the rate of CO generation was low, was extended with increasing droplet sulfur content. The peak CO evolution rate, taken from the maximum slope of each curve shown in Figure 3.2(a), was plotted in Figure 3.2(b) as a function of sulfur content. This figure shows that CO generation rate increases from 5.82×10^{-5} to a maximum of 1.04×10^{-4} mole/s for droplets with 0.014 wt% S. The sulfur content at the peak, 0.014wt%, is higher than that (0.011 wt%) previously reported by the authors ^[39]. This discrepancy is believed to be related to a change in the production technique of the droplets. The mechanism by which sulfur affects decarburization behavior will be discussed in Section 3.4.

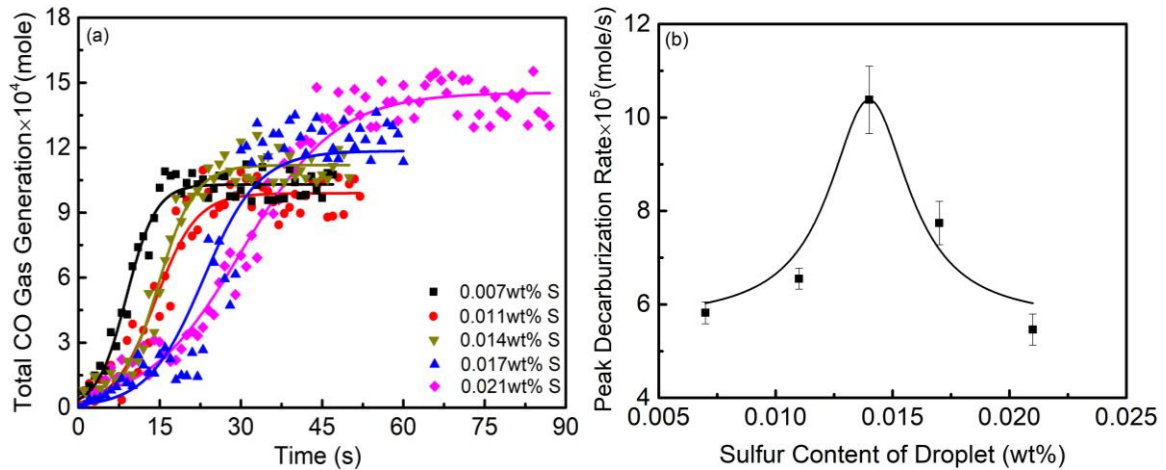


Figure 3.2 (a) CO gas generation with time and (b) peak decarburization rate as a function of metal sulfur content.

3.3.2 X-ray Fluoroscopy Observations of Droplets

A series of X-ray images, depicting the typical bloating behavior of droplets containing 0.014 wt% S are presented in Figure 3.3 (a) through (h). Once the droplet melted, ~30 seconds, and fell into the molten slag the time was set to zero. Within the next 13 seconds, the initial decarburization step takes place. During this period, the droplet was covered by a gas halo and started to float out of the dense slag. In the meantime, a foamy slag layer was formed on top of the original dense slag. The proportion of foamy slag increased at the expense of the dense slag as the reaction proceeded. During this initial period, the total increase in droplet volume was less than three times the original value.

After this incubation period, the droplet swelled rapidly and floated out of the dense slag. During this stage the volume increased by over 14 times its original value; the corresponding increase in the droplet-slag interfacial area was over 5 times. During this period, the bloated droplet remained in the foamy slag. The fast decarburization ceased after 24 seconds, and the droplet sank back into the dense slag. The reactive droplet continued to form CO gas as it fell to the bottom of the crucible. The foamy slag began to collapse at the end of the fast decarburization period, lasting approximately 40 seconds before collapsing completely.

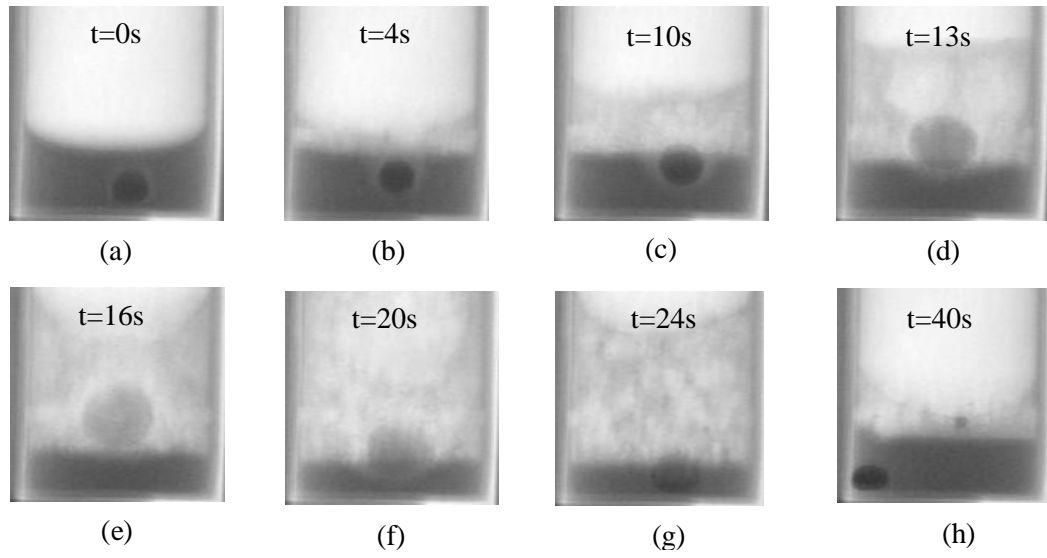


Figure 3.3 Typical behavior of a metal droplet with 0.014 wt% S observed by X-ray fluoroscopy at 1853 K.

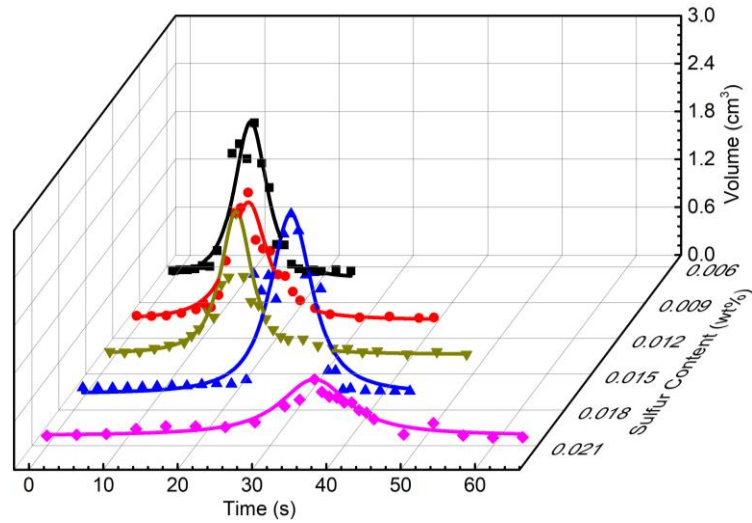


Figure 3.4 Variation of the volume of bloated droplets with respect to sulfur content and time.

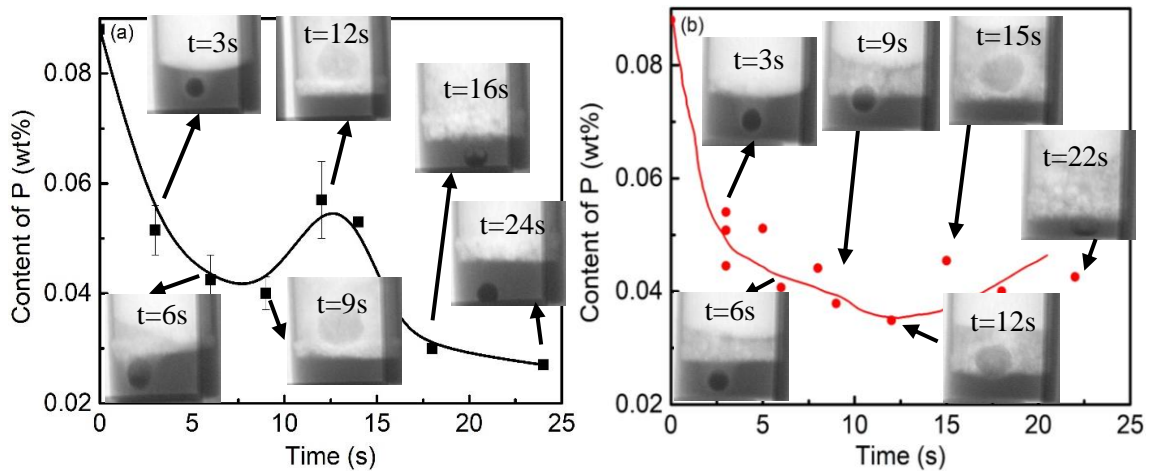
The change in the volume of droplets as a function of time and sulfur content is presented in Figure 3.4. This figure shows that as the sulfur content of droplets increased from 0.007 to 0.021 wt%, the incubation time for swelling increased from 7 to approximately 32 seconds. It also can be seen that droplets behaved similarly up to 0.018 wt% S. The droplets with 0.021 wt% S showed a much lower maximum volume but a much longer period of swelling. These droplets also had the longest incubation time and, despite the fact that they

showed similar peak decarburization rates to the droplets with 0.007 wt% S, the peak volume was considerably lower. This observation may be related to the fact that the rates of gas generation and escape were fairly close and this relatively small difference was responsible for the change in volume; a small fractional change in the rate of generation represents a fairly large change relative to the gas retained in the droplet.

3.3.3 Dephosphorization of Bloated Droplets

The change of phosphorus content of the droplet as a function of time and sulfur content is shown in Figure 3.5. It is worth noting at this point that these data are somewhat sparse, particularly when one considers any single condition. This is a direct consequence of the difficulty of quenching droplets at small time intervals, a weakness that is compounded when one considers that most of the dephosphorization is complete within a few seconds. The authors acknowledge this weakness and would not choose this technique in a study focused entirely on dephosphorization. However, the current work is focused on the interplay between dephosphorization and decarburization of bloated droplets. As such there was little choice but to actually study bloated droplets, despite any experimental difficulties that approach might present. As seen below in Section 3.4, the data show a remarkably consistent pattern. The data points shown in Figure 3.5(a) prior to the reversion point are the mean of at least three different experiments. The error bars represent the standard error of the mean. According to Figures 3.5(a) through (e), droplets were dephosphorized first on entering the dense slag, then subsequently exhibited one of two types of reversion behavior. Figure 3.5(a) shows a droplet that entered the foamy slag prior to reversion. Figure 3.5(e) shows the behavior of a droplet that remained in the dense slag for longer time and started to go through reversion in the dense slag. It is interesting to note that when the droplets, which have undergone phosphorus reversion in the foamy slag, sink back into the dense slag, dephosphorization starts again. It seems reasonable to assume that, depending on the extent to which dephosphorization has progressed prior to the droplet entering the foamy slag, a wide range of behaviors might be observed. This is seen in Figures 3.5(a) through (e) which show apparently random dephosphorization behavior as

a function of droplet sulfur content. However, when one considers that the droplet sulfur content will control, the incubation time for swelling and thereby the time the droplet enters the foamy slag, and the rate of CO formation which will control the dynamic interfacial oxygen potential and the depletion of the slag FeO, it is possible to rationalize the apparently disparate behavior. Figures 3.5(a) and (b) show that droplets with low sulfur content dephosphorized primarily in the dense slag and experienced phosphorus reversion shortly after entering the foamy slag. Alternatively, those with higher sulfur content shown in Figures 3.5(c), (d) and (e) (0.014 wt% S, 0.017 wt% S and 0.021 wt% S) went through reversion before they entered the foam. Comparing the data presented in Figure 3.5 with that in Figure 3.2 suggests that for droplets with sulfur 0.017 wt% and less, the minimum phosphorus content increased with the increasing CO evolution rate. The above observations are supported by the detailed X-ray images of droplets at each stage of reaction and agree with the established understanding of dephosphorization of iron-carbon alloys [32-34].



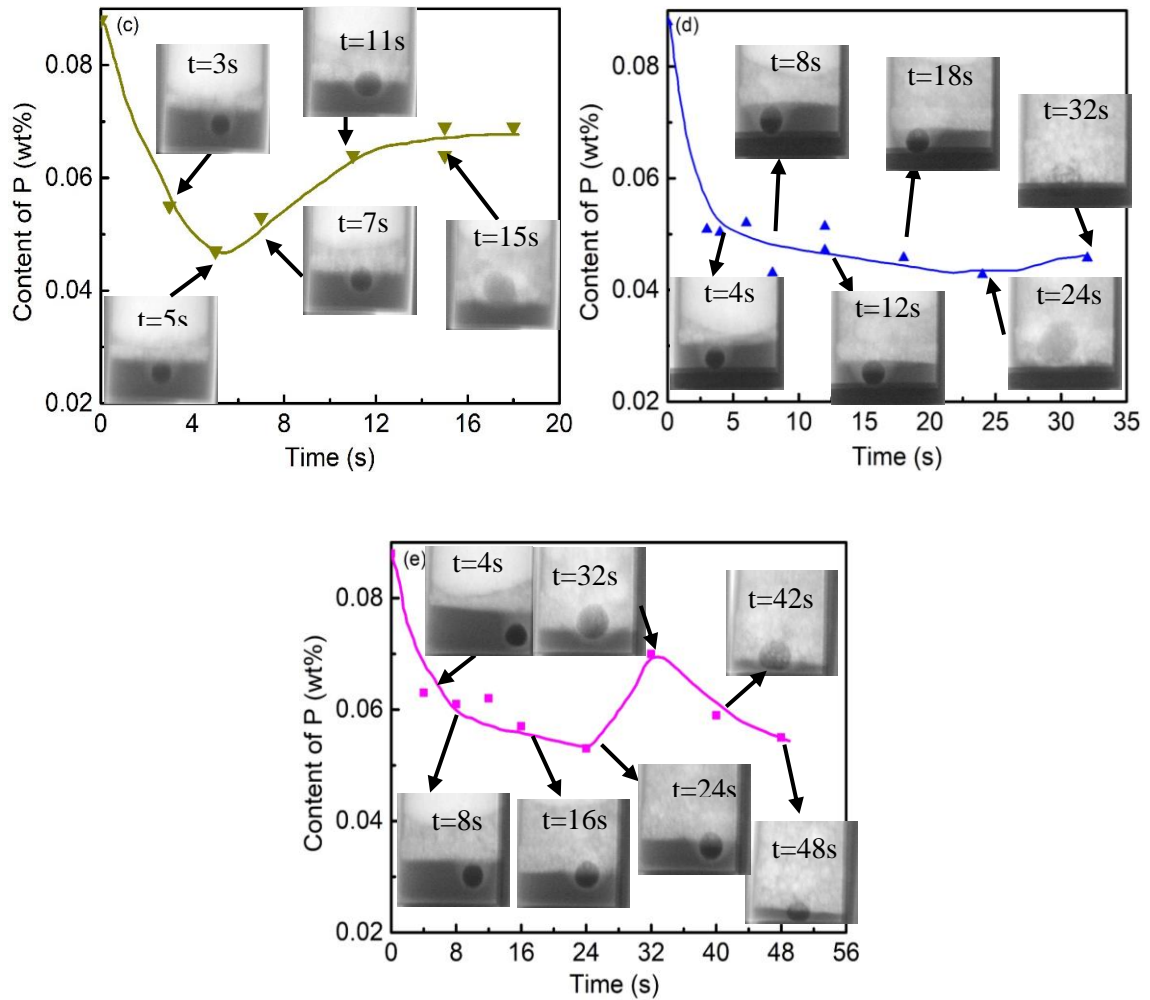


Figure 3.5 Dephosphorization as a function of time and droplet sulfur content: (a) 0.007 wt% S, (b) 0.011 wt% S, (c) 0.014 wt% S, (d) 0.017 wt% S and (e) 0.021 wt% S.

In order to present a clear view of the interplay between droplet decarburization and dephosphorization behavior, a schematic diagram is shown in Figure 3.6. This figure illustrates droplet behavior in terms of typical CO generation and dephosphorization during the course of an experiment, generalizing the behavior shown in Figures 3.2 and 3.5.

Figure 3.6 shows that the behavior of droplets can be separated into three sequential stages. During Stage I, corresponding to the incubation period for droplet swelling, droplets were dephosphorized in the dense slag. During Stage II, droplets swelled because of the high CO evolution rate and floated into the foaming slag. In this study, droplets typically experienced phosphorus reversion during stage II because of high CO evolution rate and

depletion of FeO in foaming slag, both contributing to a lower interfacial oxygen potential. Whether phosphorus reversion occurred in the dense slag or the foamy slag depended on the sulfur content of the droplet. Stage III was initiated when the rate of decarburization subsided, and the droplet sank back into the dense slag. The dense slag not having been depleted of FeO, and the decarburization of the droplet having decreased, would combine to offer a higher interfacial oxygen potential allowing renewed dephosphorization. This phenomenon is observed in the cases shown in Figures 3.5(a) and (e).

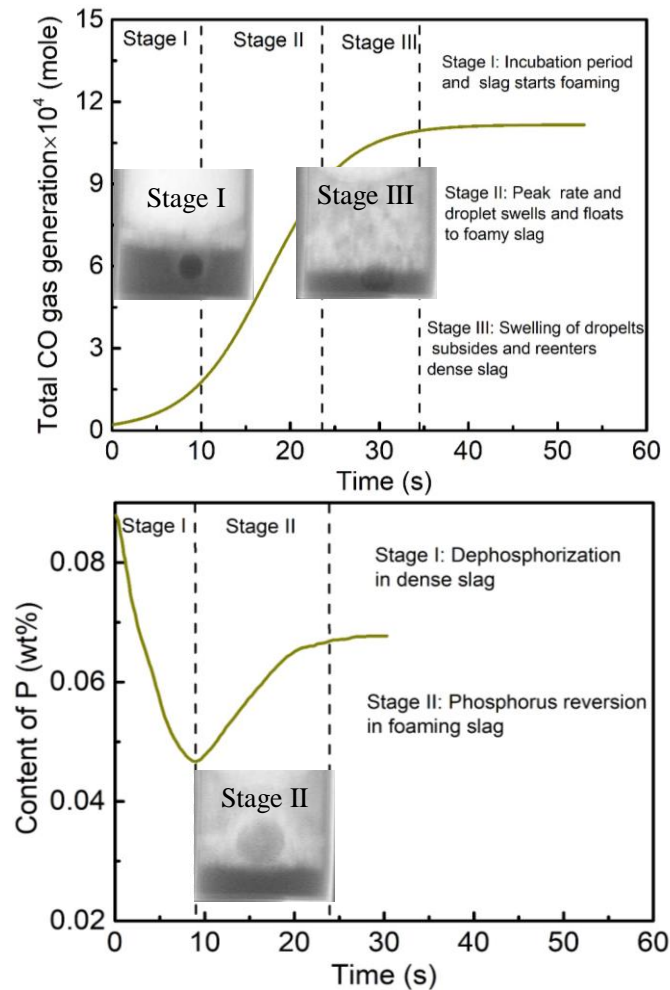


Figure 3.6 Schematic diagram of droplet behavior in terms of CO generation and dephosphorization as a function of time.

3.4 Discussion

3.4.1 Effect of Sulfur on Droplet Swelling

Figure 3.4 shows that the incubation time for droplet swelling rises with an increase in sulfur content. In order to examine this effect further, the incubation time is plotted in Figure 3.7 as a function of the activity of sulfur in the droplet. Here, the sulfur activity, h_s , was calculated using Wagner's interaction parameter formalism and data from Hino and Ito^[40].

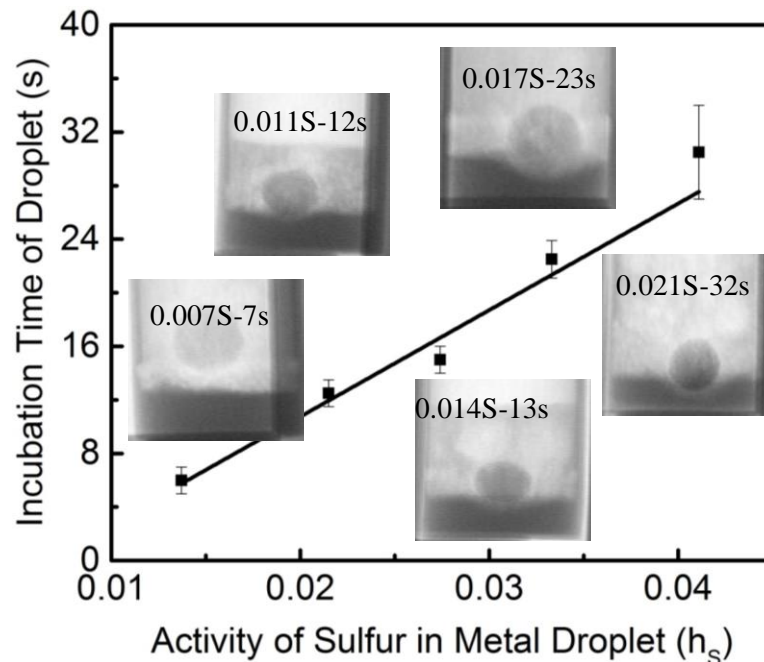


Figure 3.7 The effect of sulfur on incubation time for droplet swelling.

The linear relationship shown in Figure 3.7 is consistent with sulfur blocking reaction sites for oxygen transfer to the droplet. The delay of droplet swelling also has a strong influence on dephosphorization shown in Figure 3.5. Comparing Figures 3.5 and 3.7, offers one possible explanation for the effect of sulfur on slowing the rate of dephosphorization. Longer incubation times for droplet swelling represent longer times with less stirring in the droplet which could lead to lower mass transfer rates for phosphorus. It is also possible that

lower dephosphorization rates at higher sulfur levels are directly related to the surface poisoning effect of sulfur.

3.4.2 Effect of Sulfur on CO Evolution

As a surface active element, sulfur decreases the surface tension of metal, thereby reducing the energy barrier for CO nucleation and decreasing the minimum carbon content required to nucleate CO bubbles. The increase in the total CO production with increasing sulfur levels (Figure 3.2(a)) can be attributed to this effect.

As far as the rate of CO generation is concerned, sulfur has two opposing effects: on the one hand, it will lower the surface tension of the metal and increase the rate of gas bubble nucleation, and on the other hand, sulfur will have a negative effect on bubble growth by blocking reaction sites. Previous work in the authors' laboratory^[6] has shown that the peak rate of CO formation is proportional to the metal volume, which implies a strong influence of nucleation in controlling the rate. Although it is clear that the number of gas bubbles formed will depend on nucleation rate, the size of these bubbles at the point where they escape from the droplet will depend on their subsequent growth rate. Increasing sulfur will decrease the growth rate. These two competing effects explain the maximum in gas generation rate seen in Figure 3.2(b): at lower sulfur levels, the effect of sulfur in enhancing bubble nucleation dominates and at higher sulfur contents its effect on bubble growth is dominant. The current work has been conducted to elucidate the effect of sulfur on dephosphorization of iron carbon droplets. Some might consider the range of sulfur used in this case to be limited; however, this range was chosen as the range over which the most dramatic effect on CO generation has been observed. Several researchers^[5, 37] have shown that sulfur at these relatively modest levels can cause a significant increase in the CO formation rate. Depending on temperature and carbon content, the CO evolution rate increases by between a factor of two and a factor of five when sulfur increases from 0.003 to 0.013 wt%. The rate then subsides with increasing sulfur above 0.013 wt%. This phenomenon is shown in Figure 3.2 and is remarkably consistent amongst several different researchers; the sulfur level corresponding to the peak CO generation rate varies by not

more than 0.003 wt%. The variation in sulfur content in the current work was chosen specifically to span this peak, aiming for lower CO generation rates at both high and low sulfur contents as well as high CO generation rates at the peak. It is well established in the literature that the interfacial oxygen potential, which creates the driving force for dephosphorization, is set by the balance of oxygen supply in the slag and consumption by reaction with carbon in the metal. Therefore, it is reasonable to expect a decrease in dephosphorization extent, and possibly rate, at higher CO generation rates. The current work was specifically aimed at probing this effect for the case of bloated droplets.

The observation that faster CO evolution rates decrease the phosphorus partition (Figures 3.2 and 3.5), is consistent with the authors' previous work^[39], and agrees with the theory that the oxygen potential at the slag-metal interface is set by the balance between oxygen supply by the slag and oxygen consumption by carbon in the metal^[33]. In apparent contradiction to this, the metal phosphorus content at the reversion point, for droplets containing 0.021 wt% S, is much higher than at 0.007 wt% S although the peak CO generation rates are similar. It appears that a more detailed discussion about the effect of sulfur on phosphorus partition is required, and in addition to considering the rate of CO generation, one should also consider whether the droplet is resident in the dense slag or the foamy slag.

The existence of a phosphorus reversion point, while the carbon oxidation reaction is still going on, offers an excellent opportunity to analyze the dynamic interfacial oxygen potential. It is not generally possible to measure the phosphorus partition at the slag-metal interface and therefore the partition cannot be used to calculate the local oxygen potential. However, at the reversion point, the rate of the forward reaction for dephosphorization equals that of the backward reaction; therefore there will be no phosphorus concentration gradient in either the slag or the metal. One can assume the system is in equilibrium with regard to phosphorus and that bulk concentrations of phosphorus can be used to calculate L_P at the interface as stated in Eq. (3.1).

$$L_P = \frac{(\text{wt}\% \text{ P})_e}{[\text{wt}\% \text{ P}]_e} = \frac{(\text{wt}\% \text{ P})_i}{[\text{wt}\% \text{ P}]_i} \quad (3.1)$$

where (wt% P) represents phosphorus in the slag and [wt% P] represents phosphorus in the metal. The subscripts e and i indicate equilibrium and interface, respectively.

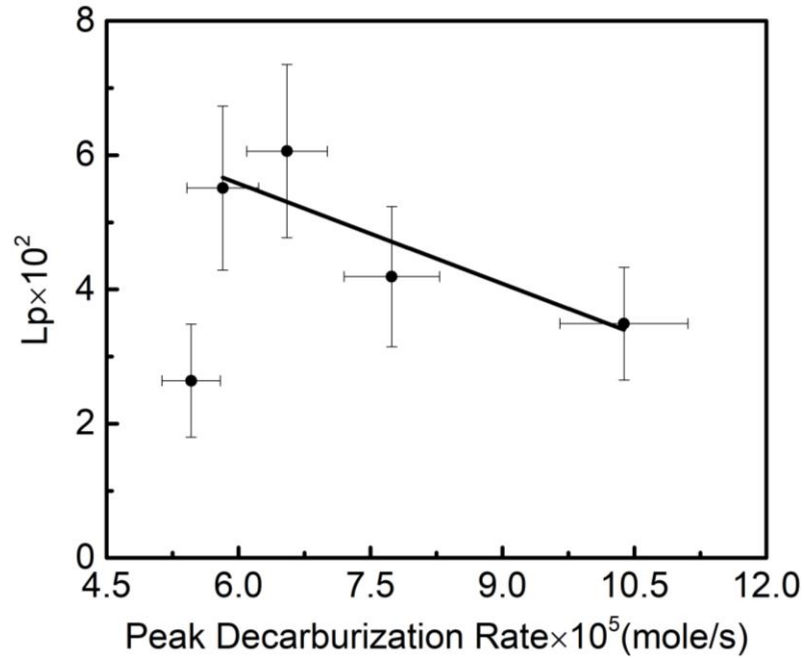


Figure 3.8 The effect of CO evolution rate on phosphorus partition coefficient.

The measured values for L_P at the reversion point are shown in Figure 3.8 as a function of peak decarburization rate. The solid line in this figure shows that the partition coefficient at reversion point for droplets containing 0.017 wt% S and less is inversely proportional to decarburization rate. Only the 0.021 wt% S droplet deviates from this relationship. This latter observation may be related to the fact that this droplet went through reversion at a much longer reaction time when the foamy slag will have been much more depleted in FeO. The resulting lower rate of oxygen supply will have caused a much lower interfacial oxygen potential.

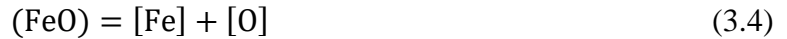
In general, it appears that CO evolution rate has a significant effect on L_P ; a faster decarburization rate leads to a faster oxygen consumption rate and a lower oxygen potential at the slag-metal interface. This decreases the driving force for dephosphorization which is

consistent with the findings of other researchers ^[32-34]. By assuming that the relationship between decarburization rate and interfacial oxygen potential is maintained throughout the residence of the droplet in the slag, we can use the data obtained for the reversion point to calculate the oxygen potential at any time during the reaction. This assumption is reasonable for either foamy slag or dense slag but cannot account for the transition from one to the other because the slag mass transfer coefficient will be considerably lower in the foamy slag. This can also be used for individual droplets in the BOF as the relationship between individual droplets and slag is no different. It is worth noting two important differences for the BOF slag; due to the low basicity (approximately 0.8) and FeO depletion of the slag in this study, the phosphorus partition coefficient at the reversion point is very small, $\sim 10^{-2}$. For droplets in oxygen steelmaking, the slag would not be depleted in FeO and the basicity would be more than three times higher. Assuming similar CO generation behavior and mass transfer coefficients in the slag, the oxygen potential for this study and typical steelmaking conditions can be calculated if we equate oxygen supply rate by FeO in the slag and oxygen consumption rate by the formation of CO in the metal:

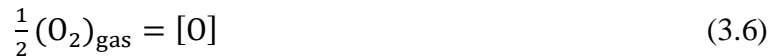
$$J_{FeO} = J_C \quad (3.2)$$

$$k_{FeO}(C_{FeO}^b - C_{FeO}^i) = \frac{1}{A} \frac{dn_{CO}}{dt} \quad (3.3)$$

By assuming local equilibrium exists at the slag-metal interface, the following two reactions ^[40] can be coupled with Eq. (3.3) to calculate the oxygen potential:



$$\Delta G^o = 122005.6 - 52.27T \text{ J/mol} \quad (3.5)$$



$$\Delta G^o = -117180.5 - 3.45T \text{ J/mol} \quad (3.7)$$

The authors are currently developing an interfacial oxygen potential model including a detailed analysis of the oxygen supply side as well as consumption. This work will be presented in detail in a subsequent publication ^[41]. For this discussion, reasonable estimates

of the slag mass transfer coefficient will be used to calculate the interfacial oxygen potential as a function of droplet decarburization rate. Molloseau and Fruehan^[5] investigated decarburization behavior between iron-carbon droplets and slag containing FeO and found that the value of k_s is in the range of 1.3×10^{-3} and 1.3×10^{-2} cm/s. Taking the average value of k_{FeO} (5.0×10^{-3} cm/s) for foamy slag and the industrial plant data for a typical slag composition^[24], the interfacial oxygen potential under typical steelmaking conditions was calculated by employing the CO generation behavior for droplets with 0.014 wt% S. In Figure 3.9 these results are compared with similar calculations for the slag used in this study. It should be noted that for consistency with the industrial case, the calculations for both slags assumed no FeO depletion.

Phosphorus partition coefficients were also included in Figure 3.9, calculated using Eq. (3.8). The phosphate capacity $C_{PO_4^{3-}}$, was calculated using the optical basicity correlation developed by Mori^[42].

$$L_P = \frac{(\text{wt}\% \text{ P})}{[\text{wt}\% \text{ P}]} = \frac{C_{PO_4^{3-}} P_{O_2}^{5/4} f_P M_P}{K_P M_{PO_4^{3-}}} \quad (3.8)$$

where K_P is the equilibrium constant for phosphorus gas in equilibrium with phosphorus in liquid iron, f_P is the Henrian activity coefficient for phosphorus in iron, and M is the molecular weight.

Figure 3.9 shows that without depletion of FeO in the slag, the interfacial oxygen potential in this study would maintain a relative high value and is close to typical steelmaking conditions. The phosphate capacity for the slag used in this study and that for a typical steelmaking slag was calculated to be 1.2×10^{17} and 1.9×10^{19} , respectively. Due to the difference in phosphate capacity, the phosphorus partition coefficient of steelmaking slag is two orders of magnitude higher than that of the current slag as shown in Figure 3.9. This difference will have a major impact on the rate controlling step for the reaction which is discussed below.

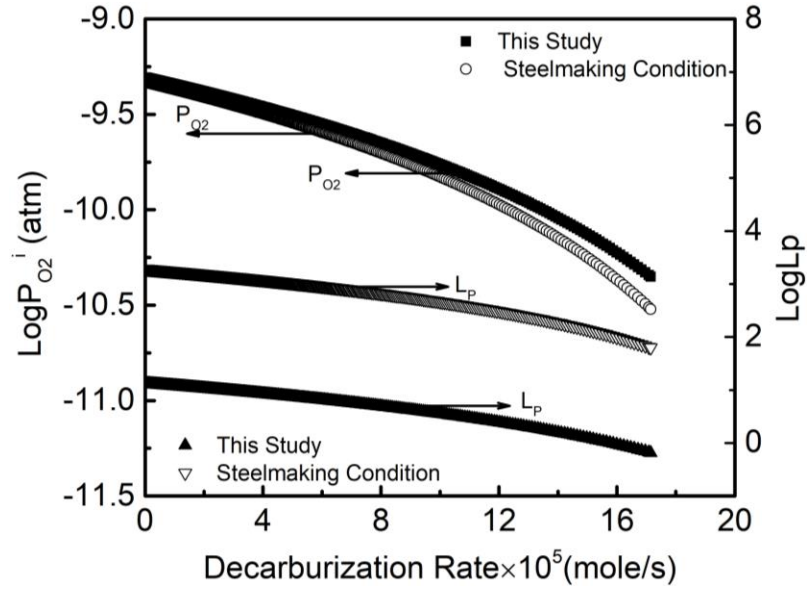


Figure 3.9 The effect of decarburization rate on interfacial oxygen potential and phosphorus partition coefficient for this study and under steelmaking condition.

3.4.3 Dephosphorization Kinetics

It is well established that most slag-metal chemical reactions reach a local equilibrium at the interface. This is consistent with the assumptions of previous researchers who have all agreed that the kinetics of phosphorus oxidation are limited by mass transfer of phosphorus in the slag, metal, or both phases [32-35]. Given the relatively higher phosphorus partition coefficient in the early stages of the reaction, the reaction is more likely to be controlled by the mass transfer of phosphorus in the metal or by a combination of mass transfer in both the slag and metal. Rate equations for control by phosphorus transfer in the metal and slag are given, respectively by Eqs. (3.9) and (3.10).

$$-\frac{d[\text{wt}\% \text{ P}]}{dt} = \frac{A}{W_m} k_m \rho_m ([\text{wt}\% \text{ P}]_b - [\text{wt}\% \text{ P}]_i) \quad (3.9)$$

$$\frac{d(\text{wt}\% \text{ P})}{dt} = \frac{A}{W_s} k_s \rho_s ((\text{wt}\% \text{ P})_i - (\text{wt}\% \text{ P})_b) \quad (3.10)$$

where W_s and W_m are the mass of slag and metal respectively, k_s and k_m are the mass transfer coefficients for phosphorus in the slag and metal, ρ_m and ρ_s are the densities of

metal and slag, $[\text{wt}\% \text{ P}]_i$ and $(\text{wt}\% \text{ P})_i$ are phosphorus content in the metal and slag at the interface.

The rate of change of phosphorus in the metal is related to that in the slag by a simple mass balance:

$$\frac{d(\text{wt}\% \text{ P})}{dt} W_s = -\frac{d[\text{wt}\% \text{ P}]}{dt} W_m \quad (3.11)$$

By combining Eqs. (3.1) and (3.9) to (3.11), the rate equation for mass transfer controlled in both the slag and metal can be expressed as ^[35]:

$$-\frac{d[\text{wt}\% \text{ P}]}{dt} = \frac{A\rho_m}{W_m} \frac{1}{\frac{\rho_m}{k_s\rho_s L_P} + \frac{1}{k_m}} ([\text{wt}\% \text{ P}]_b - \frac{(\text{wt}\% \text{ P})_b}{L_P}) \quad (3.12)$$

From Eq. (3.12), the overall mass transfer coefficient, k_o , with units of cm/s, can be written as:

$$k_o = \frac{1}{\frac{\rho_m}{k_s\rho_s L_P} + \frac{1}{k_m}} \quad (3.13)$$

In order to estimate the overall mass transfer coefficient of phosphorus, k_o , it is very common to normalize the driving force by integrating Eq. (3.12). Since the surface area of the metal droplet A in Eq. (3.12) changes with time, a time averaged area must be used in the integrated form of the rate equation. The time averaged area was calculated from the data shown in Figure 3.4 using the method developed by Rhamdhani *et al* ^[38]. By integrating Eq. (3.12), we can obtain Eq. (3.14).

$$\left(\frac{W_m}{\rho_m A} \frac{1}{1 + \frac{W_m}{L_P W_s}} \right) \text{Ln} \left[\left(1 + \frac{W_m}{L_P W_s} \right) \frac{[\text{wt}\% \text{ P}]_b}{[\text{wt}\% \text{ P}]_o} - \frac{W_m}{L_P W_s} \right] = -k_o t \quad (3.14)$$

Setting $C = \left(1 + \frac{W_m}{L_P W_s} \right) \frac{[\text{wt}\% \text{ P}]_b}{[\text{wt}\% \text{ P}]_o} - \frac{W_m}{L_P W_s}$ and $B = \left(\frac{W_m}{\rho_m A} \frac{1}{1 + \frac{W_m}{L_P W_s}} \right)$, Eq. (3.14)

becomes $B \ln C = -k_o t$.

All data shown in Figure 3.5 were plotted in Figure 3.10 according to Eq. (3.14). This figure shows that, with the exception of the droplets containing 0.021 wt% S, the dephosphorization data for reaction times less than 6 seconds, can be fitted to a single straight line, suggesting that the reaction has the same controlling step initially for droplets with 0.017 wt% S and less. The droplets with 0.021 wt% S show a much lower overall mass transfer coefficient, which suggests a possible different reaction mechanism.

The slope of the solid straight line shown in Figure 3.10 represents the initial overall mass transfer coefficient, k_o , which is 0.0284 cm/s. Using this value and considering the changing surface area of bloated droplets (changed from 1.2 to 2 cm² during the period represented by the solid straight line), the k_oA at the initial stage were calculated to be between 0.0341 and 0.0568 cm³/s. Based on our calculations in this study, the mass transfer coefficient for the dense slag, k_s , and L_P can be assumed to be 0.01 cm/s and 10, respectively. Then k_m during the initial stages of reaction was determined to be 0.085 cm/s. At a temperature of 1573 K, Wei *et al.* [43] estimated k_m was 0.05 cm/s where mechanical stirring was employed. Therefore, the value of 0.085 found in this study seems reasonable when one considers the gas stirring effect.

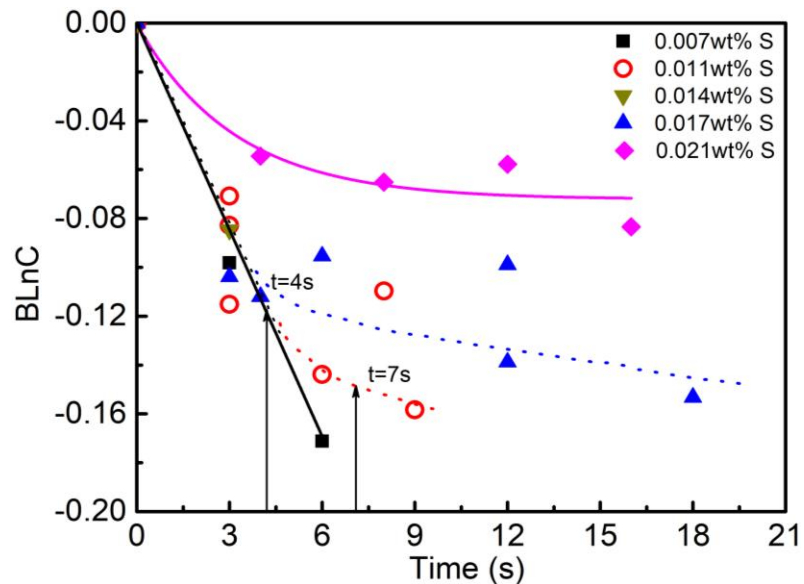


Figure 3.10 Dephosphorization data from Figure 3.5 are replotted as a function of time based on Eq. (3.14).

From Figure 3.10, it can be inferred that k_o for droplets with 0.011 wt% S (represented by the dotted line) shows a decreasing value after around 5 seconds. This deviation is probably caused by the dramatic increase in decarburization rate which would be expected to decrease the interfacial oxygen potential. This in turn would lead to a lower L_P . According to Eq. (3.13), a smaller L_P would lead to a lower k_o as evidenced by the change in slope of the dotted line in Figure 3.10. To quantify the change of L_P before and after the point of deviation, L_P at $t=4s$ and $t=7s$ for droplets with 0.011 wt% S were calculated using Eqs. (3.2) to (3.8). The resulting values were used in Eq. (3.10) to determine k_o at these two points, assuming k_s and k_m to be 0.001 and 0.01 cm/s respectively. The calculated results are given in Table 3.2.

Table 3.2 Calculated phosphorus partition ratio and overall mass transfer coefficient.

$t/(s)$	$P_{O_2}^i/(atm)$	L_P	$\frac{\rho_m}{k_s \rho_s L_P}$	$\frac{1}{k_m}$	$k_o/(cm/s)$
4	2.77E-10	6	364	100	0.0022
7	7.0E-11	1	2032	100	0.0005

Table 3.2 shows that k_o decreases by a factor of 4 because of the drop of L_P . It also shows that the contribution to resistance from the slag side increases from 79% to 95% as L_P drops from 6 to 1. This results in a shift in mechanism where the rate controlling step shifts from mixed mass transfer control in both slag and metal phase to almost pure slag mass transfer control. In Figure 3.10 droplets with 0.017 wt% S (represented by the dashed line), show a more dramatic deviation compared to droplets with 0.011 wt% S. This behavior can be understood if one considers the different decarburization rate of these two types of droplets where 0.017 wt% S droplets have a higher decarburization rate than droplets with 0.011 wt% S as shown in Figure 3.2(b). Higher decarburization rate would lead to a more dramatic decrease of interfacial oxygen potential, causing a bigger drop in L_P . All droplets except those with the highest sulfur content 0.021 wt% S, appear to follow the same reaction mechanism in the initial stages. From analysis this appears to be mixed control involving mass transport in the metal and the slag. The highest sulfur droplets follow a

very different reaction path with a much slower reaction rate even in the earliest stage. The authors cannot offer a definitive explanation for this observation at present.

3.4.4 Role of Partition Ratio on Reaction Kinetics

It is well established that the balance between control by mass transfer in the slag and by mass transfer in the metal is heavily influenced by L_p . From the discussion above, it is clear that under the conditions investigated in the current work mixed control operates, shifting to mass transport control in slag as phosphorus partition ratio decreases because of FeO depletion of the slag. This shifting balance is probably the reason why researchers are divided between mass transfer in the slag^[34] and some form of mixed control^[32, 33, 35].

From above discussion, the dynamic nature of the interfacial oxygen potential may offer a way to rationalize the range of different rate determining steps for dephosphorization reported in the literature. It is also worth noting that for a proper description of dephosphorization, a complete understanding of the factors affecting the dynamic interfacial oxygen potential is required. The current work has demonstrated the effect of sulfur on the dynamic interfacial oxygen potential for bloated droplets. The authors are developing a quantitative kinetic model for dynamic interfacial oxygen potential in bloated droplets, which will be presented in a subsequent publication^[41].

3.5 Conclusion

During reaction at 1853 K between Fe-C-P-S droplets and CaO-SiO₂-Al₂O₃-FeO slag decarburization was shown to go through a period of relatively slow reaction, followed by a period of very rapid reaction during which the droplet became bloated. The incubation period for bloating increased in length with increasing sulfur content in the droplet. The rate of decarburization during the bloating period was found to go through a maximum at 0.014 wt% S. The interaction between the decarburization and dephosphorization was studied in detail using the effect of sulfur on controlling the decarburization rate. The dephosphorization went through reversion under all conditions. The phosphorus partition

at the reversion point decreased with the increasing decarburization rate. From this study, the following conclusions may be drawn.

1. The rate of CO formation as a function of sulfur content is strongly influenced by two competing effects; sulfur decreases the metal surface tension, thereby increasing the nucleation rate of gas bubbles, while also poisoning the bubble surface to decrease the bubble growth rate. These competing effects lead to a maximum CO evolution rate observed at about 0.014 wt% S.
2. The incubation time for droplet swelling is extended by an increase in metal sulfur content most likely because the poisoning effect of sulfur hinders oxygen transfer into droplet, thereby delaying the onset of internal nucleation of CO.
3. The phosphorus partition coefficient, measured at the reversion point, shows a strong inverse relationship with increasing CO evolution rate because the associated oxygen consumption decreases the interfacial oxygen potential.
4. The complex dephosphorization-reversion-dephosphorization behavior of droplets depending on timing of their movement between the dense and foamy slag can be explained by considering the more rapid depletion of iron oxide from the foamy slag.
5. Kinetic analysis of dephosphorization shows that in the current study the rate controlling step is first mixed control by mass transport in both metal and slag, which then shifts to mass transport in slag as phosphorus partition ratio decreases because of FeO depletion in the slag.

3.6 References

1. E.W. Mulholland, G.S.F. Hazeldean and M.W. Davies: *J. Iron Steel Inst.*, 1973, vol. 211, pp. 632-39.
2. T. Gare and G.S.F. Hazeldean: *Ironmak. Steelmak.*, 1981, no. 4, pp. 169-81.
3. H. Gaye and P.V. Riboud: *Metall. Trans. B*, 1977, vol. 8B (9), pp. 409-15.
4. D.J. Min and R.J. Fruehan: *Metall. Trans. B*, 1992, vol. 23B, pp. 29-37.
5. C.L. Molloseau and R.J. Fruehan: *Metall. Trans. B*, 2002, vol. 33B, pp. 335-44.
6. E. Chen and K. S. Coley: *Ironmak. Steelmak.*, 2010, vol. 37 (7), pp. 541-45.
7. R.C. Urquhart and W.G. Davenport: *Can. Metall. Quarterly*, 1973, vol. 12 (4), pp. 507-16.

8. N. Standish and Q.L. He: *ISIJ Int.*, 1989, vol. 29 (6), pp. 455-61.
9. Q.L. He and N. Standish: *ISIJ Int.*, 1990, vol. 30 (4), pp. 305-09.
10. Q.L. He and N. Standish: *ISIJ Int.*, 1990, vol. 30 (5), pp. 356-61.
11. G. Turner and S. Jahanshahi: *Trans. ISIJ*, 1987, vol. 27, pp. 734-39.
12. S.C. Korla and K.W. Lange: *Ironmak. Steelmak.*, 1983, vol. 10 (4), pp. 160-68.
13. S.C. Korla and K.W. Lange: *Metall. Trans.*, 1984, vol. 15B, pp. 109-16.
14. S.C. Korla and K.W. Lange: *Ironmak. Steelmak.*, 1986, vol. 13 (5), pp. 236-40.
15. Subagyo, G.A. Brooks, K.S. Coley, and G.A. Irons: *ISIJ Int.*, 2003, vol. 43 (7), pp. 983-89.
16. Subagyo, G.A. Brooks, and K.S. Coley: *Steelmaking Conf. Proc.*, ISS, Warrendale, PA, 2002, vol. 85, pp. 749-62.
17. Subagyo, G.A. Brooks, and K. Coley: *Can. Metall. Quarterly*, 2005, vol. 44 (1), pp. 119-29.
18. J. Schoop, W. Resch, and G. Mahn: *Ironmak. Steelmak.*, 1978, vol. 2, pp. 72-79.
19. G. A. Brooks, Y. Pan, Subagyo and K. S. Coley: *Metall. Trans. B*, 2005, vol. 36B, pp 525-35.
20. N. Dogan, G. A. Brooks and M. A. Rhamdhani: *ISIJ Int.*, 2011, vol. 51 (7), pp. 1086-92.
21. N. Dogan, G. A. Brooks and M. A. Rhamdhani: *ISIJ Int.*, 2011, vol. 51 (7), pp. 1093-01.
22. C. Kattenbelt and B. Roffel: *Metall. Trans. B*, 2008, vol. 39B, pp764-69.
23. R. Sarkar, P Gupta, Somnath Basu, and Bharath Ballal: *Metall. Trans. B*, 2015, vol. 46, pp. 961-76.
24. C. Cicutti, M. Valdez, T. Perez, R. Donayo and J. Petroni: *Latin Am. Appl. Res.*, 2002, vol. 32, pp. 237.
25. D.J. Price: *L.D.Steelmaking*, The Institution of Mining and Metallurgy, London, UK, 1974, pp. 8-15.
26. B. Trentini: *Trans. Met. Soc. AIME*, 1968, vol. 242, pp. 2377-88.
27. P. Kozakevitch: *JOM*, 1969, vol. 22 (7), pp. 57.
28. A. Chatterjee, N.O. Lindfors, and J.A. Wester: *Ironmak. Steelmak.*, 1976, vol. 3 (1), pp. 21-32.
29. M. Pomeroy, E. Chen, K. S. Coley and G. Brown: *Proc. of the 6th European Oxygen Steelmaking Conf.*, Stockholm, 2011, vol. 38, pp. 141-151.
30. S. Basu, A.K. Lahiri and S. Seetharaman: *Revue de Métallurgie*, 2009, vol. 106, pp. 21-26.
31. A. Assis, M. Tayeb, S. Sridhar and R. Fruehan: *Metall. Trans. B*, 2015, vol. 46B, pp. 2255-63.
32. K. Mori, Y. Fukami and Y. Kawai: *Trans. ISIJ*, 1988, vol.28, 315-18.
33. P. Wei, M. Sano, M. Hirasawa, and K. Mori: *ISIJ Int.*, 1993, vol. 33, 479-87.
34. B. J. Monaghan, R.J. Pomfret, and K.S. Coley: *Metall. Trans. B*, 1998, vol. 29B, pp. 111-18.
35. C. P. Manning and R. J. Fruehan: *Metall. Trans. B*, 2013, vol. 44B, pp. 37-44.
36. A. K. Hewage, B. K. Rout, G. Brooks and J. Naser: *Ironmak. Steelmak.*, 2016, vol.43 (5), pp. 358-370.
37. E. Chen: PhD Thesis, McMaster University, Hamilton, CA, 2011, pp. 54.
38. M.A.Rhamdhani, G.A.Brooks and K.S. Coley: *Metall. Trans. B*, 2005, vol. 36B, pp. 219-27.
39. K. Gu, B. Jamieson, N. Dogan and K. S. Coley: *AISTech Conference Proceedings*, 2015, pp. 229-37.
40. M. Hino and K. Ito: *Thermodynamic Data for Steelmaking*, Tohoku University Press, Sendai. 2009, pp. 259-64.
41. K. Gu, N. Dogan and K. Coley: *Metall. Trans. B*, DOI: 10.1007/s11663-017-1000-2.
42. T. Mori: *Trans. Jpn. Inst. Metals.*, 1984, vol. 25(11), pp. 761-71.
43. P. Wei, M. Sano, M. Hirasawa and K. Mori: *Trans. ISIJ*, 1988, vol.28, pp. 637-44.

Chapter 4

The Dynamic Interfacial Oxygen Potential between Iron Carbon Droplets and Oxidizing Slag

In Chapter 4, the original concept of the model was suggested to me by Dr. Kenneth S. Coley the detailed model development and data analysis were performed almost entirely by me. Dr. Neslihan Dogan and Dr. Kenneth S. Coley provided very important guidance and discussion during model development and data analysis. This manuscript was originally drafted by me, proofread by Dr. Neslihan Dogan, and edited to the final version by Dr. Kenneth S. Coley. This work has been published in *Metallurgical and Materials Transactions B*. DOI: 10.1007/s11663-017-1000-2. The following Chapter is the pre-publication version of the article.

Abstract

The dynamic nature of the interfacial oxygen potential during dephosphorization was investigated based on the concept that P_{O_2} at the interface between slag and liquid metal is determined by the balance between oxygen supply from reducible oxides in the slag and oxygen consumption by alloying elements in the metal. Combining this approach with the knowledge that at the phosphorus reversion point the interfacial oxygen potential can be determined from the bulk phosphorus partition ratio, the mass transfer coefficient for FeO, k_{FeO} , was determined for different slags and found to increase with increasing FeO content. In foamy slags k_{FeO} was found to be a linear function of slag liquid fraction. Equating the mass transfer rate of FeO in the slag with decarburization rate, the dynamic interfacial oxygen potential was calculated over the course of the reaction and its effect on the rate determining step for dephosphorization was evaluated.

4.1 Introduction

It is well known that the oxygen potential at the interface between “Fe_tO” containing slag and liquid iron is an important process parameter, which affects the driving force for refining reactions such as desulphurization and dephosphorization. However, since direct measurement of interfacial oxygen potential is not feasible, there is often no way to define this important parameter quantitatively. Several workers have addressed the problem of interfacial oxygen potential employing kinetic data ^[1-4]. Ohguchi *et al.* ^[1] employed a coupled reaction model to study simultaneous dephosphorization and desulphurization between molten pig iron and slag containing Fe₂O₃. They found that the interfacial oxygen activity increased firstly as the silicon transfer rate decreased, and then decreased again with the progress of the reactions. Wei *et al.* ^[2] who investigated reactions between iron oxide bearing slag and molten iron with high carbon, proposed that the interfacial oxygen potential is defined by the balance of the rate of oxygen supply by FeO in the slag and consumption by carbon in the metal. They further estimated $P^i_{O_2}$ based on the assumption that equilibrium with respect to phosphorus was established in the slag-metal system at the phosphorus reversion point, and used this to show that $P^i_{O_2}$ increased with the ratio of ferric iron to total iron in the bulk slag and with the partial pressure of oxygen in the atmosphere. Using a similar approach, Monaghan *et al.* ^[3] found that the interfacial oxygen potential was controlled primarily by Fe-FeO equilibrium but did not find a significant dependency on the Fe³⁺/Fe²⁺ ratio in the slag. Based on the study of simultaneous reactions between iron-carbon alloys and slags containing different content of FeO and MnO, Shibata *et al.* ^[4] calculated that the interfacial oxygen activity for slags with high FeO content was approximately one order of magnitude higher than those with an equivalent content of MnO.

Recent work by the authors ^[5] highlighted that for iron-carbon droplets reacting with slag, the rate determining step and rate of dephosphorization can be changed dramatically by changes in interfacial oxygen potential during reaction. This work also showed that the phosphorus partition ratio at the reversion point decreased with increasing carbon oxidation

rate [2,4,5]. This latter result is qualitatively consistent with the findings of Wei *et al.* and to some extent with Shibata *et al.* and Monaghan *et al.* Given the importance of interfacial oxygen potential to refining, the current work seeks to offer a more detailed analysis of the authors' findings from dephosphorization of iron-carbon droplets and to offer comparison with previous studies under a range of reaction conditions. Experimental data from the authors' previous work is summarized in Section 4.3 and analyzed using the concept employed by Wei *et al.* [2] to provide a detailed analysis of the dynamic interfacial oxygen potential and of oxygen (FeO) transport in foamy slags. The results of this analysis are compared with similar analysis of the data of previous workers under a range of reaction conditions and finally a method to calculate the interfacial oxygen potential is used to elucidate its effect on dephosphorization kinetics.

4.2 Experimental Procedure

The primary experimental data presented in the current study are taken from a recent publication by the authors [5]. For the convenience of the reader, a brief description of the experimental procedure is repeated here. A resistance heated vertical tube furnace with an 80 mm diameter alumina working tube was used. The furnace was equipped with, X-ray imaging to observe the swelling of droplets in-situ, and a pressure transducer to measure gas evolution using the constant volume pressure increase technique (CVPI). Experiments were done at 1853 K. 25 g of slag, 32 wt% CaO-35 wt% SiO₂-17 wt% Al₂O₃-16 wt% FeO, was placed in a 45 mm diameter alumina crucible located in the hot zone of the furnace and was melted under an argon atmosphere. The Fe-C-P-S droplet, 2.62 wt% C-0.088 wt% P-(0.007 wt% to 0.021 wt%) S, was dropped into the molten slag via a small hole at the bottom of a closed end alumina tube, thus ensuring the droplet was molten before entering the slag. Samples were quenched at different reaction times and taken for chemical analysis of phosphorus in the metal droplet using Inductively Coupled Plasma Optical Emission Spectroscopy (ICP-OES).

4.3 Results

4.3.1 Decarburization and Dephosphorization of Bloated Droplets

Decarburization and dephosphorization data from our previous work ^[5] for the reaction at 1853 K between slag and iron droplets with sulfur contents from 0.007 wt% to 0.021 wt% are summarized in Figures 4.1 and 4.2.

From Figure 4.1, it is possible to know the decarburization rate at any given time which can be used in analysis of the dynamic interfacial oxygen potential. During decarburization, CO caused droplets to swell (bloating behaviour) and also caused slag foaming, resulting in a layer of foamy slag sitting on top of a thinner layer of dense slag. The greater buoyancy of the bloated droplets caused them to float into the foamy slag and then, as bloating subsided, to sink back into the dense slag. In Figure 4.2, all droplets exhibited some reversion due to the FeO depletion and a decrease in the rate of oxygen supply. In the case of the 0.007 wt% S droplet a re-initiation of dephosphorization subsequent to reversion was observed. This can be explained if one considers that reversion occurred in the foamy slag, which was readily depleted of FeO because of its low liquid volume. The droplet then returned to the dense slag where there was a higher concentration of FeO and the dephosphorization commenced again. The decarburization and dephosphorization behavior has been discussed in detail in our previous work ^[5]. In the current work the phosphorus partition ratio at the reversion point will be used, in conjunction with the decarburization data, to evaluate the dynamic interfacial oxygen potential. Images of droplets in the slag at the point of reversion are also shown in Figure 4.2 for various sulfur contents. This figure shows that for droplets with 0.007 wt%, 0.011 wt% and 0.017 wt% S, the reversion occurred when metal droplets entered the foamy slag; while for droplets with 0.014 wt% S the reversion took place when the droplet was in transition between the dense and foamy slag. Figure 4.2 also shows that droplets with 0.021 wt% S experienced reversion when sitting between dense slag and foamy slag.

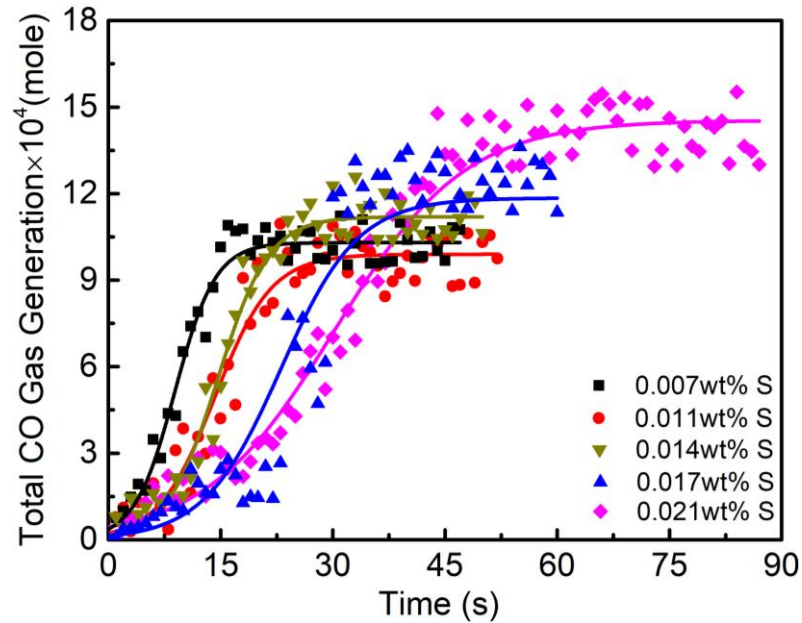


Figure 4.1 CO gas generation with time for droplets containing different sulfur content.

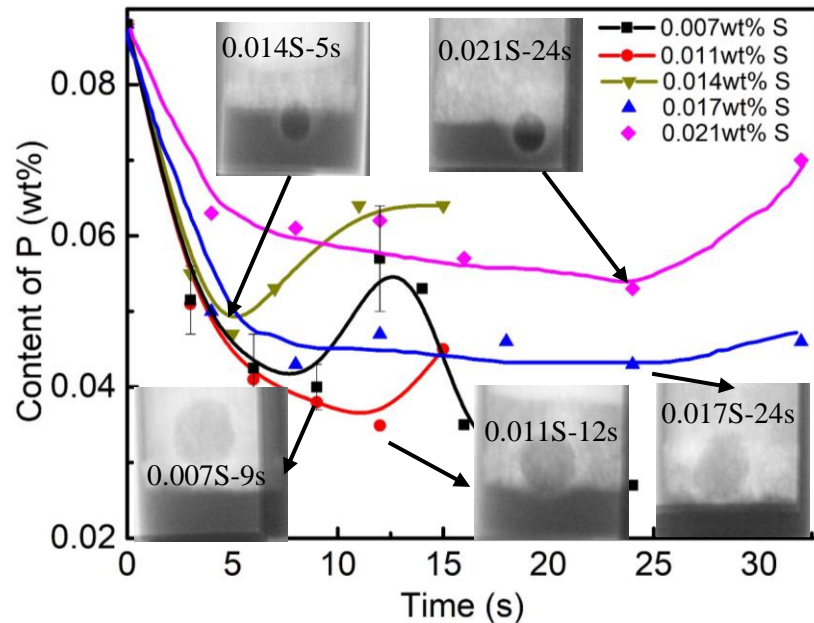


Figure 4.2 Change of phosphorus with time for droplets containing different sulfur content.

Figure 4.3 shows that once the droplet falls into the slag, a gas halo is formed around it and slag starts to foam at the top of dense slag. After few seconds of incubation time, the droplet swells and floats up to the foaming slag due to CO nucleation inside the metal droplet. The

mechanism of droplet swelling has been discussed in detail in a number of recent studies [6, 7].

Inspection of the recorded X-ray videos revealed that 0.014 wt% and 0.021 wt% S droplets, were sitting between dense slag and foamy slag for a while (ranged between 6 and 18 seconds) before completely entering the foamy slag. This is shown by the series of X-ray images in Figure 4.3. Combining Figure 4.1 and 4.3, it is possible to have a better understanding of the three types of phosphorus reversion behavior for metal droplets shown in Figure 4.2, *i.e.*, reversion in foamy slag (droplets with 0.007 wt% and 0.011 wt% S), droplets in transition but primarily in dense slag (0.014 wt% S) and between dense slag and foamy slag (droplets with 0.021 wt% S). For droplets with 0.007 wt% S, the reversion occurred entirely in the foamy slag with a low rate of transport of FeO. However, reversion in the dense slag for droplets containing 0.014 wt% S was probably caused by the high rate of decarburization, causing a low interfacial oxygen potential even at higher rates of oxygen supply. Despite the low rate of decarburization, if one considers the longer period spent between foamy slag and dense slag, droplets with 0.02 wt% S exhibited a phosphorus reversion because the lower mass transfer coefficient of FeO in the foamy slag as shown in Table 4.1.

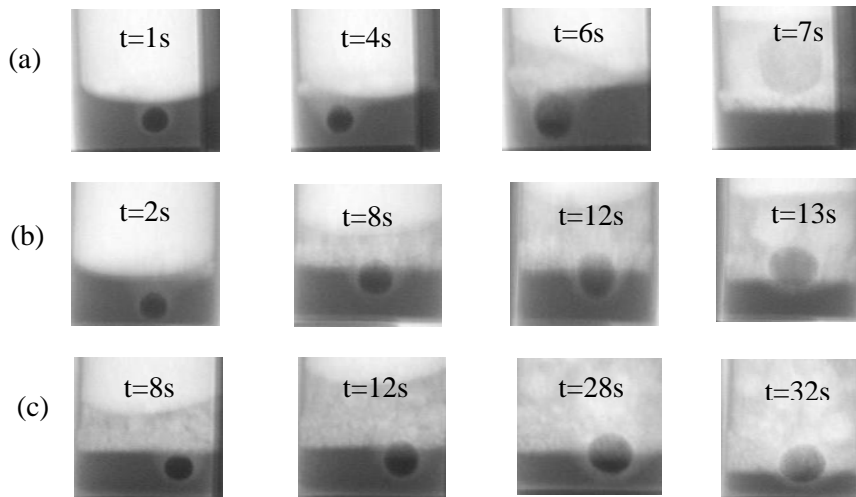


Figure 4.3 Behavior of droplets before fully entering the foamy slag: (a) 0.007 wt% S, (b) 0.014 wt% S and (c) 0.021 wt% S.

4.3.2 Mass Transfer Coefficient of FeO and Dynamic Interfacial Oxygen Potential

The interfacial oxygen potential is dictated by the balance between supply rate of FeO to the interface and the oxygen consumption by the formation of CO and P₂O₅. However, as the consumption of oxygen by phosphorus is negligible compared with that by carbon, at steady state this balance can be expressed as Eq. (4.1):

$$k_{FeO}(C_{FeO}^b - C_{FeO}^i) = \frac{1}{A} \frac{dn_{CO}}{dt} \quad (4.1)$$

Here, $\frac{dn_{CO}}{dt}$ is the CO generation rate (mole/s), C_{FeO} is the concentration of FeO, A is the surface area of the droplet, k_{FeO} describes oxygen transport in the slag conceptually defined as the mass transfer coefficient for FeO, and superscripts b and i indicate bulk and interfacial values respectively. C_{FeO}^i may be expressed in terms of activity of oxygen at the interface and C_{FeO}^b expressed as a function of the initial value C_{FeO}^o modified by the amount reduced (dn_{FeO}). If one makes these substitutions and further recognizes that dn_{FeO} is equivalent to the amount of CO generated (dn_{CO}), one may rearrange Eq. (4.1) to obtain (detailed derivation of Eq. (4.2) from Eq. (4.1) is shown in the Appendix):

$$P_{O_2}^i = \left[\frac{\gamma_{FeO} K_{Fe}}{C_s a_{Fe}^i K_O} \left(C_{FeO}^o - \frac{1}{V_S} \int_{n_{CO,t=0}}^{n_{CO,t=t}} dn_{CO} - \frac{1}{A} \frac{1}{k_{FeO}} \frac{dn_{CO}}{dt} \right) \right]^2 \quad (4.2)$$

where K_{Fe} and K_O are the equilibrium constants for FeO dissociation and oxygen dissolution in iron; γ_{FeO} is the activity coefficient for FeO in the slag, C_s is the overall molar density of the slag, C_{FeO}^o is molar concentration of FeO in the slag and V_S is the volume of slag, which could be volume of dense slag or foamy slag depending on the movement of droplet.

According to Eq. (4.2), the interfacial oxygen potential can be easily calculated by knowing k_{FeO} in the slag. Equally if knowing the interfacial oxygen potential and the decarburization rate, the k_{FeO} can be determined. In the current work the interfacial oxygen potential $P_{O_2}^i$ was calculated at the point of phosphorus reversion via Eq. (4.3):

$$L_P = \frac{(\text{wt}\% \text{ P})}{[\text{wt}\% \text{ P}]} = \frac{C_{PO_4^{3-}} P_{O_2}^{5/4} f_P M_P}{K_P M_{PO_4^{3-}}} \quad (4.3)$$

where $C_{PO_4^{3-}}$ is the phosphate capacity of the slag, f_P is the Henrian activity coefficient for phosphorus in the metal, M_P and $M_{PO_4^{3-}}$ are the molar mass of phosphorus and phosphate respectively, K_P is the equilibrium constant for the dissolution of phosphorus gas in steel. $C_{PO_4^{3-}}$ was determined based on the following correlation [8]:

$$\log C_{PO_4^{3-}} = 17.55 \Lambda + \frac{51670}{T} - 21.867 \quad (4.4)$$

where Λ is the theoretical optical basicity of slag.

As mentioned above, at the point of phosphorus reversion, the system is instantaneously in equilibrium with respect to phosphorus while interfacial oxygen potential continues to change via the interplay between oxygen supply and consumption represented by Eq. (4.2). Therefore at the reversion point the bulk concentrations of phosphorus can be used to calculate L_P and thereby determine the interfacial oxygen potential. One can then calculate k_{FeO} by substituting $P_{O_2}^i$ into Eq. (4.2).

The measured phosphorus partition coefficient, the calculated interfacial oxygen potential and mass transfer coefficient of FeO are shown in Table 4.1. The void fraction of foamy slag at the time where reversion occurred was calculated by comparing the heights of the dense and foamy slag with that of the initial unfoamed slag and is also shown in Table 4.1. For droplets situated between the foamy slag and dense slag at the point of reversion (0.014 wt% and 0.021 wt% S), an average value for the slag liquid fraction was calculated based on the fraction of the surface exposed to each type of slag.

Table 4.1 Calculated results for different metal droplets.

Sulfur content /(wt%)	$L_p \times 10^2$	$P_{O_2}^i$ /(atm)	$k_{FeO} \times$ 10^3 /(cm/s)	Liquid slag fraction	Void fraction
0.007	4.8	5.52E-12	1.44	0.10±0.007	0.90±0.007
0.011	6.1	6.65E-12	1.85	0.20±0.006	0.80±0.006
0.014	3.5	4.28E-12	10.1	0.92±0.020*	0.85±0.008
0.017	4.2	4.95E-12	2.24	0.12±0.006	0.88±0.006
0.021	2.6	3.42E-12	4.87	0.61±0.006*	0.80±0.008

*These values of liquid fraction represent a weighted average of foamy and dense slag in proportion to their contact with the droplet.

Table 4.1 shows that although the slag composition was the same, the mass transfer coefficient of FeO in the slag appears to vary with sulfur content of the droplet. This observation may be understood if one recognizes that the degree to which the slag is foamed will influence the mass transfer coefficient. The mass transfer coefficient of FeO has been determined at the point of reversion and at that point the droplet may be situated in the dense slag, in the foamy slag or a combination thereof. In addition the degree to which the slag is foamed will depend on the CO generation rate. Therefore, as the CO generation rate is strongly affected by sulfur, it is not surprising that different mass transfer coefficients for FeO were determined for experiments with different metal sulfur contents. Table 4.1 also shows that in the current work higher mass transfer coefficients were determined for slags with higher liquid fractions.

4.4 Discussion

4.4.1 Mass Transfer of FeO in the Slag

The k_{FeO} determined for each case in Table 4.1 was plotted against the liquid fraction of slag in Figure 4.4 (detailed calculation of the liquid fraction of the slag is shown in the Appendix). It shows that a linear relationship exists between k_{FeO} and the fraction of liquid slag. This result is to be expected if one considers the pathway for mass transfer to be

through the liquid, the cross sectional area of the path is dramatically reduced by the presence of bubbles. Because of that, the mass transfer coefficient of FeO for foamy slag (1.44×10^{-3} cm/s) is almost one tenth of the value for dense slag (10×10^{-3} cm/s). These values are of the same order as values reported by other workers, *i.e.*, between 10^{-2} cm/s to 10^{-3} cm/s [2, 4, 5, 9-12].

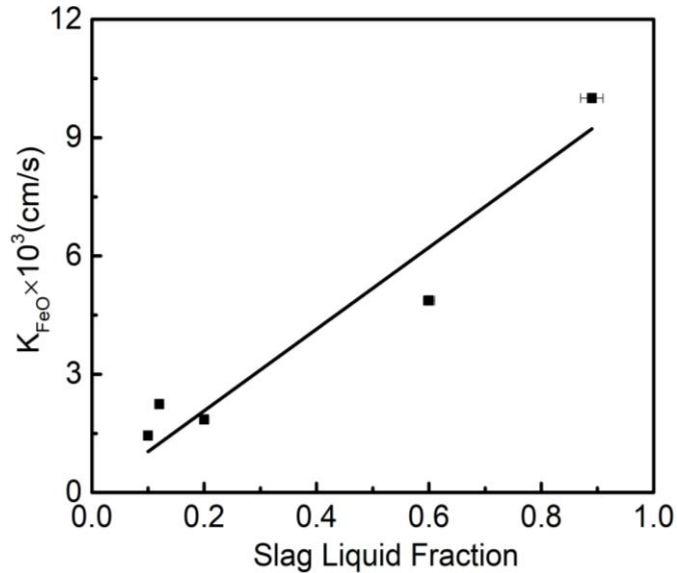


Figure 4.4 k_{FeO} as a function of the liquid fraction of slag.

Shibata *et al.* [2] and Wei *et al.* [4] have conducted similar analysis of the dynamic interfacial oxygen potential but have employed a coupled reaction model fitting all fluxes over the duration of the reaction. In their case the mass transfer coefficient for all elements in the slag was assumed to be equal. In order to compare these approaches, k_s values from these studies are shown in Table 4.2 along with k_{FeO} calculated from their data using the current approach. The experimental conditions for the work of Shibata *et al.* and Wei *et al.* are given in the Appendix along with the method used to calculate k_{FeO} . Calculated slag viscosity for each slag is also presented in Table 4.2, determined using Factsage 6.4TM employing the Melts database.

Table 4.2 Calculated k_{FeO} for different researchers' work.

Investigator	T/K	Fe _t O/(wt%)	η /poise	V_g^s /(cm/s)	$k_s \times$ 10^3 /(cm/s)	$k_{FeO} \times$ 10^3 /(cm/s)
Wei <i>et al.</i>	1573	15	0.86	0.11	3	1.37
Wei <i>et al.</i>	1573	15	0.86	0.10	3	2.09
Shibata <i>et al.</i>	1723	0	0.59	0.17	5	0.87
Shibata <i>et al.</i>	1723	5.4	0.41	0.22	6	0.88
Shibata <i>et al.</i>	1773	4.5	0.78	0.06	16.7	1.11
Shibata <i>et al.</i>	1773	29.7	0.61	0.60	13.3	15.1
Molloseau and Fruehan	1713	10	1.51	0.06		1.3
Molloseau and Fruehan	1713	20	1.02	0.4		3.8
Monaghan <i>et al.</i>	1603	38.10	0.80		3.6	
Monaghan <i>et al.</i>	1603	47.62	0.58		10	
Monaghan <i>et al.</i>	1603	57.14	0.42		28	
Monaghan <i>et al.</i>	1603	66.67	0.30		99	
This study	1853	16	1.49	0.30~0.40		1.0~10

By studying the decarburization behavior between Fe-C-S droplets and CaO-SiO₂-MgO-FeO slags, Molloseau and Fruehan^[9] also determined k_{FeO} in the slag using two different methods, *i.e.*, fitting experimental data by assuming liquid phase mass transfer was the rate controlling step, and by calculation based on penetration theory. The determined k_{FeO} for slag containing 10 wt% and 20 wt% FeO were 1.3×10^{-3} and 3.8×10^{-3} cm/s, respectively. While the values calculated from penetration model were 4.8×10^{-3} and 1.3×10^{-2} cm/s. These workers proposed that the difference obtained from these two approaches was due to the uncertainty of average diameter of CO bubbles formed during the reaction. The

experimental k_{FeO} values from Molloseau and Fruehan, 1.3×10^{-3} and 3.8×10^{-3} cm/s are used in the current work for slags containing 10 wt% and 20 wt% FeO. These have been included in Table 4.2.

By fitting dephosphorization kinetic data, Monaghan *et al.* [3] also estimated the mass transfer coefficient of phosphorus in the slag k_s for very high iron oxide slag (> 35 wt%). Based on our calculations, for slag containing high iron oxide (> 15 wt%) the determined values of k_{FeO} are close to a general value of k_s for all species reported by Wei *et al.* [2] (15 wt%) and Shibata *et al.* [4] (29.7 wt%) as shown in Table 4.2. Therefore, it has been assumed for the current discussion that the values of k_s determined in the case of Monaghan *et al.* represent a reasonable estimate of k_{FeO} .

For comparison of the mass transfer coefficients from other studies with those determined in the present work, it is important to know the slag void fraction. In order to estimate the void fraction of the slags in the work of Shibata *et al.* and Wei *et al.*, the superficial gas velocities were calculated using decarburization data. In the case of Molloseau and Fruehan, the CO gas generation rate was employed to calculate the superficial gas velocities. Laboratory studies, where superficial gas velocity is lower than 10 cm/s, typically report the void fractions of foaming slag between 0.8 and 0.9 [13, 14]. Therefore, for the slags with total iron less than 20 wt% it is reasonable to assume that a void fraction is between 0.8 and 0.9. However, in the cases of higher total iron oxide content (>29.7 wt%) the void fraction is expected to be lower; according to Jung and Fruehan [15], the foaming index is dramatically decreased with increasing of FeO in the slag.

Mass transfer coefficients from a range of studies have been presented in Table 4.2. These values were determined in a number of different ways. In the current work they have been determined specifically for FeO at the point of reversion of phosphorus. Molloseau and Fruehan employed a different method but also determined k_{FeO} . In studies of Wei *et al.* [2] and Shibata *et al.* [4] k_s was determined by fitting data for the transport of all species in the slag over the entire reaction time. This approach has the advantage of including a larger data set in the calculation but may introduce errors by assuming all species have same mass

transfer coefficient. Monaghan *et al.* [3] determined the mass transfer coefficient for phosphorus in the slag. The values of k_{FeO} presented in Table 4.2 attributed to the cases of Shibata *et al.* and Wei *et al.*, were determined as part of the present work from the original data using our approach. The values for k_s were as determined by these workers. The value of k_{FeO} from the study of Molloseau and Fruehan [9] was taken directly from their work. In the absence of the additional data, the value of k_s determined by Monaghan *et al.* is assumed to be equivalent to k_{FeO} which is considered reasonable because the mass transfer coefficients for different species seem to converge for high iron oxide slags. The data for mass transfer coefficients presented in Table 4.2 are plotted along with data from the current study against the FeO content of the slag in Figures 4.5(a) and (b) respectively for low and high liquid fraction slags. The calculated viscosities in the study of Shibata *et al.* (29.7 wt% FeO) and the study of Monaghan *et al.* (> 40 wt% FeO) are less than 0.61 poise, which is much lower compared to other cases therefore the liquid fraction for these slags would be expected to be much higher. Therefore we have compared the k_{FeO} data for droplets with 0.014 wt% and 0.021 wt% S in current study, *i.e.*, those for which the slag had a high liquid fraction with cases from Shibata *et al.* and Monaghan *et al.* containing high total iron oxide (> 29 wt%) as shown in Figure 4.5(b).

By studying reduction of iron oxide in FeO rich slag, most investigators [16-24] proposed that the reaction was first order with respect to FeO concentration in the bulk slag, and was most likely controlled by FeO mass transfer in the slag. If this is the case, the apparent rate constant can be converted to a mass transfer coefficient for FeO in the slag as done by Woolley and Pal [24]. A detailed explanation of this conversion is shown in the Appendix. Depending on the availability of required information to complete the conversion, apparent rate constants in some of those studies were converted and included in Figures 4.5(a) and (b), also listed in the appendix in Table 4.A4 . When carbon dissolved from graphite crucible was the reductant for FeO, Galgali *et al.* [17] found that the mass transfer coefficient of FeO decreased with increasing of FeO content in the slag. Although in the case of Murthy *et al.* [18] the apparent rate constant showed an increase, the converted k_{FeO} was found to decrease slightly with increasing FeO content. Apparently, a further detailed

analysis of these last two studies is required in order to understand this discrepancy. The k_{FeO} in these cases were also listed in Table 4.A4, but have not been brought into this discussion. It is worth noting that other workers [22, 24] have successfully correlated k_{FeO} with the rate of CO bubble generation to justify the effect of FeO content on k_{FeO} .

All the data presented in Figure 4.5 show an excellent fit to a parabolic relationship between total iron oxide content and mass transport coefficient of FeO in the slag. Molloseau and Fruehan [9], Sarma [10] also observed a similar effect of FeO in the slag on mass transfer coefficient of FeO but did not offer a detailed explanation. From Figure 4.5, it is interesting to note that comparing data for high and low liquid fraction slags, they scale in reasonable approximation to the ratio of liquid fraction. It is also worth pointing that in Figure 4.5(a) although the k_{FeO} in the case of Li and Barati [16] follows a parabolic function, its' values are lower than other cases due to the higher slag basicity ($B=1.8$) slag compared to that ($B\sim 1$) employed in other studies. High basicity slag would increase the effective viscosity as shown by Li and Barati [16], which leads to a higher foam index [15] and lower liquid fraction.

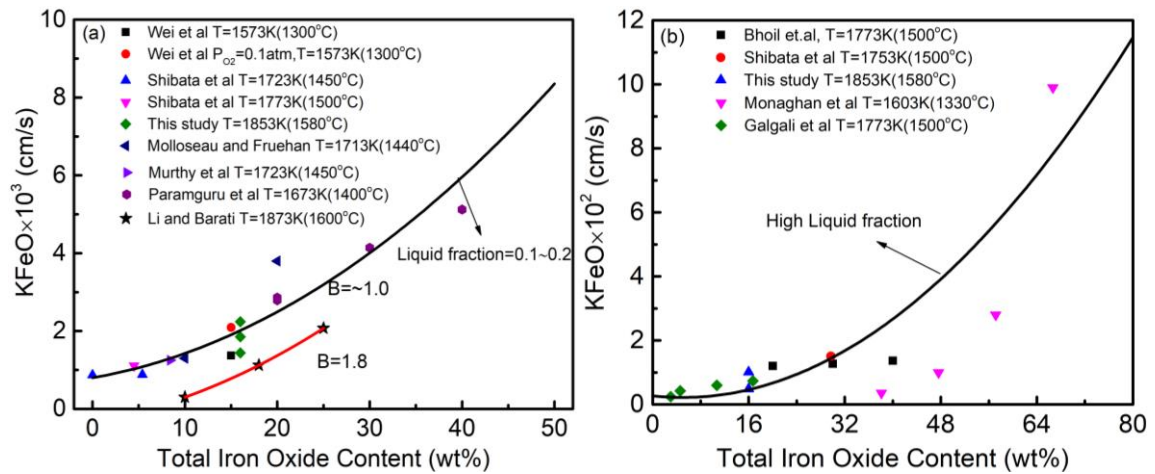


Figure 4.5 k_{FeO} as a function of total iron content in the slag: (a) low liquid fraction and (b) high liquid fraction.

In the current case we are expressing oxygen transfer as mass transport of FeO. However, it is more realistic to consider oxygen to be transported in the form of either O^{2-} or singly

charged oxygen species hopping from site to site on silicate chains. Therefore the flux will require charge balancing either by concurrent transport of cations or by countercurrent transport of electrons. Barati and Coley ^[25] demonstrated that at FeO contents of greater than 5 wt%, electronic conduction via small polaron hopping was dominant and that the electronic conductivity was a parabolic function of total iron oxide content. Therefore, if in the current case, oxygen transport is controlled by the conduction of charge balancing electrons, the nominal mass transfer coefficient of FeO, k_{FeO} can be expected to follow a parabolic relationship with total iron in the slag. All the data in Figure 4.5 from different researchers under a wide ranged temperatures shows an excellent fit, which suggests that the effect of temperature on the k_{FeO} was relatively small. This observation is not consistent with the temperature effect on electronic conductivity observed by Barati and Coley ^[26]. Employing the Melts database in Factsage 6.4TM, the activation energy of viscous flow for several cases in Figure 4.5 was estimated to have a magnitude of 100 kJ/mol. This estimation indicates that the temperature might have a larger effect on mass transfer coefficient than implied by Figure 4.5. At present the authors cannot offer a definitive explanation for this discrepancy.

4.4.2 Dynamic Interfacial Oxygen Potential

Knowing k_{FeO} in the slag, the interfacial oxygen potential between bloated metal droplets and slag can be calculated based on Eq. (4.2). According to the results in Table 4.1, mass transfer of FeO in dense slag is more than four times faster than in foamy slag. In the present work, dephosphorization was mostly complete before droplets entered the foamy slag. Therefore, only the $P_{O_2}^i$ at the initial stage before the metal droplet completely enters the foamy slag, was calculated. As examples of the range of droplet behavior observed in the current work, the dynamic interfacial oxygen potential was calculated for droplets with 0.007 wt%, 0.014 wt% and 0.021 wt% S.

To account for periods in which droplets sit between the foamy slag and dense slag, the changing fraction of droplet surface area in the foamy slag was measured and plotted in Figure 4.6 for droplets with 0.014 wt% and 0.021 wt% S. After approximately 5 seconds,

0.014 wt% S droplets start to float up into the foamy slag, while 0.021 wt% S droplets begin to float up after around 12 seconds due to their longer incubation time for swelling. The mass transfer coefficient k_{FeO} used to calculate the interfacial oxygen potential was calculated as an average of foamy slag and dense slag weighted according to the fraction of the droplet surface exposed to each.

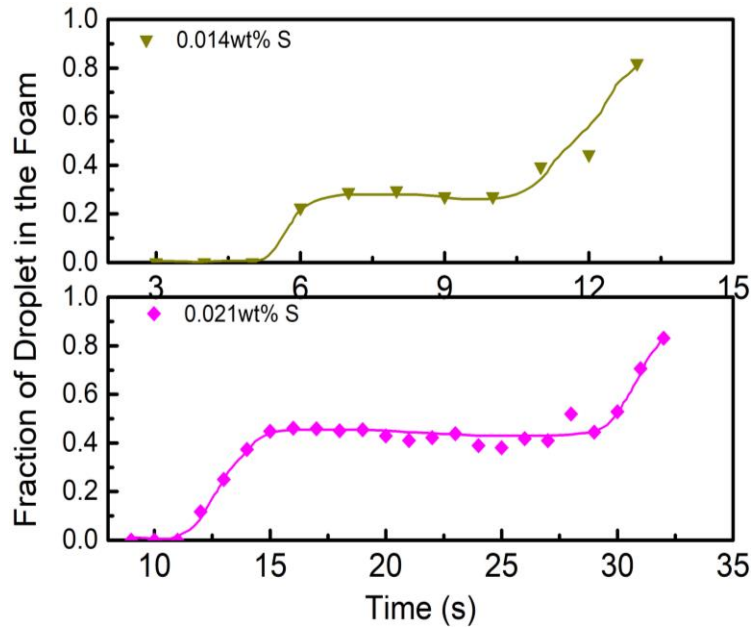


Figure 4.6 Fraction of droplet surface area in the foam as a function of time.

Based on Eq. (4.2), the dynamic interfacial oxygen potential for droplets before rising entirely into the foamy slag was calculated and is shown in Figure 4.7. It shows that $P_{O_2}^i$ for all the cases decreases as reaction proceeds but the rate of decrease varies with the decarburization rate and incubation time. For droplets with lower sulfur content (0.007 and 0.014 wt%), the $P_{O_2}^i$ drops very rapidly because their short incubation times leading to an early entry into the foamy slag which has a low mass transfer coefficient for FeO and also the low liquid volume becomes depleted of FeO. While for droplets with 0.021 wt% S, $P_{O_2}^i$ decreases much more slowly because of the lower decarburization rate coupled with the longer incubation period which causes them to remain in the dense slag with a higher mass transfer coefficient for FeO and greater reservoir of FeO. One would assume that in a real

BOF the droplets would be subject to the k_{FeO} of a foamy slag but that FeO would not be depleted because of constant replenishing via reaction with the oxygen jet.

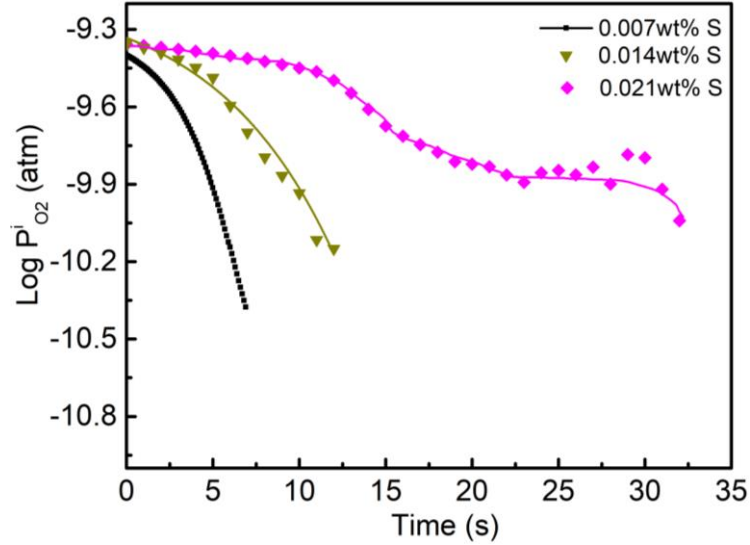


Figure 4.7 The dynamic interfacial oxygen potential between bloated droplets and slag.

4.4.3 The Effect of Dynamic Interfacial Oxygen Potential on Dephosphorization Kinetics

It is well established that the balance between control by mass transfer in the slag and by mass transfer in the metal is heavily influenced by the phosphorus partition ratio; a significant change in L_P causes a shift in reaction mechanism from one controlling step to another [2, 4, 5]. By knowing the dynamic $P_{O_2}^i$, the phosphorus partition ratio L_P and the overall mass transfer coefficient k_o can be calculated as a function of time based on Eq. (4.3) and (4.5):

$$k_o = \frac{1}{\frac{\rho_m}{k_s \rho_s L_P} + \frac{1}{k_m}} \quad (4.5)$$

where k_s and k_m are mass transfer coefficient in slag and metal phase, respectively.

Figure 4.8 shows the phosphorus partition ratio and the overall mass transfer coefficient as a function of time for bloated droplets in the current study, calculated based on the dynamic

interfacial oxygen potential. Here, k_s and k_m were chosen to be 0.01 and 0.085 cm/s based on analysis of dephosphorization presented in a previous publication by the authors [5].

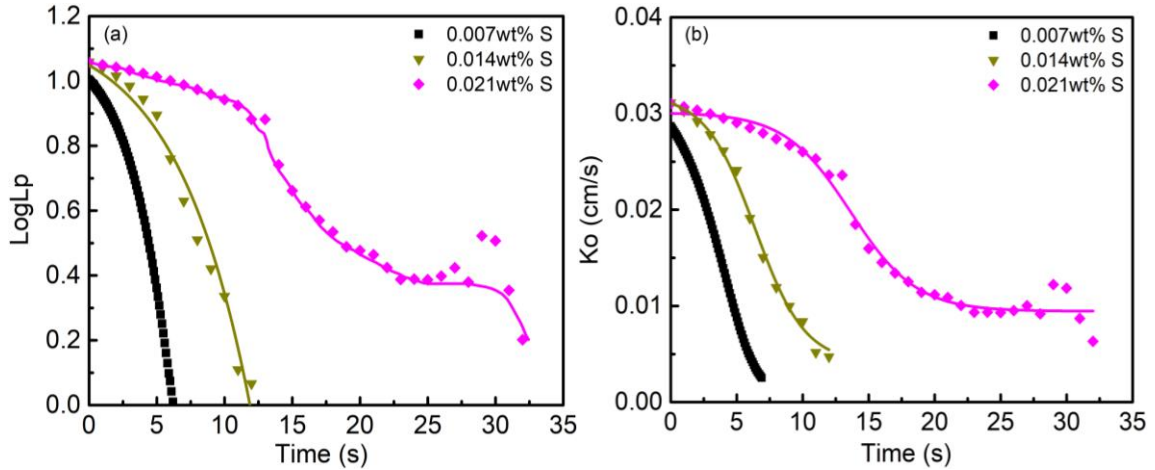


Figure 4.8 (a) phosphorus partition ratio (L_P) and (b) overall mass transfer coefficient (k_o) as a function of time for the study of bloated droplets.

Figure 4.8(a) shows that the driving force for dephosphorization, L_P , decreases with time due to the decreasing interfacial oxygen potential as reduction of FeO from the slag proceeds. Figure 4.8(b) presents the change of overall mass transfer coefficient during the dephosphorization period shown in Figure 4.2. It shows that the controlling step for dephosphorization of bloated droplets in the current study is initially mixed control by mass transport in both the metal and slag. And the value of k_o is 0.03 cm/s. As phosphorus partition ratio decreases, the rate determining step shifts to mass transport in slag with a value of k_o less than 0.01 cm/s. The changes in k_o with time agree very well with the authors' previous observations of dephosphorization kinetics [5].

Shibata *et al.* [4] conducted a similar analysis of mixed control to that presented above, however these workers presented their data as resistance to mass transfer rather than an overall mass transfer coefficient. To facilitate comparison Shibata's data analysed in terms of k_o is presented in Figure 4.9. These workers reported k_s and k_m to be 0.013 cm/s and 0.021 cm/s. Using these values, the determined L_P and k_o are shown in Figure 4.9. The trends presented in Figure 4.9 are exactly the same as those found in the current authors'

research, although the overall mass transfer coefficient is relatively lower. Deeper analysis shows that the source of the discrepancy lies in the current case having a significantly higher mass transfer coefficient for phosphorus in the metal. The authors are not able to offer a definitive explanation for this discrepancy but believe it must be related to the way in which CO gas stirs the metal. It is worth noting that in the current case CO nucleated throughout the droplet.

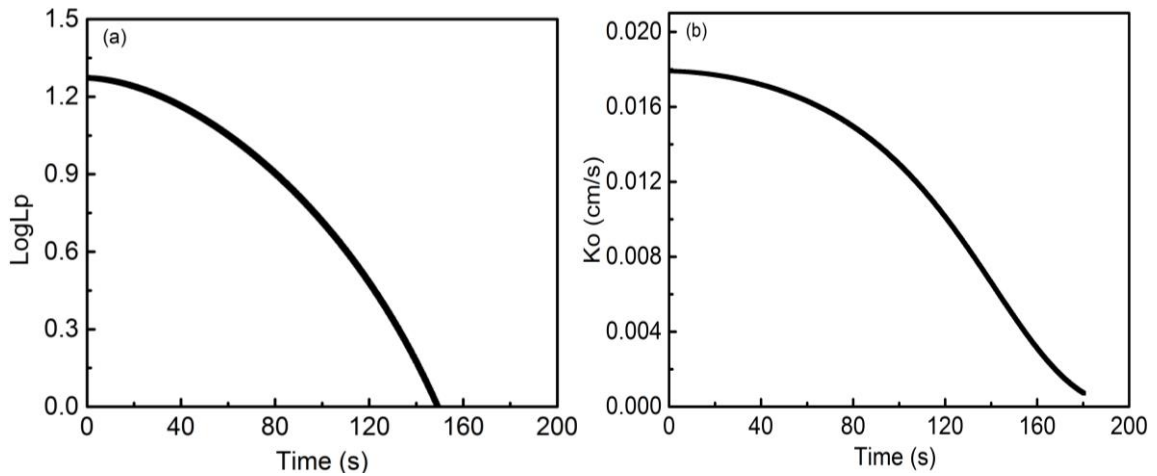


Figure 4.9 (a) L_p and (b) k_o as a function of time for the case of Shibata *et al.* [4]

The relative contribution of the metal phase to the overall resistance to mass transport was determined by Shibata *et al.* to be 95% at the beginning of the reaction decreasing to 30% towards the end of the reaction. The relatively greater fraction of control by mass transport in the metal when compared with the current work can be explained by less depletion of FeO in the slag in the case of Shibata *et al.* and by a lower mass transfer coefficient in the metal.

From above discussion, the rate controlling step of dephosphorization is dependent on the decarburization behavior of metal droplets. The prediction of rate determining step using the model developed in the current study showed very reasonable agreement with other researchers' work [2-4]. Therefore, it is worth examining how the decarburization rate might affect the rate controlling step in real steelmaking conditions. Assuming metal droplets under typical steelmaking conditions have similar decarburization behavior to droplets

with 0.014 wt% S in this study, and choosing reasonable mass transfer coefficients for slag (0.005 cm/s) and metal (0.06 cm/s) based on the above discussion, the relationship between overall mass transfer coefficient k_o and the decarburization rate has been evaluated using the above model. In this calculation, the slag composition was chosen to be 45 wt% CaO-20 wt% SiO₂-15 wt% FeO-10 wt% MnO-5 wt% MgO based on typical industrial data during the middle blow stage in the BOF [27]. The calculated result is shown in Figure 4.10. The two vertical dotted lines represent the range of decarburization rate observed in this study at 1853 K. The corresponding L_p for a steelmaking slag will be between 380 and 900. This figure shows that under steelmaking conditions dephosphorization of metal droplets in the emulsion zone is more likely to be limited by the mass transport in the metal phase. This finding is reasonable under steelmaking conditions if one considers the high basicity of slag and no depletion of FeO in the slag.

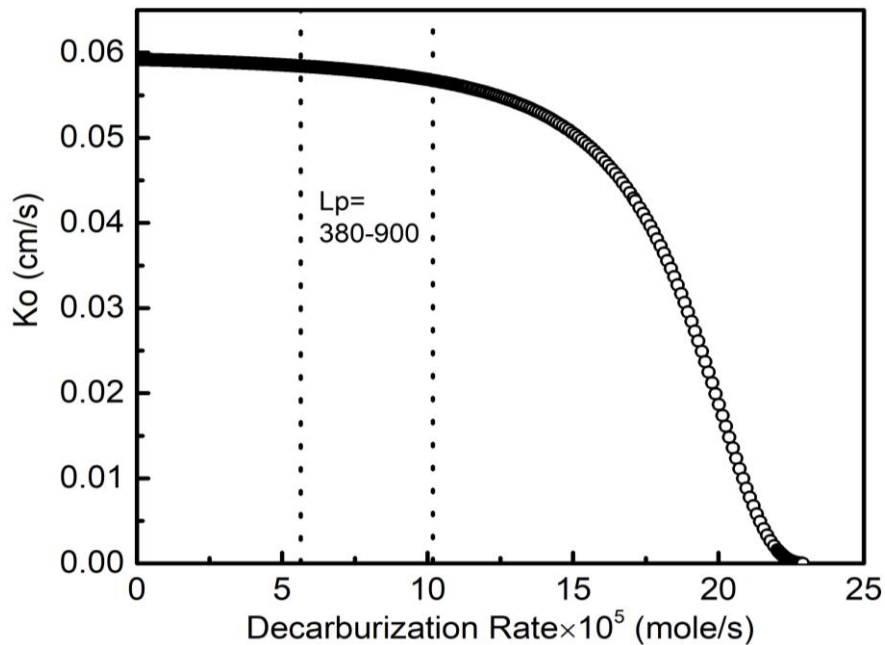


Figure 4.10 The effect of decarburization rate on overall mass transfer coefficient.

4.5 Conclusion

The dynamic interfacial oxygen potential between bloated droplets and slag was determined using the phosphorus partition ratio at the reversion point. Analysis of this data by considering the balance between oxygen supply from oxidizers in the slag and oxygen consumption by alloy elements in the metal allowed the mass transfer coefficient of “FeO” to be determined. The mass transfer coefficient was found to show a parabolic increase with total iron oxide in the slag. The calculated results also showed that the mass transfer of FeO in dense slag was much faster than in foamy slag. Knowing the mass transfer coefficient for FeO and the decarburization rate of the droplet allows the dynamic interfacial oxygen potential to be calculated at any time during the reaction. From this study, the following conclusions can be drawn.

1. When the mass transfer of oxygen in the slag is represented as mass transfer of “FeO”, the mass transfer coefficient shows a parabolic correlation with total iron oxide in the slag and is not strongly dependent on temperature. This is consistent with transport controlled by charge balancing by small polaron hopping via an $\text{Fe}^{3+}/\text{Fe}^{2+}$ couple.
2. The mass transfer coefficient of FeO in the dense slag shows a strong linear correlation with the liquid fraction in foamy slag due to transport pathways being limited to the liquid portion.
3. Calculations predict that the rate determining step for dephosphorization of bloated droplets in laboratory studies, shifts from mass transport in both metal and slag to mass transport in slag. This is caused by a decrease in the dynamic interfacial oxygen potential with time because of FeO depletion.
4. Contrary to most laboratory studies, the calculation method adopted in the current study shows that dephosphorization of metal droplets in the emulsion zone under real steelmaking conditions will be limited by mass transport in the metal phase because of the high basicity of the slag and the fact that FeO is continuously replenished.

4.6 Appendix

A-1 Derivation of Equation (4.2).

The derivation of Eq. (4.2) from Eq. (4.1) can be demonstrated as follows:

$$k_{FeO}(C_{FeO}^b - C_{FeO}^i) = \frac{1}{A} \frac{dn_{CO}}{dt} \quad (4.1)$$

where C_{FeO}^b is the instantaneous concentration of FeO in the bulk slag at any given time t , which can be calculated via Eq. (4.A1) by knowing the amount of FeO (n_{FeO}) has been reduced, *i.e.*, the amount of CO gas (n_{CO}) generated at time t .

$$C_{FeO}^b = C_{FeO}^o - \frac{1}{V_S} n_{FeO} = C_{FeO}^o - \frac{1}{V_S} \int_{n_{CO,t=0}}^{n_{CO,t=t}} dn_{CO} \quad (4.A1)$$

Substituting C_{FeO}^b into Eq. (4.1), one can obtain the concentration of FeO at the slag-metal interface.

$$C_{FeO}^i = C_{FeO}^o - \frac{1}{V_S} \int_{n_{CO,t=0}}^{n_{CO,t=t}} dn_{CO} - \frac{1}{A} \frac{1}{k_{FeO}} \frac{dn_{CO}}{dt} \quad (4.A2)$$

The equilibrium constant for dissociation of FeO at the interface can be expressed as,

$$K_{Fe} = \frac{a_{Fe}^i a_O^i}{\gamma_{FeO} X_{FeO}^i} \quad (4.A3)$$

Knowing the overall molar density of slag C_S , X_{FeO}^i can be expressed as $\frac{C_{FeO}^i}{C_S}$. Then a_O^i can be written as Eq. (4.A4) by rearranging Eq. (4.A3),

$$a_O^i = \frac{\gamma_{FeO} K_{Fe} C_{FeO}^i}{C_S a_{Fe}^i} \quad (4.A4)$$

Substituting Eq. (4.A2) into Eq. (4.A4), one can obtain,

$$a_O^i = \frac{\gamma_{FeO} K_{Fe}}{C_S a_{Fe}^i} \left(C_{FeO}^o - \frac{1}{V_S} \int_{n_{CO,t=0}}^{n_{CO,t=t}} dn_{CO} - \frac{1}{A} \frac{1}{k_{FeO}} \frac{dn_{CO}}{dt} \right) \quad (4.A5)$$

Considering the dissolution of oxygen into metal phase with the following reaction constant,

$$K_O = \frac{a_O^i}{P_{O_2}^{i/2}} \Rightarrow P_{O_2}^{i/2} = \frac{a_O^i}{K_O} \quad (4.A6)$$

The expression for calculating oxygen potential (equivalent oxygen partial pressure) at the slag-metal interface can be expressed as Eq. (4.2) finally.

$$P_{O_2}^i = \left[\frac{\gamma_{FeO} K_{Fe}}{C_S a_{Fe}^i K_O} \left(C_{FeO}^o - \frac{1}{V_S} \int_{n_{CO,t=0}}^{n_{CO,t=t}} dn_{CO} - \frac{1}{A} \frac{1}{k_{FeO}} \frac{dn_{CO}}{dt} \right) \right]^2 \quad (4.2)$$

A-2 Calculation of Void Fraction

Assuming a constant cross-sectional area for the crucible, the volume of the slag may be represented by its depth. The initial slag height h_o , the dense slag depth h_{dense} and the depth of foaming slag h_{foam} at any given time can be measured via the recorded X-ray video. Then the liquid fraction of slag in the foam was calculated based on the Eq. (4.A7).

$$F_{liquid} = \frac{h_o - h_{dense}}{h_{foam}} \quad (4.A7)$$

Then the void fraction = $1 - F_{liquid}$.

For droplets with 0.014 wt% and 0.021 wt% S, which go through phosphorus reversion while sitting between the dense slag and foaming slag as shown in Figure 4.3, the liquid fraction F_{liquid}^* of the slag in contact with the droplet was represented by a weighted average of foamy and dense slag in proportion to their contact with the droplet, *i.e.*,

$$F_{liquid}^* = \frac{V_{droplet \text{ in the foam}}}{V_{droplet}} F_{liquid1} + \frac{V_{droplet \text{ in dense slag}}}{V_{droplet}} F_{liquid2} \quad (4.A8)$$

where $V_{droplet}$, $V_{droplet \text{ in the foam}}$ and $V_{droplet \text{ in dense slag}}$ are total droplet volume, the partial volume of droplet in foaming slag and dense slag, respectively. $F_{liquid1}$ is the slag liquid fraction obtained from Eq. (4.A7), while $F_{liquid2}$ represents the liquid fraction of dense slag and is one.

The related reactions and their reaction equilibrium constants were listed in Table 4.A1 ^[28]:

Table 4.A1 Reactions and their equilibrium constants used in this study.

Reactions	Reaction Constant
$(\text{FeO}) = [\text{Fe}] + [\text{O}]$ (1)	$\log K_1 = \frac{-6372}{T} + 2.73$
$[\text{C}] + [\text{O}] = \text{CO}$ (2)	$\log K_2 = \frac{1160}{T} + 2.003$
$\frac{1}{2}(\text{O}_2)_{\text{gas}} = [\text{O}]$ (3)	$\log K_3 = \frac{6120}{T} + 0.18$
$\text{MnO} = [\text{Mn}] + [\text{O}]$ (4)	$\log K_4 = \frac{-15046.6}{T} + 6.70$
$\frac{1}{2}(\text{P}_2)_{\text{gas}} = [\text{P}]$ (5)	$\log K_P = \frac{8240}{T} - 0.28$

In this study, the empirical equation developed by Basu *et al.* ^[29] was also used to estimate γ_{FeO} .

$$\log \gamma_{\text{FeO}} = -0.7335 \log X_{\text{FeO}} - 0.2899 \quad (4.A9)$$

Slag and metal compositions taken from the work of Shibata *et al.* ^[4] and Wei *et al.* ^[2] are given in Tables 4.A2 and 4.A3. These data are employed to calculate k_{FeO} and $P_{\text{O}_2}^i$ below.

Table 4.A2 Slag compositions (wt%).

Slag	MnO	FeO	CaO	SiO ₂	CaF ₂	Li ₂ O
Shibata <i>et al.</i> (A-1)	–	29.7	29.4	32.1	8.8	
Shibata <i>et al.</i> (B-12)	22.4	4.5	30.3	33.3	9.5	
Shibata <i>et al.</i> (C-1)	39.6	5.4	22.0	23.8	9.2	
Shibata <i>et al.</i> (K-5)	36.7	–	27.6	27.0	8.8	
Wei <i>et al.</i>	15(Fe _t O)		32.6	35		17.4

Table 4.A3 Experimental conditions and initial metal compositions (wt%).

Number	T/K	C	P	Si	Mn	S
Shibata <i>et al.</i> (A-1)	1773	3.72	0.089	0.187	–	–
Shibata <i>et al.</i> (B-12)	1773	3.81	0.092	0.194	0.015	–
Shibata <i>et al.</i> (C-1)	1723	3.79	0.102	0.215	0.010	–
Shibata <i>et al.</i> (K-5)	1723	3.80	0.096	0.167	0.020	0.098
Wei <i>et al.</i> (P _{O2} =0atm)	1573	4.44	0.1			
Wei <i>et al.</i> (P _{O2} =0.1atm)	1573	4.18	0.044			

A-3 Dynamic Interfacial Oxygen Potential

The equations employed in calculating $P_{O_2}^i$ for those four cases taken from the work of Shibata *et al.* [4] and Wei *et al.* [2] listed in Table 4.A2 and 4.A3 were as follows:

A-1 slag:

$$P_{O_2}^i = \left[\frac{\gamma_{FeO} K_1}{C_s a_{Fe}^i K_3} \left(C_{FeO}^o - \frac{1}{V_s} \left(\int_{n_C, t=initial}^{n_C, t=t} dn_C + 2 \int_{n_{Si}, t=initial}^{n_{Si}, t=t} dn_{Si} \right) - \frac{1}{A} \frac{1}{k_{FeO}} \left(\frac{dn_C}{dt} + 2 \frac{dn_{Si}}{dt} \right) \right) \right]^2 \quad (4.A10)$$

K-5 slag:

$$P_{O_2}^i = \left[\frac{\gamma_{MnO} K_4}{C_s a_{Mn}^i K_3} \left(C_{MnO}^o - \frac{1}{V_s} \left(\int_{n_C, t=initial}^{n_C, t=t} dn_C + 2 \int_{n_{Si}, t=initial}^{n_{Si}, t=t} dn_{Si} \right) - \frac{1}{A} \frac{1}{k_{MnO}} \left(\frac{dn_C}{dt} + 2 \frac{dn_{Si}}{dt} \right) \right) \right]^2 \quad (4.A11)$$

Eq. (4.A10) was developed by balancing the flux of FeO to the interface with the oxidation of carbon and silicon in the metal. Eq. (4.A11) was developed in the same way replacing

FeO flux with that of MnO. Eq. (4.A12) applied the same logic but assumed oxygen supply by simultaneous flux of FeO and MnO and that Mn-MnO and Fe-FeO at the interface were in equilibrium with the same oxygen potential. Similarly, Eq. (4.A13) was developed by balancing the flux of FeO to the interface with the oxidation of carbon in the metal. In his study, Wei *et al.* defined the iron oxide in their slag as Fe_tO in recognition that some of the iron was present as Fe^{3+} , however for simplicity of calculation it has been assumed that the iron oxide was in the form of FeO.

B-12 and C-1 slag:

$$P_{O_2}^i = \left[\frac{1}{\left(\frac{C_s a_{Fe}^i k_{FeO}}{\gamma_{FeO} K_1} + \frac{C_s a_{Mn}^i k_{MnO}}{\gamma_{MnO} K_4} \right) K_3} \left[\left(k_{FeO} + \frac{k_{MnO} \gamma_{FeO} K_1 a_{Mn}^i K_4}{a_{Fe}^i \gamma_{MnO}} \right) \times \left(C_{FeO}^o - \frac{1}{V_s} \left(\int_{n_{C,t=initial}^{n_{C,t=t}} dn_C + 2 \int_{n_{Si,t=initial}^{n_{Si,t=t}} dn_{Si}} \right) - \frac{1}{A} \left(\frac{dn_C}{dt} + 2 \frac{dn_{Si}}{dt} \right) \right) \right]^2 \right. \quad (4.A12)$$

Fe_tO slag:

$$P_{O_2}^i = \left[\frac{\gamma_{FeO} K_1}{C_s a_{Fe}^i K_3} \left(C_{FeO}^o - \frac{1}{V_s} \int_{n_{C,t=initial}^{n_{C,t=t}} dn_C - \frac{1}{A} \frac{1}{k_{FeO}} \frac{dn_C}{dt} \right) \right]^2 \quad (4.A13)$$

where γ is the Raoult's activity coefficient of oxides in the slag at the interface and calculated via Eq. (A9) and regular solution model^[30], α^i represents the Henrian activity in liquid metal at the interface and obtained based on interaction coefficients for different solutes^[17]. K is the equilibrium constant for reactions listed in Table 4.A4, C_s and C^o are molar density of slag and initial concentration of oxides, respectively. V_s represents the volume of slag, $\frac{dn}{dt}$ is the reaction rate (mole/s) for Si and C which is determined empirically using experimental data.

A-4 Mass Transfer Coefficient k_{FeO} Conversion.

If the reduction of iron oxide in FeO rich slag follows first order reaction kinetics with respect to FeO in the bulk slag phase and is controlled by the mass transfer of FeO in the slag, the rate expression may be given as follows:

$$r_{FeO} = k(\%FeO)_{bulk\ slag} \quad (4.A14)$$

where r_{FeO} is reaction rate with the unit of $(\% FeO) \cdot s^{-1}$ and also equal to the reaction rate in terms of CO, *i.e.*, r_{CO} ; k is the rate constant and has a unit of s^{-1} or min^{-1} . It is well known that the first order reaction rate can also be written as:

$$r_{FeO} = k_{FeO} \frac{A}{V} (\%FeO)_{bulk\ slag} = k_{FeO} \frac{A}{Ah_o} (\%FeO)_{bulk\ slag} = \frac{k_{FeO}}{h_o} (\%FeO)_{bulk\ slag} \quad (4.A15)$$

where k_{FeO} is mass transfer coefficient of FeO, V represents slag volume in this case, A is the area of slag-metal interface and normally treated as cross-sectional area of crucible, h_o represents the slag height.

Then we are able to convert the rate constant (with unit of s^{-1}) in Eq. (4.A14) to k_{FeO} via the following expression;

$$k = \frac{k_{FeO}}{h_o} \quad (4.A16)$$

Some authors expressed the reaction rate as expressed in Eq. (4.A17) with the unit of $mol \cdot cm^{-2} \cdot s^{-1}$,

$$r_{FeO} = J_{FeO} = k_{FeO} C_{FeO\ bulk\ slag} = k_{FeO} \frac{\rho_s}{100M_{FeO}} (\%FeO)_{bulk\ slag} \quad (4.A17)$$

where ρ_s is the density of slag ($g \cdot cm^{-3}$), M_{FeO} represents the molecular weight of FeO.

Then Eq. (4.A14) can be rewritten as:

$$r_{FeO} = k'(\%FeO)_{bulk\ slag} \quad (4.A18)$$

Similarly, r_{FeO} is reaction rate but with the unit of $\text{mol} \cdot \text{cm}^{-2} \cdot \text{s}^{-1}$ and $k' = k_{FeO} \frac{\rho_s}{100M_{FeO}}$ is the rate constant with the unit of $\text{mol} \cdot \text{cm}^{-2} \cdot \text{s}^{-1}(\%FeO)^{-1}$. Therefore, k' can be converted to k_{FeO} based on Eq. (4.A17).

Table 4.A4 Converted k_{FeO} from rate constants determined by different researchers.

Investigator	T/K	B	Fe ₂ O ₃ / (wt%)	$k' \times 10^7 / (\text{mol} \cdot \text{cm}^{-2} \cdot \text{s}^{-1}(\%FeO)^{-1})$	$k \times 10^3 / (\text{s}^{-1})$	$k_{FeO} \times 10^3 / (\text{cm/s})$
Li and Barati.	1873	1.8	10	1.1		0.30
Li and Barati.	1873	1.8	18	4.1		1.12
Li and Barati.	1873	1.8	25	7.6		2.07
Paramguru <i>et al.</i>	1673	1	20		1.58	2.79
Paramguru <i>et al.</i>	1673	1	20		1.62	2.86
Paramguru <i>et al.</i>	1673	1	30		2.45	4.14
Paramguru <i>et al.</i>	1673	1	40		3.16	5.12
Bhoil <i>et al.</i>	1873	1	20		3.33	12.0
Bhoil <i>et al.</i>	1873	1	30		3.53	12.7
Bhoil <i>et al.</i>	1873	1	40		3.80	13.7
Galgali <i>et al.</i>	1773	1.2	3.0		0.82	2.45
Galgali <i>et al.</i>	1773	1.2	4.6		1.42	4.26
Galgali <i>et al.</i>	1773	1.2	10.7		2.0	6.0
Galgali <i>et al.</i>	1773	1.2	16.4		2.45	7.35
Galgali <i>et al.</i>	1773 *	1.2	5			3.78
Galgali <i>et al.</i>	1773 *	1.2	10			3.80

Table 4.A4 (Continued).

Investigator	T/K	B	Fe _t O/ (wt%)	$k' \times 10^7 / (\text{mol} \cdot \text{cm}^{-2} \cdot \text{s}^{-1} (\% \text{FeO})^{-1})$	$k \times 10^3 / (\text{s}^{-1})$	$k_{\text{FeO}} \times 10^3 / (\text{cm/s})$
Galgali <i>et al.</i>	1773*	1.2	15			2.90
Galgali <i>et al.</i>	1773*	1.2	20			2.36
Murthy <i>et al.</i>	1723 ^Δ	1.1	8.4		4.31	1.25 ^Δ
				$k \times 10^5 / (\text{mol} \cdot \text{cm}^{-2} \cdot \text{s}^{-1})$		
Murthy <i>et al.</i>	1823*	1.1	5.5	1.4		6.62
Murthy <i>et al.</i>	1823*	1.1	8.4	1.88		5.74
Murthy <i>et al.</i>	1823*	1.1	13.2	2.05		3.89
Murthy <i>et al.</i>	1823*	1.1	18	2.6		3.55

^ΔThis value of mass transfer coefficient is the mean value for slag with constant FeO content but different slag weights. *Those values were not brought into the discussion of Figure 4.5.

4.7 References

1. S. Ohguchi, D. G. C. Robertson, B. Deo, P. Grieveson and J. H. E. Jeffes: *Ironmak. Steelmak.*, 1984, vol. 11, pp. 202-13.
2. P. Wei, M. Ohya, M. Hirasawa, M. Sano and K. Mori: *ISIJ Int.*, 1993, vol. 33 (8), pp. 847-54.
3. B. J. Monaghan, R.J. Pomfret, and K.S. Coley: *Metall. Trans. B*, 1998, vol. 29B, pp. 111-18.
4. E. Shibata, H. Sun and K. Mori: *Metall. Trans. B*, 1999, vol. 30B, pp. 279-86.
5. K. Gu, N. Dogan and K. Coley: *Metall. Trans. B*, DOI: 10.1007/s11663-017-1002-0.
6. E. Chen and K. Coley: *Ironmak. Steelmak.*, 2010, vol. 37 (7), pp. 541-45.
7. H. Sun: *ISIJ Int.*, 1993, vol. 33 (11), 1560-69.
8. T. Mori: *Trans. Jpn. Inst. Met.*, 1984, vol. 25 (11), pp. 761-71.
9. C. L. Molloseau and R. J. Fruehan: *Metall. Trans. B*, 2002, vol. 33B, pp. 335-44.
10. B. Sarma: PhD Thesis, Carnegie Mellon University, Pittsburgh, PA, 1992, pp. 30-31 and 149.
11. D. J. Min and R. J. Fruehan: *Metall. Trans. B*, 1992, vol. 23B, pp. 29-37.
12. P. Wei, M. Sano, M. Hirasawa, and K. Mori: *ISIJ Int.*, 1993, vol. 33, 479-87.
13. H. Gou, G. A. Irons, and W. Lu: *Metall. Trans. B*, 1996, vol. 27B, pp. 79-88.
14. T. Zhu, M. P. King, K. S. Coley and G. A. Irons: *Metall. Trans. B*, 2012, vol. 43B, pp. 31-36.
15. S. Jung and R. J. Fruehan: *ISIJ Int.*, 2000, vol. 40 (4), pp. 348-55.

16. J. Li and M. Barati: *Metall. Trans. B*, 2009, vol. 40B, pp. 17-24.
17. R. K. Galgali, P. Datta, A. K. Ray, K. K. Prasad and H. S. Ray: *Ironmak. Steelmak.*, 2001, vol. 28 (4), pp. 321-28.
18. G. G. Krishna Murthy, Y. Sawada and J. F. Elliot: *Ironmak. Steelmak.*, 1993, vol. 20 (3), pp. 179-190.
19. G. G. Krishna Murthy, A. Hasham and U. B. Pal: *ISIJ Int.*, 1994, vol. 34 (5), 408-13.
20. R. K. Paramguru, H. S. Ray and P. Basu: *Ironmaking and Steelmaking*, 1996, vol. 23 (4), pp. 328-34.
21. R. K. Paramguru, H. S. Ray and P. Basu: *ISIJ Int.*, 1997, vol. 37 (8), 756-761.
22. R. K. Paramguru, R. K. Galgali and H. S. Ray: *Metall. Trans. B*, 1997, vol. 28B, pp. 805-10.
23. B. Bhoi, A. K. Jouhari, H. S. Ray and V. N. Misra: *Ironmak. Steelmak.*, 2006, vol. 33 (3), pp. 245-52.
24. D. E. Woolley and U. B. Pal: *ISIJ Int.*, 1999, vol. 39 (2), 103-12.
25. M. Barati and K. Coley: *Metall. Trans. B*, 2006, vol. 37B, pp. 51-60.
26. M. Barati and K. Coley: *Metall. Trans. B*, 2006, vol. 37B, pp. 41-49.
27. C. Cicutti, M. Valdez, T. Perez, R. Donayo and J. Petroni: *Latin Am. Appl. Res.*, 2002, vol. 32, pp. 237-240.
28. M. Hino and K. Ito: *Thermodynamic Data for Steelmaking*, Tohoku University Press, Sendai. 2009, pp. 259-64.
29. S. Basu, A.K. Lahiri and S. Seetharaman: *Metall. Trans. B*, 2008, vol. 39B, pp. 447-56.
30. S. Ban-ya: *ISIJ Int.*, 1993, vol. 33(1), pp. 2-11.

Chapter 5

Dephosphorization Kinetics for Bloated Metal Droplets Reacting with Slag Containing FeO: The Influence of CO Bubbles on the Mass Transfer of Phosphorus in the Metal

In Chapter 5, I proposed the concept of a modified surface renewal model, all experiments and data analysis were conducted by me. Dr. Kenneth S. Coley provided very helpful discussions on the data analysis. The first draft was written by me, with proofreading from Dr. Neslihan Dogan, and final editing by Dr. Kenneth S. Coley. This manuscript has been accepted for publication in *Metallurgical and Materials Transactions B*.

Abstract

Dephosphorization kinetics of bloated metal droplets was investigated in the temperature range from 1813 K to 1913 K. The experimental results showed that the overall mass transfer coefficient, k_o , decreased with increasing temperature because of decreasing phosphorus partition ratio, L_P . It was also found that the mass transfer coefficient for phosphorus in the metal, k_m , had the highest value at the lowest temperature (*i.e.*, 1813 K) because the formation of smaller CO bubbles increased the rate of surface renewal, leading to faster mass transport. Meanwhile, metal droplets without carbon were also employed to study the effect of decarburization on dephosphorization. The results show that although decarburization lowers the driving force significantly, k_m (6.2×10^{-2} cm/s) for a carbon containing droplet is two orders of magnitude higher than the one for carbon free droplets (5.3×10^{-4} cm/s) because of the stirring effect provided by CO bubbles. This stirring offers a faster surface renewal rate, which surpasses the loss of driving force and then leads to a faster dephosphorization rate.

5.1 Introduction

In basic oxygen steelmaking, metal droplets created by the impact of the oxygen jet are ejected into the slag, where they are decarburized and dephosphorized by reaction with iron oxide. Those droplets which swell because of internal nucleation of CO bubbles are termed bloated droplets. The behavior of bloated droplets in terms of decarburization has been studied extensively ^[1-7], although several of these studies predate the coining of the term “bloated droplet” which was first used by researchers in the authors’ laboratory ^[8]. Models for predicting residence time in the emulsion zone of the BOF based on droplet bloating behavior have also been developed ^[8,9]. Workers at Swinburne University in Australia^[10,11] have developed an overall BOF model considering the behavior of bloated droplets. The development of the bloated droplet concept and its influence on BOF modeling has recently been reviewed in detail by Brooks *et al* ^[12]. All of these studies were focused on decarburization kinetics and the causes of droplet swelling. There are very few studies on bloated droplet refining kinetics related to elements other than carbon. One example of this is dephosphorization, which occurs in competition with decarburization in the emulsion zone of the BOF. Based on pilot plant data, Hewage *et al.* ^[13] has attempted to model dephosphorization in the emulsion zone however these workers found that dephosphorization could not be explained by a simple first order equation with either static equilibrium or dynamic equilibrium values, due to the transient behavior of rate parameters such as instantaneous area, residence time and mass transfer coefficient. It is well established that dephosphorization is controlled by mass transfer in the metal, slag or both simultaneously. Therefore, it should be possible to describe the reaction using a rate equation that is first order with respect to phosphorus concentration in the metal. The terms dynamic and static used by Hewage *et al.* ^[13] refer to the equilibrium partition of phosphorus which exists at the slag metal interface. It is common practice in kinetic studies to assume that this value is constant; static equilibrium. This approach is often adequate, however, the oxygen potential at the interface will change with time, because of changes in the balance between oxygen supply and consumption; dynamic oxygen potential. Although equilibrium with respect to phosphorus is maintained at the slag-metal

interface, this equilibrium is set by the oxygen potential which changes with time, leading to a changing or dynamic equilibrium with respect to phosphorus. The concepts of dynamic oxygen potential and dynamic equilibrium with respect to phosphorus, have been discussed in detail in previous work by the authors ^[14] and others ^[15]. This becomes important when dephosphorization is accompanied by oxidation of elements which have a higher affinity for oxygen. This concept is used in Section 5.4.2 of this chapter..

In order to obtain a better understanding of dephosphorization kinetics during decarburization, more detailed work is needed. There is common agreement on some aspects of dephosphorization kinetics associated with decarburization. Firstly, droplet swelling, caused by CO formation inside the droplet increases the droplet residence time in the slag. Secondly, longer residence time favors refining reactions, especially for dephosphorization which can only take place at a significant level when metal is in contact with slag. Thirdly, decarburization will suppress dephosphorization by competing for oxygen, thereby lowering the interfacial oxygen potential ^[14-19] which controls the driving force for dephosphorization. Finally, because of droplet swelling, the slag-metal interfacial area will change with time; this must be accommodated in the rate equation.

The influence of decarburization on the thermodynamic driving force for dephosphorization has been investigated in detail ^[14-19], but the detailed effect of decarburization on the kinetics of dephosphorization is not fully understood, especially the stirring effect introduced by CO bubbles. In the present study, the role of CO bubbles on dephosphorization kinetics is investigated in detail.

5.2 Experimental Procedure

A resistance heated vertical tube furnace (see Figure 5.1), with an 80mm diameter alumina working tube was used. The furnace was equipped with, X-ray imaging to observe the swelling of droplets in-situ, and a pressure transducer with maximum measurable range of 13.8 kPa to measure gas evolution using the constant volume pressure increase technique (CVPI). This technique measures the pressure change caused by gas evolution during

reaction, the measured pressure is converted to moles of CO evolved through calibration before each experiment. By injecting known volumes of gas at the temperature of interest, the conversion coefficient between pressure changes read from pressure transducer and moles of gas can be determined. This was then used to calculate the total CO generation during the reaction. The measured decarburization data from the pressure transducer was also compared with LECO analysis for carbon, of post reaction samples. These analyses showed reasonable agreement with a difference less than 10% of the measured value. Experiments were conducted in the temperature range from 1813 K to 1913 K. Three types of droplet were used in this study, *i.e.*, carbon containing droplets with two sulfur contents: Fe-2.62 wt% C-0.088 wt% P-0.007 wt% S, and Fe-2.62 wt% C-0.088 wt% P-0.014 wt% S, as well as carbon free droplets Fe-0.088 wt% P-0.007 wt% S. The different sulfur contents were used, because previous work in the authors' laboratory ^[19] has shown that sulfur has a strong influence on CO formation rate; the rate initially increases to a peak at 0.014 wt% S. Thus, by using droplets with different sulfur contents, it was possible to determine the mass transfer coefficient of phosphorus at two CO bubbling rates. The carbon free droplet allowed the mass transfer coefficient to be determined in the absence of CO bubbling.

A slag of 25±0.5 g, composed of 32 wt% CaO-35 wt% SiO₂-17 wt% Al₂O₃-16 wt% FeO, was placed in a 45 mm diameter alumina crucible located in the hot zone of the furnace and was melted under an argon atmosphere. High-purity argon was used during the experiments. Before entering the reaction tube, the argon was passed through a gas purifying system consisting of columns filled with anhydrous CaSO₄ (drierite) and a furnace containing copper turnings running at 873 K. Prior to the start of each experiment the furnace was evacuated using a vacuum pump and back filled with argon, this process was repeated three times prior to completely sealing the furnace and starting the experiment. During the preparation of the atmosphere, the crucible containing slag was held in the hot zone of the furnace. The droplet was held by a magnet at the top of the furnace, inside an alumina tube which was sealed from the outside atmosphere. To start the experiment, the droplet was released by removing the magnet. It then fell into the slag via a small hole at

the bottom of the alumina tube. The hole in the tube was sized to ensure the droplet was molten before entering the slag. The reaction time was set to zero when the droplet was observed, by X-ray, to fall into the slag. Samples were quenched at different reaction times and taken for chemical analysis of phosphorus using Inductively Coupled Plasma Optical Emission Spectroscopy (ICP-OES). Optical microscopy was also employed to reveal the presence of cavities (the remnants of bubbles) inside quenched droplets after reaction. The rod used to support the alumina crucible in the hot zone of the furnace was held in place by an O-ring and a collar at the base of the furnace. By releasing the collar, the crucible could be dropped from the hot zone into the quench chamber (water cooled stainless steel) within 1 second.

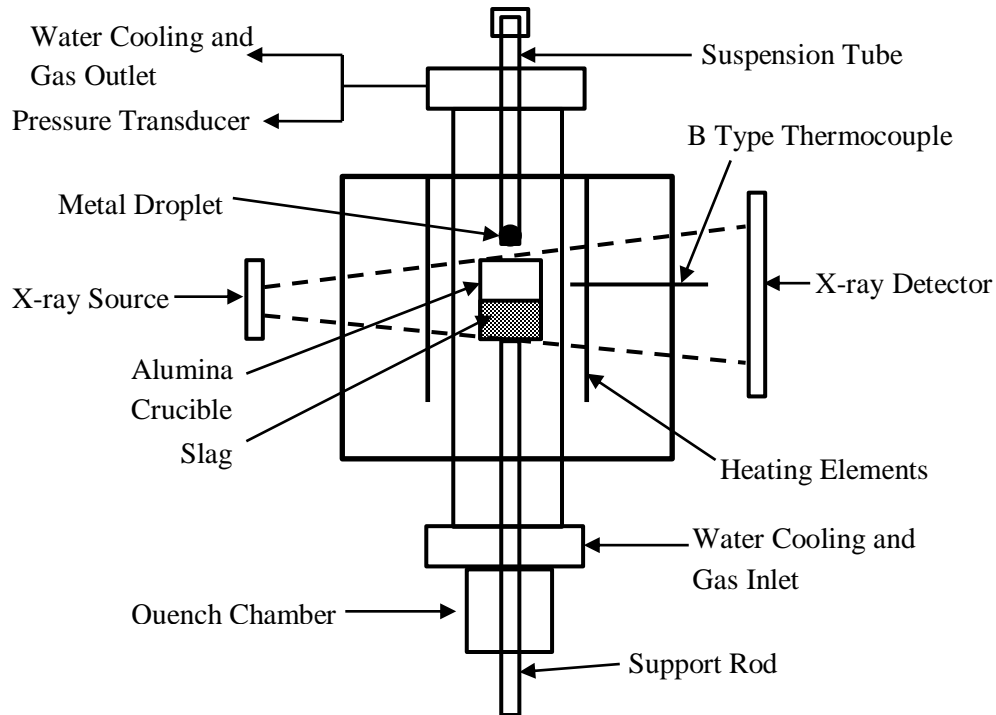


Figure 5.1 Schematic diagram of the furnace.

The experimental technique was limited by a very short reaction time which restricted the collection of data to describe the reaction kinetics in detail. Because of these limitations, the authors would not have chosen this technique to study generic dephosphorization behavior. However, in the present case the focus was on the interplay between

decarburization and dephosphorization in bloated droplets thereby limiting the authors to study bloated droplets.

5.3 Experimental Results

5.3.1 Decarburization as a Function of Temperature

Figure 5.2(a) shows the total amount of CO generated for 0.007 wt% S droplets as a function of time and temperature in the range from 1813 K to 1913 K. Figure 5.2(b) shows similar data for 0.014 wt% S droplets at 1853 K and 1913 K. All plots shown in Figure 5.2 show the same characteristic shape; an initial “incubation period” where the reaction is relatively slow, followed by a period of much faster relatively constant rate, after which the rate tails off. Strictly speaking, the incubation period could more properly be described as a period of mixed internal-external decarburization, as during this period CO gas is formed at the slag/metal interface as well as inside the droplet. The period of much faster reaction following the incubation period, coincides with a shift to internal nucleation of CO which leads to droplet swelling or bloating. In the current paper, the initial period of slow reaction will be referred to as the incubation period despite the fact the decarburization reaction is already well established at the surface of the droplet. These figures also show that the decarburization rate increases with increasing temperature. The maximum slope of each curve shown in Figure 5.2(a) was taken as the peak CO evolution rate. Based on calibration by injection of known volumes of gas and by comparing the measured decarburization with the cumulative total, the CO evolution measurements are precise to $\pm 10\%$. And the error for the determination of peak decarburization rate is $\pm 7\%$.

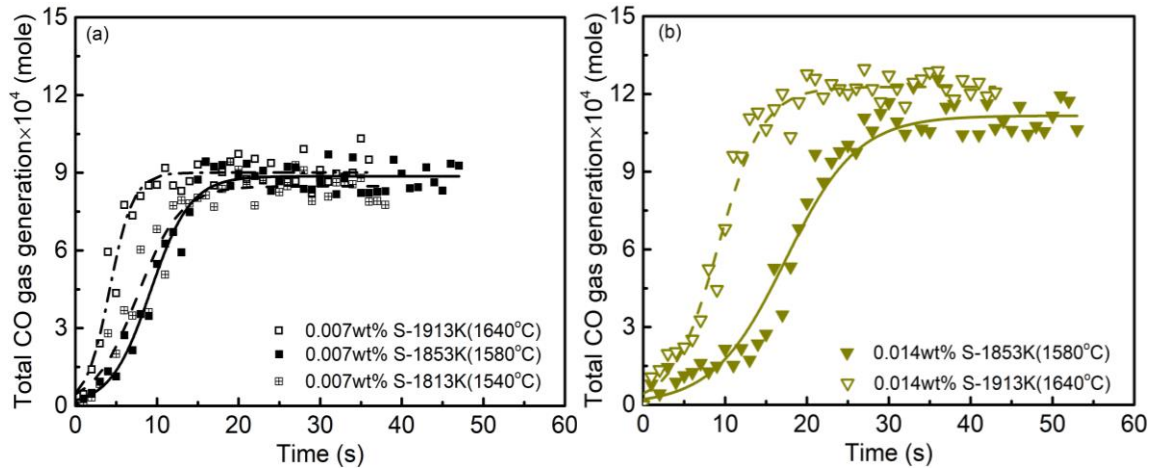


Figure 5.2 Decarburization behavior of droplets: (a) CO gas generation with time for 0.007 wt% S droplets and (b) 0.014 wt% S droplets.

The volume of CO generated in normal cubic meters is determined using the constant volume pressure increase technique. The CO/CO₂ ratio in equilibrium with the activity of FeO in the current slag ranges from 15.7 to 18.4 within the temperature range in this study. Assuming all the gas formed is CO introduces no error to the decarburization rate, but will introduce a small error to the calculated FeO depletion ($\pm 6\%$). One may therefore calculate the carbon removed from the pressure transducer data, and the FeO content of the slag by mass balance with carbon. It is worth noting that the authors have analyzed the post reaction samples for carbon and they agree fairly well with the results obtained from pressure transducer ($\pm 10\%$ of carbon content). The slag composition was chosen near alumina saturation, and from slags that have been measured the maximum alumina pickup was less than 3 wt%, which would decrease the phosphorus partition by about 15% over the total time of reaction. A difficulty in attributing composition to the part of the slag involved in the reaction arises because the slag partitions into a dense slag and a foamy slag. Once the droplet rises into the foamy slag all the stirring is above the dense slag so one can expect little mixing of the two layers. The authors have managed to obtain separate analyses for dense and foamy slag in several cases. This data shows that for samples taken after the intense period of decarburization the FeO in the foamy slag has been depleted to about 75% of the original content. Consequently, the authors have chosen to use the decarburization

data and the residence time in either the foamy slag or the dense slag, to calculate the FeO depletion. This methodology is reflected in the development of equations from 5.A1, to 5.A2 and 5.A3 described in the Appendix.

5.3.2 Droplet Swelling Behavior at Different Temperature

By inspecting the recorded X-ray videos the change in the volume of droplets was determined as a function of time and temperature, as shown in Figure 5.3 for 0.007 and 0.014 wt% S droplets. Figure 5.3(a) shows that the incubation time for droplet swelling decreases from 8 seconds to approximately 2 seconds as temperature increases from 1813K to 1913 K for 0.007 wt% S droplets. The change in incubation time can be explained by surface poisoning of oxygen dissolution by sulfur. This effect weakens as the temperature increases because sulfur becomes less surface active at higher temperatures^[20-22]. Similar behavior is observed for droplets with 0.014 wt% S shown in Figure 5.3(b). Inspection of Figure 5.2 shows that the formation of CO goes through a slower period during the early stages of reaction. Comparison with Figures 5.3(a) and (b) shows that this slower period represents an “incubation period” for droplet swelling. This period has been attributed in the authors’ previous work to the time for the oxygen concentration in the droplet to build up and the internal nucleation of CO to become fully established^[6, 7, 23].

The volume for carbon free droplets (0.007 wt% S) at 1853 K was also plotted against time in Figure 5.3(c), showing that the volume of carbon free droplets remains relatively constant throughout the course of the experiment. This is expected due to the absence of CO evolution inside droplet. It is worth noting that although the shape of carbon free droplet was not changed significantly during reaction, it oscillated horizontally. This type of interfacial phenomena was somehow different from the emulsification observed in cases of carbon free liquid iron by Manning and Fruehan^[24], Assis *et al.*^[25] and Spooner *et al.*^[26]. The difference in behavior probably arises from the lower basicity slag employed in the present study; (wt% CaO/wt% SiO₂= 0.9) in the current work and between 1.7 and 3 in the work of Manning and Fruehan^[24], Spooner *et al.*^[26] and Assis *et al.*^[25]. Assis *et al.*^[25] and

Spooner *et al.* [26] also employed slag with Fe_2O higher than 30 wt% compared with 16 wt% FeO employed in current study.

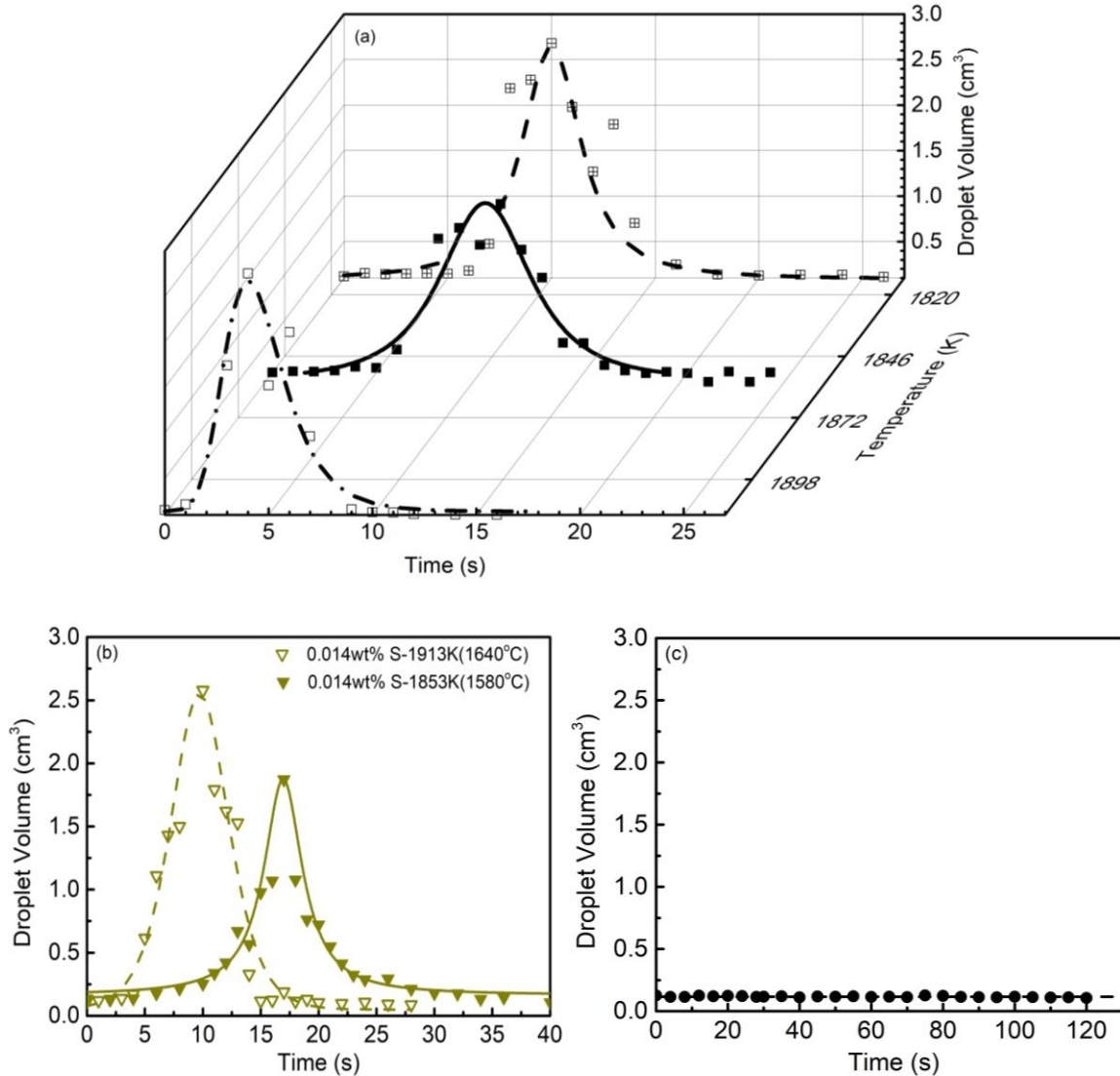
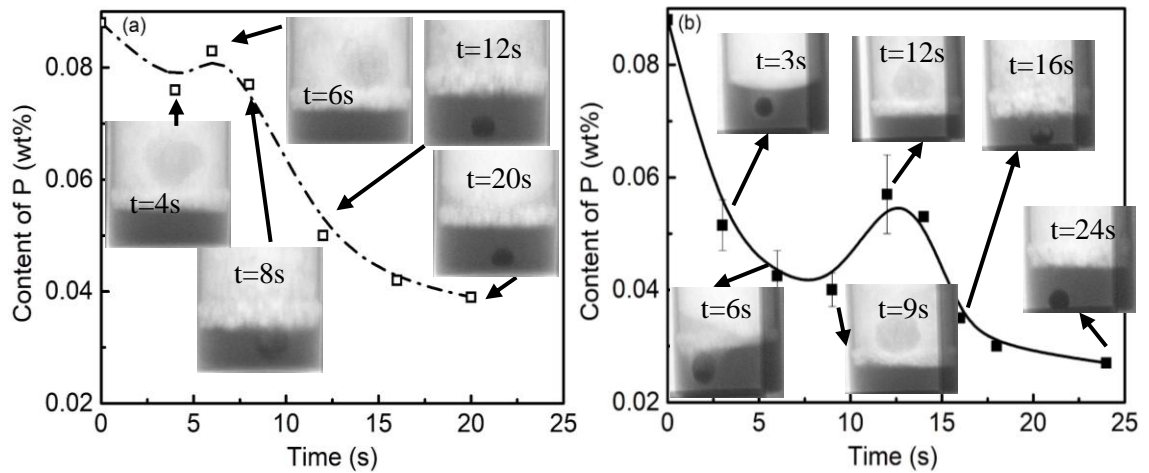


Figure 5.3 Swelling behavior of droplets: (a) 0.007 wt% S droplets at different temperature, (b) 0.014 wt% S droplets at different temperature and (c) C-free droplets (0.007 wt% S) at 1853 K.

For the relatively short reaction times which are the focus of this study, the mass of the droplet after an experiment is between 82% and 90% of the original mass. The diameter based on X-ray images ranges, over the course of an experiment, between 100% and 300% of the original. Quenched droplets are typically slightly larger than the original because of

retained gas, shown in Figure 5.6. Instead of measuring these parameters for every experiment, the authors determine the size of droplets as a function of time based on X-ray videos. It is worth noting that while the mass loss of the droplet may be interesting, it is difficult to be certain when and how the mass loss has occurred. From X-ray videos one can see a small number of extremely small metal droplets breaking away due to bubbles bursting through the surface. It is also known that the bloated droplets collapse during rapid cooling and it is believed that some of the droplet may break off at that point. The authors have accepted this uncertainty in the data, primarily because of the difficulty of quantifying the timing and the precise role of each mechanism of mass loss. This approach appears to be justified within the limitations of the technique, as the carbon content of metal droplets measured from LECO analysis agrees well with that determined from pressure transducer measurements ($\pm 10\%$ of carbon content). Dephosphorization of Droplets with and without Carbon

5.3.3 Dephosphorization of Droplets with and without Carbon



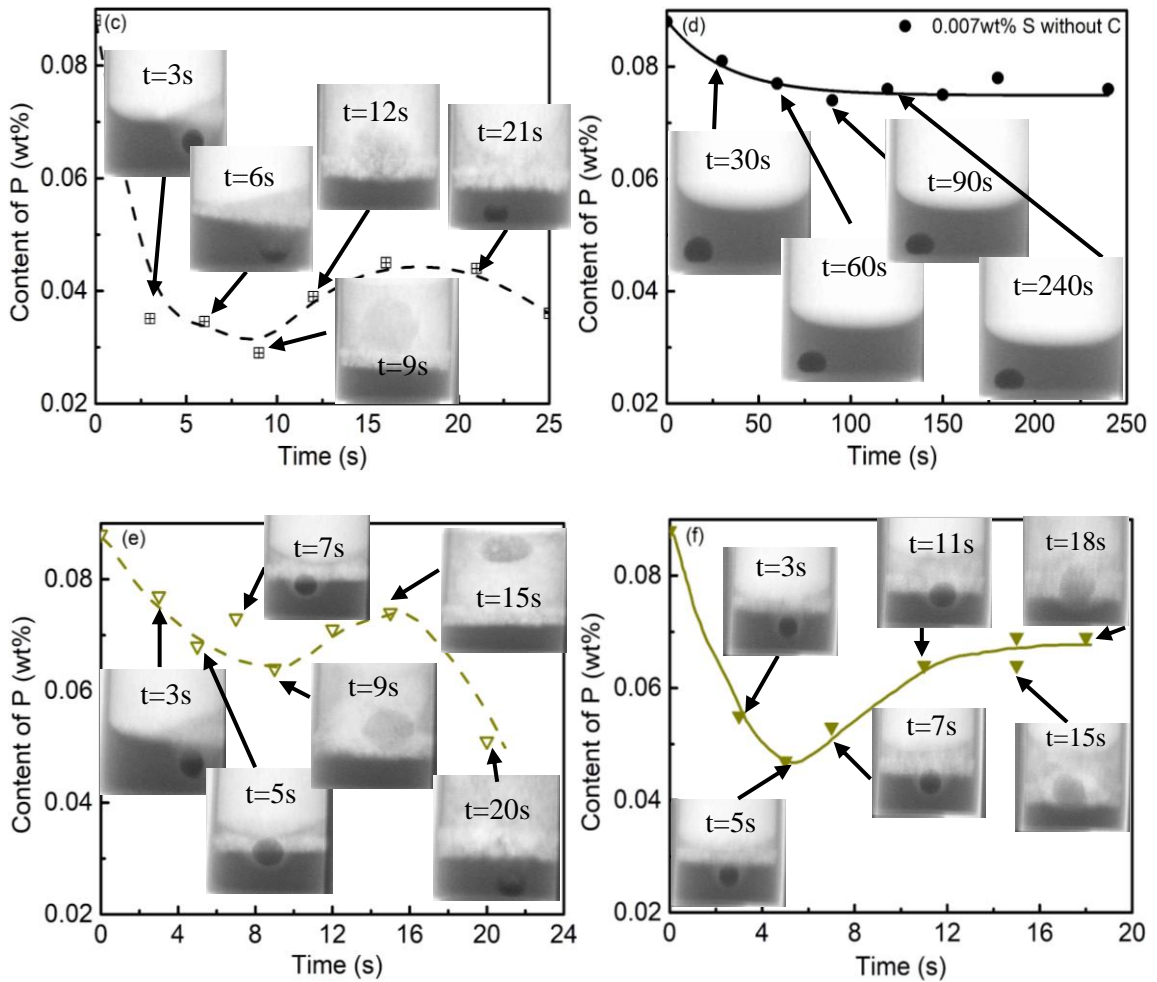


Figure 5.4 Plot of dephosphorization as a function of time: (a) 0.007 wt% S at 1913 K, (b) 0.007 wt% S at 1853 K, (c) 0.007 wt% S at 1813 K, (d) 0.007 wt% S C-free droplet at 1853 K, (e) 0.014 wt% S at 1913 K and (f) 0.014 wt% S at 1853 K.

The change of phosphorus content in metal droplets as a function of time for droplets with 0.007 and 0.014 wt% S under different temperatures is shown in Figure 5.4. Figures 5.4(a), (b) and (c) show the dephosphorization behavior of 0.007 wt% S droplets; all exhibit a complex dephosphorization-reversion-renewed dephosphorization behavior depending on their movement between the dense and foamy slag. This can be explained if one considers the difference of liquid volume and mass transfer coefficient between foamy slag and dense slag. Droplets are initially dephosphorized and at some point the oxygen potential at the interface is lowered to the extent that phosphorus is reduced back into the metal. This may occur because of a sudden increase in the rate of carbon oxidation, or because the slag

becomes depleted in FeO. In the current case when droplet bloating is initiated, the decarburization rate increases dramatically, then the droplet rises into the foamy slag. The smaller liquid slag volume in the foamy slag leads to more rapid depletion of FeO. The increase in the decarburization rate and the depletion of FeO may contribute to the phosphorus reversion. However, the extent of reversion will be limited by the liquid slag volume in the foam. When the decarburization rate subsides and the droplet sinks back into the dense slag, the droplet is reintroduced to a higher FeO slag. This higher FeO slag and the slower decarburization rate, will cause an increase in the interfacial oxygen potential which may result in renewed dephosphorization. Droplets with 0.014 wt% S show a similar behavior to 0.007 wt% S droplets as seen in Figures 5.4(e) and (f).

As observed in a previous study by the authors^[19] droplets with 0.007 wt% S experienced phosphorus reversion when metal droplets entered the foamy slag; while for droplets with 0.014 wt% S the reversion took place when the droplet was in transition between the dense and foamy slag. The dephosphorization behavior for a 0.007 wt% S droplet without carbon is also shown in Figure 4(d) where the time scale is more than one order of magnitude higher than for the other five cases where the droplet contained carbon. No phosphorus reversion is observed in Figure 5.4(d) because there was no carbon to deplete FeO. Compared to carbon containing droplets, the dephosphorization rate is much lower in the case of carbon-free droplets as shown in Figure 5.4(d).

5.4 Discussion

5.4.1 Dephosphorization Kinetics of Carbon Free Droplets

Given the relatively high FeO content in the dense slag offering a relative constant high driving force and the fast FeO transport in dense slag, (based on the authors' previous work^[17] k_{FeO} is 1.0×10^{-2} cm/s), the rate controlling step for carbon-free droplets is more likely to be mass transfer in metal phase. The integrated rate equation for phosphorus transfer in the metal can be expressed as Eq. (5.1):

$$\ln \left[\frac{[\text{wt}\% \text{ P}]_b - [\text{wt}\% \text{ P}]_e}{[\text{wt}\% \text{ P}]_o - [\text{wt}\% \text{ P}]_e} \right] \left(\frac{[\text{wt}\% \text{ P}]_o - [\text{wt}\% \text{ P}]_e}{[\text{wt}\% \text{ P}]_o} \right) \left(\frac{W_m}{\rho_m A} \right) = -k_m t \quad (5.1)$$

where W_m is the mass of the metal droplet, k_m is the mass transfer coefficient for phosphorus in the metal, ρ_m is the density of metal, $[\text{wt}\% \text{ P}]_o$, $[\text{wt}\% \text{ P}]_b$ and $[\text{wt}\% \text{ P}]_e$ are the initial, bulk and equilibrium concentration of phosphorus in the metal.

Setting $C = \frac{[\text{wt}\% \text{ P}]_b - [\text{wt}\% \text{ P}]_e}{[\text{wt}\% \text{ P}]_o - [\text{wt}\% \text{ P}]_e}$ and $B = \left(\frac{[\text{wt}\% \text{ P}]_o - [\text{wt}\% \text{ P}]_e}{[\text{wt}\% \text{ P}]_o} \right) \left(\frac{W_m}{\rho_m A} \right)$, Eq. (5.1)

becomes $B \ln C = -k_m t$.

The data shown in Figure 5.4(d) was plotted in Figure 5.5 according to Eq. (5.1). As seen in Figure 5.4(d), the phosphorus concentration $[\text{wt}\% \text{ P}]$ reaches a relatively constant value of 0.076 wt% after 90 seconds which was chosen as $[\text{wt}\% \text{ P}]_e$ in Eq. (5.1).

The slope of the line in Figure 5.5 represents the mass transfer coefficient of phosphorus in metal phase, k_m , which is 5.3×10^{-4} cm/s. This value for k_m is consistent with the value of 6.7×10^{-4} cm/s measured by Zheng *et al.* [24] at 1783 K and also shows a reasonable agreement with the finding from Rhamdhani *et al.* [25] where the mass transfer coefficients of Al in carbon free iron droplets was determined to be $1.3 \sim 1.9 \times 10^{-4}$ cm/s in the temperature range from 1823 K to 1923 K.

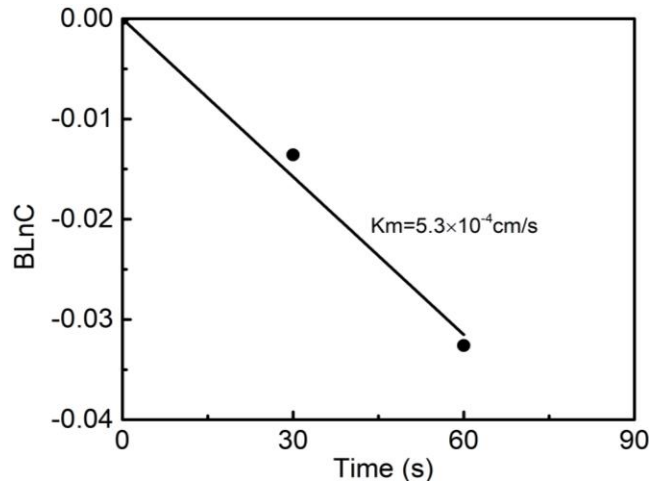


Figure 5.5 Dephosphorization data from Figure 5.4(d) is replotted as a function of time based on Eq. (5.1).

The mass transfer coefficient for phosphorus in the metal, k_m , for carbon free droplets at 1853 K is two orders magnitude lower than that determined in section 5.4.2 for droplets containing carbon under otherwise the same conditions. The high k_m values for carbon containing droplets appear to be related to the stirring provided by the formation of CO bubbles. Optical microscopy images of cross-sectioned droplets with and without carbon are shown in Figure 5.6. Figures 5.6(a) to (c) shows quenched samples of carbon containing droplets, which show a large fraction of large voids and many much smaller voids. These voids are the remnants of CO bubbles which appear to have collapsed and coalesced during quenching. No larger voids are observed in Figure 5.6(d) for carbon free droplets since CO evolution does not occur inside metal droplets, although some tiny voids are observed. This observation is consistent with the X-ray images.

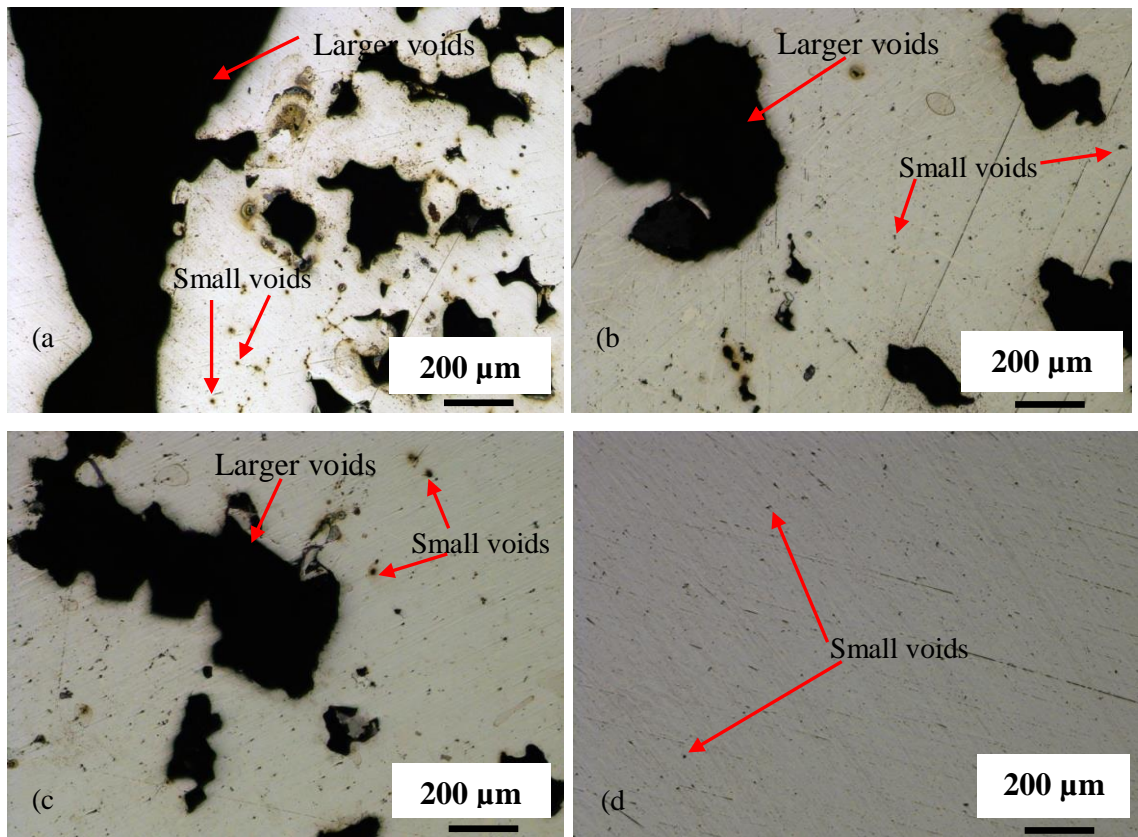


Figure 5.6 Cross-section view of quenched droplets: (a) 0.007 wt% S-1913 K, (b) 0.007 wt% S-1853 K, (c) 0.007 wt% S-1813 K and (d) 0.007 wt% S without C-1853 K.

5.4.2 Dephosphorization Kinetics of Carbon Containing Droplets

In previous work by the authors ^[19], it has been demonstrated that the rate of dephosphorization of bloated droplets prior to reversion was under mixed control by mass transfer in both metal and slag phase, as described by the following rate equation:

$$\left(\frac{W_m}{\rho_m A} \frac{1}{1 + \frac{W_m}{L_P W_s}} \right) \ln \left[\left(1 + \frac{W_m}{L_P W_s} \right) \frac{[\text{wt}\% \text{ P}]_b}{[\text{wt}\% \text{ P}]_o} - \frac{W_m}{L_P W_s} \right] = -k_o t \quad (5.2)$$

Using a similar approach to that for Eq. (5.1), setting $C = \left(1 + \frac{W_m}{L_P W_s} \right) \frac{[\text{wt}\% \text{ P}]_b}{[\text{wt}\% \text{ P}]_o} - \frac{W_m}{L_P W_s}$ and

$B = \left(\frac{W_m}{\rho_m A} \frac{1}{1 + \frac{W_m}{L_P W_s}} \right)$, Eq. (5.2) becomes $B \ln C = -k_o t$. In Eq. (5.2), k_o the overall mass

transfer coefficient with the units of cm/s is defined as:

$$k_o = \frac{1}{\frac{\rho_m}{k_s \rho_s L_P} + \frac{1}{k_m}} \quad (5.3)$$

where k_s and k_m are the mass transfer coefficients for phosphorus in the slag and metal, ρ_m and ρ_s are the densities of metal and slag, L_P is the phosphorus partition coefficient.

All data for carbon containing droplets shown in Figure 5.4 were plotted in Figure 5.7 according to Eq. (5.2). It is worth noting that as most of the dephosphorization is over within a few seconds, it is difficult to obtain enough data for meaningful kinetic plots as shown in Figure 5.7 with only two data points in some curves. The authors acknowledge this weakness, however, the data presented in Figure 5.7 show a remarkably consistent pattern where k_o decreases as temperature rises in the case of both 0.007 and 0.014 wt% S droplets. The value of k_o drops by one order of magnitude as temperature increases from 1813 K to 1913 K.

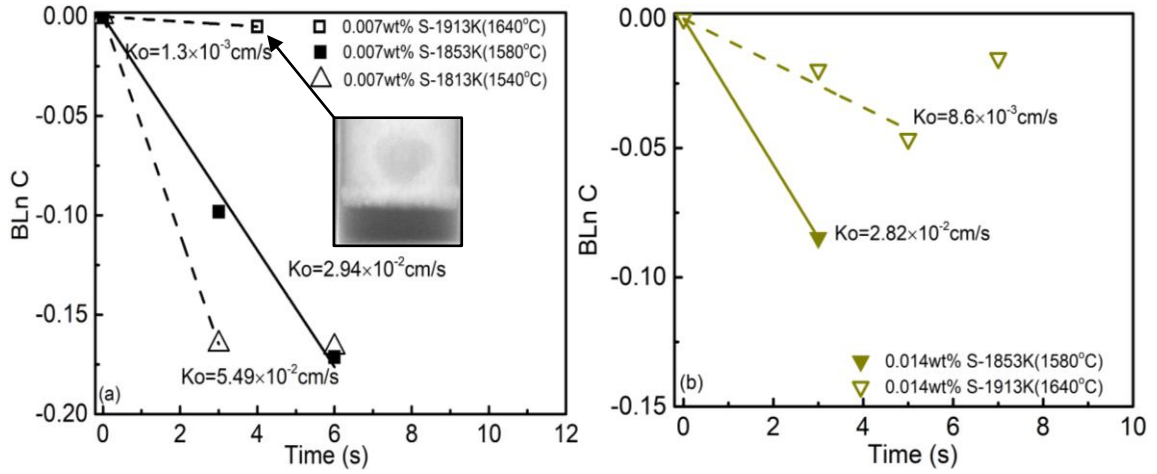


Figure 5.7 Dephosphorization data from Figure 5.4 are replotted as a function of time for different temperature based on Eq. (5.2): (a) 0.007 wt% S and (b) 0.014 wt% S.

Temperature affects three terms in Eq. (5.3), *i.e.*, k_s , L_P and k_m , leading to a change of k_o . In order to determine the most significant factor, the effects of temperature on k_s , L_P and k_m are evaluated in the following section.

It is well known that the diffusivity in liquids is proportional to temperature but inversely proportional to viscosity according to the Stokes-Einstein and the Eyring equations:

$$D \propto \frac{T}{\eta} \quad (5.4)$$

Combining Higbie's penetration theory^[29] with Eq. (5.4), one can obtain

$$k_s \propto \left(\frac{T}{\eta}\right)^{1/2} \quad (5.5)$$

Therefore, knowing the viscosity of the slag as a function of temperature and the mass transfer coefficient, k_s , at one temperature, the values at other temperatures can be estimated. As shown in Figure 5.4, droplets with 0.007 wt% S and 0.014 wt% S are primarily dephosphorized in the dense slag except for the case of 0.007 wt% S at 1913 K which had the shortest incubation time. That special case will be discussed later. Assuming k_{FeO} is a reasonable estimate for k_s , data obtained from previous work by the authors may be employed. In the authors' previous work^[14], k_{FeO} in the dense slag was

calculated to be 1.0×10^{-2} cm/s at 1853 K. Determining the viscosity of slag for different temperatures using Factsage 6.4™ employing the Melts database, k_{FeO} under different temperatures was calculated and listed in Table 5.1. It shows that the temperature effect on mass transfer coefficient k_{FeO} is negligible.

Table 5.1 Calculated k_{FeO} at different temperature.

T/K	η /(poise)	$k_{FeO} \times 10^2$ /(cm/s)	Initial L_P
1813	1.81	0.92	18
1853	1.49	1.01	13
1913	1.11	1.18	8

The initial value of L_P determined using Eq. (5.7) in combination with a method developed by the authors^[14] to determine the interfacial oxygen potential is also presented in Table 5.1. For completeness, this method, based on balancing the oxygen supply from reducible oxides in the slag and oxygen consumption by alloying elements in the metal, is described in detail in the Appendix. The data presented in Table 5.1 shows that the initial L_P decreases with increasing temperature. The phosphorus partition coefficient at the reversion point taken from Figure 5.4 is presented in Figure 5.8 as a function of temperature, which includes results from the work of Mori *et al.*^[30] They investigated dephosphorization between liquid iron (Fe-3.6 wt% C-0.1 wt% P) and slag containing FeO. The related experimental conditions in their work including decarburization rate are listed in Table 5.2. In addition, the current authors have added viscosities of different slags calculated using Factsage 6.4™ and maximum L_P calculated from reversion points as expressed in Eq. (5.6).

$$L_P = \frac{(\text{wt}\% \text{ P})_{\text{max.}}}{[\text{wt}\% \text{ P}]_{\text{min.}}} \quad (5.6)$$

Table 5.2 Slag compositions (wt%) and extracted results from Mori *et al.* [30]

No.	T/K	CaO	SiO ₂	FeO	NaCl/(g)	η /(poise)	Max. L_P	Initial L_P	DeC. rate $R \times 10^4 / (\text{mole/s})$
A4	1583	34.2	35.6	27.8		1.97	11.4	380.1	8.80
A5	1573	34.2	35.6	27.8	1.0	1.21	32.2	270.1	8.84
B9	1653	44.3	41.8	13.8		2.71	1.2	292.0	9.43
B10	1653	44.3	41.8	13.8	2.0	0.95	9.0	116.6	13.6
C6	1733	40.7	40.2	18.0		1.39	2.2	112.2	10.0
C7	1723	40.7	40.2	18.0	1.0	0.93	3.2	76.8	11.8

Knowing $P_{O_2}^i$ at $t=0$, the initial L_P ($t=0$) can be calculated based on Eqs. (5.7) and (5.8). The initial L_P in the case of Mori *et al.* [30] were calculated and also listed in Table 5.2.

$$L_P = \frac{(\text{wt}\% \text{ P})_i}{[\text{wt}\% \text{ P}]_i} = \frac{C_{PO_4^{3-}} - P_{O_2}^i}{K_P M_{PO_4^{3-}}} f_P M_P^{5/4} \quad (5.7)$$

where $C_{PO_4^{3-}}$ is the phosphate capacity of the slag, f_P is the Henrian activity coefficient for phosphorus in the metal, M_P and $M_{PO_4^{3-}}$ are the molar mass of phosphorus and phosphate respectively, K_P is the equilibrium constant for the dissolution of phosphorus gas in steel.

In this study, phosphate capacity was determined based on the following correlation [31]:

$$\log C_{PO_4^{3-}} = 17.55 \Lambda + \frac{51670}{T} - 21.867 \quad (5.8)$$

where Λ represents the theoretical optical basicity of slag, optical basicity values for individual oxides were taken from the literature [32].

Eq. (5.7) assumes that the activity coefficient of P_2O_5 is independent of P_2O_5 concentration. Turkdogan^[33] demonstrated that at low concentrations of P_2O_5 (up to 1 wt%) the activity coefficient is independent of temperature. In the current work although the maximum concentration of P_2O_5 in the slag is less than 0.02 wt% the authors have accepted the temperature dependence proposed by Mori *et al.*^[31], which has been well validated by experimental data.

In a study of dephosphorization equilibria between liquid iron and highly basic CaO-based slags saturated with MgO, Ishii and Fruehan^[34] investigated the effect of Al_2O_3 additions by correlating the phosphate capacity of the slags with the theoretical optical basicity using Mori's correlation^[31]. Although the theoretical optical basicity for slags used by Ishii and Fruehan^[34] was higher than 0.73, the results fitted were well represented by Mori's correlation^[31], which was obtained in the range of optical basicity from 0.53 to 0.73. In a similar study to Ishii and Fruehan^[34], Li *et al.*^[35] investigated the effect of Na_2O and Al_2O_3 on dephosphorization of molten steel using high basicity MgO saturated CaO- FeO_x - SiO_2 slag. They proposed a correlation that was qualitatively consistent with Mori's correlation but predicted phosphate capacities which were an order of magnitude higher. Based on these observations and the agreement of Mori's correlation^[31] for similar slag compositions to those in the current work, the authors have chosen to employ Eq. (5.8).

Figure 5.8 shows that the temperature coefficient of L_P for this study is different from that found in the work of Mori *et al.*^[30] By examining Eq. (5.7), for a given slag composition the only term for which the temperature dependency could change with specific circumstances is interfacial oxygen potential which decreases as decarburization proceeds. Although $\log C_{PO_4^{3-}}$ changes significantly with temperature, the deviation of temperature coefficient of L_P probably arises from the effect of decarburization.

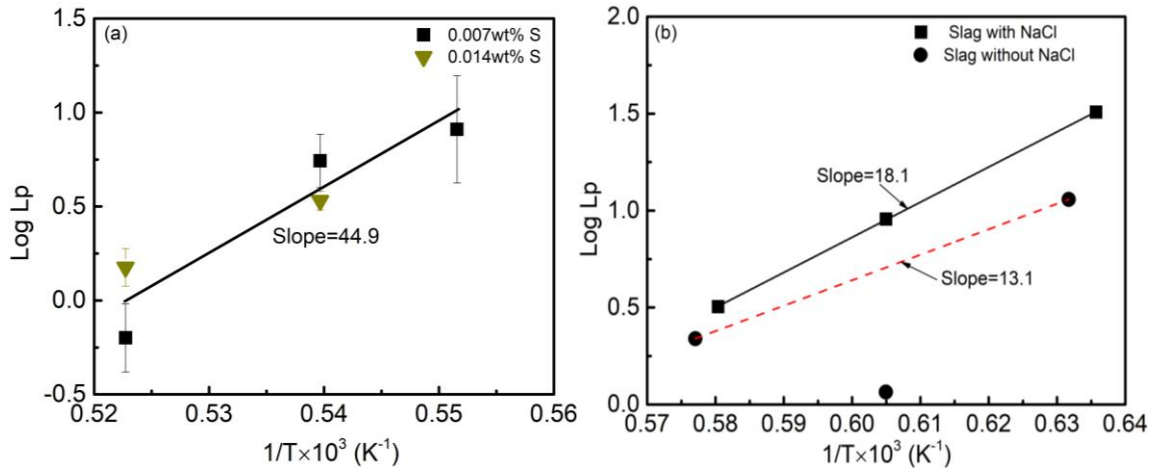


Figure 5.8 The effect of temperature on phosphorus partition coefficient (L_p) at the reversion point: (a) this study and (b) calculated results for the case of Mori *et al.* [30]

In order to understand the reason for the different temperature coefficients of L_p in this study and that of Mori *et al.* [30], the decarburization rate as a function of temperature for each of these studies is plotted in Figure 5.9 according to an Arrhenius type expression, where N_{CO} is the maximum decarburization rate. The data for 0.007 wt% S droplets show a very good fit to the Arrhenius relationship, with apparent activation energy of 118 kJ/mol. This figure also shows an apparent activation energy of 34.1 kJ/mol for the case of Mori *et al.* [30], which is approximately one quarter of the value found in this study.

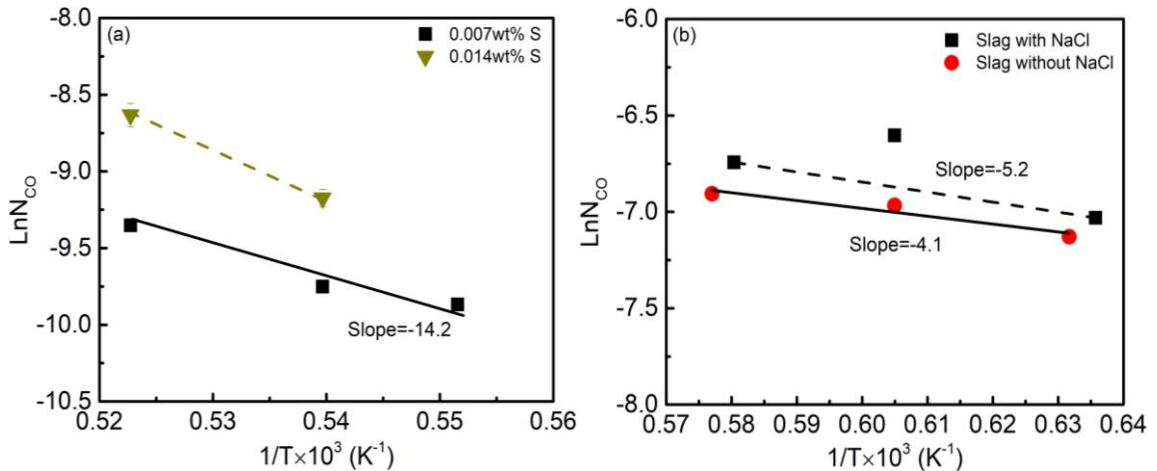


Figure 5.9 Decarburization rate as a function of temperature: (a) this study and (b) calculated results based on the work of Mori *et al.* [30]

Taking the logarithm of Eq. (5.7) and separating each term, one can obtain:

$$\log L_P = \log C_{PO_4^{3-}} + \frac{5}{4} \log P_{O_2}^i - \log K_P + \log D \quad (5.9)$$

where $D = \frac{f_P M_P}{M_{PO_4^{3-}}}$, all are constants at given temperature.

The effect of each term in Eq. (5.9) on the temperature dependency of $\log L_P$ can be expressed as Eq. (5.10).

$$\frac{\partial \log C_{PO_4^{3-}}}{\partial \frac{1}{T}} = \frac{\partial \log L_P}{\partial \frac{1}{T}} - \frac{5}{4} \frac{\partial \log P_{O_2}^i}{\partial \frac{1}{T}} + \frac{\partial \log K_P}{\partial \frac{1}{T}} \quad (5.10)$$

According to Eq. (5.10), the sum of right hand side (RHS) should be similar for this study and that of Mori *et al.* [30], and equal to $\frac{\partial \log C_{PO_4^{3-}}}{\partial \frac{1}{T}}$, which is the same for all the slag. The temperature coefficient of interfacial oxygen potential can be estimated based on Eqs. [5.A3] (developed in the Appendix), (5.11) and (5.12):

$$\log P_{O_2}^i = 2 \log \left[\frac{\gamma_{FeO} K_{Fe}}{C_s a_{Fe}^i K_O} \left(C_{FeO}^o - \frac{1}{V_S} \int_{n_{CO,t=0}}^{n_{CO,t=t}} dn_{CO} - \frac{1}{A} \frac{1}{k_{FeO}} \frac{dn_{CO}}{dt} \right) \right] = 2 \log \left(\frac{\gamma_{FeO} K_{Fe}}{C_s a_{Fe}^i K_O} \right) + 2 \log \left(C_{FeO}^o - \frac{1}{V_S} \int_{n_{CO,t=0}}^{n_{CO,t=t}} dn_{CO} - \frac{1}{A} \frac{1}{k_{FeO}} \frac{dn_{CO}}{dt} \right) \quad (5.11)$$

$$\frac{\partial \log P_{O_2}^i}{\partial \frac{1}{T}} = 2 \frac{\partial \log \left(\frac{\gamma_{FeO} K_{Fe}}{C_s a_{Fe}^i K_O} \right)}{\partial \frac{1}{T}} + 2 \frac{\partial \log \left(C_{FeO}^o - \frac{1}{V_S} \int_{n_{CO,t=0}}^{n_{CO,t=t}} dn_{CO} - \frac{1}{A} \frac{1}{k_{FeO}} \frac{dn_{CO}}{dt} \right)}{\partial \frac{1}{T}} \quad (5.12)$$

Setting $E = \frac{\partial \log \left(\frac{\gamma_{FeO} K_{Fe}}{C_s a_{Fe}^i K_O} \right)}{\partial \frac{1}{T}}$ and $F = \frac{\partial \log \left(C_{FeO}^o - \frac{1}{V_S} \int_{n_{CO,t=0}}^{n_{CO,t=t}} dn_{CO} - \frac{1}{A} \frac{1}{k_{FeO}} \frac{dn_{CO}}{dt} \right)}{\partial \frac{1}{T}}$, one can estimate $E \approx$

$\frac{\partial \log(K_{Fe})}{\partial \frac{1}{T}} - \frac{\partial \log(K_O)}{\partial \frac{1}{T}} = -12.5$ from the reported thermodynamic data [36], which is same for

this study and the case of Mori *et al.* [30] In present study, $C_{FeO}^o = 6.68 \times 10^{-3}$ mol/cm³,

$\frac{1}{V_S} \int_{n_{CO,t=0}}^{n_{CO,t=t}} dn_{CO}$ is less than 4.5×10^{-5} mol/cm³ estimated from Figure 5.2 from time

zero to the time of phosphorus reversion for all the cases.

Then this term $C_{FeO}^o - \frac{1}{V_S} \int_{n_{CO,t=0}}^{n_{CO,t=t}} dn_{CO}$ can be viewed as constant C . Knowing that $\ln(N_{CO}) = \frac{a}{T} + b$ from Figure 5.8 and the fact that k_{FeO} shows a negligible dependency on temperature established in earlier discussion, one can work out that term F is essentially equal to $\frac{\partial \log \left(C \frac{1}{Ak_{FeO}} \frac{dn_{CO}}{dt} \right)}{\partial \frac{1}{T}} \approx -\frac{\partial \ln(N_{CO})}{\partial \frac{1}{T}}$. Assuming this approach is also valid in the work of Mori *et al.* [30], then the value of each term in Eq. (5.10) can be determined by taking the slopes from Figures 5.8 and 5.9, and these are listed in Table 5.3.

Table 5.3 Determined temperature coefficients for terms in Eq. (5.10).

	$\frac{\partial \log C_{PO_4^{3-}}}{\partial \frac{1}{T}}$	$\frac{\partial \log L_P}{\partial \frac{1}{T}}$	$\frac{\partial \log P_{O_2}^i}{\partial \frac{1}{T}}$	$\frac{\partial \log K_P}{\partial \frac{1}{T}}$	Sum of RHS
This study	51.7	44.9	3.4	8.2	48.9
Mori <i>et al.</i> [30]	51.7	18.1	-14.6	8.2	44.6

From Table 5.3, it can be seen that the sum of RHS of Eq. (5.10) are identical for this study and that of Mori *et al.* [30] and essentially equal to $\frac{\partial \log C_{PO_4^{3-}}}{\partial \frac{1}{T}}$, which shows that the deviation of temperature coefficient of L_P is related to the temperature effect on decarburization and thereby on oxygen potential.

5.4.3 Estimation of k_m at Different Stages of Reaction

Knowing k_o , L_P , k_{FeO} at different temperatures, it is worth employing Eq. (5.3) to calculate k_m under different temperatures. In the current study although L_P decreases as the reaction proceeds, the initial L_P may still reasonably be used to estimate the mass transfer coefficient during the initial stages of reaction because as shown in Figure 5.10.

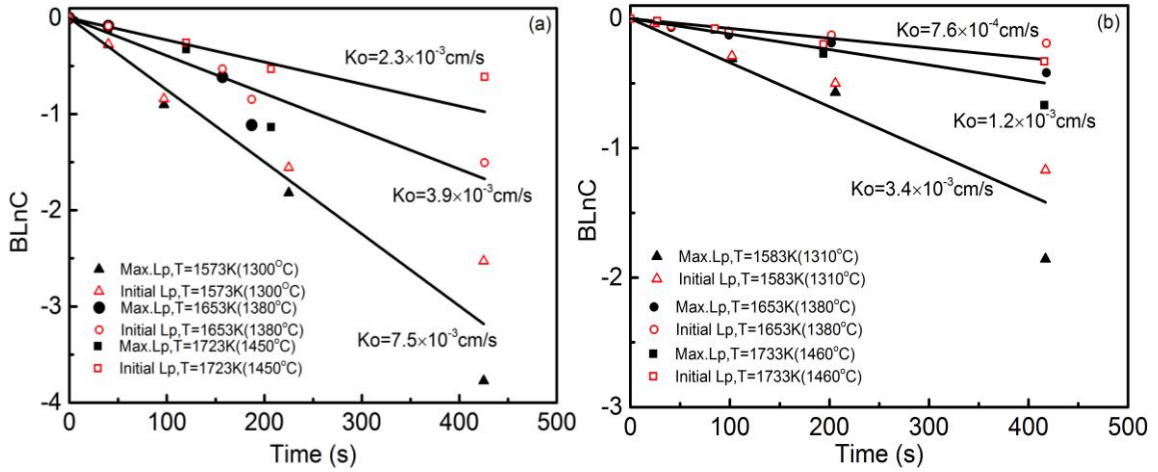


Figure 5.10 Dephosphorization as a function of time and temperature plotted according to Eq. (5.2) using the data in the work of Mori *et al.* [30]: (a) slag with NaCl and (b) slag without NaCl.

The dephosphorization data from the work of Mori *et al.* [30] under the experimental conditions listed in Table 5.2, were reproduced and replotted in Figure 5.10 according to Eq. (5.2). The open data points were calculated using initial L_P while the solid data points were obtained using maximum L_P . It shows that at the initial stage of reaction the data calculated based on initial L_P and maximum initial L_P overlap and can be fitted by a single line, which suggest that initial L_P can be used to determine the mass transfer coefficient without any significant loss of precision. k_m determined from k_o for a range of conditions is presented in Table 5.4 for this study and in Table 5.5 for the case of Mori *et al.* [30]

Table 5.4 Mass transfer coefficients calculated from experimental data.

T/K	$k_o \times 10^2 / (\text{cm/s})$ using max. $L_P - 0.007$ wt% S	$k_o \times 10^2 / (\text{cm/s})$ using Initial L_P	$k_m \times 10^2 / (\text{cm/s}) -$ 0.007 wt% S	$k_o \times 10^2 / (\text{cm/s})$ using max. $L_P - 0.014$ wt% S	$k_m \times 10^2 / (\text{cm/s}) -$ 0.014 wt% S
1813	5.49	3.32	24.57		
1853	2.94	2.25	6.16	2.82	5.65
1913	0.13	0.12	0.13	0.86	1.10

Table 5.5 Mass transfer coefficients for the case of Mori *et al.* [30]

No.	T/K	$k_o \times 10^3/(cm/s)$	$k_m \times 10^3/(cm/s)$
A4	1583	3.4	3.4
A5	1573	7.5	7.5
B9	1653	0.8	0.7
B10	1653	3.9	4.1
C6	1733	1.2	1.2
C7	1723	2.3	2.3

Tables 5.4 and 5.5 show that the temperature has a strong effect on k_m in this study and the case of Mori *et al.* [30] where k_m decreases with increasing temperature. This result is contradicted by the general observation that mass transfer coefficients are usually slightly increased as temperature rises. This contradiction appears to arise from the stirring effect introduced by the formation of CO bubbles inside the droplet, which varies with temperature.

In this study, k_m can be estimated based on Higbie's penetration theory [29] which is expressed as:

$$k_m = 2\left(\frac{D\mu}{\pi d}\right)^{1/2} \quad (5.13)$$

where D is diffusivity (cm^2/s), of phosphorus in this case [37], μ represents the velocity of the gas, which is CO evolution rate per unit area (cm^3/cm^2s) and d is the average diameter of the CO bubbles (cm).

According to Eq. (5.13), if the size of CO bubbles is assumed to be independent of temperature within the temperature range investigated, one should expect a larger k_m at higher temperature due to the higher decarburization rate. Again this is contradicted by the

results in Tables 5.4 and 5.5. Therefore the only possible explanation is that the size of CO bubbles is smaller at lower temperature, leading to a faster surface renewal rate as predicted by Eq. (5.13), thereby offering a higher, k_m , which will be addressed in detail in section 5.4.4.

The behavior of the droplets in this study is complex; the metal droplets first spent a short incubation time in dense slag before they bloat and float into the foamy slag, then, as bloating subsides, they sink back into the dense slag again. During this cycle, the control for dephosphorization changes from transport in both slag and metal to transport in the slag. The mixed control case has been evaluated in recent publications by the authors^[14, 19]. To acquire a complete picture of droplet refining, it is necessary to estimate the phosphorus mass transfer coefficient in the metal phase, k_m , at different stages, *i.e.*, high decarburization rates (bloomed droplet) and low decarburization rates (dense droplet). At 1913 K k_m for 0.007 wt% S droplets seems unreasonably low compared with that for droplets with 0.014 wt% S especially if one consider those two have similar k_o and k_m values at 1853 K, as shown in Table 5.4. Inspection of X-ray images reveals that the metal droplet is floating in the foamy slag as shown in Figure 5.7, which suggests that k_o in the case of 0.007 wt% S droplet at 1913 K represents, or at least partially represents, mass transfer in foamy slag. This would lead to an error in determining k_m based on the assumption of a k_s value representative of dense slag. To make a more reasonable estimate of k_m , it is possible to make use of the similarity between mass transport in the metal for the 0.007 wt% and 0.014 wt% S cases. Table 5.4 shows that k_m for 0.007 wt% S droplets (6.16×10^{-2} cm/s) and 0.014 wt% S droplets (5.65×10^{-2} cm/s) are similar at 1853 K, *i.e.*, $\left(\frac{\mu}{d}\right)_{0.007 \text{ wt\% S}}^{1/2} \approx \left(\frac{\mu}{d}\right)_{0.014 \text{ wt\% S}}^{1/2}$ according to Eq. (5.13). If one assumes the same relationship exists at 1913 K, the initial k_m of dense droplet in the case of 0.007 wt% S droplet can be recalculated to be 1.60×10^{-2} cm/s by knowing CO gas evolution rate from Figure 5.2. This recalculated value was listed in Table 5.6, which also includes parameters used to estimate k_m for bloated droplets in the foamy slag based on Eq. (5.13). The initial value of k_m for a dense droplet based on Figure 5.7 is also presented in Table 5.6.

Table 5.6 Parameters for calculating k_m of 0.007 wt% S bloated droplets in the foam.

Parameter	1813 K	1853 K	1913 K
Initial DeC. rate $\times 10^5$ /(mol/s)	2.47	2.73	6.52
Peak DeC. rate $\times 10^5$ /(mol/s)	5.18	5.82	7.28
End DeC. rate $\times 10^5$ /(mol/s)	0.1~1.0	0.1~1.2	0.1~1.0
Initial average A/(cm ²)	1.32	1.40	1.56
Peak average A/(cm ²)	7.71	6.87	7.67
End average A/(cm ²)	1.32	1.51	1.37
Diffusivity $\times 10^2$ /(cm ² /s) ^[37]	1.33	1.33	1.33
$k_m \times 10^2$ /(cm/s) of bloated droplet	14.7	4.05	1.33
Initial $k_m \times 10^2$ /(cm/s) of dense droplet	24.6	6.16	1.60*

*Recalculated value based on Eq. (5.13).

The calculated values of k_m for bloated droplets in foamy slag shows that if one assumes no growth of CO bubbles during the course of the experiment, k_m in foamy slag is slightly smaller than the initial k_m for dense droplets due to the larger surface area as shown in Table 5.6. Although the bloated droplets have higher decarburization rate, the effect of increased surface area off-sets the affect of higher CO generation rate.

From Figures 5.4(a), (b), (c) and (e), it can be seen that metal droplets experienced renewed dephosphorization on falling back into the dense slag, especially in the case of Figure 5.4(a) and (b). In both of these cases, there is sufficient data to analyze the kinetics of this second period of dephosphorization. Since the droplet continued to form CO gas as it sank

into the dense slag, it is reasonable to assume that the reaction of dephosphorization was controlled by mass transfer in both metal and slag phase but without the depletion of FeO due to the relative lower decarburization rate as shown in Table 5.6. Therefore, the data from Figure 5.4(a) and (b) from the point where renewed dephosphorization starts are replotted in Figure 5.11 based on Eq. (5.2). The time plotted starts from the time the droplet is estimated to have dropped back into the dense slag. The initial phosphorus was taken at the same time.

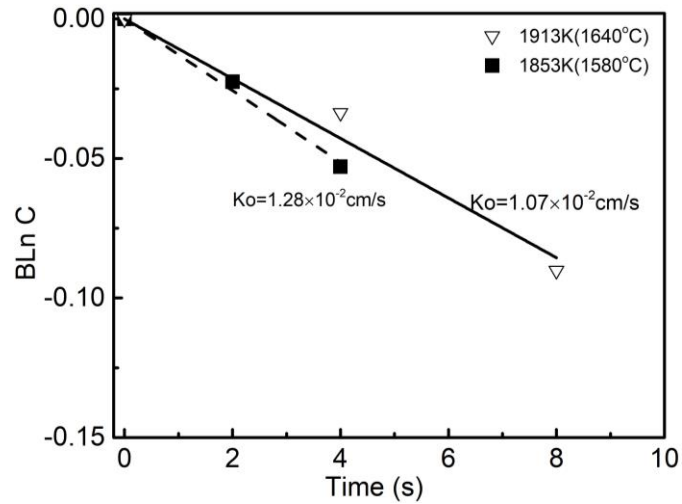


Figure 5.11 Re-dephosphorization data from Figures 5.4(a) and (b) are replotted as a function of time via Eq. (5.2).

After the droplet sinks back into the dense slag, the rate controlling step for dephosphorization shifts to mass transfer in both metal and slag phase again. This shift is due to the higher concentration of FeO in dense slag, leading to a relative higher k_o , *i.e.*, 1.07×10^{-2} and 1.28×10^{-2} cm/s. Knowing the k_{FeO} and L_p for dense slag listed in Table 5.1, k_m during the final stage for droplets with 0.007 wt% S was calculated and is shown in Table 5.7.

Table 5.7 Calculated k_m at different stages.

T/K	$k_m \times 10^2$ /(cm/s) at initial stage	$k_m \times 10^2$ /(cm/s) in the foam	$k_m \times 10^2$ /(cm/s) at final stage
1813	24.6	14.7	
1853	6.16	4.05	1.66
1913	1.60*	1.33	1.46

*Recalculated value based on Eq. (5.13).

Table 5.7 shows that k_m at the final stage of reaction is lower than that during the incubation period for decarburization, due to the weaker stirring in the final stage with much lower decarburization rate as shown in Table 5.6. For example at 1853 K, the decarburization rate during the initial stage is approximately 4 times higher than the average value at the end, which would lead to a higher k_m value by at least a factor of 2 according to Eq. (5.13). That is to some extent consistent with the results in Table 5.7, *i.e.*, k_m is 6.16×10^{-2} cm/s at initial stage and 1.66×10^{-2} cm/s at the end.

All mass transfer coefficients including k_o , k_m and k_{FeO} are summarized in Figure 5.12, which shows that during the life of a bloated droplet the controlling step for dephosphorization changes. In dense slag corresponding to initial dephosphorization stage and re-dephosphorization stage, the rate is under mixed control by mass transfer in both metal and slag phase at which k_o sits in the range between k_m and k_s , except for the case of initial dephosphorization at 1913 K where the value of k_o is lower and close to k_s . One possible explanation for the latter observation, is that since the measured k_o for this case shown in Figure 5.7(a) does not represent k_o for initial dephosphorization in dense slag as it does for the other conditions, but is based on the renewed dephosphorization which might alter the values of both k_s and k_m . The overall mass transfer coefficient k_o is slightly higher during the initial stage of dephosphorization compared with renewed dephosphorization which occurs when the decarburization reaction is almost over. This observation may be attributed the larger mass transfer coefficient for phosphorus in the metal caused by the higher decarburization rate during the initial period. While in the

foamy slag, the rate control is found to be mass transfer in the slag at which k_o is approximately equal to k_{FeO} in the foamy slag. The shift to control by mass transport in the slag may be attributed to the low phosphorus partition caused by the combined effect of a lower k_{FeO} in the foamy slag, depletion of FeO in the limited liquid volume of the foamy slag and the high decarburization rate associated with bloating. These factors would lead to the rate controlled by mass transport in the slag. In the present case we have assumed that $k_{FeO} = k_s$, however it seems unlikely that the mass transport of phosphate in the slag would be as fast as that of oxygen (nominally treated as FeO). In the absence of a better estimation we have chosen to use k_{FeO} .

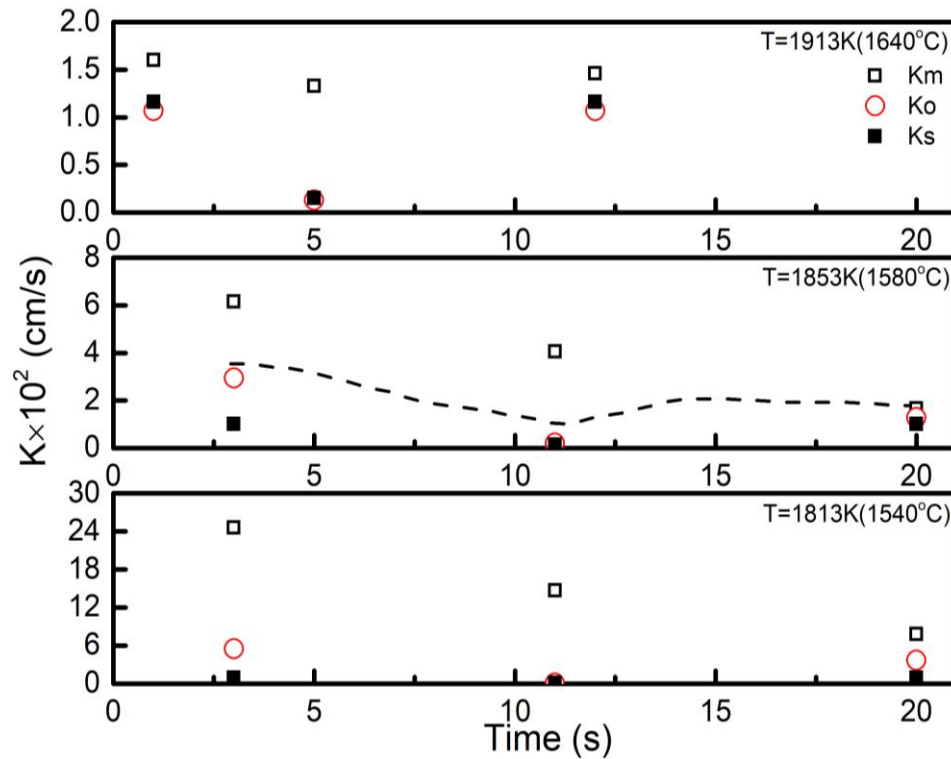


Figure 5.12 Mass transfer coefficients for the whole life of bloated droplet.

The dash line in Figure 5.12 shows the calculated pathway of overall mass transfer k_o during the reaction. k_o is initially high but first decreases due to the decreasing of interfacial oxygen potential as decarburization proceeds and the metal droplet moves from the dense slag to foamy slag. This stage has been successfully modeled, at a single

temperature, in previous work by the authors [14]. That work shows excellent agreement with the current results. It should be recognized that in the case of droplets in a real BOF the slag will be foamy for the residence time of the droplet, and over the life of an individual droplet the FeO content of the slag will remain essentially constant. These factors will change the trajectory of k_o presented in Figure 5.12 however the insights developed in this work and the data obtained should be sufficient to allow prediction of dephosphorization for a droplet by droplet basis in a kinetic model of the BOF. On going work in the authors' laboratory is aiming to embed the current kinetic data in a holistic model of the BOF.

5.4.4 The Effect of Temperature on k_m

Based on the above discussion, the only possible explanation for the higher k_m at lower temperature in this study is that the CO bubbles are smaller at lower temperatures, leading to a faster surface renewal rate as predicted by Eq. (5.13), thereby offering a higher k_m . For the nucleation of CO bubbles, the relationship between the pressure inside the critical nucleus and its' radius r^* can be estimated from Young-Laplace equation:

$$\Delta P = (P_{ve} - P_l) = \frac{2\sigma}{r^*} \quad (5.14)$$

where in the case of CO bubble nucleation, P_{ve} is the pressure in the bubble at equilibrium (supersaturation pressure), P_l is the liquid pressure (1 atm), σ represents the surface tension of liquid metal, r^* is the radius of critical nucleus. Due to the high supersaturation pressure for CO nucleation, $(P_{ve} - P_l) \approx P_{ve}$. It is worth noting that there is no change in ferrostatic pressure in the current work. In the BOF, the atmospheric pressure in the vessel may change with time. However, the supersaturation pressure based on calculated activities of carbon and oxygen is about 125 atm which will render any pressure change in a real BOF negligible.

If the formation of CO bubbles follows reaction (5.15) [36],



$$\Delta G^o = -22200 - 38.34T \text{ (J/mol)} \quad (5.16)$$

Then the equilibrium constant can be written as:

$$K_{CO} = \frac{P_{ve}}{h_C h_O} \quad (5.17)$$

where h_C and h_O are the Henrian activity of carbon and oxygen in liquid metal.

Combing Eqs. (5.15) and (5.17), one can obtain,

$$r^* = \frac{2\sigma}{K_{CO} h_C h_O} \quad (5.18)$$

Considering the negligible temperature effect on activity of carbon and oxygen for a given metal composition based on the calculation using reported interaction parameters [36], the change of CO bubble critical size mainly arises from the change of the equilibrium constant. According to Eq. (5.18), as temperature increases the equilibrium constant, K_{CO} , decreases. The surface tension for liquid iron containing sulfur also increases with temperature. Both the aforementioned effects lead to a larger critical radius. The smaller CO bubbles which form at lower temperature offer a faster surface renewal thereby leading to a higher mass transfer coefficient as observed in Table 5.7.

Combining Eqs. (5.13) and (5.18), the following equation can be derived:

$$k_m = \left(\frac{h_C h_O D \mu}{\pi \sigma} K_{CO} \right)^{1/2} \quad (5.19)$$

k_m is plotted in Figure 5.13 according to an Arrhenius type expression based on the values presented in Tables 5.7 and 5.5 for this study and the case of Mori *et al.* [30]

It can be seen that in Figure 5.13, the apparent activation energy in this study is approximately 5 times higher than that from the work of Mori *et al.* [30] This result is consistent with the results from Figure 5.8 where the apparent activation energy for decarburization in this study is 4 times higher than that in the case of Mori *et al.* [30]

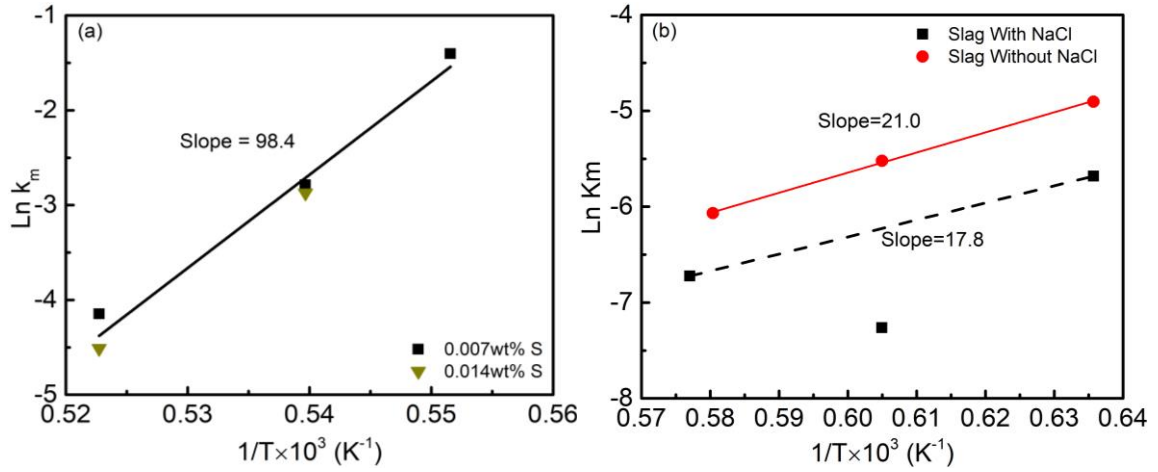


Figure 5.13 The plot of k_m as a function of temperature: (a) this study, (b) calculated results based on the work of Mori *et al.* [30]

Again, taking the logarithm of Eq. (5.19) and separating each term, one can obtain:

$$\ln k_m = \frac{1}{2} (\ln K_{CO} + \ln \mu - \ln \sigma + \ln D + \ln P) \quad (5.20)$$

where $P = \frac{hc h_0}{\pi}$ is assumed to be a constant since the change of h_c , h_0 with temperature is negligible in comparison to the other terms considered in Eq. (5.20).

The relationship between the temperature dependencies of all terms in Eq. (5.20) can be expressed as Eq. (5.21).

$$\frac{\partial \ln K_{CO}}{\partial \frac{1}{T}} = 2 \frac{\partial \ln k_m}{\partial \frac{1}{T}} - \frac{\partial \ln \mu}{\partial \frac{1}{T}} - \frac{\partial \ln D}{\partial \frac{1}{T}} + \frac{\partial \ln \sigma}{\partial \frac{1}{T}} \quad (5.21)$$

Setting $M_1 = \left(2 \frac{\partial \ln k_m}{\partial \frac{1}{T}} \right)_1 - \left(\frac{\partial \ln \mu}{\partial \frac{1}{T}} \right)_1 - \left(\frac{\partial \ln D}{\partial \frac{1}{T}} \right)_1$ and $N_1 = \left(\frac{\partial \ln \sigma}{\partial \frac{1}{T}} \right)_1$, and the other two similar terms can be written for M_2 and N_2 , where subscript 1 and 2 represent this study and the case of Mori *et al.* [30], respectively.

Since $\frac{\partial \ln K_{CO}}{\partial \frac{1}{T}}$ is $\frac{\Delta H}{R}$ for reaction (5.15) and should have the same value for both cases, then one would expect the sum of right hand side (RHS) of Eq. (5.21) for this study and the case of Mori *et al.* should equal the left hand side (LHS) for Eq. (5.21). By reading values from

Figures 5.9 and 5.13, one can obtain $M_1=222$ and $M_2=58$, where M_1 is approximately 4 times higher than M_2 which suggests N_1 is to be smaller than N_2 , *i.e.*, the temperature coefficient of surface tension in this study should be smaller than the one in the case of Mori *et al.* [30]

Chung and Cramb [22] investigated the effect of sulfur and temperature on the surface tension of Fe-4 wt% C alloys, and developed the following equation to calculate the surface tension as expressed in Eq. (5.22), where the temperature was extended to 1913 K for this study.

$$\sigma = 1913 + 0.43[1823 - T] + 67.75[\%C] - 0.107T[\ln 1 + K_S a_S] - 0.153T[\ln 1 + K_O a_O] \quad (5.22)$$

where K_S and K_O are the adsorption coefficients for sulfur and oxygen respectively in liquid-iron alloys, a_S and a_O are activities of sulfur and oxygen, which can be calculated based on interaction coefficients [36].

There is a possibility that the surface tension will change with time because of changes in droplet chemistry. However, changes in the sulfur content will be negligible given the slag basicity (wt% CaO/wt% SiO₂=0.9) and the oxygen potential ($\sim 10^{-9.4}$ atm). The interfacial oxygen activity does change with time so it is likely that the oxygen potential inside the droplet will change. However, in analyzing the effect of surface tension on the temperature dependency, it was necessary to choose a specific condition. Given that the mass transfer coefficient is constant over the time period considered, one may assume that any unaccounted for change of surface tension has not introduced a significant error.

Based on Eq. (5.22), without sulfur and oxygen the temperature coefficient of surface tension for pure iron is -0.43. Therefore $N_2 = \left(\frac{\partial \ln \sigma}{\partial T} \right)_2$ for the case of Mori *et al.* [30] was calculated to be 0.52. In this study where metal droplets contain 0.007 wt% and 0.014 wt% S and around 0.005 wt% O [19, 28], N_1 was calculated to be -6.46 and -7.36 for 0.007 and 0.014 wt% S droplets, respectively. Taking the average value of -6.91, N_1 is around 10

times lower than N_2 . Even assuming liquid iron in the work of Mori *et al.* has the same amount of oxygen 0.005 wt% O as this study; N_2 was calculated to be -2.67, which is still more than 2 times higher than N_1 .

From above calculation, the values of right hand side (RHS) in Eq. (5.21) for this study and the case of Mori *et al.* [30] are 215 and 58.5, respectively, which shows that in neither the current study nor the work of Mori *et al.* [30] does the RHS of Eq. (5.21) yield standard formation enthalpy of CO (10 kJ/mol) [36] within a reasonable experimental error. The authors are not able to offer an explanation for this except to note that Chen and Coley [23] and Kwak and Oh [38] pointed out that the nucleation of CO in this case does not follow classical nucleation theory. If that is indeed the case Eq. (5.19) may require additional terms that have not been included.

In this study, the authors have proposed that high mass transfer coefficients for phosphorus in metal phase may be attributed to stirring inside the metal droplet caused by internal evolution of CO. One may argue that it is unlikely to form CO nuclei inside metal droplet due to a very high supersaturation requirement. However, CO formation inside the droplet is supported by experimental observation in the current work as shown in Figure 5.4 (droplet swelling) and in several other studies. [6,7] It is also shown, in at least three separate studies in our lab, that the CO generation rate is proportional to droplet mass. [6, 7, 39] The only explanation for these observations is that the gas nucleates homogeneously (or pseudo-homogeneously) within the metal droplet. Despite its theoretical “impossibility”, the authors suggest that the fact of CO gas nucleating inside metal droplets is well established [23, 38, 40-44]

5.4.5 Industrial Relevance

In this study, 1.0 g droplets with a diameter of 6.4 mm were used for experimental convenience. Ciccutti *et al.* [45] reported the diameter of droplets sampled from the BOF ranged from 0.23 to 3.35 mm. A range between 0.16 and 3.36 mm was also reported by Meyer *et al.* [46] The diameter of 6.4 mm used in the current study is above average diameter

of droplets found in the BOF. However, according to several previous studies in the authors' laboratory [6, 7, 39] the CO evolution rate within the droplet has been found to scale with the droplet volume, therefore the decarburization rate can easily be determined for smaller droplets. Because the CO evolution rate controls the mass transfer of phosphorus, the dephosphorization rate can be calculated for smaller droplets and within reason for larger droplets where the internal nucleation is likely to hold. The authors have recently prepared a draft manuscript detailing the effect of droplet size on dephosphorization kinetics [39]. That paper shows that the methodology presented in the current paper, for dealing with mass transport can readily accommodate different droplet diameters over the range ($7.4 \text{ mm} > d > 5 \text{ mm}$). Although it is not experimentally feasible to use smaller sizes the mechanism of mass transport should allow scaling to the sizes relevant to the BOF.

In the authors' view the most significant finding of this paper is that for all sized droplets the dephosphorization rate is fast (complete in < 6 seconds) relative to the residence time of the droplet (a few seconds to 60 seconds for bloated droplets). The overall dephosphorization rate may be calculated at any time during the blow by knowing the local equilibrium partition and the rate of droplet generation. The authors are currently working to build this finding into an overall model of the BOF.

5.5 Conclusion

The effects of temperature on the dephosphorization kinetics of bloated metal droplets containing 0.007 and 0.014 wt% S, was investigated in detail employing a mixed mass transfer control model in the temperature range from 1813 K to 1913 K. The mass transfer coefficient of phosphorus in the metal, k_m , was affected by CO gas stirring at different stages of reaction was estimated by combining the surface renewal model with a model for nucleation of CO. Metal droplets without carbon were also studied to elucidate the effect of decarburization on dephosphorization. The pathway of the overall mass transfer coefficient k_o for dephosphorization was evaluated over the whole course of reaction. Finally, the effect of temperature on k_m was investigated for a temperature range of 1813K to 1913 K. The following conclusions can be drawn from the current study.

1. In this study, the rate controlling step of dephosphorization for metal droplets without carbon is mass transfer in metal phase, and the k_m is calculated to be 5.3×10^{-4} cm/s, which is two orders of magnitude lower than for carbon containing droplets.
2. For droplets containing carbon, the analysis of dephosphorization kinetics shows that the overall mass transfer coefficient, k_o , decreases with increasing temperature due to the enhanced decarburization, which reduces the phosphorus partition ratio, L_p , by lowering the dynamic interfacial oxygen potential.
3. The mass transfer coefficient for phosphorus in the metal, k_m , for carbon bearing droplets is also found to decrease with increasing temperature because the size of CO bubbles are larger at higher temperature which decreases the rate of surface renewal.

5.6 Appendix

In the authors' previous study^[14], it was shown that by balancing the oxygen supply from reducible oxides in the slag and oxygen consumption by carbon in the metal, the P_{O_2} at the interface between slag and liquid metal can be determined via Eq. (5.A1).

$$k_{FeO}(C_{FeO}^b - C_{FeO}^i) = \frac{1}{A} \frac{dn_{CO}}{dt} \quad (5.A1)$$

Here, $\frac{dn_{CO}}{dt}$ is the CO generation rate (mole/s), C_{FeO} is the concentration of FeO, A is the surface area of the droplet, k_{FeO} describes oxygen transport in the slag conceptually defined as the mass transfer coefficient for FeO. C_{FeO}^i may be expressed in terms of activity of oxygen at the interface and C_{FeO}^b expressed as a function of the initial concentration of FeO modified by the amount reduced (dn_{FeO}). If one makes these substitutions, and further recognizes that dn_{FeO} is equivalent to the amount of CO generated (dn_{CO}), one may rearrange Eq. (5.A1) to obtain Eqs. (5.A2) and (5.A3).

$$P_{O_2}^i = \left[\frac{\gamma_{FeO} K_{Fe}}{C_s a_{Fe}^i K_O} \left(C_{FeO}^b - \frac{1}{A} \frac{1}{k_{FeO}} \frac{dn_{CO}}{dt} \right) \right]^2 \quad (5.A2)$$

$$P_{O_2}^i = \left[\frac{\gamma_{FeO} K_{Fe}}{C_S a_{Fe}^i K_O} \left(C_{FeO}^o - \frac{1}{V_S} \int_{n_{CO,t=0}}^{n_{CO,t=t}} dn_{CO} - \frac{1}{A} \frac{1}{k_{FeO}} \frac{dn_{CO}}{dt} \right) \right]^2 \quad (5.A3)$$

where K_{Fe} and K_O are the equilibrium constants for FeO dissociation and oxygen dissolution in iron; γ_{FeO} is the activity coefficient for FeO in the slag, C_S is the overall molar density of the slag and V_S is the volume of slag. The term, $C_{FeO}^o - \frac{1}{V_S} \int_{n_{CO,t=initial}}^{n_{CO,t=t}} dn_{CO}$, represents the FeO content of the slag at time t. It is important to note that V_S must be defined as either the volume of dense slag or the foamy slag depending on the location of the droplet.

The middle term, $\frac{1}{V_S} \int_{n_{CO,t=initial}}^{n_{CO,t=t}} dn_{CO}$, in Eq. (5.A3) describes the amount of carbon oxidized, which is taken from experimental measurements. To use this equation for a specific reaction time one will be required to calculate the concentration of FeO. This instantaneous FeO concentration can be calculated from the initial concentration of FeO and the amount of carbon oxidized between time zero and time t. Using the X-ray videos one can calculate the volume of foamy slag and dense slag at any given time, thereby determining the amount of liquid slag in each phase. Assuming no mixing between the two after the droplet is in the foamy slag, one can calculate the change in FeO for the foamy slag.

5.7 References

1. E. W. Mulholland, G. S. F. Hazeldean and M. W. Davies: *J. Iron Steel Inst.*, 1973, vol. 211, pp. 632-39.
2. T. Gare and G.S.F. Hazeldean: *Ironmak. Steelmak.*, 1981, vol. 4, pp. 169-81.
3. H. Gaye and P.V. Riboud: *Metall. Trans. B*, 1977, vol. 8B, pp. 409-15.
4. D.J. Min and R.J. Fruehan: *Metall. Trans. B*, 1992, vol. 23B, pp. 29-37.
5. C.L. Molloseau and R.J. Fruehan: *Metall. Trans. B*, vol. 33B, 2002, pp. 335-44.
6. E. Chen: PhD Thesis, McMaster, Hamilton, CA, 2011, pp.59-79.
7. M. Pomeroy: Master Thesis, McMaster, Hamilton, CA, 2011, pp.42-66.
8. G. A. Brooks, Y. Pan, Subagyo and K.Coley: *Metall. Trans. B*, 2005, vol. 36B, pp. 525-35.
9. Subagyo, G.A. Brooks, and K. Coley: *Can. Metall. Quarterly*, 2005, vol. 44 (1), pp.119-29.
10. N. Dogan, G. A. Brooks and M. A. Rhamdhani: *ISIJ Int.*, 2011, vol. 51 (7), pp. 1086-92.
11. N. Dogan, G. A. Brooks and M. A. Rhamdhani: *ISIJ Int.*, 2011, vol. 51 (7), pp. 1093–01.
12. G. Brooks, B. Rout, A. Rhamdhani and Z. Li: *CAMP-ISIJ*, 2015, vol.28, pp. 509-12.
13. A. K. Hewage, B. K. Rout, G. Brooks and J. Naser: *Ironmak. Steelmak.*, 2016, vol. 43 (5), pp. 358-70.

14. K. Gu, N. Dogan and K. Coley: *Metall. Trans. B*, 2017, DOI: 10.1007/s11663-017-1000-2.
15. P. Wei, M. Ohya, M. Hirasawa, M. Sano and K. Mori: *ISIJ.Int.*, 1993, vol. 33 (8), pp. 847-54.
16. P. Wei, M. Sano, M. Hirasawa, and K. Mori: *ISIJ Int.*, no. 3, vol. 33 (3), 1993, p. 479-87.
17. E. Shibata, H. Sun and K. Mori: *Metall. Trans. B*, 1999, vol. 30B, pp. 279-86.
18. B. J. Monaghan, R.J. Pomfret, and K.S. Coley: *Metall. Trans. B*, 1998, vol. 29B, pp. 111-18.
19. K. Gu, N. Dogan and K. Coley: *Metall. Trans. B*, 2017, DOI: 10.1007/s11663-017-1002-0.
20. Z. Li, K. Mukai, M. Zeze and K. C. Mills: *J. Mater. Sci.*, 2005, vol. 40, pp. 2191-95.
21. K. Nakashima and K. Mori: *ISIJ Int.*, 1992, vol. 32 (1), pp. 11-18.
22. Y. Chung and A. Cramb: *Metall. Trans. B*, 2000, vol. 31B, pp. 957-71.
23. E. Chen and K. Coley: *Ironmak. Steelmak.*, 2010, vol. 37 (7), pp. 541-45.
24. C. P. Manning and R. J. Fruehan: *Metall. Trans. B*, 2013, vol. 44B, pp. 37-44.
25. A. Assis, J. Warnett, S. Spooner, R. Fruehan, M. Williams and S. Sridhar: *Metall. Trans. B*, 2015, vol. 46B, pp. 568-76.
26. S. Spooner, A. Assis, J. Warnett, R. Fruehan, M. Williams and S. Sridhar: *Metall. Trans. B*, 2016, vol. 47B, pp. 2123-32.
27. S. Zheng, W. Chen, J. Cai, J. Li, C. Chen and X. Luo: *Metall. Trans. B*, 2010, vol. 41B, pp. 1268-72.
28. M. A. Rhamdhani, G. A. Brooks and K. S. Coley: *Metall. Trans. B*, 2005, vol. 36B, pp. 219-27.
29. R. Higbie: *Trans. Am. Inst. Chem. Eng.*, 1935, vol. 31, pp. 365-89.
30. K. Mori, Y. Fukami and Y. Kawai: *Trans. ISIJ*, 1988, vol.28, 315-18.
31. T. Mori: *Trans. Jpn. Inst. Met.*, 1984, vol. 25 (11), pp. 761-71.
32. V. D. Eisenhuttenleute: *Slag Atlas*, 2nd editions, 1995, pp. 10-19.
33. E. T. Turkdogan: *ISIJ Int.*, 2000, vol. 40 (10), pp. 964-70.
34. H. Ishii and R. J. Fruehan: *ISS Trans.*, February, 1997, pp. 47-54.
35. G. Li, T. Hamano and F. Tsukihashi: *ISIJ Int.*, 2005, no. 1, vol. 45, pp. 12-18.
36. M. Hino and K. Ito: *Thermodynamic Data for Steelmaking*, Tohoku University Press, Sendai. 2009, pp. 259-64.
37. Y. Kawai and Y. Shiraishi: *Handbook of Physico-chemical Properties at High Temperatures*, 1988, Chapter 7, pp. 196.
38. H. Kwak and S. Oh: *J. Colloid interface Sci.*, 1998, vol. 198, pp. 113-18.
39. K. Gu, N. Dogan and K. Coley: *Metall. Trans. B*, 2017, Unpublished research.
40. S. D. Lubetkin: *Langmuir*, 2003, 19, pp. 2575-87.
41. N. H. Ei-Kaddah and D. G. Robertson, *J. Colloid interface Sci.*, 1977, vol. 60, pp. 349-60.
42. K. S. Coley, E. Chen and M. Pomeroy: *Celebrating the Megascale*, Wiley, 2014, pp. 289-02.
43. H. S. Levine: *Metall. Trans. B*, 1973, vol. 4B, pp. 777-82.
44. H. S. Levine: *Metall. Trans. B*, 1974, vol. 5B, pp. 953-55.
45. C. Ciccutti, M. Valdez, T. Perez, J. Petroni, A. Gomez, R. Donayo and L. Ferro: 6th Int. Con. on Molten, Slags, Fluxes and Salts, 2000, paper 367.
46. H. W. Meyer, W. F. Porter, G. C. Smith and J. Szekel: *JOM*, 1968, July, pp.35-42.

Chapter 6

An Assessment of the General Applicability of the Relationship between Nucleation of CO Bubbles and Mass Transfer of Phosphorus in Liquid Iron Alloys

In chapter 6, all experiments and the initial data analysis were conducted by me. Dr. Kenneth S. Coley offered lots of insightful discussion on equation derivation to enrich the data analysis. The draft of this manuscript was written by me, and proofread by Dr. Neslihan Dogan. The final version was revised by Dr. Kenneth S. Coley. The manuscript of this work has been submitted to *Metallurgical and Materials Transactions B*.

Abstract

The current paper seeks to demonstrate the general applicability of the authors' recently developed treatment of surface renewal during decarburization of Fe-C-S alloys and its effect on the mass transport of phosphorus in the metal phase. The proposed model employs a quantitative model of CO bubble nucleation in the metal to predict the rate of surface renewal, which can then in turn be used to predict the mass transfer coefficient for phosphorus. A model of mixed transport control in the slag and metal phase was employed to investigate the dephosphorization kinetics between a liquid iron alloy and oxidizing slag. Based on previous studies of the mass transfer coefficient of FeO in the slag, it was possible to separate the mass transfer coefficient of phosphorus in metal phase, k_m , from the overall mass transfer coefficient k_o . Using this approach, k_m was investigated under a wide range of conditions and shown to be very well predicted by the mechanism proposed. The mass transfer model was tested against results from the literature over a wide range of conditions. The analysis showed that the FeO content in the slag, silicon in the metal and the

experimental temperature have strong impact on, k_m , almost entirely because of their effect on decarburization behavior.

6.1 Literature Review

Dephosphorization of hot metal has been studied extensively from the perspective of phosphate capacity of slag and phosphorus partition ratio between hot metal and slag, including Na₂O slag and CaO based slag systems as well as calcium sulfate flux^[1-7]. Based on a thermodynamic equilibrium approach, these studies have fully investigated the effect of different slag components on phosphate capacity and phosphorus partition ratio under a wide range conditions. Studies on correlating phosphate capacity of slag with optical basicity have been reviewed by Mills^[8]. Mori^[9] derived an empirical equation to describe the relationship between phosphate capacity and optical basicity by reassessing different CaO-Fe_tO based slag systems, which was employed in several studies^[10-12] to determine phosphate capacity of slag. More recently, by reviewing the existing of experimental data, Turkdogan^[13] demonstrated that at low concentrations of P₂O₅ (up to 1 wt%) the activity coefficient was independent of temperature, whilst it became temperature dependent when the content of P₂O₅ was greater than 10wt%. In a study of dephosphorization equilibria between liquid iron and highly basic CaO-based slags saturated with MgO, Ishii and Fruehan^[10] investigated the effect of Al₂O₃ additions by correlating the phosphate capacity of the slags with the theoretical optical basicity, and showed that the results were fitted reasonably by Mori's correlation^[9]. In a similar study to Ishii and Fruehan^[10], Li *et al.*^[11] investigated the effect of Na₂O and Al₂O₃ on dephosphorization of molten steel using high basicity MgO saturated CaO-FeO_x-SiO₂ slag, they proposed a correlation that was qualitatively consistent with Mori's correlation^[9] but predicted phosphate capacities which were an order of magnitude higher.

Several studies have been carried out to investigate the rate of dephosphorization between carbon saturated iron and slag^[14-17]. Inoue *et al.*^[14] studied the influence of temperature as well as silicon and manganese in the iron on dephosphorization of a carbon saturated iron alloy (Fe-C_{sat}-0.1 wt% P-0.05 wt% S) using a calcium sulfate flux. They found that

the rate and extent of dephosphorization at 1623 K was higher than at 1523 K, while dephosphorization at 1723 K showed the lowest dephosphorization rate and extent. They also found that silicon and manganese in the carbon saturated iron slowed the reaction rate, but had a negligible effect on extent of dephosphorization. However, using a soda slag system, Suito *et al.* [15], Moriya *et al.* [16] and Pak and Fruehan [17] observed that silicon content in hot metal had a significant effect on both reaction rate and the extent of dephosphorization. Suito *et al.* [15], and Moriya *et al.* [16] also observed that the dephosphorization rate and extent of dephosphorization decreased with increasing temperature.

Later researchers employed kinetic models to investigate the dephosphorization mechanisms by considering different rate-determining steps. Ohguchi *et al.* [18] employed a coupled reaction model to study simultaneous dephosphorization and desulphurization between molten pig iron and slag containing Fe_2O_3 . They found that dephosphorization occurred only after the cessation of vigorous desiliconization for molten iron containing silicon from 0.13 to 0.34 wt%. Mori *et al.* [19] and Wei *et al.* [20] studied the relationship between dephosphorization and decarburization for carbon saturated iron and slag containing FeO. They proposed that CO evolution was chemical reaction controlled at the slag-metal interface while other reactions were controlled by mass transfer in both slag and metal. These workers included the effect of temperature, FeO content in the slag and oxygen partial pressure of the furnace atmosphere. After investigating the effect of Fe_2O_3 , basicity and CaF_2 on dephosphorization, Monaghan *et al.* [12] proposed that the rate determining step was mass transfer in the slag. Employing similar approach to Mori *et al.* [19] and Wei *et al.* [20], Shibata *et al.* [21] investigated the reaction kinetics of dephosphorization associated with decarburization and desiliconization by varying FeO and MnO content in the slag. They found that for FeO slag, the fraction attributed to the metal phase, of the overall resistance to dephosphorization, decreased from approximately unity to around 0.3 as the reaction proceeded. The fraction of resistance attributed to the metal phase for MnO slag, remained relatively constant at 0.2 throughout the reaction. Kitamura *et al.* [22] carried out a study of dephosphorization kinetics using melts of up to 70 kg. They found that k_m

increased in proportion to the stirring energy, and was greater than k_s by approximately a factor of 10. This ratio did not show a clear dependence on stirring energy, temperature and flux composition. Using a mixed control model, *i.e.*, mass transfer in both slag and metal phase, Diao *et al.* [23] studied the dephosphorization of high phosphorus hot metal using slag of high basicity (wt% CaO/wt% SiO₂ ≈ 4), and high Fe₂O₃ (>66 wt%). They found that the overall mass transfer coefficient, k_o , decreased by a factor of 6 as the silicon content in the hot metal increased from 0.04 to 0.48 wt%. More recently, Hewage *et al.* [24] investigated the dephosphorization kinetics in the BOF using data from the IMPHOS pilot plant trials. [25] These workers found that dephosphorization could not be explained by a simple first order rate equation with either static equilibrium or dynamic equilibrium values, due to the transient behavior of rate parameters such as instantaneous area, residence time and mass transfer coefficient. The terms dynamic and static, used by Hewage *et al.* [24], refer to the equilibrium partition ratio for phosphorus at the slag metal interface. When used in rate equations, this ratio is often considered to be constant; static equilibrium. Although the assumption of static equilibrium, often offers a reasonable approximation for laboratory data, in reality it will change with the oxygen potential; dynamic equilibrium. The dynamic oxygen potential, and its effect on the local equilibrium phosphorus partition are discussed in earlier papers by the authors [26, 27] and is an important concept in the current work.

Kunisada *et al.* [28] investigated the dephosphorization reaction between Fe-0.1 wt% P alloy and Na₂O-SiO₂ based slag. The effect of Fe₂O₃ and Na₂CO₃ in the slag, slag basicity and temperature on the rate and the extent of dephosphorization were studied in detail, but the rate determining processes were not considered. The dephosphorization kinetics between Fe-0.1 wt% P alloy and CaO-SiO₂-Fe₂O₃ slag were investigated by Nasu *et al.* [29] using a coupled reaction model. Based on the significant effect of slag viscosity, they proposed that mass transfer in the slag phase must be, wholly or in part, the rate controlling step. Assuming the rate was under mixed control by mass transport in both slag and metal phases, Manning and Fruehan [30] investigated the dephosphorization kinetics between an Fe-P alloy and CaO-SiO₂-FeO-MgO slag. They showed that the effective overall mass transfer

coefficient (k_oA) decreased by a factor of up to 16 as the reaction proceeded. They attributed this observation to a decrease in slag-metal emulsification towards the end of the reaction. Recently, Assis *et al.* [31] and Spooner *et al.* [32] used micro X-ray computer tomography (XCT) to study emulsification between Fe-P alloy droplets and high basicity (wt% CaO/wt% SiO₂>2), high FeO_t (>30wt%) slag. They found that the surface area of an Fe-P alloy droplet increased by a factor of up to 10 due to oxygen transfer across the slag-metal interface. In the authors' previous work [33], the dephosphorization kinetics between Fe-P-S droplets and CaO-SiO₂-FeO-Al₂O₃ slag were investigated while observing changes of the droplet size and shape using X-ray imaging. It was found that the rate determining step for dephosphorization of Fe-P was likely to be the mass transfer in metal phase.

In recent work by the authors [33], the mass transfer coefficient for phosphorus in molten iron was obtained for a wide range of conditions and analyzed using Higbie's Penetration Theory [34] based on the formation rate and size of CO bubbles and modified to include calculation of bubble size as a function of reaction conditions. The objective of the current work is to demonstrate the general applicability of the authors' approach, first through a systematic study of mass transfer coefficient as a function of bubble velocity across the interface and secondly by analyzing dephosphorization data reported in the published literature [14-16, 19-23].

6.2 Theoretical Framework

Dephosphorization of iron is often under mixed control. Therefore in order to quantify the effect of CO formation on mass transfer of phosphorus in the metal phase, one must first isolate mass transfer in the metal from other potential rate determining steps. It is well established that dephosphorization kinetics between liquid iron and oxidizing slag can be described by Eq. (6.1) for mixed control by mass transfer in both the slag and metal.

$$\left(\frac{W_m}{\rho_m A} \frac{1}{1 + \frac{W_m}{L_P W_S}} \right) \text{Ln} \left[\left(1 + \frac{W_m}{L_P W_S} \right) \frac{[\text{wt}\% \text{ P}]_b}{[\text{wt}\% \text{ P}]_o} - \frac{W_m}{L_P W_S} \right] = -k_o t \quad (6.1)$$

where k_s and k_m are respectively the mass transfer coefficients for phosphorus in the slag and metal, ρ_m and ρ_s are the densities of metal and slag, L_P is the phosphorus partition coefficient.

Setting $C = \left(1 + \frac{W_m}{L_P W_s}\right) \frac{[\text{wt}\% \text{ P}]_b}{[\text{wt}\% \text{ P}]_o} - \frac{W_m}{L_P W_s}$ and $B = \left(\frac{W_m}{\rho_m A} \frac{1}{1 + \frac{W_m}{L_P W_s}}\right)$, Eq. (6.1) becomes $B \ln C = -k_o t$. In Eq. (6.1), k_o the overall mass transfer coefficient with the units of cm/s, k_o , is defined as:

$$k_o = \frac{1}{\frac{\rho_m}{k_s \rho_s L_P} + \frac{1}{k_m}} \quad (6.2)$$

It is worth noting that for high values of L_P ($>10^2$) Eq. (6.1) becomes Eq. (6.3) and the rate will be controlled entirely by mass transport in the metal where $k_o = \frac{1}{\frac{\rho_m}{k_s \rho_s L_P} + \frac{1}{k_m}} \cong k_m$.

$$\ln \left[\frac{[\text{wt}\% \text{ P}]_b - [\text{pct P}]_e}{[\text{wt}\% \text{ P}]_o - [\text{pct P}]_e} \right] \left(\frac{[\text{wt}\% \text{ P}]_o - [\text{wt}\% \text{ P}]_e}{[\text{wt}\% \text{ P}]_o} \right) \left(\frac{W_m}{\rho_m A} \right) = -k_m t \quad (6.3)$$

The current work examines a wide range of conditions and, for most cases, it will be necessary to obtain k_o from Eq. (6.1) then use Eq. (6.2) to isolate k_m . The process of quantifying mass transfer coefficients is further complicated by the dynamic nature of the conditions; L_P , defined at the slag-metal interface is affected by the balance between supply and consumption of oxygen, which is likely to change during the course of the reaction. The theoretical framework employed to address this issue is described below.

Obtaining k_o by fitting experimental data to Eq. (6.1), one needs to estimate ρ_m , ρ_s , L_P and k_s for each case in order to separate and determine k_m from Eq. (6.2). Densities of Fe-C-P alloys can be estimated based on equations from Kawai and Shiraishi^[35]. All alloys considered in the current work range from 6.87~7.02 g/cm³ which is less than 1% difference between maximum and minimum therefore the value of 7 g/cm³ (ρ_m) will be employed for all cases. The slag density for each case was calculated based on the partial molar volume model from the Slag Atlas^[36].

In a previous work ^[27], the authors demonstrated that the mass transfer coefficient of FeO, k_{FeO} , showed a parabolic correlation with total iron oxide in the slag and was not strongly dependent on temperature. Assuming k_{FeO} is a reasonable estimate for k_s , k_s for slag containing different FeO content can be determined based on this empirical correlation.

Because the current work analyzes data from a number of different sources, it is necessary to devise a set of rules regarding the choice of interfacial phosphorus partition, L_P , such that Eqs. (6.1) and (6.2) may be applied in a reasonably consistent manner. Therefore, the following rules were employed:

For the cases where phosphorus reversion occurred, L_P based on the slag and metal composition at the reversion point was used in Eq. (6.1) to determine k_o , otherwise the minimum content of phosphorus was employed to define L_P , *i.e.*, $L_P = \frac{(\text{wt}\% \text{ P})_{\text{max.}}}{[\text{wt}\% \text{ P}]_{\text{min.}}}$.

It is well established that L_P would normally decrease as the reaction proceeds because reaction of carbon with the slag reduces FeO, thereby decreasing the interfacial oxygen potential. However, in a previous study ^[33] the authors demonstrated that the initial value of L_P can normally be used to determine the mass transfer coefficient without significant loss of precision. The difference of mass transfer coefficient between the values calculated using initial L_P and the one determined by minimum phosphorus content is normally less than 10% for most cases. Therefore, the initial L_P calculated via Eqs. (6.4) to (6.6) was employed to separate k_m from the overall mass transfer coefficient, k_o .

In a previous study ^[27], the authors were able to balance the oxygen supply from reducible oxides in the slag and oxygen consumption by carbon in the metal to determine the P_{O_2} at the slag-metal interface. This balance is represented by Eq. (6.4a). It is also worth noting that Eq. (6.4a) may be extended to include reactions with other solute elements such as silicon.

$$k_{FeO}(C_{FeO}^b - C_{FeO}^i) = \frac{1}{A} \frac{dn_{CO}}{dt} \quad (6.4a)$$

Here, $\frac{dn_{CO}}{dt}$ is the CO generation rate (mol/s), C_{FeO} is the concentration of FeO, A is the surface area of the droplet, k_{FeO} describes oxygen transport in the slag conceptually defined as the mass transfer coefficient for FeO, and superscripts b and i indicate bulk and interfacial values, respectively. C_{FeO}^i may be expressed in terms of activity of oxygen at the interface and C_{FeO}^b expressed as a function of the initial value C_{FeO}^o modified by the amount reduced (dn_{FeO}). If one makes these substitutions and further recognizes that dn_{FeO} is equivalent to the amount of CO generated (dn_{CO}), one may rearrange Eq. (6.4a) to obtain:

$$P_{O_2}^i = \left[\frac{\gamma_{FeO} K_{Fe}}{C_s a_{Fe}^i K_O} \left(C_{FeO}^o - \frac{1}{V_s} \int_{n_C, t=initial}^{n_C, t=t} dn_C - \frac{1}{A} \frac{1}{k_{FeO}} \frac{dn_C}{dt} \right) \right]^2 \quad (6.4b)$$

where K_{Fe} and K_O are the equilibrium constants for FeO dissociation and oxygen dissolution in iron, γ_{FeO} is the activity coefficient for FeO in the slag, C_s is the overall molar density of the slag and V_s is the volume of slag. The term, $C_{FeO}^o - \frac{1}{V_s} \int_{n_C, t=0}^{n_C, t=t} dn_{CO}$, represents the FeO content of the slag at time t. It is important to note that V_s must be defined as either the volume of dense slag or the foamy slag depending on the location of the droplet. A detailed derivation of Eq. (6.4b) from Eq. (6.4a) can be found in the authors' previous work [27].

Using Eq. (6.4) to calculate $P_{O_2}^i$ at $t=0$, the initial L_P ($t=0$) can be calculated based on Eqs. (6.5) and (6.6).

$$L_P = \frac{(\text{wt}\% \text{P})_i}{[\text{wt}\% \text{P}]_i} = \frac{C_{PO_4^{3-}} P_{O_2}^i{}^{5/4} f_P M_P}{K_P M_{PO_4^{3-}}} \quad (6.5)$$

where $C_{PO_4^{3-}}$ is the phosphate capacity of the slag, f_P is the Henrian activity coefficient for phosphorus in the metal, M_P and $M_{PO_4^{3-}}$ are the molar mass of phosphorus and phosphate respectively, K_P is the equilibrium constant for the dissolution of phosphorus gas in steel.

Given the extensive application of optical basicity to calculate phosphate capacity^[8], the correlation expressed as Eq. (6.6) proposed by Mori^[9] was employed to calculate the phosphate capacity in this study as has been done by other researchers^[10-12]. This choice is justified by more recent work by Li *et al.*^[11] who proposed correlations that gave close quantitative agreement with Eq. (6.6).

$$\log C_{PO_4^{3-}} = 17.55 \Lambda + \frac{51670}{T} - 21.867 \quad (6.6)$$

In Eq. (6.6), Λ represents the theoretical optical basicity of slag, optical basicity values for individual oxides were taken from the literature^[8].

In a recent work^[33], the authors demonstrated that k_m is enhanced by CO bubble formation and that the enhancement can be quantified by applying Higbie's penetration theory^[34]. In that study the authors showed that by considering the formation of a CO bubble (reaction (6.7)^[37]) and combining Eqs. (6.7) and (6.9) with surface renewal theory, k_m can be calculated via Eq. (6.11).



$$\log K_{CO} = \frac{1160}{T} + 2.003 \quad (6.8)$$

$$K_{CO} = \frac{P_{ve}}{h_c h_o} \quad (6.9)$$

$$\Delta P = (P_{ve} - P_l) = \frac{2\sigma}{r^*} \quad (6.10)$$

$$k_m = \left[\frac{h_c h_o D \mu}{\pi \sigma} K_{CO} \right]^{1/2} \quad (6.11)$$

where h_c and h_o are the Henrian activity in liquid iron of carbon and oxygen respectively, σ represents the surface tension of the liquid metal. D is the diffusivity of phosphorus in the metal, and μ is CO gas velocity (rate of CO formation/surface area), r^* is the radius of critical nucleus. P_{ve} is the pressure in the bubble at equilibrium (supersaturation pressure), P_l is the liquid pressure (1 atm). Due to the high supersaturation pressure for CO nucleation,

$(P_{ve} - P_l) \approx P_{ve}$ [38]. It is worth noting that there is no change in liquid pressure in the current work. In the BOF, the atmospheric pressure in the vessel may change with time. However, the supersaturation pressure based on calculated activities of carbon and oxygen in current study is about 125 atm which will render any pressure change in a real BOF negligible.

From Eq. (6.11), it is clear that factors affecting h_o , h_c , σ , μ and K_{CO} will also affect the mass transfer coefficient. Such factors include: other alloy elements in metal, iron oxide in slag, temperature, and the presence of surface active species. The effect of temperature on k_m for iron alloy without silicon was recently investigated by the authors and shown to be consistent with the above mechanism [33]. As noted in an earlier publication [33], it is worth recognizing that provided the droplets are sufficiently small for general internal nucleation of CO to occur, they will be well mixed and the mass transfer coefficient will be determined by surface renewal caused by CO bubbles. As CO evolution rate is known to scale with droplet mass, [33, 38, 39] and the bubble size can be determined as a function of time, k_m will be scaled with the ratio of droplet mass to instantaneous surface area. Therefore it should be possible to calculate k_m for droplets of different sizes based on the data presented in this paper.

6.3 Experimental Procedure

In previous work by the authors [33], Eq. (6.11) was proposed to determine the mass transfer coefficient for phosphorus in the metal as a result of CO evolution. This equation was developed to explain experimental observations. The purpose of the current work is to validate the approach over a wider range of conditions. While much of this will be done using data from the literature, a targeted series of experiments was conducted to validate the key components of the proposed mechanism. Specifically, a series of experiments was conducted with different sized Fe-C-P droplets to test Eq. (6.11) at different CO velocities across the slag-metal interface.

The details of the experimental set-up and procedure were identical to the authors' previous work [26]. Here, only a brief description of the experimental procedure is repeated for the convenience of the reader. A resistance heated vertical tube furnace with an 80 mm diameter alumina working tube was used. The furnace was equipped with, X-ray imaging to observe the swelling of droplets in-situ, and a pressure transducer to measure gas evolution using the constant volume pressure increase technique (CVPI). Gas evolution measurements were calibrated immediately prior to each experiment, by injecting known quantities of gas into a sealed hot furnace and measuring the pressure increase. The calibration was subsequently checked after the experiment was complete using LECO analysis of the metal droplet and comparing the change in carbon concentration with that expected from CO evolution. Experiments were conducted at a temperature of 1913 K using Fe-2.62 wt% C-0.088 wt% P-0.007 wt% S droplets with mass of 0.5, 1.0 and 1.5 g. 25±0.5 g of slag, 32 wt% CaO-35 wt% SiO₂-17 wt% Al₂O₃-16 wt% FeO, was placed in a 45 mm diameter alumina crucible located in the hot zone of the furnace and was melted under an argon atmosphere. The droplet was dropped into the molten slag via a small hole at the bottom of an alumina tube, thus ensuring the droplet was molten before entering the slag. Samples were quenched at different reaction times and taken for chemical analysis of phosphorus in the metal using Inductively Coupled Plasma (ICP-OES). The experimental results on decarburization and dephosphorization are as follows.

6.3.1 Decarburization as a Function of Droplet Mass

Figure 6.1(a) shows the total amount of CO generated for 0.007 wt% S droplets as a function of time and droplet mass at 1913 K. It shows that the amount of CO generated increases as the increasing of droplet mass. The extracted peak decarburization rate from Figure 6.1(a) is plotted against the mass of metal droplet, and is shown in Figure 6.1(b). It can be seen that there is a linear relationship between peak decarburization rate and droplet mass, which is consistent with findings from previous studies in our lab [39, 40].

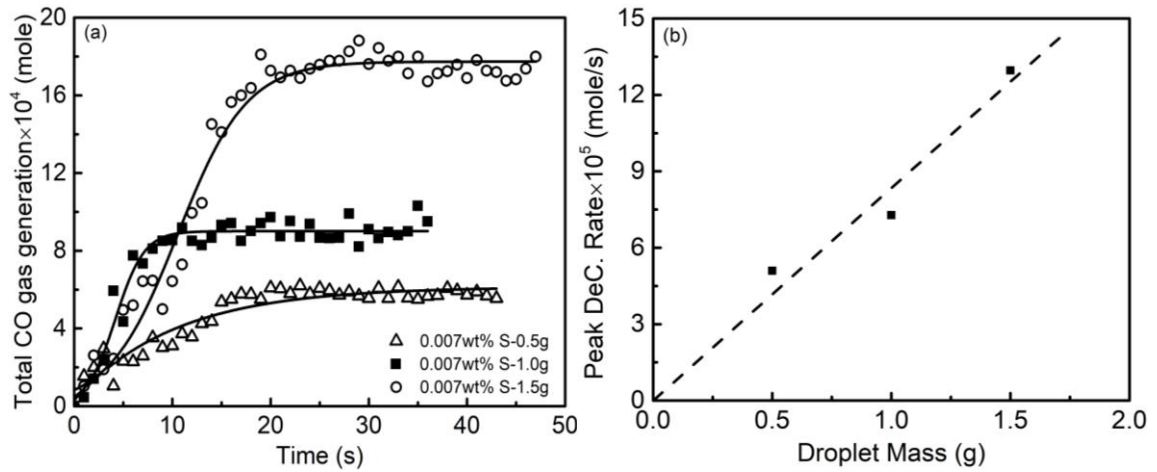


Figure 6.1 (a) CO gas generation with time for different droplet mass and (b) the relationship between peak decarburization rate and metal droplet mass.

6.3.2 Swelling Behavior of Droplets with Different Mass

By inspecting the recorded X-ray videos the change in the volume of droplets was determined as a function of time and droplet mass. This data is presented in Figure 6.2, which shows that the incubation time for swelling of 0.5 g, 1.0 g and 1.5 g droplets is 0 second, 2 seconds and 8 seconds, respectively. Figure 6.2 also shows that the maximum volume of the bloated droplet for 1.0 g is twice that of the 0.5 g droplet, but the value for the 1.5 g droplet is only slightly higher than that for 1.0 g droplet. The latter observation is probably because the relative rates of CO gas generation and gas escape are similar for both 1.0 g and 1.5 g droplets. The increase in incubation time with droplet mass is most likely related to the decreasing specific surface area, leading to longer times for oxygen saturation. This observation is consistent with the findings of Pomeroy^[39] and Sun^[41] who found that the time for nucleation of CO bubbles within the liquid metal would be shorter for a smaller droplet.

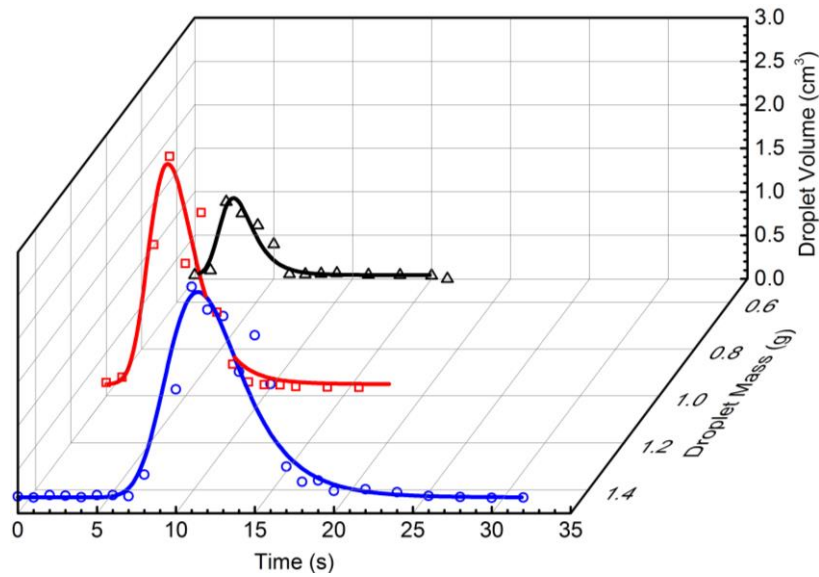


Figure 6.2 Swelling behavior of 0.007 wt% S metal droplets with different mass.

6.3.3 Dephosphorization of Droplets with Different Mass

The change of phosphorus content in metal droplets as a function of time and droplet mass is shown in Figure 6.3. This figure also shows X-ray images of the droplet during reaction with the slag. This shows that once active decarburization starts, a layer of foamy slag forms over a layer of dense slag. The droplet may be situated in either the foamy slag or the dense slag, depending on how much it has bloated. Figure 6.3(a), (b) and (c) show the distinct dephosphorization behavior of droplets of a particular size, depends to some extent on their movement between the dense and foamy slag, *i.e.*, the incubation time and duration of bloating. The 1.5 g droplets, they are initially dephosphorized and go through phosphorus reversions very fast due to the sudden increase in the rate of carbon oxidation, which leads to the droplet rising into the foamy slag and will also lower the interfacial oxygen potential. Figure 6.3(b) shows that the shorter incubation time for bloating of the 1.0 g droplets cause a short reversion in the foamy slag followed by a renewed dephosphorization when they sank back into the dense slag. The initial reversion is caused by a combination of the rapid CO evolution and FeO depletion in the low liquid volume foamy slag. The renewed dephosphorization is caused by the higher FeO in dense slag and

the slower decarburization rate, which combine to offer an increase in interfacial oxygen potential. Figure 6.3(a) also shows phosphorus reversion in the foamy slag, which can be explained if one considers the depletion of FeO from the relatively small liquid volume in the foam. The longer time over which this happens compared with Figure 6.3(b) and the relatively limited renewed dephosphorization, may be explained by the relatively longer time the droplet spends in the foamy slag.

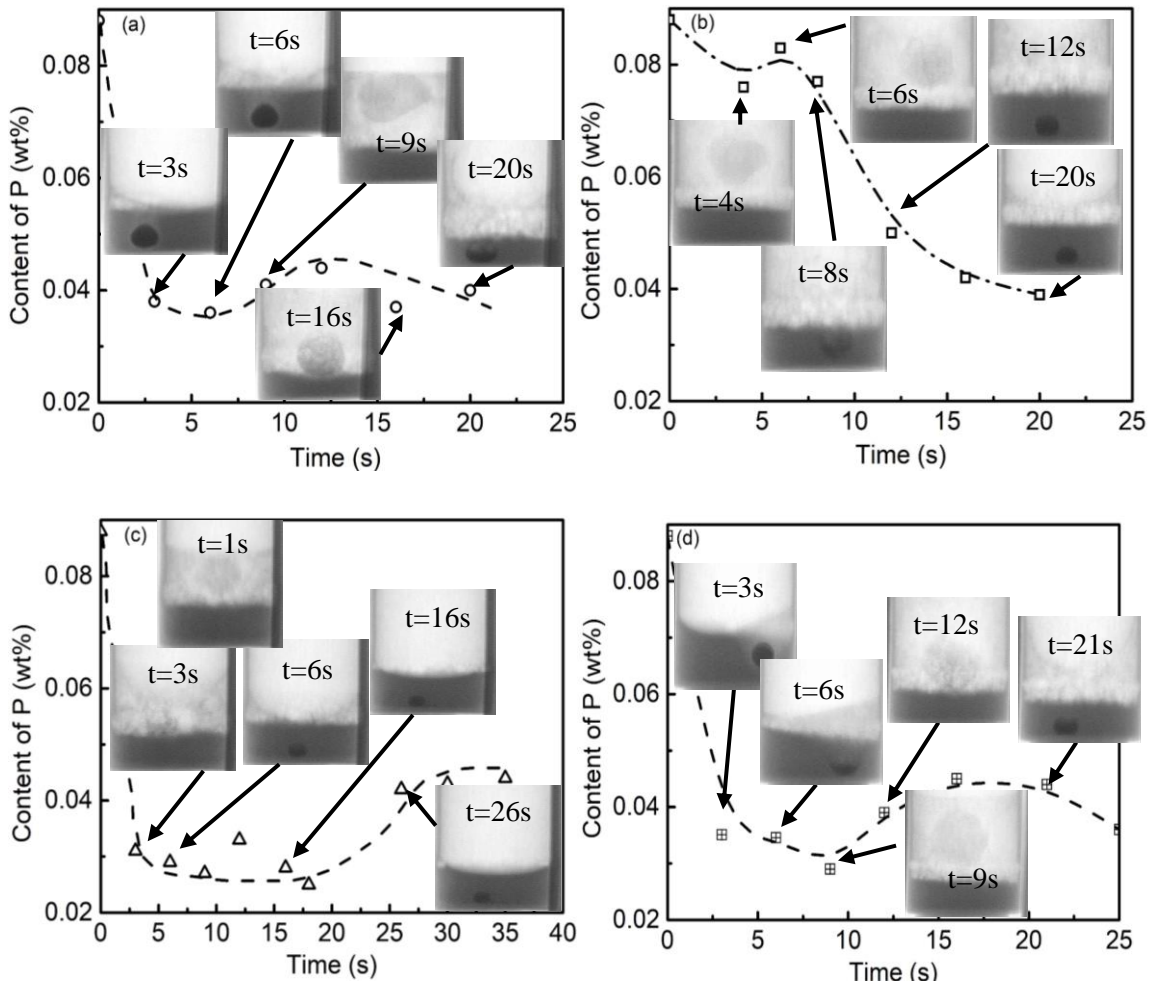


Figure 6.3 Plot of dephosphorization as a function of time at 1913 K: (a)1.5 g, (b)1.0 g, (c) 0.5 g and (d)1.0 g at 1813 K.

Figure 6.3(c) shows that the 0.5 g droplet is present in the foamy slag for the first two seconds of reaction. The droplet dephosphorizes very rapidly with no reversion until after

20 seconds. This is probably because the droplet is not resident in the foamy slag for enough time to deplete the FeO and the larger liquid volume in the dense slag takes much longer to deplete. Because of zero incubation time and a very short residence time in the foam, it is difficult to obtain sufficient kinetic data for 0.5 g droplet.

For comparison, Figure 6.3(d) shows the dephosphorization behavior of 1.0 g droplets at 1813 K, taken from the authors' previous work ^[33]. Based on X-ray images shown in Figures 6.3(a) and Figure 6.3(d), the droplets show a similar swelling behavior. The dephosphorization behavior is also similar, however for the 1.5 g droplet at 1913 K almost all of the dephosphorization occurs in the dense slag and the reversion which occurs on entering the foamy slag is limited.

6.4 Results and Discussion

Based on the approach described in Section 6.4, the overall mass transfer coefficient of phosphorus was determined and then in turn used in Eq. (6.2) to determine k_m . These calculations were carried out for carbon containing alloys under a wide range of conditions including this study and dephosphorization data from literature ^[14-16, 19-23].

6.4.1 Effect of Droplet Mass

The dephosphorization behavior of droplets with different mass shown in Figure 6.3, was analyzed using Eq. (6.1) and (6.2). The calculated mass transfer coefficient of phosphorus in the metal is summarized in Table 6.1. It is worth noting that, based on the data presented in Figure 6.3(b), the 1.0 g droplet at 1913 K exhibits a very short initial dephosphorization period prior to entering the foamy slag which makes it difficult to evaluate the kinetics. For this droplet, the kinetics of dephosphorization after the droplet reenters the dense slag has been employed to determine the data presented in Table 6.1.

Table 6.1 Mass transfer coefficients calculated based on data shown in Figure 6.3.

Droplet Size/(g)	$k_o \times$ $10^2/(cm/s)$	Initial L_p	$k_s \times$ $10^2/(cm/s)$	$k_m \times$ $10^2/(cm/s)$	DeC. rate $\times 10^5$ /(mol/s)	Average A/(cm ²)	CO gas velocity (cm/s)
0.5	1.73	8	1.18	3.0	5.10	3.12	2.57
1.0	1.07	8	1.18	1.46	1.0	2.03	1.93
1.5	3.63	8	1.18	42.1	8.55	1.64	8.23
1.0- 1813 K	5.49	18	0.92	24.6	5.18	1.36	5.67

According to Eq. (6.11), the mass transfer coefficient of phosphorus in the metal phase k_m is a function of $\mu^{1/2}$, *i.e.*, the square root of CO gas velocity. In the present case the CO gas velocity is taken to be the rate of CO formation divided by surface area of droplet mass. From Figure 6.1(b) it is clear that the rate of CO formation is a linear function of droplet mass, therefore it should be possible to analyze the effect of CO velocity by employing data over a range of different sized droplets. The resulting mass transfer coefficients for different droplet masses have been plotted against $\mu^{1/2}$ in Figure 6.4(a). It is possible to fit the data in Figure 6.4(a) to a straight line as expected from Eq. (6.11), however the lack of data at intermediate velocities weakens the impact of this result.

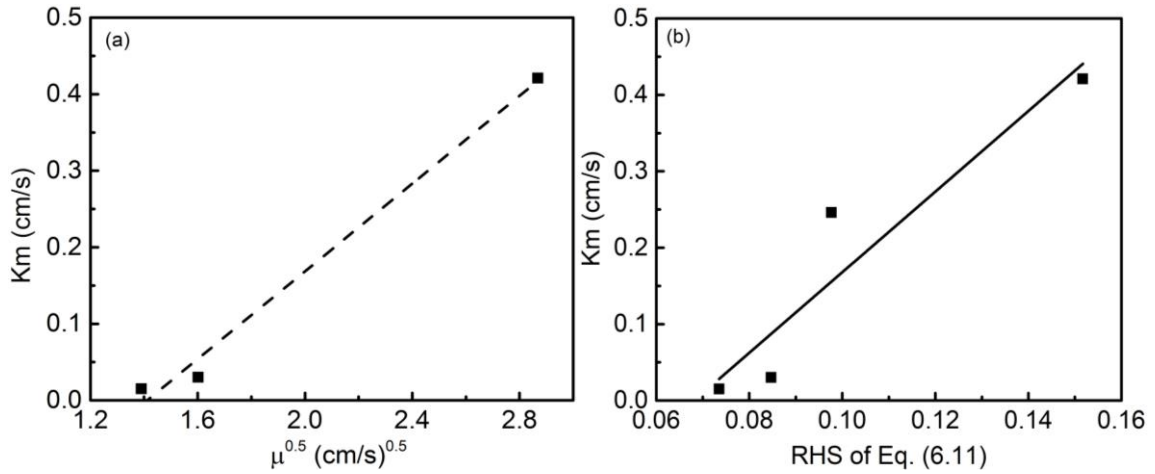


Figure 6.4 (a) k_m as a function of CO gas velocity and (b) plot of k_m based on Eq. (6.11).

It is worth noting that Table 6.1 also contains data for a 1.0 g droplet at 1813 K which does exhibit a CO velocity in the intermediate range. This data cannot be meaningfully plotted in Figure 6.4(a) because of the temperature dependency of k_m . However, if k_m were plotted against $\left[\frac{h_c h_o D \mu}{\pi \sigma} K_{CO}\right]^{1/2}$, right hand side (RHS) of Eq. (6.11), data from different temperatures may be included in the same plot. D was taken from Kawai and Shairashi^[35] and σ was estimated from the model developed by Chung and Cramb^[42]. A plot of k_m as versus the RHS of Eq. (6.11) (essentially measured versus calculated mass transfer coefficients) is shown in Figure 6.4(b). Figure 6.4(b) shows that the data can be represented well by a straight line. However, the straight line does not follow the expected 1:1 relationship; Eq. (6.11) under predicts the mass transfer coefficient at higher values and over predicts at lower values. The most likely reason for this discrepancy is in the calculation of bubble size. The bubble size calculation is based on classical nucleation theory and the assumption that the bubbles do not grow subsequent to nucleation. Previous work^[33] has shown that classical nucleation does not adequately represent the behaviour for CO nucleation in iron carbon droplets and it is also likely that both nucleation and growth apply to CO bubbles formed in bloated droplets. Further investigation of the factors affecting the mass transfer coefficient is required to develop a more quantitative prediction. Given the qualitative agreement with this model, other factors affecting CO gas formation

rate, *i.e.*, reactive alloy elements in metal, iron oxide in slag and temperature were investigated in following sections, using published dephosphorization data to demonstrate the general applicability of the approach.

6.4.2 Effect of Silicon

Several researchers [14-16, 23] have investigated the the effect of silicon on hot metal dephosphorization. Theses studies are brought into discussion here. The experimental conditions for these studies are summarized in Appendix. k_o was determined from the original experimental data via Eq. (6.1), as presented in Figure 6.5, and listed in Table 6.2. For the current analysis, the initial value for L_P for the case of Diao *et al.* [23] was determined based on Eqs. (6.4) to (6.6). Since the Na_2CO_3 slag system and hot metal pre-treatment would normally offer a high L_P (up to 10^4) [1, 2, 43], a typical value of 1000 was listed in Table 6.2 as initial phosphorus partition ratio L_P for the cases of Inoue *et al.* [14], Suito *et al.* [15], and Moriya *et al.* [16] It is also worth noting that k_m will be essentially equal to k_o according to Eq. (6.2) for cases with high L_P .

The overall mass transfer coefficient k_o listed in Table 6.2 decreases with increasing silicon in the metal. It is well known that under the temperature of hot metal pretreatment, silicon will suppress the oxidation of carbon and of phosphorus. The effect on phosphorus will decrease L_P thereby decreasing k_o but this effect has been accounted for by determining a value of L_P for each condition. The suppression of carbon oxidation will weaken the stirring obtained from the formation of CO bubbles. Moriya *et al.* [16] measured the quantity of CO gas formed during the reaction and found that the CO gas generation rate and total gas generation was decreased from approximately 7.44×10^{-3} mole/s to 2.98×10^{-3} mole/s and 2.59 to 1.12 total moles, as the silicon content increased from 0 to 0.60 wt%. Therefore, it is reasonable to conclude that the decrease in k_o with increasing silicon is at least partially because of a lower rate of surface renewal by CO bubbles due to a weakening of the decarburization.

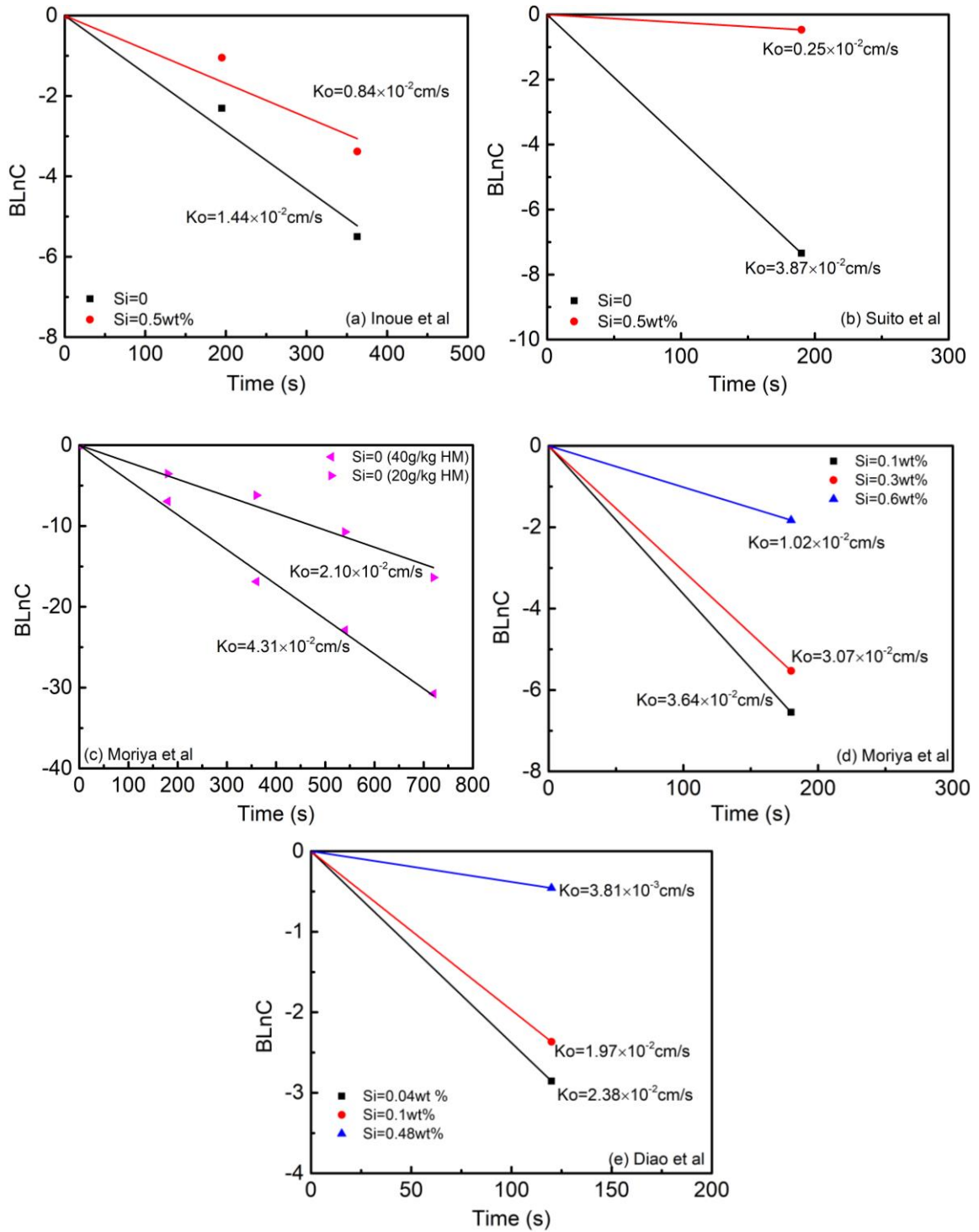


Figure 6.5 Dephosphorization data from different researchers are replotted as a function of time and silicon content based on Eq. (6.1): (a) Inoue *et al.* ^[14], (b) Suito *et al.* ^[15], (c) and (d) Moriya *et al.* ^[16] and (e) Diao *et al.* ^[23]

Table 6.2 Mass transfer coefficients calculated from experimental data.

Investigator	Si	Fe ₂ O ₃ /(wt%) or Na ₂ CO ₃ (g)	$k_o \times$ 10 ² /(cm/s)	Initial L_p	$k_s \times$ 10 ² /(cm/s)	$k_m \times$ 10 ² /(cm/s)
Diao <i>et al.</i> ^[19]	0.04	66.04	2.25	19500	7.67	2.38
Diao <i>et al.</i>	0.1	66.04	1.72	19500	7.67	1.97
Diao <i>et al.</i>	0.48	66.04	0.56	19500	7.67	0.38
Moriya <i>et al.</i> ^[11]	0	40	4.3	1000	0.1	4.78
Moriya <i>et al.</i>	0	20	2.1	1000	0.1	2.21
Moriya <i>et al.</i>	0.1	20	3.64	1000	0.1	3.98
Moriya <i>et al.</i>	0.3	20	3.07	1000	0.1	3.31
Moriya <i>et al.</i>	0.6	20	1.02	1000	0.1	1.04
		CaCO ₃ -CaSO ₄				
Inoue <i>et al.</i> ^[9]	0	40g	1.44	1000		1.44
Inoue <i>et al.</i>	0.5	40g	0.84	1000		0.84
		2Na ₂ CO ₃ ·Na ₂ SO ₄				
Suito <i>et al.</i> ^[10]	0	20g	3.87	1000		3.87
Suito <i>et al.</i>	0.5	20g	0.25	1000		0.25

In another case of the work of Moriya *et al.*^[16], k_m for the case of Si=0 and 40 g/kg HM Na₂CO₃ is almost two times higher than that for Si=0 and 20 g/kg HM Na₂CO₃. This discrepancy may be explained if one considers the amount of CO gas generated during the

reaction. According to Moriya's measurements, the total gas generated for the case of 40 g/kg HM Na₂CO₃ and the case of 20 g/kg HM Na₂CO₃ were 2.59 and 1.0 moles, respectively. This explains why the k_m for 40 g/kg HM Na₂CO₃ is two times higher than that for 20 g/kg HM Na₂CO₃ presented in Table 6.2. If one considers the same slag-metal interfacial area, a higher amount of gas generated would lead to a higher gas velocity across the interface offering a faster surface renewal rate, thereby enhancing the mass transfer, which is consistent with the conclusion in Section 6.4.1.

By assuming that for metal containing silicon the activity of oxygen in the melt is controlled by reaction (6.12), Eq. (6.11) can be rewritten as Eq. (6.15) by replacing h_o with Eq. (6.14).



$$\log K_{\text{Si}} = \frac{-30110}{T} + 11.40 \quad (6.13)$$

$$h_o = \left(K_{\text{Si}} \frac{a_{\text{SiO}_2}}{h_{\text{Si}}} \right)^{1/2} \quad (6.14)$$

$$k_m = \left[\frac{h_C D \mu K_{\text{CO}} \sqrt{K_{\text{Si}} \frac{a_{\text{SiO}_2}}{h_{\text{Si}}}}}{\pi \sigma} \right]^{1/2} \quad (6.15)$$

Based on Figure 6.1(b), we can assume the CO generation rate is equal to the CO nucleation rate, then μ in Eq. (6.15) can be expressed as:

$$\mu = \frac{N_{\text{CO}}}{A} = J_s \left(\frac{n_e}{N_A} \right) \frac{V_m}{A} \quad (6.16)$$

where N_{CO} is CO generation rate, A represents the area of the slag metal interface, V_m is volume of metal, J_s is CO nucleation rate, n_e is the number of molecules in an embryo and N_A is Avogadro's number.

A modified version of classical nucleation theory expressed as Eq. (6.17) ^[38], which requires a surface tension modifying parameter φ was shown by Levine ^[44, 45] to work well

in determining the rate of nucleation of gases formed from solutes dissolved in liquids. Chen and Coley^[40] determined values for the surface tension modifying parameter under conditions relevant to the current study.

$$J_s = N_o \exp\left(\frac{-\Delta H}{kT}\right) \left[\frac{2(\varphi\sigma)}{\pi m}\right]^{1/2} \exp\left(\frac{-16\pi(\varphi\sigma)^3}{3kT(P_{ve}-P_l)^2}\right) \quad (6.17)$$

$$N_o = \frac{W_m[\text{wt}\% \text{O}]N_A}{M_O V_m} = \frac{W_m h_O N_A}{M_O V_m f_O} \quad (6.18)$$

where σ is the surface tension at the liquid-gas interface, ΔH is the heat of formation of one CO molecule; m is the mass of one molecule; T is the temperature in Kelvin, k is the Boltzmann constant; φ represents surface tension modifying parameter and ranges between 0 and 1. P_{ve} is the pressure in the vapour bubble at equilibrium, and P_l is liquid pressure where $P_{ve} - P_l \approx P_{ve}$. N_o is the number concentration of CO embryos in the liquid, which depends on the concentration of oxygen in this case where the metal has a high carbon activity^[38]. N_o can be estimated using Eq. (6.18). W_m is the weight of metal, M_O represents mass of oxygen molecule, h_O and f_O are oxygen activity and activity coefficient, respectively.

Combine Eqs. (6.16) to (6.18), Eq. (6.15) can be written as Eq. (6.19):

$$k_m = \left[\frac{h_C D K_{CO} \frac{K_{Si} a_{SiO_2}}{h_{Si}} \frac{n_e W_m}{A M_O f_O} \exp\left(\frac{-\Delta H}{kT}\right) \left[\frac{2(\varphi\sigma)}{\pi m}\right]^{1/2} \exp\left(\frac{-16\pi(\varphi\sigma)^3}{3kT(h_C K_{CO} \sqrt{\frac{K_{Si} a_{SiO_2}}{h_{Si}}})^2}\right)}{\pi\sigma} \right]^{1/2} \quad (6.19)$$

Taking the logarithm of Eq. (6.19) and rearranging, one can obtain:

$$\ln k_m = -\frac{1}{2} \ln h_{Si} - \frac{8\pi(\varphi\sigma)^3}{3kT(h_C K_{CO})^2 K_{Si} a_{SiO_2}} h_{Si} + \frac{1}{2} \ln \left[\frac{h_C D K_{CO} K_{Si} a_{SiO_2} \frac{n_e W_m}{A M_O f_O} \exp\left(\frac{-\Delta H}{kT}\right) \left[\frac{2(\varphi\sigma)}{\pi m}\right]^{1/2}}{\pi\sigma} \right] \quad (6.20)$$

From Eq. (6.20), it can be seen that $\ln k_m$ is a function of $-\frac{1}{2} \ln h_{Si} - \frac{8\pi(\varphi\sigma)^3}{3kT(h_C K_{CO})^2 K_{Si} a_{SiO_2}} h_{Si}$.

If rearranging Eq. (6.20), one can further obtain the following equation,

$$\ln k_m h_{Si}^{1/2} = -\frac{8\pi(\varphi\sigma)^3}{3kT(h_C K_{CO})^2 K_{Si} a_{SiO_2}} h_{Si} + \frac{1}{2} \ln \left[\frac{h_C D K_{CO} K_{Si} a_{SiO_2}}{\pi\sigma} \frac{n_e w_m}{A M_{O f o}} \exp\left(\frac{-\Delta H}{kT}\right) \left[\frac{2(\varphi\sigma)}{\pi m}\right]^{1/2} \right] \quad (6.21)$$

Then one can plot $\ln k_m h_{Si}^{1/2}$ against h_{Si} as is presented in Figure 6.6.

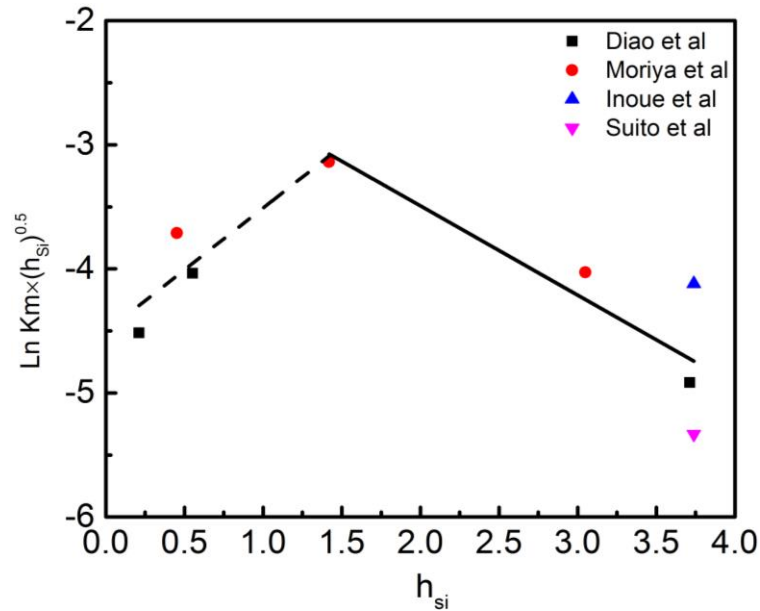


Figure 6.6 The relationship between h_{Si} on $\ln k_m h_{Si}^{1/2}$ based on Eq. (6.21).

Figure 6.6 shows a reasonable agreement with Eq. (6.21) except at lower activities of silicon. This deviation is quite reasonable if one considers that silicon is unlikely to control the oxygen potential when present at lower concentrations. The carbon content of hot metal in all the cases presented in Figure 6.6 is higher than 3.5 wt%, leading to a high activity of carbon. For example, for the case where $h_{Si} = 0.21$, the calculated oxygen potentials in equilibrium with carbon and silicon are 4.2×10^{-17} and 4.2×10^{-15} atm, respectively. Therefore, one might expect that the effect of silicon on mass transfer coefficient of

phosphorus in the metal phase would be negligible at lower concentrations as observed in Figure 6.6. The apparent reversal of the dependency at lower silicon concentrations is an artefact introduced by the term that is plotted; when k_m becomes independent of h_{Si} , $k_m h_{Si}^{1/2}$ will decrease with decreasing h_{Si} .

6.4.3 Effect of Temperature

Kitamura *et al.* [22] investigated the temperature effect on the mass transfer coefficient in the metal phase under fixed stirring energy using liquid iron containing silicon. The related experimental conditions are listed in Appendix. They measured k_m by using hot metal desiliconization tests (case A) rather than dephosphorization, and found that k_m was temperature dependent with activation of 125 kJ/mol. From hot metal dephosphorization tests (case B), they estimated the decarburization rate under different temperatures which is also listed in Table 6.3, where different numbers in one cell represent multiple different experiments conducted under nominally the same conditions.

Table 6.3 Mass transfer coefficients and decarburization rate from Kitamura *et al.* [22]

T/K		1873	1773	1723	1673	1623
Case A	$k_m \times 10^2 / (\text{cm/s})$	11.7, 10.9		9.6		9.2, 7.6, 6.9, 5.6
	Decarburization rate $\times 10^5 / (\text{mol/cm}^2\text{s}^{-1})$		0.07, 0.07, 0.55	0.24		0.1, 0.43, 0.23, 0.31, 0.37, 0.28

The k_m values listed in Table 6.3 were plotted in Figure 6.7(a) using an Arrhenius type expression, showing that k_m follows the Arrhenius equation, increasing as temperature increases. This result appears to contradict the authors' recent work [33] where k_m was found to decrease with increasing temperature for melts that did not contain silicon; this data is shown in Figure 6.7(b).

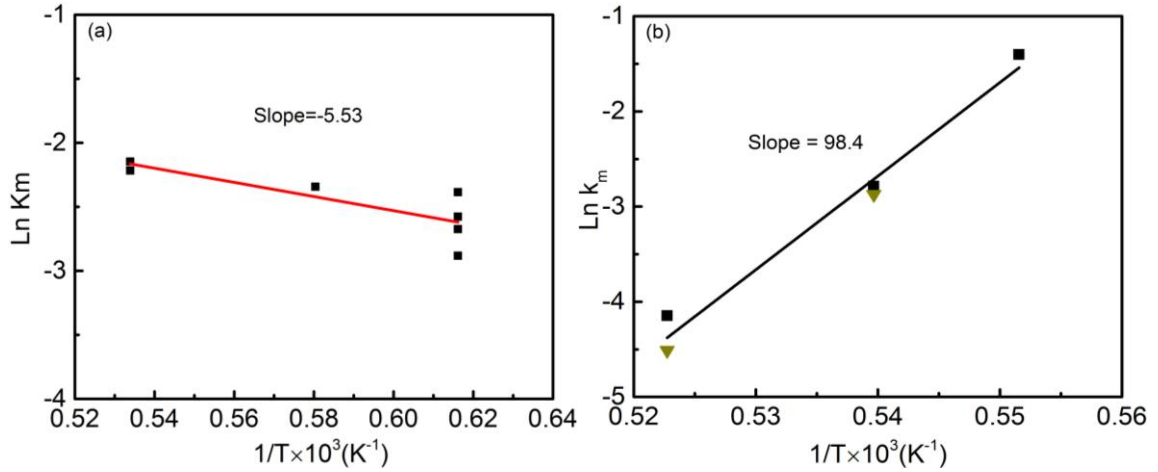


Figure 6.7 The effect of temperature on k_m : (a) using the data from Kitamura *et al.* [22], (b) from the authors' previous work [33].

Taking the logarithm of Eq. (6.15), one can obtain:

$$\ln k_m = \frac{1}{2} \ln K_{CO} + \frac{1}{4} \ln K_{Si} + \frac{1}{4} \ln a_{SiO_2} - \frac{1}{4} \ln h_{Si} + \frac{1}{2} \ln \mu - \frac{1}{2} \ln \sigma + \frac{1}{2} \ln D + \frac{1}{2} \ln C \quad (6.22)$$

where C is a constant. We can then express the temperature dependence of $\ln k_m$ as follows:

$$\frac{\partial \ln k_m}{\partial \frac{1}{T}} = \frac{1}{2} \frac{\partial \ln K_{CO}}{\partial \frac{1}{T}} + \frac{1}{4} \frac{\partial \ln K_{Si}}{\partial \frac{1}{T}} + \frac{1}{4} \frac{\partial \ln a_{SiO_2}}{\partial \frac{1}{T}} - \frac{1}{4} \frac{\partial \ln h_{Si}}{\partial \frac{1}{T}} + \frac{1}{2} \frac{\partial \ln \mu}{\partial \frac{1}{T}} - \frac{1}{2} \frac{\partial \ln \sigma}{\partial \frac{1}{T}} + \frac{1}{2} \frac{\partial \ln D}{\partial \frac{1}{T}} \quad (6.23)$$

From Eq. (6.8) and (6.13), the values of $\frac{1}{2} \frac{\partial \ln K_{CO}}{\partial \frac{1}{T}}$ and $\frac{1}{4} \frac{\partial \ln K_{Si}}{\partial \frac{1}{T}}$ were calculated to be 1.34 and -17.34, which suggests that term $\frac{1}{4} \frac{\partial \ln K_{Si}}{\partial \frac{1}{T}}$ contributes a large negative effect on the stirring rate. Based on the empirical equation developed by Chung and Cramb [42], the effect of temperature on the surface tension of Fe-4wt% C alloys containing sulfur, $\frac{1}{2} \frac{\partial \ln \sigma}{\partial \frac{1}{T}}$, was calculated to be -0.53. Since the decarburization rate for case A was not given in the original publication, $\frac{\partial \ln \mu}{\partial \frac{1}{T}}$ corresponding to case B taken directly from the

reported value by Kitamura *et al.* [22] was used for both case A and case B. $\frac{\partial \ln D}{\partial \frac{1}{T}}$ was calculated based on published data [35], while $\frac{\partial \ln a_{SiO_2}}{\partial \frac{1}{T}}$ and $\frac{\partial \ln h_{Si}}{\partial \frac{1}{T}}$ were obtained via FactSage^{TM6.4} Equilib program. The relevant temperature coefficients are summarized in Table 6.4. Using this data the sum of the right hand side (RHS) of Eq. (6.23) is calculated to be -9.98, which is higher than the value of -5.53 determined from Figure 6.7(a) but seems to offer a reasonable agreement given the uncertainties inherent in the measurements and in the assumptions employed in the analysis.

Table 6.4 Determined temperature coefficients for terms in Eq. (6.23).

Term	$\frac{\partial \ln K_{CO}}{\partial \frac{1}{T}}$	$\frac{\partial \ln K_{Si}}{\partial \frac{1}{T}}$	$\frac{\partial \ln \sigma}{\partial \frac{1}{T}}$	$\frac{\partial \ln \mu}{\partial \frac{1}{T}}$	$\frac{\partial \ln h_{Si}}{\partial \frac{1}{T}}$	$\frac{\partial \ln D}{\partial \frac{1}{T}}$	$\frac{\partial \ln a_{SiO_2}}{\partial \frac{1}{T}}$	Sum of RHS
	2.68	-69.48	1.06	18.04	-9.67	-11.93	0.09	-9.98

Table 6.4 shows that the term K_{Si} , reaction equilibrium constant for silicon oxidation makes a large negative contribution to the temperature effect on k_m . From a qualitative perspective this observation supports the reversal of slope related the authors' findings in the absence of silicon, shown in Figure 6.7(b). In the authors' previous work [33] a similar analysis predicted a slope for Figure 6.7(b) of -8.73, which is much lower than the experimentally measured value (98.4). At present the authors are not able to offer a definitive explanation for this discrepancy but suggest the following possibilities: CO nucleation inside the droplet does not follow classical nucleation theory and may require additional terms that have not been identified [38, 46], or the oxygen potential in the metal is fixed by a complex balance of supply and consumption. This latter effect has been evaluated on an empirical basis which may have hidden important factors. A detailed theoretical analysis may help explain the discrepancy between Figures 6.7(a) and (b). The analysis presented in this paper offers qualitative, and in some cases quantitative support for a model of mass transfer based on surface renewal by CO bubble formation inside the

metal. The authors believe that the proposed model offers a basis for future development of a fully quantitative model.

6.4.4 Effect of Iron Oxide in the Slag

Mori *et al.* [19], Wei *et al.* [20] and Shibata *et al.* [21] all investigated the effect of FeO content on dephosphorization. The experimental conditions for these three studies are summarized in Appendix.

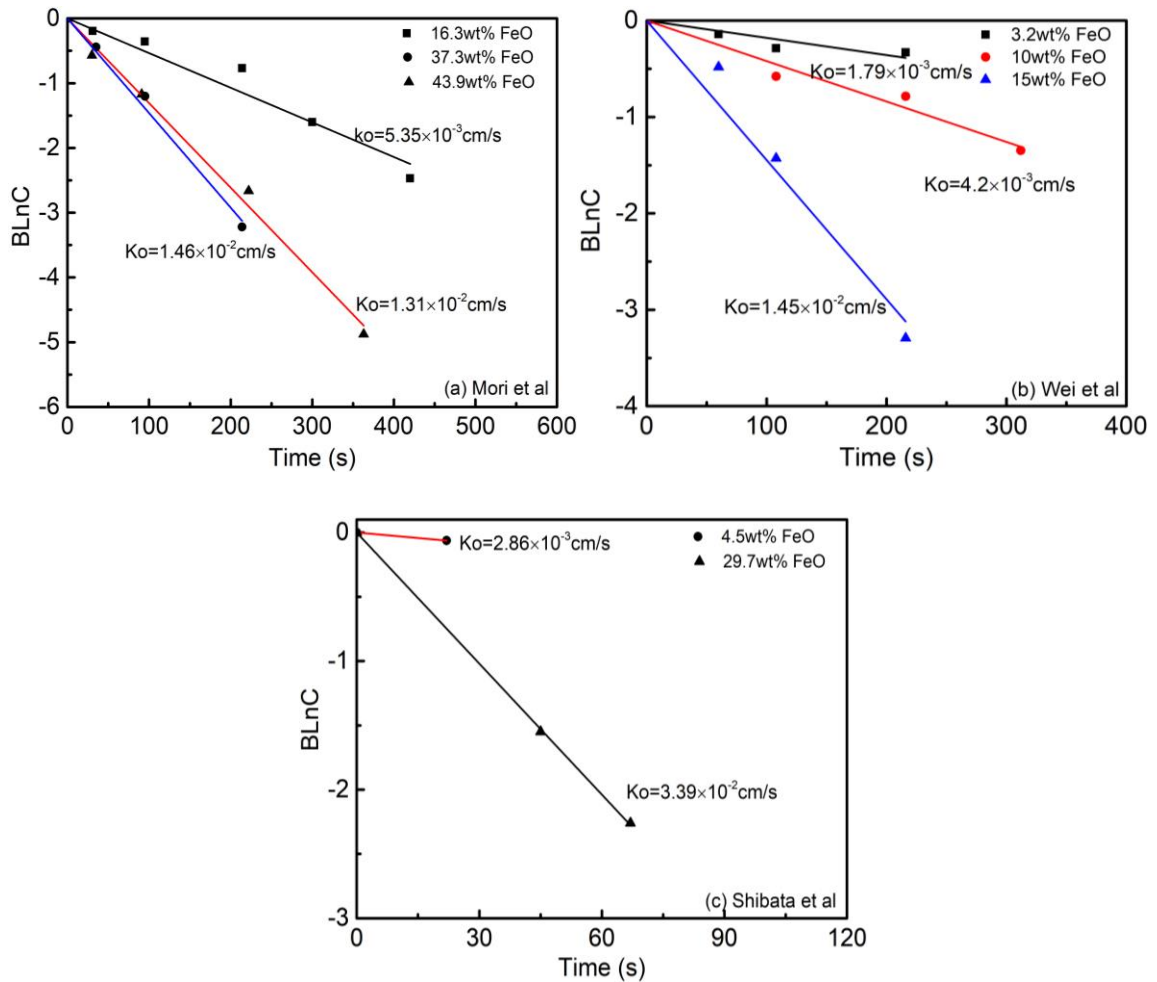


Figure 6.8 Dephosphorization data from different researchers are replotted as a function of time and FeO content based on Eq. (6.1): (a) Mori *et al.* [19], (b) Wei *et al.* [20] and (c) Shibata *et al.* [21]

All dephosphorization data were reassessed using Eq. (6.1) to determine k_o , and are presented in Figure 6.8. The initial partition ratio, L_p , was calculated via Eqs. (6.4) to (6.6),

k_{FeO} was estimated empirically based on results from the authors' previous study [27]. k_m was determined using Eq. (6.2). All of these parameters are presented in Table 6.5 including one case from Diao *et al.* [23]. In the studies of Mori *et al.* [19] and Wei *et al.* [20] and Shibata *et al.* [20], the silicon and manganese content were in the range of 0~0.2 wt% and 0~0.017 wt%, respectively. Therefore, in order to have a consistent basis for comparison, only one data set in the study of Diao *et al.* [23] was chosen where the metal silicon and manganese content were 0.04 wt% and 0.07 wt%, respectively. These data are presented in Figure 6.8 and used to determine k_m .

Table 6.5 Mass transfer coefficients calculated from experimental data [19-21, 23].

Investigator	wt% FetO	$k_o \times$ $10^2/(cm/s)$	Initial L_p	$k_{FeO} \times$ $10^2/(cm/s)$	$k_m \times$ $10^2/(cm/s)$
Mori <i>et al.</i> [19]	16.3	0.54	258	0.20	0.55
Mori <i>et al.</i>	37.3	1.46	184	2.31	1.47
Mori <i>et al.</i>	43.9	1.31	155	3.25	1.32
Wei <i>et al.</i> [20]	3.16	0.18	8263	0.10	0.18
Wei <i>et al.</i>	10	0.42	47032	0.14	0.42
Wei <i>et al.</i>	15	1.45	47826	0.19	1.45
Shibata <i>et al.</i> [21]	4.5	0.29	334	0.10	0.30
Shibata <i>et al.</i>	29.7	3.40	30	1.44	4.15
Diao <i>et al.</i> [23]	66.04	2.25	19500	7.67	2.38

If one replaces the oxygen activity h_o in Eq. (6.11) with Eq. (6.26) and the gas velocity μ with Eq. (6.16), one can obtain Eq. (6.27). This equation is similar to Eq. (6.19) but in this case the oxygen activity is assumed to be set by the FeO/Fe equilibrium. The empirical equation developed by Basu *et al.* [47] (Eq. (6.28)) can be used to estimate the activity coefficient of FeO, γ_{FeO} .

$$(\text{FeO}) = [\text{Fe}] + [O] \quad (6.24)$$

$$\log K_{Fe} = \frac{-6372}{T} + 2.73 \quad (6.25)$$

$$h_O = \frac{K_{Fe} a_{FeO}}{h_O a_{Fe}} \quad (6.26)$$

$$k_m = \left[\frac{h_C D K_{CO} \left(\frac{K_{Fe} a_{FeO}}{a_{Fe}} \right)^2}{\pi \sigma} \frac{n_e W_m}{AM_{OFe}} \exp \left(\frac{-\Delta H}{kT} \right) \left[\frac{2(\varphi\sigma)}{\pi m} \right]^{1/2} \exp \left(\frac{-16\pi(\varphi\sigma)^3}{3kT \left(h_C K_{CO} \frac{K_{Fe} a_{FeO}}{a_{Fe}} \right)^2} \right) \right]^{1/2} \quad (6.27)$$

$$\log \gamma_{FeO} = -0.7335 \log X_{FeO} - 0.2899 \quad (6.28)$$

where X_{FeO} is mole fraction of FeO in the slag.

Taking the logarithm of Eq. (6.27) and rearranging, one can obtain:

$$\ln k_m = \ln a_{FeO} - \frac{8\pi(\varphi\sigma)^3}{3kT(h_C K_{CO} K_{Fe}/a_{Fe})^2} \frac{1}{a_{FeO}^2} + \frac{1}{2} \ln \left[\frac{h_C D K_{CO} \left(\frac{K_{Fe}}{a_{Fe}} \right)^2}{\pi \sigma} \frac{n_e W_m}{AM_{OFe}} \exp \left(\frac{-\Delta H}{kT} \right) \left[\frac{2\varphi\sigma}{\pi m} \right]^{1/2} \right] \quad (6.29)$$

From Eq. (6.29), it can be seen that $\ln k_m$ is a function of $\ln a_{FeO} - \frac{8\pi(\varphi\sigma)^3}{3kT(h_C K_{CO} K_{Fe}/a_{Fe})^2} \frac{1}{a_{FeO}^2}$.

Similarly rearranging Eq. (6.29) yields the following equation,

$$\ln \frac{k_m}{a_{FeO}} = - \frac{8\pi(\varphi\sigma)^3}{3kT(h_C K_{CO} K_{Fe}/a_{Fe})^2} \frac{1}{a_{FeO}^2} + \frac{1}{2} \ln \left[\frac{h_C D K_{CO} \left(\frac{K_{Fe}}{a_{Fe}} \right)^2}{\pi \sigma} \frac{n_e W_m}{AM_{OFe}} \exp \left(\frac{-\Delta H}{kT} \right) \left[\frac{2\varphi\sigma}{\pi m} \right]^{1/2} \right] \quad (6.30)$$

Then $\ln \frac{k_m}{a_{FeO}}$ for all cases in Table 6.5 can be plotted against $\frac{1}{a_{FeO}^2}$, as presented in Figure 6.9.

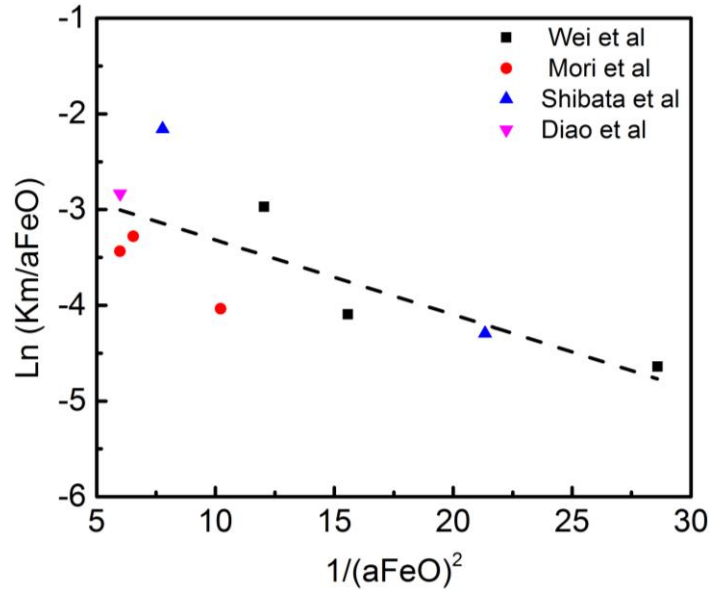


Figure 6.9 The relationship between $\ln \frac{k_m}{a_{FeO}}$ and $\frac{1}{a_{FeO}^2}$ based on Eq. (6.30).

The slope of the dashed line in Figure 6.9 is -0.078. Using this value, the surface tension modifying parameter, φ is calculated to be 0.0078 for the case of Wei *et al.* [20], which is consistent with the value determined by Chen [40] which varied from 0.0019 to 0.0053 for slag containing FeO from 3 wt% to 10 wt%. However, there is some scatter in the data presented in Figure 6.9. This may merely be a consequence of combining data obtained under a range of experimental conditions but may also suggest that instead of considering the oxygen activity in the melt to be in equilibrium with FeO in the slag, one should consider kinetic factors in determining the oxygen activity. A strong argument could be made that the oxygen activity driving CO nucleation is set by a similar balance of supply and consumption used to define the driving force for dephosphorization.

6.5 Conclusion

Employing the mixed mass transport control model for dephosphorization of iron-carbon alloy, the mass transfer coefficient of phosphorus in metal phase k_m was determined for a wide range of conditions and analyzed assuming a penetration model based on CO bubble formation. The effect of droplet mass on the dephosphorization kinetics of bloated metal

droplets was determined and analyzed to elucidate the influence of CO gas velocity on k_m . Published dephosphorization data was used to demonstrate the general applicability of the modified surface renewal equation by investigating factors affecting k_m , such as silicon in the metal, iron oxide in slag and temperature. The following conclusions can be made from the current study.

1. The measured values for k_m increase with CO gas velocity across the interface, which was in qualitative agreement with surface renewal based on gas bubbles crossing the slag-metal interface.
2. Increasing silicon in the metal decreased k_m by holding down the oxygen potential thereby suppressing the formation of CO bubbles. Quantitative analysis of this effect agreed fairly well with theoretical predictions based on surface renewal by CO bubbles.
3. For the hot metal containing silicon, k_m increased as temperature increased in reasonable accord with the temperature dependency of silicon oxidation.
4. The effect of FeO in the slag on k_m is in general agreement with mass transfer based on surface renewal by CO bubbles. However, quantitative analysis suggests that the transport limitations to the supply of oxygen by FeO should be included in the calculation.

6.6 Appendix

In the case of Diao *et al.* [23], all experiments were conducted at 1623 K using a slag of 22.64 wt% CaO-5.66 wt% SiO₂-5.66 wt% Na₂O-66.04 wt% Fe₂O₃ with a viscosity of 0.381 poise. Moriya *et al.* [16] had investigated the hot metal dephosphorization using single Na₂O₃ component at 1523 K under a variety of conditions. Inoue *et al.* [14] studied the influence of silicon in the iron on dephosphorization of a carbon saturated iron alloy using a calcium sulfate flux at 1523 K. Suito *et al.* [15] investigated the effect of silicon on hot metal dephosphorization using sodium carbonate-sodium sulfate flux at 1523 K. Metal compositions for all these cases are shown in Table 6.A1.

Table 6.A1 Metal composition used in other researchers' work (wt%)^[14-16, 23].

	Metal(g)	Si	Mn	P	S	C
	100	0.04	0.07	0.42	0.013	3.78
Diao <i>et al.</i> ^[23]	100	0.1	0.3	0.36	0.015	3.9
	100	0.48	0.3	0.35	0.3	4.4
	7000	0	0.7	0.25	0.03	3.5
Moriya <i>et al.</i> ^[16]	7000	0	0.7	0.25	0.03	3.5
	7000	0.1	0.7	0.25	0.03	3.5
	7000	0.3	0.7	0.25	0.03	3.5
	7000	0.6	0.7	0.25	0.03	3.5
Inoue <i>et al.</i> ^[14]	430	0		0.1	0.05	saturated
	430	0.5		0.1	0.05	saturated
Suito <i>et al.</i> ^[15]	430	0		0.1		saturated
	430	0.5		0.1		saturated

Kitamura *et al.*^[22] investigated the temperature effect on mass transfer coefficient in metal phase under fixed stirring energy using 70 kg liquid iron containing silicon using 9.1 wt% CaO-90.9 wt% Fe₂O₃ flux. The metal composition is listed in Table 6.A2.

Table 6.A2 Metal compositions (wt%) in the work of Kitamura *et al.*^[22]

	T/K	Si	Mn	P	S	C
Case	1623					4.0-
A	1873	1.2-1.5	<0.30	<0.1	<0.05	4.5
Case	1623	0.10-	0.30-	0.10-	0.03-	4.0-
B	1823	0.15	0.40	0.15	0.04	4.5

Mori *et al.*^[19] investigated dephosphorization kinetics of Fe-4 wt% C-0.1 wt% P alloy using different slag compositions at 1653 K. Wei *et al.*^[20] studied the dephosphorization of Fe-C_{sat}-0.1 wt% P varying the iron oxide content and oxygen partial pressure in the atmosphere at 1573 K. Varying the amount of FeO and MnO, Shibata *et al.*^[21] investigated

the kinetics of simultaneous reactions between liquid iron-carbon alloys and slag. The related slag compositions used in this study from those researchers are listed in Table 6.A3.

Table 6.A3 Slag Compositions used in this study from other researchers (wt%) ^[19-21].

Investigators	CaO	SiO ₂	FeO	NaCl/CaCl ₂	LiO ₂	CaF ₂	MnO
	29	27.92	16.33	16.67			
Mori <i>et al.</i> ^[19]	21.75	20.94	37.25	12.5			
	19.44	18.72	43.91	11.17			
	32.63	34.93	15.01		17.42		
Wei <i>et al.</i> ^[20]	34.78	37.23	9.42		18.57		
	37.22	39.84	3.06		19.87		
	29.4	32.1	29.7			8.8	
Shibata <i>et al.</i> ^[21]	30.3	33.3	4.5			9.5	22.4

6.7 References

1. K. ITO and N. Sano: *Trans. ISIJ*, 1985, vol. 25, pp. 355-62.
2. J. J. Pak and R. J. Fruehan: *Metall. Trans. B*, 1986, vol. 17B, pp. 797-03.
3. C. Nassaralla and R. J. Fruehan: *Metall. Trans. B*, 1992, vol. 23B, pp. 117-123.
4. J. IM, K. Morita and N. Sano: *ISIJ Int.*, 1996, no. 5, vol. 36, pp. 517-521.
5. W. H. Van Niekerk: *Metall. Trans. B*, 1998, vol. 29B, pp. 147-152.
6. J. O. Borode: *Ironmak. Steelmak.*, 1998, vol. 25 (2), pp. 144-49.
7. C. M. Lee and R. J. Fruehan: *Ironmak. Steelmak.*, 2005, vol. 32 (6), pp. 503-507.
8. V. D. Eisenhuttenleute: *Slag Atlas*, 2nd editions, 1995, pp. 10-19.
9. T. Mori: *Trans. Jpn. Inst. Metals*, 1984, vol. 25 (11), pp.761-71.
10. H. Ishii and R. J. Fruehan: *ISS Trans.*, February, 1997, pp. 47-54.
11. G. Li, T. Hamano and F. Tsukihashi: *ISIJ Int.*, 2005, no. 1, vol. 45, pp. 12-18.
12. B. J. Monaghan, R.J. Pomfret, and K.S. Coley: *Metall. Trans. B*, 1998, vol. 29B, pp. 111-18.
13. E. T. Turkdogan: *ISIJ Int.*, 2000, vol. 40 (10), pp. 964-70.
14. R. Inoue and H. Suito: *Trans. ISIJ*, 1981, vol. 21, pp. 165-72.
15. H. Suito, A. Ishizaka, R. Inoue and Y. Takahashi: *Trans. ISIJ*, 1981, vol. 21, pp. 156-64.

16. T. Moriya and M. Fujii: *Trans. ISIJ*, 1981, vol. 21, pp. 732-741.
17. J. J. Pak and R. J. Fruehan: *Metall. Trans. B*, 1987, vol. 17B, pp. 687-92.
18. S. Ohguchi, D. G. C. Robertson, B. Deo, P. Grieveson and J. H. E. Jeffes: *Ironmak. Steelmak.*, 1984, vol. 11, pp. 202-13.
19. K. Mori, Y. Fukami and Y. Kawai: *Trans. ISIJ*, 1988, vol.28, 315-18.
20. P. Wei, M. Sano, M. Hirasawa, and K. Mori: *ISIJ.Int.*, 1993, vol. 33, 479-87.
21. E. Shibata, H. Sun and K. Mori: *Metall. Trans. B*, 1999, vol. 30B, pp. 279-86.
22. S. Kitamura, T. Kitamura, K. Shibata, Y. Mizukami and S. Mukawa and J. Nakagawa: *ISIJ Int.*, 1991, vol. 31 (11), pp. 1322-28.
23. J. Diao, X. Liu, T. Zhang and B. Xie: *International Journal of Minerals, Metallurgy and Materials*, 2015, no. 3, vol. 22, pp. 249-53.
24. A. K. Hewage, B. K. Rout, G. Brooks and J. Naser: *Ironmak. Steelmak.*, 2016, vol.43 (5), pp. 358-370
25. M. S. Millman, A. Kapilashrami, M. Bramming and D. Malmberg: Final Report of Imphos, European Commission, 2011.
26. K. Gu, N. Dogan and K. S. Coley: *Metall. Trans. B*, DOI: 10.1007/s11663-017-1002-0.
27. K. Gu, N. Dogan and K. S. Coley: *Metall. Trans. B*, DOI: 10.1007/s11663-017-1000-2.
28. K. Kunisada and H. Iwai: *Trans. ISIJ*, 1986, vol. 26, pp. 121-27.
29. M. Nasu, K. C. Mills, B. J. Monaghan A. Jakobsson and S. Seetharaman: *Ironmak. Steelmak.*, 1999, vol.26 (5), pp. 353-57.
30. C. P. Manning and R. J. Fruehan: *Metall. Trans. B*, 2013, vol. 44B, pp. 37-44.
31. A. Assis, J. Warnett, S. Spooner, R. Fruehan, M. Williams and S. Sridhar: *Metall. Trans. B*, 2015, vol. 46B, pp. 568-76.
32. S. Spooner, A. Assis, J. Warnett, R. Fruehan, M. Williams and S. Sridhar: *Metall. Trans. B*, 2016, vol. 47B, pp. 2123-32.
33. K. Gu, N. Dogan and K. S. Coley: *Metall. Trans. B*, Manuscript # [E-TP-17-79-B](#).
34. R. Higbie: *Trans. Am. Inst. Chem. Eng.*, 1935, vol. 31, pp. 365-89.
35. Y. Kawai and Y. Shiraishi: *Handbook of Physico-chemical Properties at High Temperatures*, 1988, pp. 13-14.
36. V. D. Eisenhuttenleute: *Slag Atlas*, 2nd edition, 1995, pp. 345-46.
37. M. Hino and K. Ito: *Thermodynamic Data for Steelmaking*, Tohoku University Press, Sendai. 2009, pp. 259-64.
38. E. Chen and K. S. Coley: *Ironmak. Steelmak.*, 2010, vol. 37(7), pp. 541-45.
39. M. Pomeroy: Master Thesis, McMaster, Hamilton, CA, 2011, pp.42-66.
40. E. Chen: PhD Thesis, McMaster, Hamilton, CA, 2011, pp.59-99.
41. H. Sun: *ISIJ Int.*, 2006, vol. 46 (11), pp. 1560-69.
42. Y. Chung and A. Cramb: *Metall. Trans. B*, 2000, vol. 31B, pp. 957-71.
43. S. Seetharaman, A. Mclean, R. Guthrie and S. Sridhar: *Treatise on Process Metallurgy*, 2014, vol. 3, pp. 195.
44. H. S. Levine: *Metall. Trans. B*, 1973, vol. 4, pp. 777-82.
45. H. S. Levine: *Metall. Trans. B*, 1974, vol. 5, pp. 953-55.
46. H. Kwak and S. Oh: *J. Colloid and Interface Sci.* 198, 1998, pp.113-18.
47. S. Basu, A.K. Lahiri and S. Seetharaman: *Metall. Trans. B*, 2008, vol. 39B, pp. 447-56.

Chapter 7

Application of High Basicity Slag

In chapter 7, experiments were performed jointly by Philip Drain (PhD student from The University of Wollongong) and myself. I assisted him with droplet preparation and in developing his experimental technique. He conducted most of the experiments. The data analysis shown in this chapter was conducted by me with input from Philip Drain and Dr. Kenneth S. Coley. The chapter will form part of a collaborative publication with The University of Wollongong and has been included here with the permission of Dr. Brian Monaghan and Philip Drain (University of Wollongong’s Australian Research Council Research Hub for Australian Steel Manufacturing and the School of Mechanical, Materials, Mechatronic and Biomedical Engineering).

7.1 Introduction

This short chapter describes the application of the results and ideas contained in this thesis to real steelmaking slag with high basicity. This is designed to test concepts developed in the foregoing chapters to conditions more relevant to steelmaking. It consists of three sections, the first describes the experimental procedure, the second presents experimental results on dephosphorization and decarburization behavior of metal droplets and the third offers some discussion of the results.

7.2 Experimental Procedure

The experimental setup and procedure was as described in Chapter 3 with some important modifications. Instead of an Al_2O_3 crucible, a MgO crucible with 38.1 mm diameter and 76.2 mm height was used. The metal droplet was 1.0 g and with composition of Fe-2.51 wt% C-0.007 wt% S-0.072 wt% P. The slag composition employed here was 50.6 wt% CaO-19.9 wt% SiO_2 -4.8 wt% MgO -24.7 wt% FeO. All experiments were carried out at

1923 K; 10 degrees higher than the one employed in the other experiments presented in this thesis.

7.3 Experimental Results

Figure 7.1 shows the total amount of CO gas generated during the reaction as a function of time. It can be seen that the initial decarburization rate is 4 times higher than the secondary rate, 47.1×10^{-5} mole/s versus 11.4×10^{-5} mole/s. Unlike the other cases presented in this thesis where there is a slow initial decarburization period prior to the internal nucleation of CO. This case exhibits zero incubation time, as demonstrated by the instant swelling of the droplet shown in Figure 7.2.

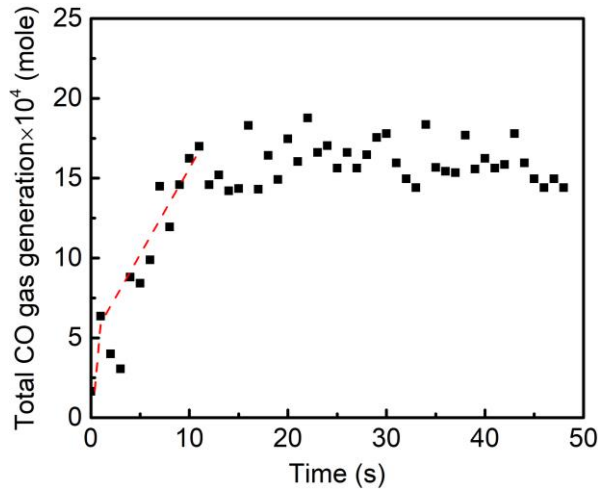


Figure 7.1 CO gas generation with time.

Figure 7.2 shows the change in the volume of droplets as a function of time. It can be seen that the volume of the metal droplet increases by 4 times almost as soon as it fell into the slag. High basicity slag containing FeO can offer larger oxygen flux ^[75, 92-93] as will higher temperature, hastening the onset of internal CO nucleation.

The dephosphorization behavior of a 1.0 g droplet is presented in Figure 7.3, showing that phosphorus in the droplet is removed very rapidly, dropping from 0.072 wt% to 0.019 wt% within 1 second, thereafter gradually decreasing.

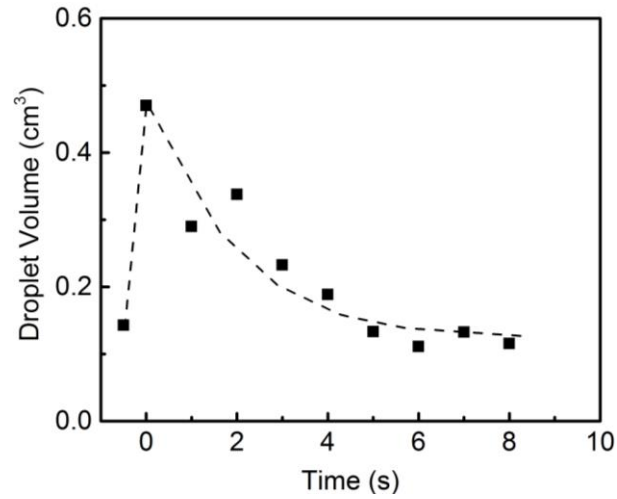


Figure 7.2 The change of droplet volume as a function of time.

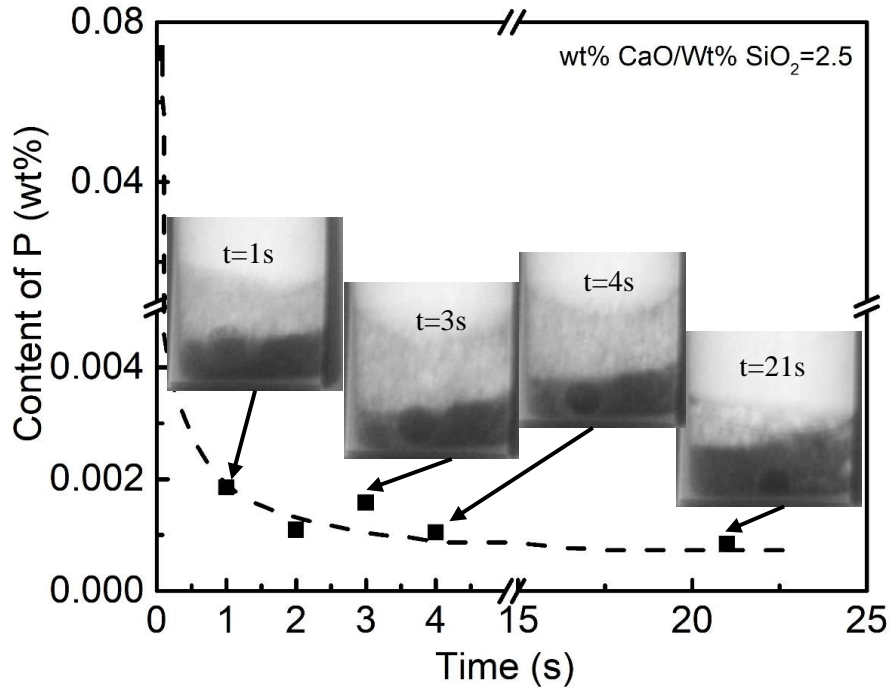


Figure 7.3 Plot of dephosphorization as a function of time at 1923 K.

7.4 Discussion

Using the approach described in the earlier chapters of this thesis, the initial partition coefficient was calculated to be approximately 10^4 . The measured value based on the minimum concentration of phosphorus in the metal was 14, a hundred times higher than

for the low basicity slags considered in earlier chapters. Given this relatively high initial partition coefficient, the rate controlling step for dephosphorization under real steelmaking slag is more likely to be mass transfer in metal phase. Then the following integrated rate equation for phosphorus transfer in the metal can be used to estimate k_m :

$$\ln \left[\frac{[\text{wt}\% \text{ P}]_b - [\text{wt}\% \text{ P}]_e}{[\text{wt}\% \text{ P}]_o - [\text{wt}\% \text{ P}]_e} \right] \left(\frac{[\text{wt}\% \text{ P}]_o - [\text{wt}\% \text{ P}]_e}{[\text{wt}\% \text{ P}]_o} \right) \left(\frac{W_m}{\rho_m A} \right) = -k_m t \quad (7.1)$$

where W_m is the mass of the metal droplet, k_m is the mass transfer coefficient for phosphorus in the metal, ρ_m is the density of metal, $[\text{wt}\% \text{ P}]_o$, $[\text{wt}\% \text{ P}]_b$ and $[\text{wt}\% \text{ P}]_e$ are the initial, bulk and equilibrium concentrations of phosphorus in the metal.

Setting $C = \frac{[\text{wt}\% \text{ P}]_b - [\text{wt}\% \text{ P}]_e}{[\text{wt}\% \text{ P}]_o - [\text{wt}\% \text{ P}]_e}$ and $B = \left(\frac{[\text{wt}\% \text{ P}]_o - [\text{wt}\% \text{ P}]_e}{[\text{wt}\% \text{ P}]_o} \right) \left(\frac{W_m}{\rho_m A} \right)$, Eq. (7.1) becomes $B \ln C = -k_m t$.

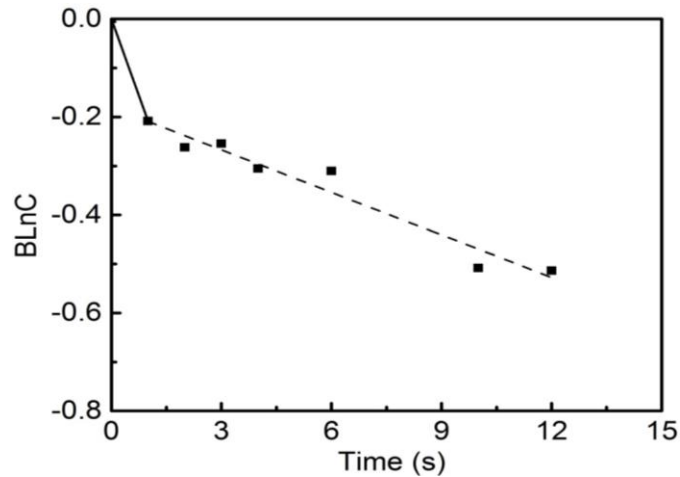


Figure 7.4 Dephosphorization data from Figure 7.3 is replotted as a function of time based on Eq. (7.1).

The data shown in Figure 7.3 was plotted in Figure 7.4 according to Eq. (7.1). Figure 7.4 shows that the data follow two distinct slopes representing two different mass transfer coefficients for phosphorus. It is worth noting that the only data point for the first stage of reaction is the initial droplet composition. In plotting Figure 7.4, it has been assumed that the first reaction stage ends at the first data point in the second stage. Whilst there is no justification for this choice, it offers the most conservative estimate of the mass transfer

coefficient in the initial stage of reaction. The mass transfer coefficient estimated for the initial stage is 20.9×10^{-2} cm/s, which is 7 times higher than the value of k_m determined for the second stage of dephosphorization (2.89×10^{-2} cm/s). Given the higher decarburization rate during the initial stage, a higher mass transfer coefficient would be expected due to faster surface renewal.

According to surface renewal theory expressed as Eq. (7.2), assuming the CO bubbles are the same size at different stages, the ratio of the mass transfer coefficient in the initial stage to that for the second stage would be equal to the square root of the ratio of the CO gas velocities shown as Eq. (7.3).

$$k_m = 2 \left(\frac{D\mu}{\pi d} \right)^{1/2} \quad (7.2)$$

$$\frac{k_{m1}}{k_{m2}} = \left(\frac{\mu_1}{\mu_2} \right)^{1/2} \quad (7.3)$$

Using the decarburization data and droplet surface area, the predicted ratio of the initial to final value of k_m was 1.5, which is a factor of 5 lower than the measured ratio. One possible reason for this discrepancy is the bubble size. According to Eq. (5.19), the bubble size would be expected to be smaller if, as is likely, a higher oxygen potential, was operating during the initial stage of reaction. In Chapter 5, it is demonstrated that the bubble sizes have a significant influence on mass transfer coefficient of phosphorus in the metal phase. Therefore, instead of assuming the same bubble size, different values should be considered in Eq. (7.2) at different stages of reaction. It is also worth noting that lower decarburization rate leads to a smaller mass transfer coefficient, this phenomenon had also been observed in the case of low basicity slag, and demonstrated to apply across a range of conditions as shown in Chapters 5 and 6. In Chapter 5, it was shown that k_m at the stage of renewed dephosphorization was lower than the initial dephosphorization period due to the weaker stirring at the final stage with a much lower decarburization rate.

It is worth considering the rather surprising observation, that increasing the basicity of the slag increases the mass transfer coefficient in the metal. In the case of low basicity slag but

similar metal droplet composition, the mass transfer coefficient of phosphorus was calculated to be 1.6×10^{-2} cm/s at 1913 K, compared with 20.9×10^{-2} cm/s for higher basicity slag at 1923 K. This observation may be attributed in part to the decarburization rate, 6.5×10^{-5} mole/s for experiments with lower basicity slag compared to 47.1×10^{-5} mole/s for the case of high basicity slag. However, the dephosphorization rate increased by a factor of 13 in going from low basicity slag to higher basicity slag whereas the increase in the decarburization rate was a factor of 7. If one recognizes that the faster decarburization rate is related to faster transport of oxygen in the slag, it is likely that the oxygen potential in the metal will be higher for higher basicity slags. Bearing in mind that the critical nucleus size for CO bubbles will be smaller at higher oxygen potentials, it is likely that the CO bubble size will be smaller for experiments involving higher basicity slags. The additional effect of bubble size could quite reasonably account for the difference between the increase in decarburization rate and the increase in mass transfer coefficient for phosphorus.

7.5 Summary

1. When high basicity slag is employed, the dephosphorization of metal droplets is much faster compared to the case of low basicity slag, with mass transfer coefficient $k_m = 20.9 \times 10^{-2}$ cm/s. This is most likely due to the combined effects of faster decarburization and smaller CO bubbles. The effect of basicity on both decarburization rate and bubble size appears to be associated with faster oxygen transport in the basic slag.
2. The proposed mechanism for mass transfer of phosphorus in metal phase via surface renewal theory based on CO bubble generation, can be used to explain the high mass transfer coefficient for phosphorus in the metal observed in the case of high basicity slag.

Chapter 8

Concluding Remarks

This thesis has focused on understanding dephosphorization kinetics of bloated metal droplets in the emulsion zone of a basic oxygen furnace, which is associated with intensive decarburization. By combining kinetic data for dephosphorization of metal droplets with their decarburization behavior, *i.e.*, swelling behavior and CO evolution rate, the interplay between dephosphorization and decarburization has been investigated. This work represents a thorough analysis of the influence of decarburization on the driving force and kinetics of dephosphorization of bloated droplets.

8.1 Key Findings and Contributions

8.1.1 General Overview

Chapters 1 and 2 highlight the importance of bloated droplets to dephosphorization in BOF steelmaking and outline the key parameters required to model dephosphorization:

1. droplet residence time in the slag;
2. driving force for dephosphorization as defined by phosphate capacity and the competition between oxygen supply and consumption;
3. the overall mass transfer coefficient of phosphorus as determined by combining mass transfer coefficients for the metal and slag with the partition coefficient of phosphorus.

The role of droplet bloating on residence time has been tackled by other workers. In the current study the focus has been on quantifying a dynamically changing driving force, and the factors affecting mass transfer of phosphorus.

Chapters 3 and 4 combine to address the role of a driving force which changes with time. Chapter 3 contributes an understanding of the effects decarburization rate and metal sulfur content, on the interfacial oxygen potential. Chapter 4 presents a model to calculate the dynamic interfacial oxygen potential and analyzes its effect, on the balance between control by mass transport in the metal and the slag. Chapter 4 also introduces additional understanding of oxygen transport in a foamy slag.

Chapters 5 and 6 address the transport properties of phosphorus in the metal. Chapter 5 proposes the combination of surface renewal theory with the theory of CO bubble nucleation, successfully describing the effect of various parameters on the mass transport of phosphorus. Chapter 6 illustrates the general application of the mass transport mechanism proposed in Chapter 5. Chapter 7 applies the ideas developed in Chapters 3-6 to the analyze data for dephosphorization of bloated droplets using a typical basic slag of real steelmaking conditions.

8.1.2 Specific Findings

Experimental measurements and theoretical analysis have been conducted on dephosphorization kinetics for Fe-C-S-P droplets in CaO-SiO₂-Al₂O₃-FeO slag. The research objectives presented in chapter 1 have been achieved, and key findings of this work include:

1. The influence of decarburization rate on dephosphorization kinetics has been investigated in Chapter 3 of this work by varying sulfur content in metal droplet that strongly affects CO evolution rate. It was found that the phosphorus partition ratio, the driving force of dephosphorization, showed a strong inverse relationship with increasing CO evolution rate because the associated oxygen consumption decreases the interfacial oxygen potential.
2. In Chapter 3, kinetic analysis of dephosphorization for bloated metal droplets showed that the rate controlling step is first mixed control by mass transport in both metal and slag and then shifts to mass transport in slag as the phosphorus partition ratio decreases because

of FeO depletion in the slag. This observation may help rationalize different findings in literature on rate controlling steps of dephosphorization, which are divided between mass transfer in the slag and some form of mixed control.

3. In Chapter 4, a mathematical approach was developed to calculate the dynamic interfacial oxygen potential during dephosphorization between an iron carbon alloy and oxidizing slag. With this model, the shifts of rate determining step for dephosphorization due to the dynamic interfacial oxygen potential was successfully predicted in an agreement with the experimental observations, that the rate control changes from mass transport in both metal and slag phases to mass transport in slag. Employing this approach, the dephosphorization kinetics for metal droplets in the emulsion zone under real steelmaking conditions was investigated and found to be limited by mass transport in the metal phase, which is contrary to most laboratory studies.

4. In Chapter 4 the mass transfer coefficient of “FeO” in slag was determined over a range of conditions showing that k_{FeO} is a strong linear function of the fraction of liquid slag, the transport pathways being limited to the liquid portion. In addition, k_{FeO} shows a parabolic correlation with total iron oxide in the slag which is consistent with transport being controlled by charge balancing by small polaron hopping via an Fe^{3+}/Fe^{2+} couple. This finding offers important insight into the mechanism of oxygen transport, a factor of general importance in slag-metal reactions.

5. In Chapter 5 dephosphorization kinetics were investigated for two types of droplet, *i.e.*, carbon containing droplets and carbon free droplets, to elucidate the influence of CO bubbles on mass transfer of phosphorus in the metal phase. An approach was proposed to separate mass transfer coefficient k_m from overall mass transfer coefficient k_o . This analysis showed that k_m for carbon containing droplet is two orders of magnitude higher than that for carbon free droplets because of the stirring effect provided by CO bubbles, which offers a faster surface renewal rate.

6. The well established surface renewal theory was modified to include CO generation rate

and bubble size. These effects were used to explain the temperature effect on the mass transfer coefficient of phosphorus in metal phase. The analysis showed that the formation of smaller CO bubbles is responsible for the higher k_m at lower temperature, which increases the rate of surface renewal and leads to faster mass transport. The modified surface renewal theory offers us a new approach to investigate the influence of CO bubbles on mass transfer coefficient and to explain the effect of a number of factors.

7. Chapter 6 demonstrates the general applicability of the relationship between nucleation of CO bubbles and the mass transfer coefficient of phosphorus in the metal phase. A series of dephosphorization experiments were carried out to study the effect on k_m of CO gas velocity across the slag-metal interface, the modified surface renewal theory, yielded good agreement with experimental data.

8. In Chapter 6 surface renewal theory was combined with theoretical relations for CO nucleation to investigate the effect on k_m , of silicon in the metal, iron oxide in slag and temperature. Published data under a wide range of conditions showed excellent qualitative agreement with the modified surface renewal theory.

9. Results from Chapter 7 demonstrated that dephosphorization is very rapid and reaches local equilibrium almost instantaneously when real steelmaking slag is employed. This observation greatly simplifies the modeling of dephosphorization in the BOF, where assuming the residence time is longer than a few seconds, we can ignore the kinetics of dephosphorization and assume each individual droplet reaches equilibrium with the dynamic oxygen potential existing at that time in the blow.

8.2 Future Work

Studies of dephosphorization kinetics by using high sulfur content droplets are needed to understand the observed slower dephosphorization rate for 0.021 wt% S droplets compared to other lower sulfur droplets in Chapter 3.

The approach, tied the modified surface renewal theory to CO nucleation equation, has

been demonstrated to be a promising method to explain the relationship between the formation of CO bubbles and the mass transfer in metal phase. However, a complete model with the combination of surface renewal theory and CO nucleation process inside metal droplet would be useful to predict the kinetics of refining reactions between metal droplet and slag in emulsion zone.

Finally, this work has showed that dephosphorization of metal droplet is fast enough and reaches local equilibrium within few seconds, which enable us to simplify the modeling of dephosphorization in BOF by ignoring kinetic process. It would be interesting to test this conclusion by using industrial data. Therefore, based on these observations, modeling of dephosphorization in real BOF would be the next step in this project.

Appendix

Error Analysis

The uncertainty involved in the experimental data includes random and systematic error. There are two approaches to determine random errors introduced in the processed experimental results ^[134]. In one approach, random error can be estimated by repeating measures and using the standard deviation of the mean $S_{\bar{X}}$ as the absolute error. For example, the mean of N measurements on the same variables can be calculated by:

$$\bar{X} = \frac{1}{N} \sum_1^N X_i \quad (\text{A.1})$$

The standard deviation represents the average uncertainty in the individual measurement, which is calculated via Eq. (A.2):

$$S_X = \sqrt{\frac{1}{N-1} \sum (X_i - \bar{X})^2} \quad (\text{A.2})$$

Then the standard deviation of the mean is given by:

$$S_{\bar{X}} = \frac{S_X}{\sqrt{n}} \quad (\text{A.3})$$

The relative uncertainty can be determined by the following formula:

$$\delta_{\bar{X}} = 100\% \frac{S_{\bar{X}}}{\bar{X}} \quad (\text{A.4})$$

In another approach, when the repeat of measurements is not available, the uncertainty in the desired quantity is evaluated by propagating errors of the original parameters, which are used to calculate the desired quantity. Given a function

$$y = f(x_1, x_2, \dots, x_i) \quad (\text{A.5})$$

where x_1, x_2, \dots, x_i are independent variables and the standard deviations are given by $\delta_{x_1}, \delta_{x_2}, \dots, \delta_{x_i}$. If the errors of these measurements are independent of each other, the standard deviation of y is given by the following formula:

$$\delta_y^2 = \left(\frac{\partial f}{\partial x_1}\right)^2 \delta_{x_1}^2 + \left(\frac{\partial f}{\partial x_2}\right)^2 \delta_{x_2}^2 + \dots + \left(\frac{\partial f}{\partial x_i}\right)^2 \delta_{x_i}^2 \quad (\text{A.6})$$

Then the error of the desired quantity is equal to

$$100\% \frac{\delta_y}{|y|} \quad (\text{A.7})$$

Not all of the experiments have been repeated in this study. The random errors for some measurements are calculated and listed in Table A.1 where N represents the number of measurements.

Table A.1 Calculated errors for some experiment results.

Variables	N1	N2	N3	N4	N5	N6	average	Error %
[wt% P] _o	0.089	0.077	0.076	0.093	0.084	0.100	0.087	4.15
[wt% C] _o	2.60	2.58	2.68				2.62	1.0
[wt% C] _o	2.63	2.60	2.483	2.468	2.483	2.412	2.513	1.25
[wt% S] _o	0.0076	0.0077	0.0062	0.0087	0.0071	0.0070	0.0074	0.30
Decarburization rate-0.007 wt% S,1853 K($\times 10^5$ /mole/s)				6.06	5.59		5.82	2.84
Decarburization rate-0.014 wt% S,1853 K($\times 10^5$ /mole/s)				10.53	11.19	9.44	10.39	4.01

The determination of phosphorus partition coefficient L_P was taken for example to show the calculation of the propagation of errors in this study. The uncertainties for L_P are mainly considered to be a combination of the uncertainties in the concentration determination by ICP and weight-loss determination. L_P can be calculated via Eq. (A.8),

$$L_P = \frac{(\text{wt}\% \text{ P})_e}{[\text{wt}\% \text{ P}]_e} = \frac{W_m}{W_s} \left(\frac{[\text{wt}\% \text{ P}]_o}{[\text{wt}\% \text{ P}]_e} - 1 \right) \quad (\text{A.8})$$

where W_m and W_s are mass of metal droplet and of slag, respectively; $[\text{wt}\% \text{ P}]_o$ is initial phosphorus concentration while $[\text{wt}\% \text{ P}]_e$ is phosphorus concentration at the reversion.

The relative uncertainty for each term in Eq. (A.8) and the calculated propagated error are given in Table A.2.

The systematic errors in this study are mainly from the chemical analysis and the calibration of the pressure transducer. For chemical analysis such as ICP and LECO measurements, standard samples were used to reduce the error from instruments. Efforts also have been made to get accurate measurements from the pressure transducer, such as calibrated the pressure transducer periodically, and checked the leakage of the furnace at high temperature. The calibrated results from pressure transducer were also confirmed with results from LECO tests. As discussed in the previous random error part, the uncertainties in these experimental measurements are around 5%, which are within acceptable limits.

Table A.2 Uncertainty sources and estimation.

Source	uncer. contribution	estimation	relative uncertainty %
ICP	concentration	repeat measurement	± 5
scale	slag mass	0.5 g/25g	± 2
scale	droplet mass	0.05g/1g	± 5
Propagation of uncertainty (0.007 wt% S at 1853 K)			± 13.34

Reference

- [1] T. Fuji, *Steelmaking*, Transactions of Iron and Steel Institute of Japan, 1985. 25(7): p. 658-69.
- [2] T. A. Bloom, D. R. Fosnacht and D. M. Haezebrouck, *The influence of Phosphorus on the Properties of Sheet Steel Products and Methods Used to Control Steel Phosphorus Levels in Steel Product Manufacturing-Part I*, Iron and Steelmaker (I and SM), 1990, 17(9), p. 35-41.
- [3] A. Scholes, *Segregation in Continuous Casting*, Ironmaking and Steelmaking, 2005, 32(2), p. 101-108.
- [4] H.W.Meyer, W.F.Porter, G.C.Smith and J.Szekely, *Slag-Metal Emulsions and Their Importance in BOF Steelmaking*, Journal of Metals, 1968, July, p.35-42.
- [5] Paul Kozakevitch, *Foams and Emulsions in Steelmaking*, Journal of Metals, 1969, July, p.57-68.
- [6] E.W.Mulholland, G.S.F Hazeldean, and M.W.Davies, *Visualization of Slag Metal Reactions by X-ray Fluoroscopy:Decarburization in Basic oxygen steelmaking*, Journal of the Iron and Steel Institute, 1973, September, p.632-639
- [7] Subagyo, G.A.Brooks and K.S.Coley, *Residence Time of Metal Droplets in Slag Metal Gas Emulsions through Top Gas Blowing*, Canadian Metallurgy Quarterly, 2005, 44(1), p.119-30.
- [8] Geoffrey Brooks and Yuhua Pan, Subagyo and Ken.Coley, *Modeling of Trajectory and Residence Time of Metal Droplets in Slag Metal Gas Emulsion in Oxygen Steelmaking*, Metallurgical and Materials Transactions B, 2005, 36B, p. 525-35.
- [9] Price, L. D. *Steelmaking: Significance of the Emulsion in Carbon Removal*, Process Engineering of Pyrometallurgy, 1974, pp.8-15
- [10] R.C.Urquhart and W.G.Davenport: *Foams and Emulsions in Oxygen Steelmaking*, Canadian Metallurgical Quarterly, 1973, 12(4), p. 507-17.
- [11] E. Chen, *Kinetic Study of Droplet Swelling in BOF Steelmaking*, Ph.D. Thesis, McMaster University, Hamilton, ON, 2011.
- [12] H. Gaye and P. V. Riboud, *Oxidation Kinetics of Iron Alloy Drops in Oxidizing Slags*, Metallurgical and Materials Transactions B, 1977, 8B, p. 409-415.
- [13] C. L. Molloseau, *Waste Oxide Recycling during Oxygen Steelmaking*, PhD thesis, Carnegie-Mellon University, Pittsburgh, PA, 1999.
- [14] C. L. Molloseau and R. J. Fruehan, *The Reaction Behavior of Fe-C-S Droplets in CaO-SiO₂-FeO Slags*, Metallurgical and Materials Transactions B, 2002, 33B, p. 335-44.
- [15] E. Chen and K. Coley, *Kinetic Study of Droplet in BOF Steelmaking*, Ironmaking and Steelmaking, 2010, 37(7), p. 541-45.
- [16] H. Momokawa, N. Sano, *The effect of Oxygen Potential on Phosphorus in the CaO-Al₂O₃ System*, Metallurgical and Materials Transactions B, 1982, 13B, p. 643-44.
- [17] P. Wei, M. Sano, M. Hirasawa, and K. Mori, *Kinetics of Phosphorus Transfer between Iron Oxide Containing Slag and Molten Iron of High Carbon Concentration under Ar-O₂ Atmosphere*, ISIJ International, 1993, 33(4), p. 479-87.

- [18] B.J. Monaghan, R.J. Pomfret, and K.S. Coley, *The Kinetics of Dephosphorization of Carbon-Saturated Iron Using an Oxidizing Slag*, Metallurgical and Materials Transactions B, 1998, 29B, p. 111-18.
- [19] E.T. Turkdogan, *Assessment of P₂O₅ Activity Coefficients in Molten Slags*, ISIJ International, 2000, 40(10), p. 946-970.
- [20] D. Li, G.M. Bancroft, M. Kasrai, M.E. Fleet, X.H. Feng, and K.H. Tan, High-resolution Si and P K- and L-edge XANES Spectra of Crystalline SiP₂O₇ and Amorphous SiO₂-P₂O₅, *American Mineralogist*, 1994, 79(7-8), p. 785–88.
- [21] D. Li, M.E. Fleet, G.M. Bancroft, M. Kasrai, and Y. Pan, *Local Structure of Si and P in SiO₂-P₂O₅ and Na₂O-SiO₂-P₂O₅ glasses: A XANES Study*, *Journal of Non-Crystalline Solids*, 1995, 188(1-2), p. 181–89.
- [22] T.P. Colclough, *The Constitution of Basic Slags: Its Relation to Furnace Reactions*, *Journal of Iron and Steel Institute*, 1923, 107 (1), p. 267–99.
- [23] T.P. Colclough, *A Study of the Reactions of the Basic Open-Hearth Furnace*, *Transactions of the Faraday Society*, 1925, 21, p. 202–23
- [24] C.H. Herty Jr, *Chemical Equilibrium of Manganese, Carbon, and Phosphorus in the Basic Open-Hearth Process*, *Transactions of the Metallurgical Society of AIME*, 1926, 73, p. 1107–34.
- [25] W. Fix, H. Heymann, R. Heinke, *Subsolidus Relations in the System 2CaO-SiO₂-3CaO·P₂O₅*, *Journal of the American Ceramic Society*, 1969, 52(6), p. 346-47.
- [26] H. Preßlinger, M. Mayr and R. Apfelterer, *Quantitative Phase Evaluation of Converter Slags*, *Steel Research International*, 1990, 70(6), p. 209-214.
- [27] H. Hoshino, M. Iwase and A. Mclean, *An Electrochemical Study of Equilibria involving Di-calcium and Tri-calcium Phosphates*, *High Temperature Materials and Processes*, 2004, 23(5-6), p. 377-82.
- [28] H. Takeshita, M. Hasegawa, Y. Kashiwaya and M. Iwase, *Formation Free Energies of Solid Solution between Tri-Calcium Phosphate and Di-Calcium Silicate*, *Steel Research International*, 2010, 81(2), p. 100-04.
- [29] M. Hasegawa, Y. Kashiwaya and M. Iwase, *Thermodynamic Properties of Solid Solutions between Di-Calcium Silicate and Tri-Calcium Phosphate*, *High Temperature Materials and Processes*, 2012, 31(4-5), p. 421-30.
- [30] K.J. Barker, J.R. Paules, N. Rymarchyk and R. M. Jancosko: *Oxygen Steelmaking Furnace Mechanical Description and Maintenance Considerations*, The AISE Steel Foundation, 1998, p.498.
- [31] S. Basu, A. K. Lahiri and S. Seetharaman, *A Model for Activity Coefficient of P₂O₅ in BOF Slag and Phosphorus Distribution between Liquid Steel and Slag*, *ISIJ International*, 2007, 47(8), p.1236-38.
- [32] S. Basu, *Studies on Dephosphorization during Steelmaking*, Doctoral Thesis, Royal Institute of Technology, Stockholm, Sweden, 2007.
- [33] A. Assis, M. Tayeb, S. Sridhar and R. Fruehan, *Phosphorus Equilibrium between Liquid Iron and CaO-SiO₂-MgO-Al₂O₃-FeO-P₂O₅ Slag Part 1: Literature Review, Methodology, and BOF Slags*, *Metallurgical and Materials Transactions B*, 2015, vol. 46B, pp. 2255-63.

- [34] K. Balajiva, A.G. Quarrell and P. Vajragupta, *A Laboratory Investigation of The Phosphorus Reaction in the Basic Steelmaking Process*, The Journal of the Iron and Steel Institute, 1946, 153, p.115-150.
- [35] K. Balajiva, and P. Vajragupta, *The Effect of Temperature on the Phosphorus Reaction in the Basic Steelmaking Process*, The Journal of the Iron and Steel Institute, 1947, 155(4), 1947, p.563-567.
- [36] R.G. Ward: *An Introduction to the Physical Chemistry of Iron and Steel Making*, Edward Arnold, 1962.
- [37] G.W. Healy, *A New Look at Phosphorus Distribution*, The Journal of the Iron and Steel Institute, 1970, 208, p. 664–68.
- [38] H. Suito, R. Inoue, and M. I. Takada, *Phosphorus Distribution between Liquid Iron and MgO Saturated Slags of the System CaO-MgO-FeOx-SiO₂*, Transactions of the Iron and Steel Institute of Japan, 1981, 21(4), p. 250-59.
- [39] H. Suito and R. Inoue, *Effect of Calcium Fluoride on Phosphorus Distribution between CaO-MgO-FeO-SiO₂-Slags and Liquid Iron*, Transactions of the Iron and Steel Institute of Japan, 1982, 22(11), p. 869-77.
- [40] H. Suito, and R. Inoue, *Effect of Na₂O and BaO Additions on Phosphorus Distribution between MgO Saturated Slags of the System CaO-MgO-FeOx-SiO₂ and Liquid Iron*, Transactions of the Iron and Steel Institute of Japan, 1984, 24(1), p. 47-53.
- [41] H. Suito, and R. Inoue, *Phosphorus Distribution between MgO Saturated Slags of the System CaO-MgO-FeO-SiO₂-P₂O₅-MnO and Liquid Iron*, Transactions of the Iron and Steel Institute of Japan, 1984, 24(4), p. 40-46.
- [42] H. Suito and R. Inoue, *Thermodynamic Assessment of Hot Metal and Steel Dephosphorization with MnO-containing BOF Slags*, ISIJ International, 1995, 35(3), p. 258-265.
- [43] X. F. Zhang, I.D. Sommerville, and J.M. Toguri, *Equation for the Equilibrium Distribution of Phosphorus between Basic Slags and Steel*, Transactions of the Iron & Steel Society, 1985, 6, p.29-35.
- [44] S. Basu, A. K. Lahiri and S. Seetharaman, *Phosphorus Partition between Liquid Steel and CaO-SiO₂-FeOx-P₂O₅-MgO Slag Containing 15 to 25 Pct FeO*, Metallurgical and Materials Transactions B, 2007, 38B, p.623-30.
- [45] S. Basu, A. K. Lahiri and S. Seetharaman: *Phosphorus Partition between Liquid Steel and CaO-SiO₂-P₂O₅-MgO Slag Containing low FeO*, Metallurgical and Materials Transactions B, 2007, 38B, p.357-66.
- [46] M. Hasegawa, M. Iwase, K. Wakimoto, and A. Mclean, *A thermochemical Study of the CaO+P₂O₅+FeO System-Regions in Equilibrium with Solid Ca₃P₂O₈*, Scandinavian Journal of Metallurgy, 2003, 32, 47-52.
- [47] J. Im, K. Morita, and N. Sano, *Phosphorus Distribution Ratios between CaO-SiO₂-FeO Slags and Carbon-saturated Iron at 1573 K*, ISIJ International, 1996, 36(5), pp.517-21.
- [48] B.O. Mysen, Relationships between Silicate Melt Structure and Petrologic Processes, Earth-Science Reviews, 1990, 27(4), p. 281-365
- [49] E. T. Turkdogan: *Fundamentals of steelmaking*, 1996, p.139.

- [50] C. Bodsworth and H. B. Bell: *Physical Chemistry of Iron and Steel Manufacture*, Longman, 1972, pp.96.
- [51] N. Sano and F. Tsukihashi, *Thermodynamics of Redox Equilibrium in Slags*, High Temperature Materials and Processes, 2001, 20(3-4), pp.263-268.
- [52] J. H. Pak, D. J. Min and H. S. Song, *Amphoteric Behavior of Alumina in Viscous Flow and Structure of CaO-SiO₂-(MgO)-Al₂O₃ Slags*, Metallurgical and Materials Transactions B, 2004, 35B, p.269-275.
- [53] Q. J. Li, *Thermodynamic Study on Vapourization of Niobium Oxides from Slag Melts*, Ph.D. Thesis, McMaster University, Hamilton, ON, 2009.
- [54] E. T. Turkdogan, *Physicochemical Aspects of Reactions in Ironmaking and Steelmaking Processes*, Transactions of the Iron and Steel Institute of Japan, 1984, 24, pp.591-611.
- [55] A. Mclean, Y. D. Yang, I. D. Sommerville, Y. Uchida and M. Iwase, *The Science and Technology of Slags for Iron and Steelmaking*, High Temperature Materials and Processes, 2001, 20, pp.185-193.
- [56] G. W. Toop and C.S. Samis, Activities of Ions in Silicate Melts, Transactions of the Metallurgical Society of AIME, 1962, 224, p. 878-87.
- [57] J. A. Duffy and M. D. Ingram, *An Interpretation of Glass Chemistry in terms of the Optical Basicity Concept*, Journal of Non-crystalline Solids, 1976, 21, p. 373-10.
- [58] J. A. Duffy and M. D. Ingram, Optical Basicity-IV: Influence of Electronegativity on the Lewis Basicity and Solvent Properties of Molten Oxyanion Salts and Glasses, Journal of Inorganic and Nuclear Chemistry, 1975, 37, p. 1203-06.
- [59] V. D. Eisenhuttenleute, *Slag Atlas*, Verlag Stahleisen GmbH, 1995, pp. 11.
- [60] T. Mori, *On the Phosphorus Distribution between Slag and Metal*, Transactions of the Japan Institute of Metals, 1984, 25, p. 761-71.
- [61] R. Nakamura, Y. Ueda, F. Noguchi: Proc. of 2nd Intl. Conf. of Metall. Slags and Fluxes, Metallurgical Society of AIME, 1984, p. 1005-13.
- [62] D. J. Sosinsky, D. I. Sommerville, The Composition and Temperature Dependence of the Sulfide Capacity of Metallurgical Slags, Metallurgical and Materials Transactions B, 1986, 17B, p. 331-37.
- [63] A. Bergman, Representation of Phosphorus and Vanadium Equilibria between Liquid Iron and Complex Steelmaking Slags, Transactions of the Iron and Steel Institute of Japan, 1988, 28(11), p. 945-51.
- [64] D. R. Gaskell, Optical Basicity and the Thermodynamic Properties of Slags, Metallurgical and Materials Transactions B, 1989, 20B, p. 113-18.
- [65] J. A. Duffy and M. D. Ingram, Comments on the Application of Optical Basicity to Glass, Journal of Non-Crystalline Solids, 1992(144), p. 76-80.
- [66] C. Wagner, *The Concept of the Basicity of Slags*, Metallurgical and Materials Transactions B, 1975, 6B, p. 405-409.
- [67] D. R. Gaskell, *On the Correlation between the Distribution of Phosphorus between Slag and Metal and the Theoretical Optical Basicity of the Slag*, Transactions of the Iron and Steel Institute of Japan, 1982, 22, p. 997-00.
- [68] A. Bergman, A. Gustafsson, *On the Relation between Optical Basicity and Phosphorus Capacity of Complex Slags*, Steel Research, 1988, 59, p. 281-89.

- [69] R. A. Young, *Use of the Optical Basicity Concept for Determining Phosphorus and Sulphur Slag/Metal Partitions*, EEC Report EUR 13176 EN, 1991.
- [70] J. O. Borode, *Phosphorus Partition Ratio and Phosphate Capacity of Na₂O-SiO₂ at 1400 °C*, *Ironmaking and Steelmaking*, 1998, 25(2), p. 144-49.
- [71] H. Suito, R. Inoue and M. Takada, *Phosphorus Distribution between Liquid Iron and MgO Saturated Slags of the System CaO-MgO-FeOx-SiO₂*, *Tetsu to Hagane*, 1981, 67(16), p. 2645-54.
- [72] A. Bergman, *The Application of Optical Basicity to Dephosphorization Equilibria*, *Steel Research*, 1990, 61, p. 347-52.
- [73] A.T. Morales and R.J. Fruehan, *Thermodynamic of MnO, FeO and Phosphorus in Steelmaking Slags with High MnO Contents*, *Metallurgical and Materials Transactions B*, 1997, 28B, p. 1111-18.
- [74] M. Hino and K. Ito, *Thermodynamic Data for Steelmaking*, Tohoku University Press, Sendai. 2009, p. 259-64.
- [75] S. Ohguchi, D. G. C. Robertson, B. Deo, P. Grieveson and J. H. E. Jeffes, *Simulation Dephosphorization and Desulphurization of Molten Pig Iron*, *Ironmaking Steelmaking*, 1984, 11, p. 202-13.
- [76] K. Mori, Y. Fukami and Y. Kawai, *Rate of Dephosphorization of Liquid Iron-Carbon Alloys by Molten Slags*, *Transactions of the Iron and Steel Institute of Japan*, 1988, 28, p. 315-18.
- [77] E. Shibata, H. Sun and K. Mori, *Kinetics of Simultaneous Reactions between Liquid Iron-Carbon Alloys and Slags Containing MnO*, *Metallurgical and Materials Transactions B*, 1999, 30B, p. 279-86.
- [78] C. P. Manning and R. J. Fruehan, *The Rate of the Phosphorus Reaction Between Liquid Iron and Slag*, *Metallurgical and Materials Transactions B*, 2013, 44B, p. 37-44.
- [79] A. Assis, J. Warnett, S. Spooner, R. Fruehan, M. Williams and S. Sridhar, *Spontaneous Emulsification of a Metal Drop Immersed in Slag Due to Dephosphorization: Surface Area Quantification*, *Metallurgical and Materials Transactions B*, 2015, 46B, p. 568-76.
- [80] S. Spooner, A. Assis, J. Warnett, R. Fruehan, M. Williams and S. Sridhar, *Investigation into the Cause of Spontaneous Emulsification of a Free Steel Droplet; Validation of the Chemical Exchange Pathway*, *Metallurgical and Materials Transactions B*, 2016, 47B, p. 2123-32.
- [81] M. S. Millman, A. Kapilashrami, M. Bramming and D. Malmberg: *Improving Phosphorus Refining*, European Commission, Luxembourg, 2011.
- [82] A. K. Hewage, B. K. Rout, G. Brooks and J. Naser, *Analysis of steelmaking kinetics from IMPHOS pilot plant data*, *Ironmaking and Steelmaking*, 2016, 43(5), p. 358-70
- [83] M.A. Rhamdhani, G.A. Brooks and K.S. Coley, *Kinetics of Metal/Slag Reactions during Spontaneous Emulsification*, *Metallurgical and Materials Transactions B*, 2005, vol. 36B, pp. 219-27.
- [84] K. ITO and N. Sano, *Phosphorus Distribution between Basic Slags and Carbon-saturated Iron at Hot-metal Temperatures*, *Transactions of the Iron and Steel Institute of Japan*, 1985, 25, p. 355-62.

- [85] J. J. Pak and R. J. Fruehan, *Soda Slag System for Hot Metal Dephosphorization*, Metallurgical and Materials Transactions B, 1986, 17B, pp. 797-03.
- [86] S. Seetharaman, A. Mclean, R. Guthrie and S. Sridhar, *Treatise on Process Metallurgy*, 2014, 3, p. 195.
- [87] K. Miyamoto, K. Naito, I. Kitagawa and M. Matsuo, *Estimation of Oxygen Potential at Slag/Metal Interface and Effect of Initial Slag Condition on Hot Metal Dephosphorization*, Tetsu-to Hagane, 2009, 95(3), p. 199-06
- [88] P. Wei, M. Sano, M. Hirasawa, M. Sano and K. Mori, *Estimation of Slag-Metal Interfacial Oxygen Potential in Phosphorus Reaction between FetO Containing Slag and Molten Iron of High Carbon Concentration*, ISIJ International, 1993, 33(8), 847-54.
- [89] J. O. M. Bockris, J. A. Kitchener, S. Ignatowicz, and J. W. Tomlinson, *Electric Conductance in Liquid Silicates*, Transactions of the Faraday Society, 1952, 48, p.75-91.
- [90] W. R. Dickson and E.B. Dismukes, *Electrolysis of FeO-CaO-SiO₂ Melts*, Transactions of the Metallurgical Society AIME, 1962, 224, p. 505-11.
- [91] M. T. Simnad, G. Derge, and I. Gerorge, *Ionic Nature of Liquid Iron-Silicate Slags*, Transactions of the Metallurgical Society AIME, 1954, 200, p. 1386-90.
- [92] K. Mori and Y. Matsushita, *The Electrical Conductivity of Molten Binary Slags*, Tetsu-to Hagane, 1952, 38(5), p. 6-12.
- [93] E. A. Dancy and D.J. Derge, *The Electrical Conductivity of FeO-CaO Slag*, Transactions of the Metallurgical Society AIME, 1966, 236, p.1642-48.
- [94] J. L. Speelman, W. F. Caley and K. G. Leewis, *Electrochemical Transport Through A Lime-Silica-Alumina Slag*, Metallurgical and Materials Transactions B, 1989, 20B, p. 31-37.
- [95] M. Sasabe and A. Asamura, *Transport Phenomenon of Oxygen through Molten Slags*, Proceeding 2nd International Symposium On Metallurgical Slags and Fluxes, TMS-AIME, Warrendale, PA., 1984, P. 651-67.
- [96] N.F. Mott, *Conduction in Glasses Containing Transition Metal Ions*, Journal of Non-crystalline Solids, 1968, 1, p. 1-17.
- [97] M. Barati and K. Coley, *Electrical and Electronic Conductivity of CaO-SiO₂-FeO_x Slags at Various Oxygen Potentials: part II. Mechanism and A Model of Electronic Conduction*, Metallurgical and Materials Transactions B, 2006, 37B, pp. 51-60.
- [98] M. Barati and K. Coley, *Electrical and Electronic Conductivity of CaO-SiO₂-FeO_x Slags at Various Oxygen Potentials: Part I. Experimental Results*, Metallurgical and Materials Transactions B, 2006, 37B, pp. 41-49.
- [99] N. Standish and Q. L. He, *Drop Generation Due to An impinging Jet and The Effect of Bottom Blowing in The Steelmaking Vessel*, ISIJ International, 1989, 29(6), p. 455-461
- [100] Q. L. He and N. Standish, *A Model Study of Droplet Generation in the BOF Steelmaking*, ISIJ International, 1990, 30(4), p. 305-309
- [101] R. Li and R. L. Harris: *Interaction of Gas Jets with Model Process Liquids*, Pyrometallurgy 95 Conference Proceeding, IMM, London, 1995, p.107.

- [102] Subagyo, G. A. Brooks, and K. S. Coley, *Generation of Droplets in Slag Metal Emulsion through Top Gas Blowing*, ISIJ Internatioanl 2003, 43(7), p.983-989.
- [103] Subagyo, G. A. Brooks, and K. S. Coley, *Interfacial Area in Top Blown Oxygen Steelmaking*, Ironmaking Conference Proceeding, 2002, pp.837-50.
- [104] S. C. Koria and K. W. Lange, *A New Approach to Investigate the Drop Size Distribution in Basic Oxygen Steelmaking*, Metallurgical and Materials Transactions B, 1984, 15B, p. 109-116.
- [105] S. C. Koria and K. W. Lange, *Estimation of Drop Sizes in Impinging Jet Steelmaking Processes*, Ironmaking and Steelmaking, 1986, 13(5), p.236-240.
- [106] J. Schoop, W. Rech and G. Mahn, *Reactions Occurring During the Oxygen Top Blown Process and Calculation of Metallurgical Control Parameters*, Ironmaking and Steelmaking, 1978, 2, p.72-79.
- [107] F. Oeters, *Kinetic Treatment of Chemical Reactions in Emulsion Metallurgy*, Steel Research International, 1985, 56, p.69-74.
- [108] F. Oeters, *Metallurgy of Steelmaking*, 1994, Verlag Stahleisen mH, Dusseldorf, pp. 368.
- [109] L. A. Baker and R. G. Ward, *Reaction of an Iron Carbon Droplet during Free Fall through Oxygen*, Journal of The Iron and Steel Institute, 1967, 205, p. 714-17.
- [110] L. A. Baker, N. A. Warner and A. E. Jenkins, *Decarburization of a Levitated Iron Droplet in Oxygen*, Transactions of The Metallurgical Society of AIME, 1967, 239, p. 857-64.
- [111] L. A. Baker, N. A. Warner and A. E. Jenkins, *Kinetics of Decarburization of Liquid Iron in an Oxidizing Atmosphere Using the Levitation Technique*, Transactions of The Metallurgical Society of AIME, 1964, 230, p. 1228-35.
- [112] H. Sun, K. Gao, V. Sahajwalla, K. Mori and R. D. Pehlke, *Kinetics of Gas Oxidation of Liquid Fe-C-S Alloys and Carbon Boil Phenomenon*, ISIJ International, 1999, 39(11), pp. 1125-33.
- [113] K. Gao, V. Sahajwalla, H. Sun, C. Wheatley and R. Dry, *Influence of Sulfur Content and Temperature on the Carbon Boil and CO Generation in Fe-C-S Drops*, ISIJ International, 2000, 40(4) , p. 301-08.
- [114] H. Sun, *Reaction Rates and Swelling Phenomenon of Fe-C Droplets in FeO bearing Slag*, ISIJ International, 2006, 46(11), p.1560-69.
- [115] G. G. Krishna Murthy, Y. Sawada and J. F. Elliott, *Reduction of FeO Dissolved in CaO-SiO₂-Al₂O₃ Slags by Fe-C Droplets*, Ironmaking and Steelmaking, 1993, 20(3), p.179-190.
- [116] S. D. Lubetkin, *Why is it Much Easier to Nucleate Gas Bubbles Than Theory Predicts?*, Langmuir, 2003, 19, p. 2575-87.
- [117] R. S. Kaplan and W. O. Philbrook, *The Rate of CO Bubble Nucleation at Oxide Metal Interfaces within Liquid Iron Alloys*, Metallurgical and Materials Transactions B, 1972, 3B, p. 483-87.
- [118] H. S. Levine, *Homogeneous Nucleation of CO Bubbles in Fe-C-O Melts*, Metallurgical and Materials Transactions B, 1973, vol. 4, p. 777-82.
- [119] H. S. Levine, *Surface Structure Concepts in the Theory of Homogeneous Bubble Nucleation*, Metallurgical and Materials Transactions B, 1974, 5, p. 953-55.

- [120] H. S. Levine, *Formation of Vapor Nuclei in High Temperature Melts*, Journal of Physical Chemistry, 1972, 76(18), p. 2609-14.
- [121] H. Kwak and S. Oh, *A Model of Homogeneous Bubble Nucleation of CO Bubbles in Fe-C-O Melts*, Journal of Colloid and Interface Science 198, 1998, pp.113-18.
- [122] T. Gare and G. S. F. Hazeldean, *Basic Oxygen Steelmaking: Decarburization of Binary Fe-C Droplets and Ternary Fe-C-X Droplets in Ferruginous Slags*, Ironmaking and Steelmaking, 1981, 8(4), p.169-181.
- [123] D. G. C. Robertson and A. E. Jenkins, *The Reaction of Liquid Iron and Its Alloys in Pure Oxygen: Heterogeneous Kinetics at Elevated Temperatures*, University of Pennsylvania, Philadelphia, PA, 1970, p.393-408.
- [124] N. H. Ei-Kaddah and D. G. Robertson, *Homogeneous Nucleation of Carbon Monoxide Bubbles in Iron Drops*, Journal of Colloid and Interface Science, 1977, 60, p. 349-60.
- [125] M. Volmer, *Kinetic of Phase Formation*, Theodor Steinkopff, Dreseden, 1939, p.149-154.
- [126] V. P. Carey, *Liquid-vapor Phase Change Phenomena*, 2008, New York, Taylor & Francis.
- [127] P. G. Bowers, K. Bar-Eli and R. M. Noyes, *Unstable Supersaturated Solutions of Gases and Nucleation Theory*, Journal of Chemical Society, Faraday Transactions, 1996, 92(16), pp.2843-49.
- [128] T. K. K. Ankit, *Modeling of Dephosphorization using Bloated Droplet Theory in Basic Oxygen Steelmaking*, 4th National Conference on Processing and Characterization of Materials, IOP Publishing, (2015)
- [129] N. Dogan, G. A. Brooks and M. A. Rhamdhani, *Comprehensive Model of Oxygen Steelmaking Part 1:Model Development and Validation*, ISIJ International, 2011, 51(7), pp. 1086-92.
- [130] N. Dogan, G. A. Brooks and M. A. Rhamdhani, *Comprehensive Model of Oxygen Steelmaking Part 2:Application of Bloated Droplet Theory for Decarburization in Emulsion Zone*, ISIJ International, 2011, 51(7), pp. 1093–01.
- [131] N. Dogan, G. A. Brooks and M. A. Rhamdhani, *Comprehensive Model of Oxygen Steelmaking Part 3: Decarburization in Impact Zone*, ISIJ International, 2011, 51(7), pp. 1102–09.
- [132] B. K. Rout, G. Brooks and M. Rhamdhani, *Transient Behavior of Dephosphorization Kinetics in Oxygen Steelmaking*, AISTech 2015 Proceedings, 2015, 3225-37.
- [133] B. K. Rout, G. Brooks, Z. Li and M. Rhamdhani, *Dynamic Modeling of Oxygen Steelmaking Process:A Multi-Zone Kinetic Approach*, AISTech 2017 Proceedings, (2017), 1315-25.
- [134] John R. Taylor, *An Introduction to Error Analysis: The Study of Uncertainties in Physical Measurements*, University Science Books, 1997.